Universidade de São Paulo
Instituto de Geociências

TECTONIC EVOLUTION OF THE SOUTHERN ESPINHAÇO FRONT IN SERRA DO CIPÓ-MG

Henrique Chaves Joncew

Orientador: Ginaldo A. C. Campanha

2024

Universidade de São Paulo
Instituto de Geociências

TECTONIC EVOLUTION OF THE SOUTHERN ESPINHAÇO FRONT IN SERRA DO CIPÓ-MG

Henrique Chaves Joncew

Tese apresentada ao Programa de Pós-Graduação em Geoquímica e Geotectônica como requisito para a obtenção do título de Doutor em Ciências.

Área de concentração: Geotectônica

Orientador: Prof. Dr. Ginaldo Ademar da Cruz Campanha

2024

Serviço de Biblioteca e Documentação do IGc/USP
Ficha catalográfica gerada automaticamente com dados fornecidos pelo(a) autor(a)
via programa desenvolvido pela Seção Técnica de Informática do ICMC/USP

Bibliotecários responsáveis pela estrutura de catalogação da publicação:
Sonia Regina Yole Guerra - CRB-8/4208 | Anderson de Santana - CRB-8/6658

Joncew, Henrique Chaves
Tectonic evolution of the Southern Espinhaço Front in Serra do Cipó-MG / Henrique Chaves Joncew; orientador Ginaldo Ademar da Cruz Campanha. -- São Paulo, 2024.
248 p.

Tese (Doutorado - Programa de Pós-Graduação em Geoquímica e Geotectônica) -- Instituto de Geociências, Universidade de São Paulo, 2024.

1. Fold-and-thrust belt. 2. Strain analysis. 3. Geochronology. 4. EBSD. 5. Fluid inclusions. I. Campanha, Ginaldo Ademar da Cruz, orient. II. Título.

Universidade de São Paulo
Instituto de Geociências

TECTONIC EVOLUTION OF THE SOUTHERN ESPINHAÇO FRONT IN SERRA DO CIPÓ-MG

Henrique Chaves Joncew

Orientador: Prof. Dr. Ginaldo Ademar da Cruz Campanha

Tese de doutorado
N° 673

COMISSÃO JULGADORA

Dr. Ginaldo Ademar da Cruz Campanha
Dr. Luiz Guilherme Knauer
Drª. Gláucia Nascimento Queiroga
Drª. Renata da Silva Schmitt
Dr. Carlos José Archanjo

São Paulo
2024

Mom,

Dad,

Dany,

Amanda.

“A blade of grass is a commonplace on Earth; it would be a miracle on Mars.”

– Carl Sagan

"If you try and take a cat apart to see how it works, the first thing you have on your hands is a non-working cat."

– Douglas Adams

“I try all things, I achieve what I can.”

– Herman Melville

“If we knew what it was we were doing, it would not be called research, would it?”

– Albert Einstein

ACKNOWLEDGEMENTS

This thesis was no easy task. I had to face a lot of stuff I was not prepared for. I had to move to a city I had little in common with (twice!). I had to leave my family and friends behind. I had to work in isolation through a pandemic. I had to endure systemic disregard and sabotage to universities, public education and scientific thinking. And I had to learn to live with myself. Too many nuances with so many people involved, so they definitely deserve some recognition here.

Acknowledgements such as this usually begin with the professional part, moving on later to personal notes. These last few years, though, blurred the lines between those two and called to attention the fact that a good support team is valuable for good work. In fact, building a support frame, weak or strong, always precedes the bulk of the work, so I will straight up switch that order around.

I start by thanking Amanda, my light and life companion, for her support and patience in all aspects of our lives. Also, my mom, my dad and my sister who made me realize I left BH, but I never left home. Speaking of home, thanks are in order also to Vilma, who has always made incredible effort to keep us all cared for.

Not a thing changed with the distance to my friends from school, college and life. Or maybe it did, I feel we are closer now than we were before. And, though I like to mostly keep to myself, I made a few good connections in São Paulo as well.

Some of these people did not only support me, but also played a role in getting this work actually done, namely Amanda (again), Ruy, Raphael, Leandro, Tayná and Raul.

Times got rough for me personally too, so I cannot stress how important my sessions with Rita were over the course of the past years. I also encourage everyone reading this to care for their mental health, even if it does not seem like you need to.

I thank my advisor, Ginaldo, for his, well, advice, as well as his help, for taking such an invested and helping role during the entire course of this work. I also congratulate him on somehow managing to survive my company in the meantime.

Thanks are in order to Professor Pedro Rossi-Vieira, from Uni-BH, and his class, for exchanging views and field points and descriptions that were very important for me to finish the map and have a better look of and at some lithological contacts.

I also must thank all the staff of the CPGeo-IGC-USP, Melina Esteves, Klaus Wemmer, Ruy (again), Bruno Ribeiro and Leonardo Lagoeiro, who were so attentive and helpful. Without them, all the work done here with radiometric dating, statistics, fluid inclusions and EBSD would, simply put, not exist, or at the very least would be quite questionable.

I am also grateful for the inputs, tips and advice to my work by Profs. Frederico and Bley. I am also somewhat impressed and thankful for getting the opportunity to work at the Institute of Geoscience of the University of São Paulo. The university does not make the student, but high-level facilities, personnel and community surely make studying a lot easier.

More than thank them, I want to congratulate all the USP and IGc staff for keeping such a fantastic structure working at high level and in pristine conditions of performance, yes, but also hygiene. I like to think them as represented by Neuza, with whom I exchanged nice little chats, and her cleaning crew.

When I joined the program, we did not have a funded project at the time. We could work with some funds, but a lot of our research could only happen after Ginaldo received a grant from FAPESP (2019/25599-9), so I thank them for that. Speaking of funding, I would not be able to sustain myself in São Paulo and work closely with my research at all times without the stipends from CAPES.

To anyone who has played any role helping finish my doctorate, I thank you very, very much and wish you all the best.

A FORE NOTE ABOUT THE STRUCTURE OF THIS THESIS

The original plan for the structure of this thesis was to follow a traditional “research report” format. Taking the time to explain and guide the reader through your steps makes reading easier. On the other hand, more often than not works following this structure end up with tomes hundreds of pages long and, naturally, demand a long time to write.

As time went by and the volume of data we acquired during our work grew, we found that changing to the format of a collection of articles would be more suitable to getting the thesis finished within the deadline. This style has the advantage of leaving candidates (in this case, me) to whatever title they are pursuing (my doctorate) more time to focus on getting their data ready for publication, while also producing shorter and, thus, quicker-to-write texts.

However, though (and because) a scientific article is much more objective than a research report, it is also a heavier read. In terms of language, the limits academic journals impose limits to the number of pages an article may have to meet standards for publication. This calls not only for an objective layout, but also for textual constructions that make the texts dense. Authors do not gloss over the goal of their work, the methods deployed, the results obtained and their interpretations, but less is offered to familiarize the reader with the problem at hand and, more importantly, to describe the chains of thought that led to the conclusions drawn from the work. The reader must mentally fill in some blanks and connect some dots to follow what is on paper – and, if necessary, give feedback.

For the more experienced, that becomes natural through practice, but for beginners, not so much. With that in mind, we made an effort to make the articles and the thesis accessible for the widest public possible, but we cannot give up the academic rigor of its circumstances.

Another aspect of the article format that makes it not so appealing is that the structure of the text becomes repetitive. In (geological, in this case) journals, an article about an Omani ophiolite may be followed by another about a Canadian fold-and-thrust belt. But within a thesis or dissertation, articles address the same target area. While methods, results, discussions and conclusions differ, there is also a series of abstracts, introductions and contextualization addressing the same region, making the read more tiring. Not only that, with many topics covering similar themes, the reader might have trouble to go back and forth on the text to find desired pieces of information.

After we had the layouts of the academic papers set, and after some discussions, we finally landed on a hybrid format. We broke the articles apart and reorganized the many pieces in an order closer to the research report structure. The result is as follows:

Chapter 1 introduces the problems we tackle in each article. Next come brief reviews on the state of the art of the knowledge about foreland fold-and-thrust belts (Chapter 2), the Southern

Espinhaço Range and the São Francisco Craton (Chapter 3). Our bibliographic reviews are brief, as a kind of support material for a better understanding of the work executed for this thesis.

Chapters 4 to 9 contain the practical side and the results of our work. Unique chapters were dedicated to the methods used in this study. In each chapter, we offer a brief review of the principles behind each method, how it was applied in this study and its respective results, discussions and conclusions. We aimed to make each chapter independent from the others, in case a reader is interested only in particular aspects of our work, but the order we present the methods in was chosen to make for a cohesive text and a logical, coherent read.

In Chapter 4, we present the results of the geological mapping and characterization of the structural framework of the region of Serra do Cipó, also commenting how our observations meet or go against those made in previous studies on the area. A particular stratigraphic discussion follows in Chapter 5, which brings U-Pb ages of detrital zircons from quartzitic units from the region of study area. Structural aspects are expanded on in Chapters 6 and 7: Chapter 6 brings strain analyses by the Shape Preferred Orientation (SPO) method and reconstructions of strain axes and ellipsoids; and Chapter 7 presents electron backscatter diffraction analyses. Chapter 8 changes focus to the conditions of pressure and temperature in force during regional deformation, estimated via the analysis of fluid inclusions. Chapter 9, in turn, brings the age of said deformation, obtained by K-Ar and Rb-Sr in mica from the study area.

This structure is effective and makes chapters self-contained. However, it also leaves little space for further deliberations. Chapter 10 ties the loose ends left behind by this approach, including where our work sits in the light of previous studies and how the various results obtained in this work and their interpretation connect with each other to refine our overall interpretation of data.

Chapter 11 brings the thesis to a close and summarizes our findings.

References cited in the text are organized chronologically (earlier releases first) and, for works published in the same year, alphabetically by first author surname. At the end of the thesis, we list all the references cited, organized alphabetically by first author surname and, for works under the same authorship, by publish year (earlier releases first). This organization follows the standard norm of the Geological Society of America (GSA), commonly used by the main journals in the field of Geoscience

Other materials are presented in the Appendices. Appendices A, B bring, respectively, our revised geological map of the area and respective cross-sections. We also include a map with the field points described in the area in Appendix C.

It would be impractical to include the full results of a number of our methods in the text body, namely the full tables of results obtained by the U-Pb analyses of detrital zircons, the K-S test results and the *in situ* Rb-Sr dating of muscovite. These data are located, respectively, in Appendices D, E and F.

Our descriptions of methodological approaches, results and discussions were taken, with minor alterations for textual cohesion, from the academic articles produced during the course of this study.

This way, we hope to deliver a thesis that makes for a lighter (or less heavy) read than a sequence of academic papers, but still managing to present itself objectively and where the reader may readily find a particular group of information of their interest. The author (henriquecj.geologia@gmail.com) and the advisor (ginaldo@usp.br) put themselves at the service of anyone who wishes help to understand this text, more information about the research, or to discuss our findings.

ABSTRACT

The tectonic evolution of the Southern Espinhaço Front was characterized in the region of Serra do Cipó-MG, using geologic mapping and field structural, strain, quartz crystallographic axes patterns by EBSD and fluid inclusion analyses, as well radiometric dating by K-Ar and *in situ* Rb-Sr of mica and U-Pb of detrital zircons. The region was divided in two main tectonic domains: the Foreland (west) and the Fold-and-Thrust Belt (east). The stratigraphy of the Foreland Domain is composed by the São João da Chapada Formation (Espinhaço Supergroup), and the Sete Lagoas and Serra de Santa Helena formations (Bambuí Group). The Fold-and-Thrust Domain is made up by upper formations of the Espinhaço Supergroup – Galho do Miguel, Santa Rita and Córrego dos Borges. The limit between these domains is the Southern Espinhaço Front, marked by a main thrust fault or shear zone, with a NNW-SSE trend, and stratigraphic inversion of the Santa Rita and Sete Lagoas formations. A series of parallel thrust faults are present in both domains, accompanied by development of east-dipping flattening foliations and stretch lineations, and structures associated with the deformation, such as tight folds and asymmetric kinematic indicators, all indicating tectonic vergence from east to west. In the Foreland Domain, the São João da Chapada Formation is a local rigid basement to the Bambuí Group, sitting below a basal detachment separating it from the Sete Lagoas Formation. Strain analysis showed predominant oblate ellipsoids, with east low-dipping flattening planes (XY) and lineations (X) coherent with the regional context. At intracrystalline level, quartz [c] and <a> axes suggest a combination of pressure dissolution and dislocation glide mechanisms. Pressure dissolution is the primary deformation mechanism for the fine-grained fractions of the rocks, while dislocation glide is the main mechanism for the larger grains. The rhombohedral system is the most active for dislocation glide, but the basal system is also significant in the foreland domain. Fluid inclusion analysis has shown that the circulation of metamorphic fluids was very limited in the area during deformation. The populations of fluid inclusions in each compartment are different, suggesting most likely an origin from intra-basinal brines. By crossing metamorphic paragenesis, fluid inclusion, illite crystallinity and EBSD data, we estimate that deformation occurred within 300-411 ºC and 1.7-6.0 kbar ranges in the foreland, while the fold-and-thrust belt experienced conditions of 385-450 ºC and 2.8-8.0 kbar. *In situ* Rb-Sr dating of muscovite indicate a metamorphic peak age of 548.8 ± 17.1 Ma, while K-Ar ages of fine fractions of the same mineral yielded results of 510.3 ± 5.3 to 432.6 ± 7.5 indicating successive cooling stages. We propose that the fold-and-thrust belt evolved as a Coulomb wedge driven by the tectonic forces generated by the lateral spread and the buoyancy of the orogenic building. In this context, the region experienced progressive deformation, which caused crustal thickening until the system reached a critical taper condition, when a new thrust would cause the advance of the

orogenic front onto the foreland, and the process would repeat itself until the orogenic activity ceased and isostatic equilibrium was achieved.

Keywords: Fold-and-thrust belt, strain analysis, geochronology, fluid inclusions, EBSD.

RESUMO

Este trabalho caracteriza a evolução do *Front* do Espinhaço Meridional na região da Serra do Cipó-MG por meio de mapeamento geológico e análises estruturais de campo, *strain*, eixos cristalográficos de quartzo por EBSD e inclusões fluidas em veios de quartzo, além de datações radiométricas K-Ar e Rb-Sr *in situ* em mica e U-Pb em zircões detríticas. A região foi dividida em dois domínios tectônicos: o antepaís (oeste) e o cinturão de dobras e cavalgamentos (leste). O antepaís é composto pela Formação São João da Chapada (Supergrupo Espinhaço) e pelas formações Sete Lagoas e Serra de Santa Helena (Grupo Bambuí). O cinturão de dobras e cavalgamentos é constituído por formações superiores do Supergroup Espinhaço (Galho do Miguel, Santa Rita e Córrego dos Borges). A fronteira entre os domínios é demarcada pelo *Front* do Espinhaço, um empurrão ou zona de cisalhamento reversa de direção NNW-SSE, e pela inversão estratigráfica das formações Santa Rita e Sete Lagoas. Uma série de falhas de empurrão e zonas de cisalhamento reversas paralelas à estrutura principal ocorrem em ambos os compartimentos, acompanhadas pelo desenvolvimento de foliação de achatamento e lineações de estiramento mergulhantes para leste e por estruturas associadas à deformação como dobras assimétricas e indicadores cinemáticos, invariavelmente apontando vergência para oeste. No Domínio do Antepaís, a Formação São João da Chapada constitui o embasamento rígido do Grupo Bambuí. Essas unidades são separadas por uma superfície de descolamento. A análise de *strain* apontou elipsoides de deformação predominantemente oblatos, e planos de achatamento (XY) e direções de estiramento (X) coerentes com o contexto regional. Em nível intracristalino, os eixos [c] e <a> de quartzo sugerem deformação por uma combinação de dissolução por pressão e deslizamento de defeitos intracristalinos. A dissolução por pressão é o principal mecanismo nas frações granulométricas mais finas das rochas, enquanto o deslizamento de defeitos intracristalinos é o mecanismo primário nas frações mais grossas. O sistema romboédrico de deslizamento foi o mais ativo durante a deformação, porém há evidências da ocorrência de deslizamento ao longo do plano basal em rochas do antepaís. Cada domínio tectônico contém sua própria população de inclusões fluidas, sugerindo que os fluidos que originaram os veios de quartzo eram provavelmente salmouras e águas meteóricas intrabacinais. Combinando-se as paragêneses metamórficas e dados de inclusões fluidas, cristalinidade da ilita, e EBSD, é possível estimar que a deformação ocorreu a 300-411 ºC e 1.7-6.0 kbar no antepaís e a 385-450 ºC e 2.8-8.0 kbar no cinturão de dobras e cavalgamentos. Segundo a datação Rb-Sr *in situ* em muscovita, o pico metamórfico local ocorreu há 548.8 ± 17.1 Ma, e idades de frações finas do mesmo mineral foram datadas entre 510.3 ± 5.3 e 432.6 ± 7.5 Ma, com indicativo de estágios sucessivos de resfriamento. A proposta aqui apresentada é a de que o cinturão de dobras e cavalgamentos evoluiu segundo o modelo de cunha de Coulomb, controlado

pelas forças tectônicas geradas pelo espalhamento lateral e pelo empuxo das raízes do edifício orogênico. Nesse contexto, a região de estudo passou por uma sucessão de períodos de espessamento crustal – marcado por deformação progressiva – até que se alcançasse o ângulo de abertura crítico da cunha, o que, no incremento de deformação posterior, causou a formação das frentes de empurrão que marcam as fases de avanço do cinturão de cavalgamentos sobre o antepaís. O processo permaneceu ativo até o fim da atividade orogênica e o reestabelecimento do equilíbrio isostático.

Palavras-chave: Cinturão de dobras e cavalgamentos, análise de deformação, geocronologia, inclusões fluidas, EBSD.

CONTENTS

LIST OF FIGURES

LIST OF TABLES

1. INTRODUCTION

Since the 19th Century, the Espinhaço Range, in all its extension, and its surroundings are major targets of the Geoscience community. Countless pioneering studies have significantly contributed to the original definitions of the São Francisco Craton and the Araçuaí Belt – and other orogenic belts – by Almeida (1967, 1977). Ever since, another myriad of works have consolidated and deepened our knowledge about both provinces.

In short, the São Francisco Craton is a peninsular remnant of the São Francisco-Congo paleocontinent. The Araçuaí Orogen, together with its African counterpart, the West Congo Belt (or the Araçuaí-West Congo Orogen), was built with the closure of the Adamastor Ocean, an oceanic basin that separated the São Francisco peninsula from the Congo landmass (Pedrosa-Soares et al., 1992, 1998; Alkmim et al., 2006), as one of the many Ediacaran-Cambrian belts erected during the Brasiliano-Pan African Orogenic Cycle, which ended with the formation of the West Gondwana megacontinent. In this context, the Southern Espinhaço Range (SER) is a west-verging foreland fold-and-thrust belt marking the limit between the Araçuaí Orogen, to the east, and the São Francisco Craton, to the west (Alkmim et al., 2007).

However, when it comes to Structural Geology, some aspects still demand more studies. This gap, together with the emergence of new data in other fronts, naturally leaves some questions about the geological history of the São Francisco Craton and the Araçuaí Orogen – and, by extension, the South American Platform – unanswered, e.g.:

A) How extense was the Adamastor Ocean?

B) What role, if any, did intracontinental deformation play in the formation of West Gondwana?

C) Did the various Ediacaran-Cambrian epicontinental seas share any form of connection?

D) What kind of imprints did the Araçuaí Orogeny leave in Bambuí Group, the foreland cover of the São Francisco Craton?

E) How did the accretion of Archean tectonostratigraphic terranes affect the final structure of the Araçuaí Orogen?

Points **A**, **B** and **C** have been and remain to be constantly object of discussion (e.g. Pedrosa-Soares et al., 1998; Aracema et al., 2000; Alkmim et al., 2006; Cavalcante et al., 2019; Fossen et al., 2020; Konopásek et al., 2020; Amaral et al., 2020; Caxito and Alkmim, 2023). Point **D** was been addressed by Magalhães (1988), Uhlein (1991), Alkmim and Martins-Neto (2001), Reis (2016) and Reis et al. (2017). At local scale, this was done by Oliveira (1994) and Knauer (1999), but further development is needed after new stratigraphic data concerning the Bambuí Group (e.g. Pimentel et al., 2011; Paula-Santos et al., 2015, 2017; Moreira et al., 2020; Tavares et al., 2020) has come to light, a task recently taken up by Taufner et al. (2021). Point **E**, in turn, has been historically overlooked.

This thesis was part of the project *Tectonic analysis of key areas of the Southern Espinhaço thrust front*, which originally tackled the aforementioned points **D** and **E** through the study of five areas situated on the craton-orogen transition (1 and 3), the interaction with the Guanhães Block (2 and 4), in the fold-and-thrust domain of the Araçuaí Orogen. Later on, an area inside the São Francisco Craton, in an inverted aulacogen (Area 5), was added to the scope of the project to analyze point **B** above. The target of this work is Area 1, at the border between the Cipó Range, a segment of Southern Espinhaço Range at its southern end, and the São Francisco Craton, where we study the evolution of the foreland fold-and-thrust belt and its effects on the Espinhaço Supergroup and the Bambuí Group (Figure 1).

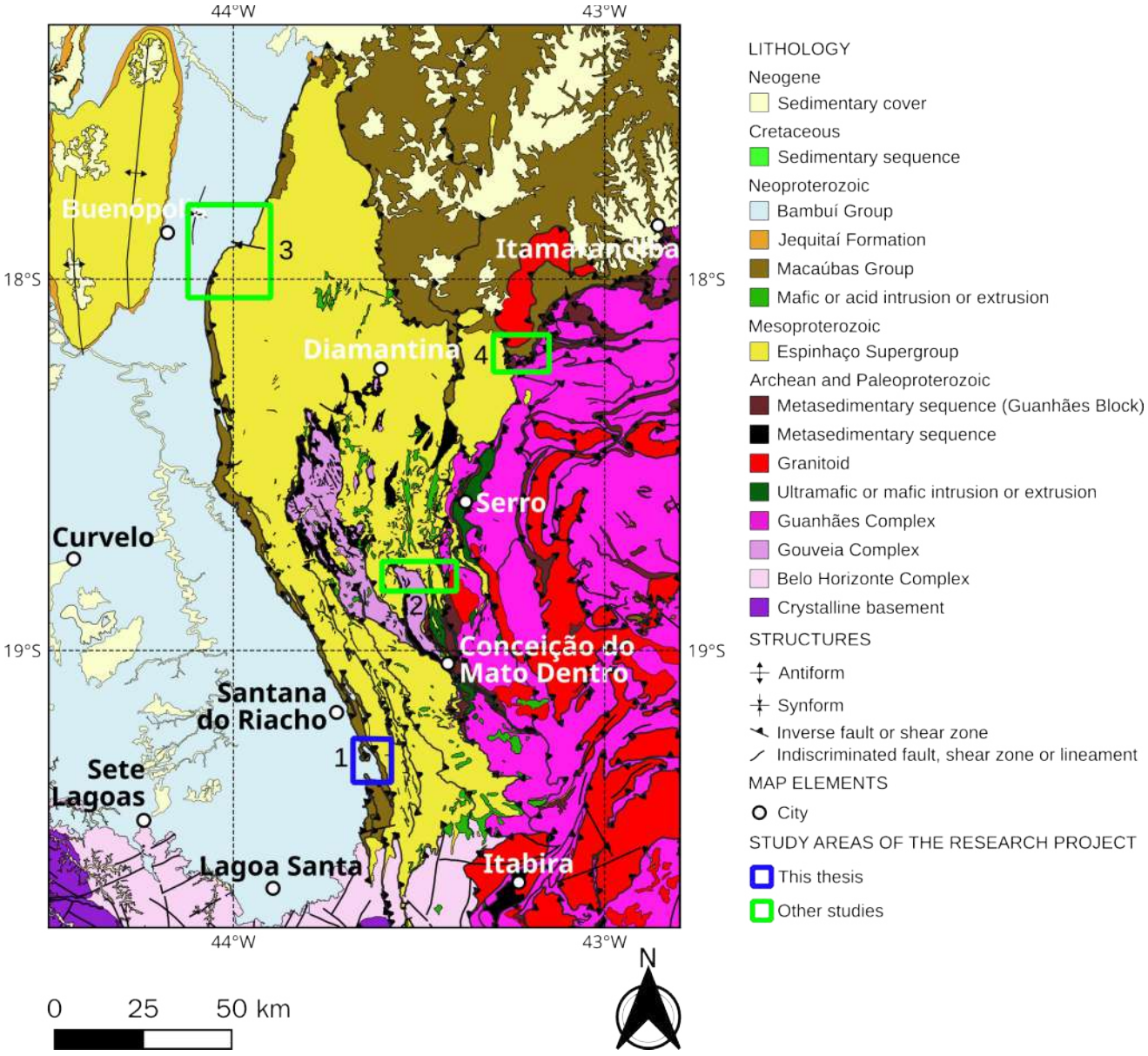

Figure 1. Map of the Southern Espinhaço Range and its limit with the São Francisco Craton (modified from Cordani et al., 2016). Rectangles indicate locations of areas contemplated by the research project Análise tectônica de áreas-chave do front de empurrões do Espinhaço Meridional (blue: this study, green: remaining areas).

The study area encompasses the vicinities of the Serra do Cipó district, central Minas Gerais state, Brazil, situated approximately 70 km northeast of Belo Horizonte, the state capital (Figure 2). The adjacent range and the district get their names from the Cipó River, the most important local drainage agent. The Southern Espinhaço Front is the dominant structure in the region, separating the fold-and-thrust domain of the orogen from the continental foreland with a NNW-SSE trend. The front heaves the Mesoproterozoic Espinhaço Supergroup over the Ediacaran-Cambrian Bambuí Group. The contact between these units marks the conventional border of the Araçuaí Orogen and the São Francisco Craton. The E-W trending Bocaina Fault is another important structure of the region, cutting both compartments and the thrust front, with normal slump of the terrane north of the fault surface.

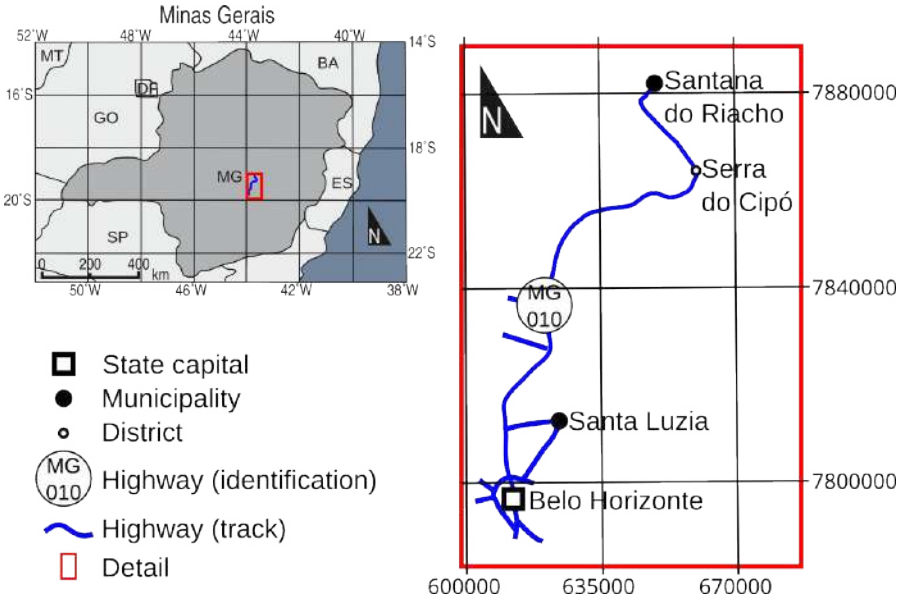

Figure 2. Situation and access to Serra do Cipó from Belo Horizonte-MG.

1.1. The main problem

While the assembly of West Gondwana has been interpreted as finished in the Ediacaran, based on geochronological and geotectonic evidence (Pisarevsky et al., 2008; Cordani et al., 2009, 2013; Amaral et al., 2012; Pimentel, 2016), even studies that adopt this premise call for a refinement concerning sedimentary provenance and the possibility of multiple non-synchronous collisions for the construction of some of the orogenic segments (Pimentel et al., 2011; Meira et al., 2015). Moreover, the Bambuí Group represents the foreland sedimentation associated with the Brasília and Araçuaí Orogenic fronts (Chang et al., 1988; Pimentel et al., 2001; Martins-Neto et al., 2001; Martins-Neto, 2009), and new U-Pb ages show that deposition of the unit had merely started (~635Ma) in the Ediacaran Period, extending into the Cambrian Period up until 524 Ma (Caxito et al., 2012; Moreira

et al., 2020; Tavares et al., 2020). This raises questions about the duration of orogenic activity of systems involved in the deposition of the Bambuí Group and, thus, the formation of West Gondwana.

The craton-orogen limits are ideal zones to elucidate such questions. For the Araçuaí Orogen, Magalhães (1988), Uhlein (1991), Oliveira (1994), Knauer (1999), Araújo et al. (2020) and Taufner et al. (2021) addressed the structural relations between the fold-and-thrust and foreland domains. Three of these studies (Magalhães, 1988; Oliveira, 1994; Taufner et al., 2021) were conducted in the region of Serra do Cipó. Together with regional maps by Oliveira et al. (1997) and Ribeiro (2010), these works provided an excellent cartographic and structural start points for this thesis.

1.2. The secondary problem

During the course of this work, we observed that the various stratigraphic models proposed for the quartzites and metaconglomerates found in Serra do Cipó did not fit the characteristics of the rocks observed on the field, making it difficult to define the nature of contacts and stratigraphic and structural relations between these units and, thus, to propose a coherent tectonic evolution model for the Espinhaço fold-and-thrust front in the region. Furthermore, these models never made their reasons to classify rocks from the region into one lithological unit or another explicit.

1.3. Objectives

The main objective of this thesis is to characterize the tectonic evolution of the Espinhaço fold-and-thrust front and its impacts on the structure of the Espinhaço Supergroup and the Bambuí Group in the region of Serra do Cipó. For that, we described the local structural framework and analyzed the age, geometry (that is, the spatial distribution and shape of the deformation ellipsoids) and conditions of pressure and temperature of the deformation that affected the region in the Ediacaran-Cambrian. In addition, we surveyed the U-Pb age spectra of the quartzites and metaconglomerates from the study area to increase the reliability of our proposed stratigraphy, geological map and tectonic model.

1.4. Methodological approach

To achieve our goals, we resorted to a multiproxy approach, including field and laboratory methods. Our field campaigns amounted to 21 days and were dedicated to the description of macro and mesoscopic descriptions of rocks and geological structures, complemented later by petrographic analyses on thin sections. We also performed a series of analytical studies as follows:

1. U-Pb dating of detrital zircons via the LA-ICP-MS method;
2. Dating of micaceous minerals via the *in situ* Rb-Sr and K-Ar in fine fraction methods;
3. Shape Preferred orientation (SPO) analysis;

4. Electron back scatter diffraction (EBSD);

5. Fluid inclusion analysis.

The concepts and our application of each method are addressed over the course of this thesis, in their respective chapters, followed by the results yielded by each study.

2. FORELAND FOLD-AND-THRUST BELTS

The Southern Espinhaço Range is the outermost compartment of the Araçuaí Orogen to the west, a foreland fold-and-thrust belt encompassing the Cipó Range at its southern end, with the São Francisco Craton acting as the foreland region during the orogeny (Marshak and Alkmim, 1989; Pedrosa-Soares et al., 2001; Alkmim et al., 2007). Being the geotectonic setting of this thesis, a brief review of the concepts concerning compartments of this nature is in order.

2.1. Geotectonic environment and driving forces

Though foreland fold-and-thrust belts are located along the margins between orogens and the contiguous continental areas (the foreland), their formation is directly driven by the evolution of the crystalline core. The construction of mountain arcs through injection of juvenile magmas and crustal shortening (in the horizontal direction) also makes the crust become thicker (in the vertical direction), with expression on the surface, with mountains reaching the highest altitudes on Earth, but most importantly in the crustal roots: while the average thickness of the continental crust is of the order of 35 km, it may reach 70 to 100 km in orogenic cores (Paul et al., 2006; Hacker et al., 2015). Isostatic imbalance follows: the weight concentrated in the crystalline core causes its subsidence, balanced by an uplift of contiguous area.

For foreland fold-and-thrust belts, the consequences are twofold:

First, the subsidence of the mountain arc and the uplift of the foreland flexes the lithosphere (Figure 3). This gives the region the characteristic shape of a wedge, and originates foreland basins (Moores and Twiss, 1995; van der Pluijm and Marshak, 2004; Condie, 2005; Nemčok et al., 2005; Kearey et al., 2009).

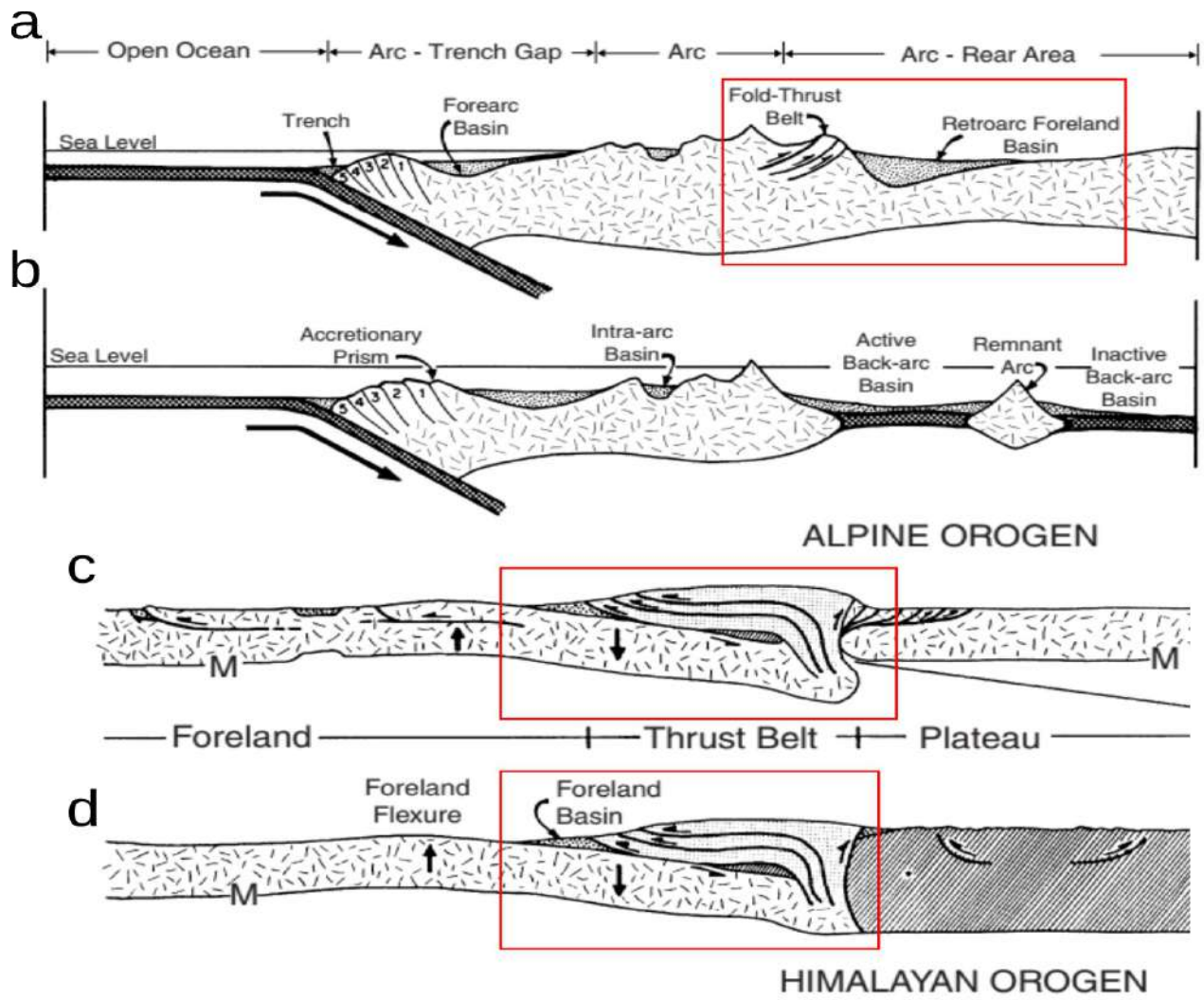

Figure 3. a, b) Tectonic compartmentalization of orogens, including accretionary and oceanic subduction settings; c, d) Isostatic compensations resulting from the construction of orogenic system in examples of the Alps (c) and the Himalayas (d). Red rectangles highlight the regions corresponding to the foreland fold-and-thrust belt, with their characteristic wedge shape, and the adjacent foreland basins (Condie, 2005).

Second, aside from the general tectonic convergence, two additional forces emerge from the thickening of the crust. One is the buoyancy exerted on the deep crustal roots, surrounded by the denser material of the lithospheric mantle. The other is the gravity spreading of the orogen, a mechanism that tends to compensate the difference of pressure between confined points in the mountain range and adjacent points under a smaller rock column or free air (Figure 4). When gravity spread becomes the dominant force in the system, the orogen expands its margins, developing a compressive system at its base, and when its topography becomes unstable in higher areas, the orogen is said to enter a stage called gravitational collapse, characterized by the development of normal or gravitational faults. Even when the convergence ends, gravity spread and buoyancy remain active until equilibrium is achieved (Pfiffner, 2017).

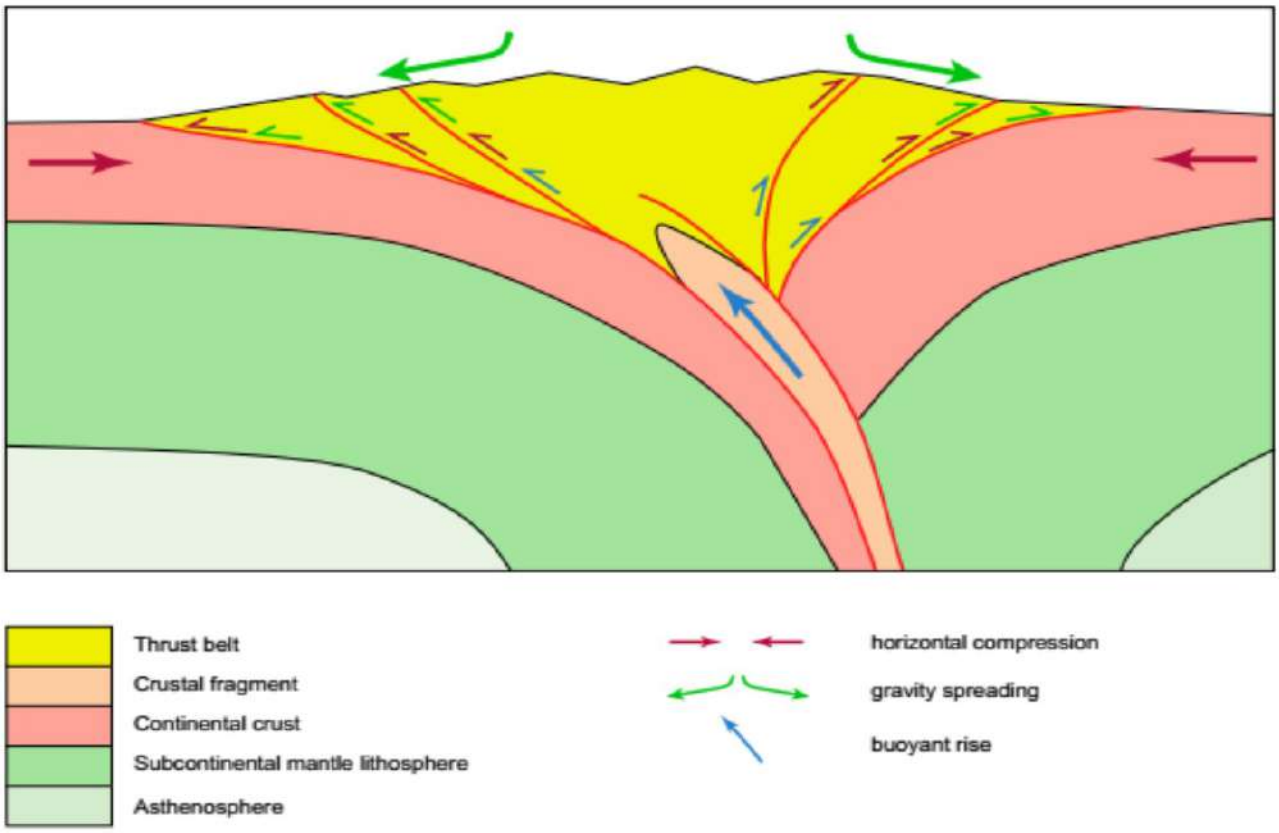

Figure 4. Scheme of the forces acting on an orogen (Pfiffner, 2017).

2.2. Evolution mechanism

As the name suggests, foreland fold-and-thrust belts are built basically over a frame of thrusts and folds, as well as subordinate structures, dipping mainly away from and verging towards the foreland (Chapple, 1978). The main framework is a sequence of thrust faults where the strain is concentrated on the hanging wall under the form of fault-related folds and shear bands, while rocks of the footwall remain relatively preserved from further deformation increments. In most foreland fold-and-thrust belts, thrust fronts stem from a basal detachment surface, a kilometric low-dip thrust surface that establishes itself at rheologically weak zones such as contacts, schistosities, fragile layers and fractures (van der Pluijm and Marshak, 2004; Nemčok et al., 2005).

The propagation of a foreland fold-and-thrust belt follows the break-forward pattern, meaning that successive generations of structures are younger towards the foreland domain (Suppe, 1983; Dahlen, 1990).

2.2.1. The critical taper theory

In a lesser scale when compared to the crystalline core, foreland fold-and-thrust belts are also regions where thrusting makes the crust thicker, reaching up to 45 km (Paul et al., 2006; Lammie et al., 2020), and systematically advance into the foreland following the break-forward pattern. To understand how this process works, Davis et al. (1983), Dahlen et al. (1984) and Dahlen (1990) created an empirical numerical model to describe the evolution of a fold-and-thrust front, called the critical taper model. Ever since its proposal, the initial proposal has been reviewed and perfected by several authors, who incorporated several rheological, mechanical and thermal properties of materials to it, including those arising from anthropic intervention (Burbidge and Braun, 2002; Smit et al., 2003; Suppe, 2007; Graveleau et al., 2012; Yang et al., 2013; Li and Mitra, 2017; McQuarrie and Ehlers, 2017; Tesei et al., 2021).

In this model (Figure 5), the crustal wedge of fold-and-thrust fronts thickens until it reaches a critical taper angle, defined by the sum of the topographic slope and the dip of the detachment surface, is achieved. Until this condition is satisfied, the system is said to be in equilibrium. When this critical value is achieved, the following increment of deformation makes the wedge unstable, and is accommodated by the propagation of the basal detachment into the (then) undeformed region of the foreland (Davis et al., 1983; Dahlen et al., 1984; Dahlen, 1990). The critical taper angle given by

$$\alpha+\beta \approx \frac{\left(1-\frac{\rho_f}{\rho}\right)\beta+\mu_b\left(1-\lambda_b\right)+\frac{C_b}{\rho g h}}{\left(1-\frac{\rho_f}{\rho}\right)+\sigma_{ci}\left(\frac{m_b\left(1-\lambda\right)}{\sigma_{ci}}+\frac{s}{\rho g h}\right)^a\left(\rho g h\right)^{a-1}}, \qquad \textbf{(Equation 1)}$$

whose parameters are listed and described on Table 1. The term $\left(1-\frac{\rho_f}{\rho}\right)\beta+\mu_b\left(1-\lambda_b\right)+\frac{C_b}{\rho g h}$ is defines the shear strength of the basal detachment, and is often simplified to a parameter F. The term $\sigma_{ci}\left(\frac{m_b\left(1-\lambda\right)}{\sigma_{ci}}+\frac{s}{\rho g h}\right)^a\left(\rho g h\right)^{a-1}$ represents what is called the internal strength of the wedge, and is commonly represented as the W parameter. Thus, a basal detachment with more resistance to increments of shear leads to wedges that can reach larger thicknesses. On the other hand, an internal composition that causes the wedge to resist increments of deformation limits the amount of thickening that the system can accommodate before it advances over the foreland.

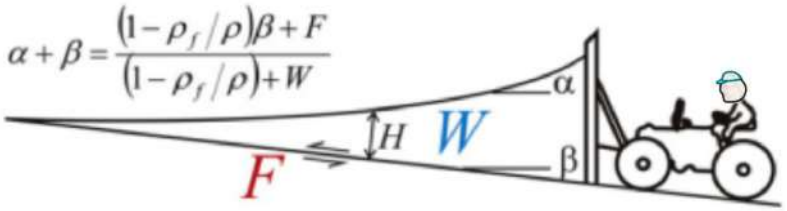

Figure 5. Didactic illustration of the critical taper model (Yang et al., 2016).

Table 1. Parameters of the calculus of the critical taper of a fold-and-thrust wedge.

Parameter	Pertains	Description
g	Earth	Gravity acceleration
α	Terrane (surface)	Slope
ρ	Wedge	Average density of rocks
ρ_f		Average density of fluids contained in the wedge
σ_{ci}		Uniaxial compressive strength
m_b		Geomechanical parameters of resistance and integrity based on the geological strength index (GSI) and accounting for disturbances resulting from explosions and/or excavations
s		
a		
λ		Partial fluid pressure
H		Thickness
β	Basal detachment	Dip
μ_b		Friction coefficient
C_b		Internal cohesion
λ_b		Partial fluid pressure

In geological terms, the condition of equilibrium does not mean that no deformation occurs in the wedge. Rather, it means that it is accommodated with the development of folds, shear bands and slip along the existing fault surfaces, contributing to the thickening of the wedge and the increase of its taper angle (Davis et al., 1983; Dahlen et al., 1984; Dahlen, 1990; Graveleau et al., 2012).

Occasionally, a supercritical condition may be achieved after an uplift pulse. When it happens, a special set of structures are formed to bring the wedge back to stability by reducing the topographic slope. A period of gravitational collapse ensues, forming normal faults within the fold-and-thrust domain. In systems experiencing gravitational collapse, the movement of mass towards the toe of normal faults may create local compressive increments, which may cause the development of thrusts not necessarily following the break-forward pattern, that is, not advancing the fold-and-thrust front into the foreland. These younger generations of faults are called out-of-sequence thrusts. When their dip is opposed to the global vergence of the wedge, these structures are called backthrusts (Davis and Engelder, 1985; Morley, 1988; Smit et al., 2003; Graveleau et al., 2012).

2.3. Styles: thin-skinned *versus* thick-skinned tectonics

As a foreland fold-and-thrust belt evolves and the tectonic wedge thickens, the basal detachment and related structures may reach deep levels in the crust. Depending on various factors (e.g. pressure, temperature, duration of the orogenesis, rheological contrasts), this may eventually cause the involvement of the crystalline basement in the deformation (van der Pluijm and Marshak, 2004; Pfiffner, 2006; Twiss and Moores, 2007; Davis et al., 2012). When deformation is restricted to the supracrustal (sedimentary and metasedimentary) rocks (Figure 6.a), the style of the fold-and-thrust belt is described as thin-skinned. When the crystalline basement is involved (Figure 6.b), the style is said to be thick-skinned. Pfiffner (2006, 2017) proposes a more rigorous concept for thick-skinned tectonics, reserving the term for cases where the detachment cuts the entire extension of the continental crust down to the Mohorovičić Discontinuity (Figure 6.c). We, however, adopt the notion posing that any kind of involvement of the crystalline basement in the deformation of a fold-and-thrust belt means a thick-skinned style.

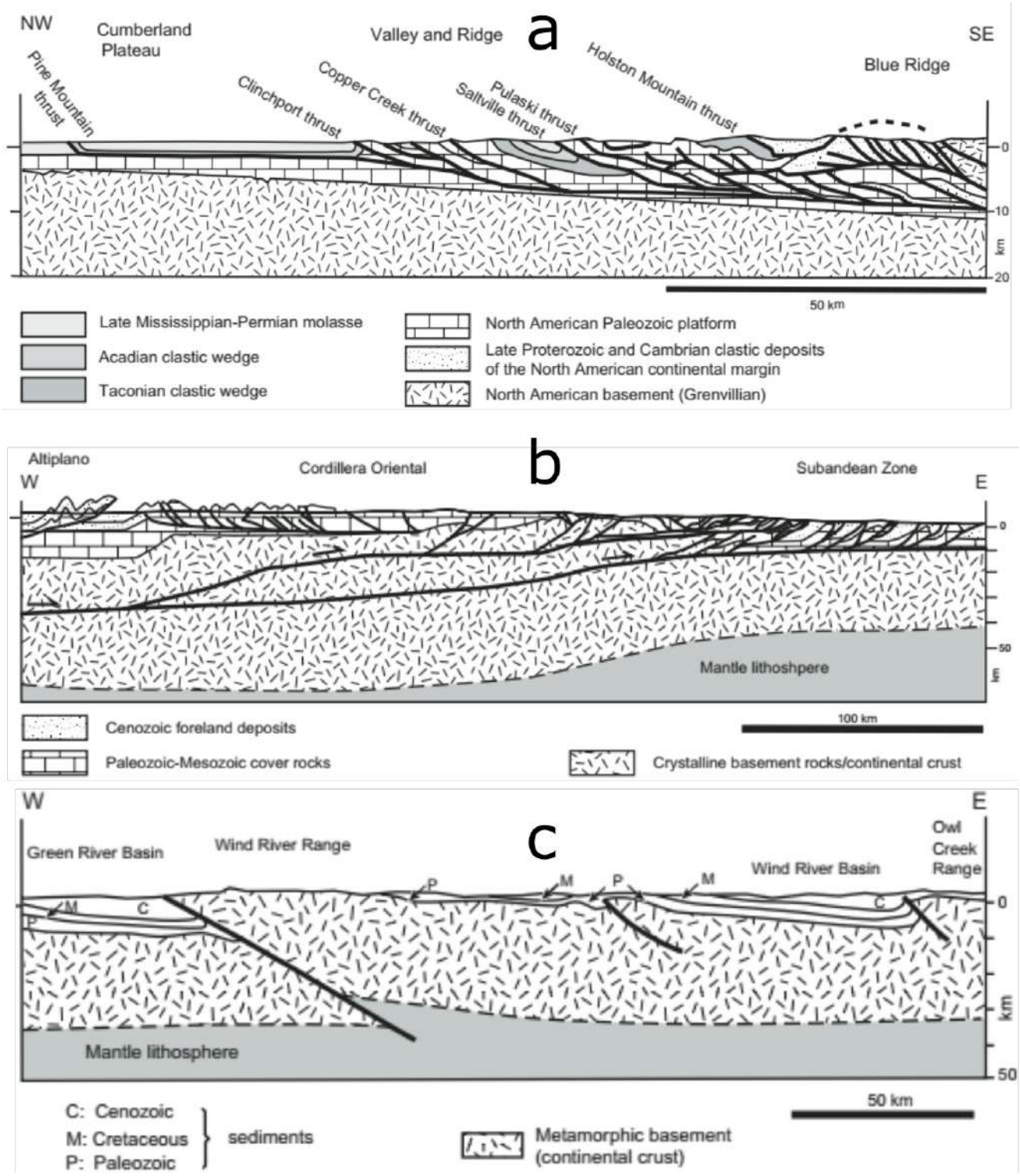

Figure 6. Styles of foreland fold-and-thrust belts (Pfiffner, 2006). a) Thin-skinned tectonics in the Western Appalachians, United States. b) Thick-skinned tectonics in the Andean Oriental Cordillera, Bolivia. c) Thick-skinned tectonics in the Wind River Chain of the Rocky Mountains, United States.

3. THE SÃO FRANCISCO CRATON AND SOUTHERN ESPINHAÇO RANGE

The geotectonic context of the target area of this study is the limit between the São Francisco Craton and the Southern Espinhaço Range, respectively the western foreland and fold-and-thrust domains established during the orogenic cycle that built the Araçuaí-West Congo Orogen. In this chapter, we review aspects of both compartments that are important within our scope, thus excluding their Phanerozoic evolution posterior to the deposition of the Bambuí Group (e.g. breakup during the opening of the Atlantic Ocean and contemporary sedimentation), as well as several stratigraphic units found only in the northern portions of the craton and/or the orogen.

3.1. The São Francisco Craton

The São Francisco Craton was a peninsula of the São Francisco-Congo paleocontinent, formed by various Archean and Paleoproterozoic greenstone belts, TTG suites, granitoids and supracrustal successions (Teixeira et al., 2000; Barbosa and Sabaté, 2004; Alkmim and Martins-Neto, 2012). The São Francisco Peninsula was connected to the Congolian block to the north, by the Bahia-Gabão Bridge (Porada, 1989). Aborted rifting pulses affected the continent in the Statherian and Calymmian periods, creating space for the deposition of the Espinhaço Supergroup (Schobbenhaus, 1996; Martins-Neto, 1998). Later, starting in the Tonian Period, a complete rift system in the same region led to the formation of the Adamastor Ocean and the sedimentation of the Macaúbas Group (Pedrosa-Soares et al., 1992, 1998, 2001; Amaral et al., 2020).

The São Francisco-Congo continent was one of the many landmasses (e.g. Amazonas, Kalahari, Rio Apa, among others) amalgamated in the Brasiliano-Pan African Orogeny in the Ediacaran-Cambrian transition, an event that caused the construction of a several mountain chains and culminated with the formation of the West Gondwana megacontinent (Almeida, 1967, 1977; Porada, 1989; Brito-Neves and Cordani, 1991; Alkmim et al., 1993; Almeida et al., 2000; Cordani et al., 2003, 2009; Alkmim, 2004).

3.2. Nutcracker tectonics

On the western border of the São Francisco Peninsula, the closure of the Goiás-Pharusian Ocean and the subsequent collision with the Amazonian Craton erected the Tocantins-Araguaia and the Brasília Orogens (Brito-Neves et al., 1999), and caused the peninsula to pivot eastwards around the Bahia-Gabão Bridge, towards the Congo Block. Between these two landmasses existed a restricted oceanic basin, the Adamastor Ocean. The rotation of the São Francisco peninsula towards the Congo Block closed this ocean and eventually constructed a confined accretionary-collisional

mobile belt in its place, the Araçuaí-West Congo Orogen (Figure 7). This model was proposed by Alkmim et al. (2006, 2017) and is known as Nutcracker Tectonics.

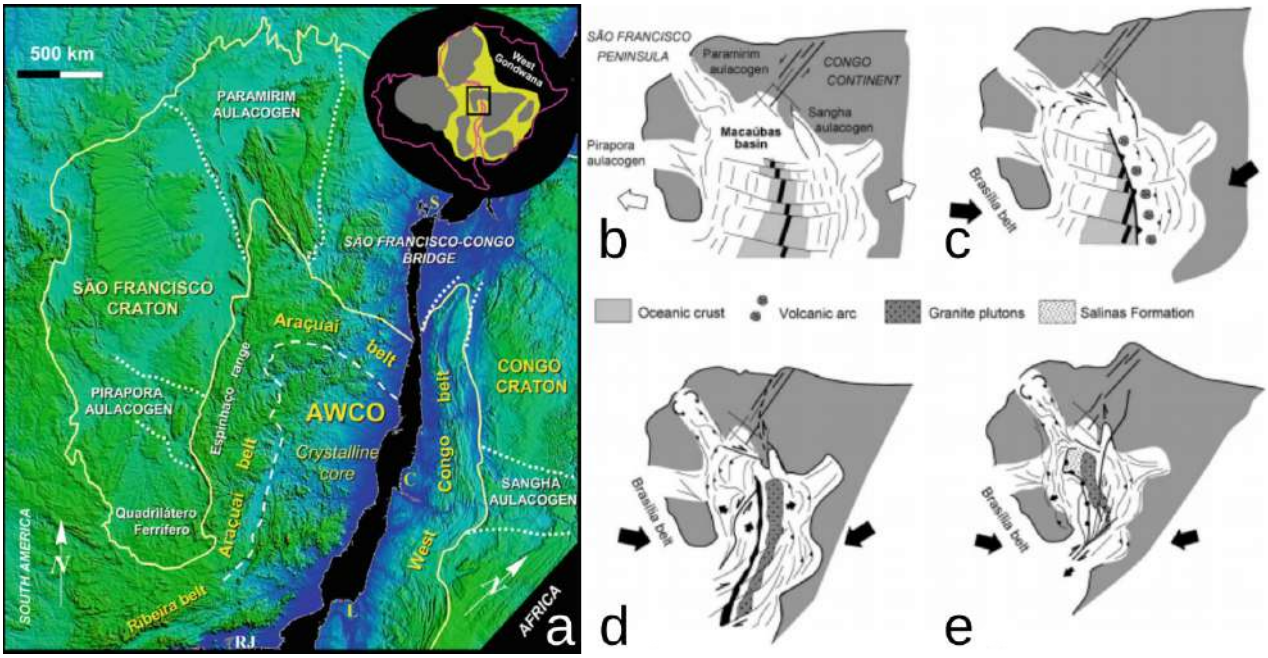

Figure 7. a) Reconstruction of the Araçuaí-West Congo Orogen (Alkmim et al., 2007, 2017) in the context of the West Gondwana megacontinent as per De Wit et al. (1988), and its stages of orogenic evolution according to the nutcracker model (Alkmim et al., 2006): b) Opening of the Adamastor oceanic basin,x followed by pivoting of the São Francisco Peninsula towards the Congolian landmass in the c) accretionary stage and d) collisional stage, ending with e) a stage of lateral escape.

3.3. The Southern Espinhaço Range, the São Francisco Craton as a foreland and the Bambuí Basin

The anatomy of the Araçuaí-West Congo Orogen follows the conventional model for the structure of orogens (3), with an extense system of shear zones in eastern Minas Gerais and western Rio de Janeiro (the Manhuaçu and Abre Campo shear zones) as possible representatives of the suture zone (Pedrosa-Soares et al., 2001; Peixoto et al., 2015; Degler et al., 2018; Amaral et al., 2020). Alkmim et al. (2007) divided the orogen, in its entirety, in ten compartments (Figure 8.a). The Southern Espinhaço Range occupies the western portion of the orogen as a west-verging foreland fold-and-thrust belt, marking the boundary with the eastern border of the São Francisco Craton. Thus, the São Francisco Craton served as the western foreland domain to the Araçuaí-West Congo Orogen. Various authors identified two ruptile-ductile, coaxial stages of nucleation of structures, resulting in a north-trending imbricated thread of inverse faults and shear zones and asymmetric folds (e.g. Herrgesell and Pflug, 1986; Magalhães, 1988; Kalt, 1991; Oliveira, 1994; Knauer, 1999).

Because of the presence of the several orogens at its borders, the São Francisco Craton experienced deformation and crustal flexure driven by isostatic processes. For its center and south segments, the São Francisco Basin, this was caused by the growth of the Brasília (to the east) and

Araçuaí-West Congo orogens, resulting in a structure divided in three compartments (Figure 8.b): an east-verging compartment in the west, a central undeformed compartment and a west-verging compartment in the East (Magalhães, 1988; Alkmim and Martins-Neto, 2001). Flexing of the crust originated a large foreland basin, with deposition of the Bambuí Group, the largest cratonic cover (Chang et al., 1988; Pimentel et al., 2001; Martins-Neto et al., 2001; Martins-Neto, 2009). The conventional cartographic border between the São Francisco Craton and the Southern Espinhaço Range was defined by Almeida (1977), at the tectonic inversion where the Espinhaço Supergroup is thrusted above the Bambuí Group.

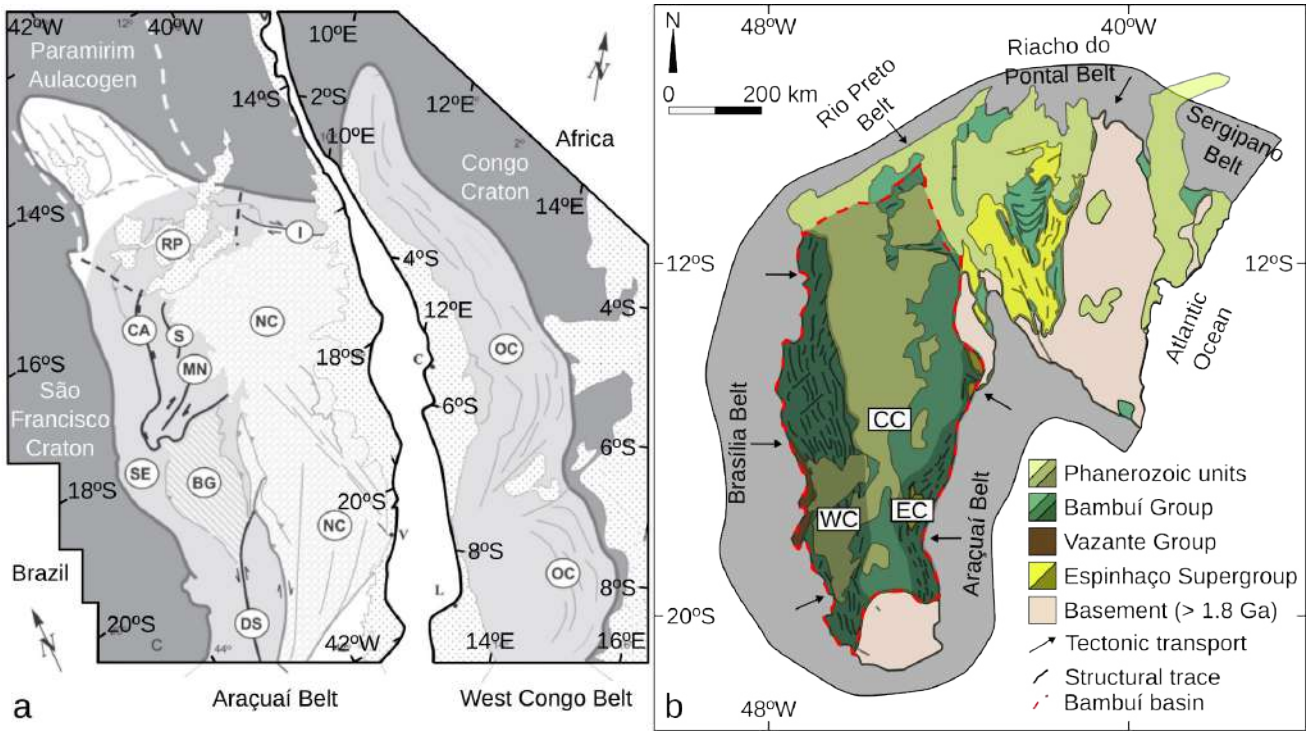

Figure 8. a) Tectonic compartments of the Araçuaí-West Congo Orogen (Alkmim et al., 2007): SE – Southern Espinhaço Range Thrust Belt, CA – Chapada Acauã Shear Zone, S – Salinas Fold Zone, MN – Minas Novas Transpressive Corridor, RP – Rio Pardo Salient, BG – Guanhães Block, DS – Dom Silvério Shear Zone, I – Itapebi Shear Zone, NC – Crystalline Core, OC – West Congo Belt; b) Tectonic compartments of the São Francisco Craton: WC – West Compartment, CC – Central Compartment, EC – East Compartment (Alkmim and Martins-Neto, 2001).

3.4. Stratigraphy

The stratigraphy of the São Francisco Craton and the Southern Espinhaço Range comprises several granite-gneiss complexes, crustal blocks and supracrustal units, many of which are far beyond the scope of our thesis. For objectivity, we focus this section on units described in the southern regions surrounding the interaction zones between both compartments, according to the existing geological literature. Detrital zircon U-Pb ages will be further addressed in Chapter 5 so as to give context to our stratigraphic discussions.

3.4.1. Crystalline basement

The regional crystalline basement is composed in the by a number of granitoids and gneisses divided as follows:

A) The **Migmatitic Granite-Gneiss Complex**, defined by Pflug (1965) and Schöll and Souza (1970, apud Oliveira et al., 1997), is composed by medium-grained and discretely banded gray orthogneisses derived from granites and granodiorites originally crystallized ca. 2.78 Ga and reworked around 2.10 Ga (Teixeira et al., 1987; Machado et al., 1992).

B) The **Belo Horizonte Complex** (Dorr et al., 1957; Noce et al., 1994; Noce, 1995) is a TTG suite composed by gneisses and migmatites, the latter dating at ca. 2.78 Ga and with posterior metamorphism around 2.04 Ga (Noce, 1995; Noce et al., 1998).

C) The **Guanhães Complex** is a TTG Archean continental core, at times affected by migmatization (Pedrosa-Soares et al., 1994; Grossi-Sad, 1997). Its crystallization occurred mainly between 3150 and 2710 Ma, with formation peak ages at 3140, 2900 and 2750 Ma (Peixoto et al., 2015; Barrote, 2016) with younger juvenile intrusions dating around 2151 and 2014 Ma (Grochowski et al., 2021).

3.4.2. Pre-Espinhaço metasedimentary basement

Aside from crystalline complexes, a series of Archean and Paleoproterozoic metasedimentary sequences act as the cratonic basement. Conventionally, the units to which this role is attributed are have maximum deposition ages older than the setting of the Statherian Espinhaço Rift System, and referred to as “Pre-Espinhaço” (Almeida et al., 1981). From these units, the Meloso (Serra da Serpentina Group) and Barão do Guaicuí (Costa Sena Group) formations will be addressed in following stratigraphic discussions, and, hence, are briefly contextualized in the next item.

3.4.2.1. <u>The Meloso Formation and the Costa Sena Group</u>

Despite not having been described in our study area, the stratigraphic concerns that arose over the course of this study (discussed in Chapter 5) make necessary for the cohesion of upcoming chapters of this thesis a review of the Meloso Formation, found in the Serpentina Range, located along the eastern border of the Southern Espinhaço Range, and the Costa Sena Group, with which it has been correlated (Rolim, 2016; Rolim et al., 2016).

The **Meloso Formation** (Rolim et al., 2016) is the basal unit of the Serra da Serpentina Group (Dussin, 1985). This formation is composed, at is base, by decametric quartzite lenses interlayerd with schist, followed by characteristically hematite-bearing, white-greenish schist, which grades to gray-silver banded phyllite, also bearing hematite and containing graphite-rich lenses. The Meloso

Formation is gradually topped by the **Serra do Sapo Formation** (Almeida-Abreu et al., 1989), composed predominantly by banded iron formations, locally followed by discontinuous layers of dolomite at the top. Sparse lenses of quartzite, schist, phyllite and banded iron-manganese-rich rocks (Figure 9). The Serra da Serpentina Group (Rolim, 2016; Rolim et al., 2016), described in the region of Diamantina and Gouveia, is correlated to the Costa Sena Group (Figure 10). Deposition of the Serra da Serpentina Group has been associated to a back-arc setting related to the Minas-Bahia Orogeny in Rhyacian-Orosirian (Pagung et al., 2023).

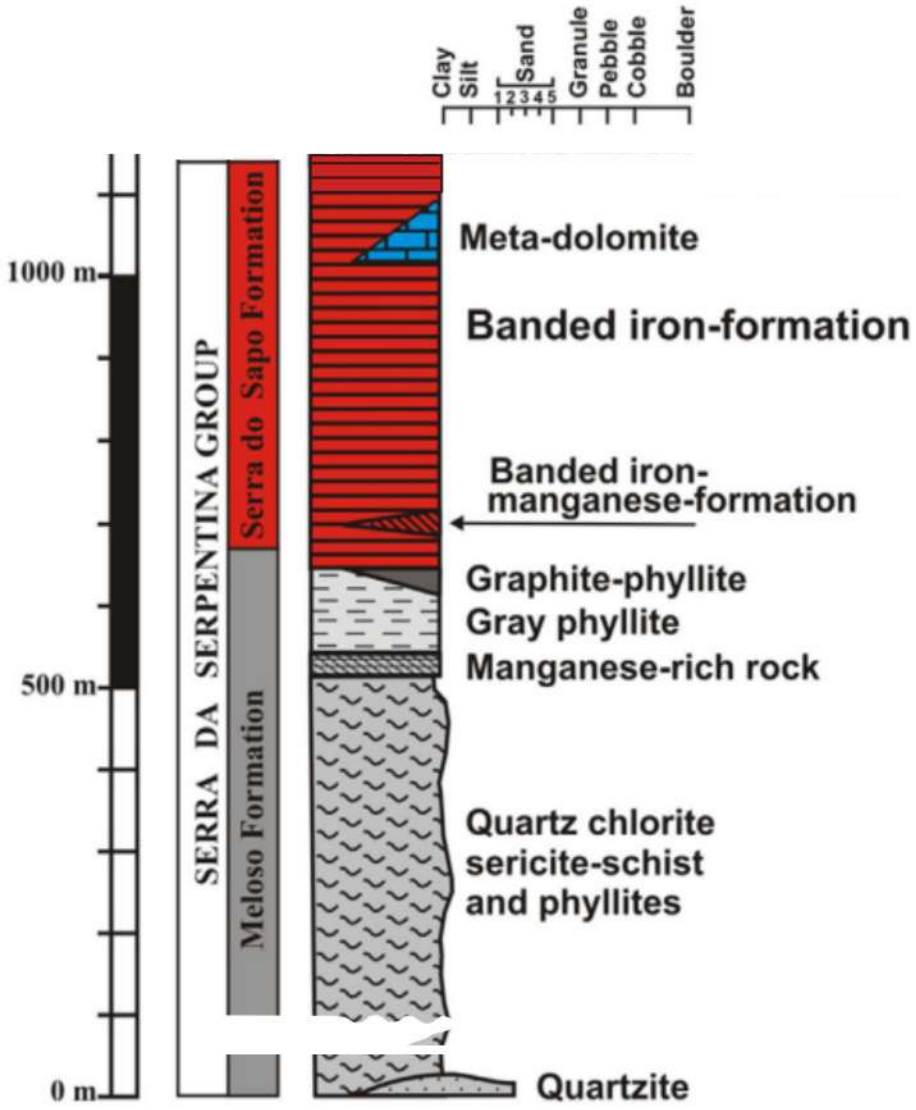

Figure 9. Stratigraphic column of the Serra da Serpentina Group (Rolim et al., 2016).

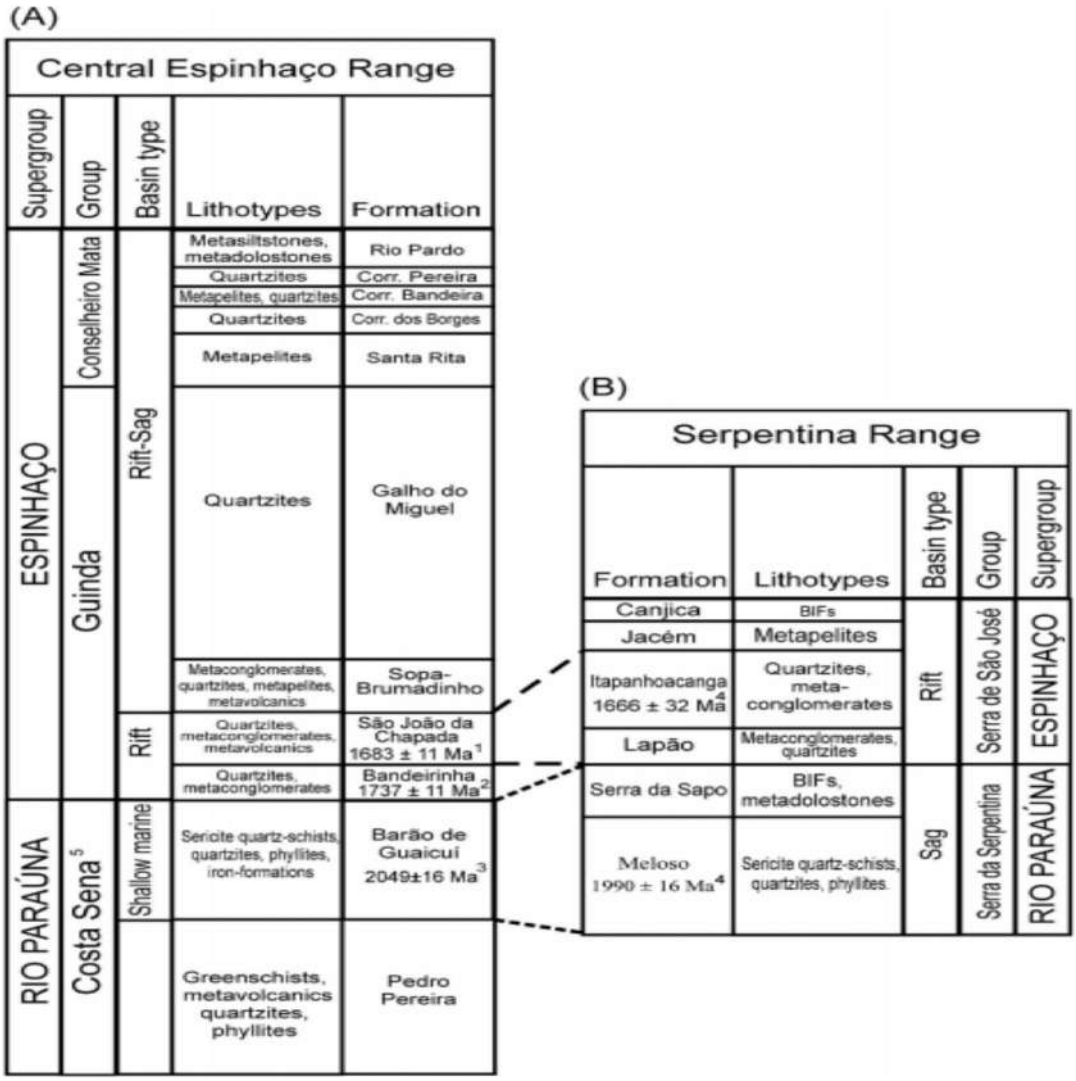

Figure 10. Correlation between the Costa Sena Group and the Espinhaço Supergroup (A), and the Serra da Serpentina and Serra de São José groups (B)(Rolim et al., 2016).

Top constituent of the Paleoproterozoic Rio Paraúna Supergroup (Fogaça et al., 1984), the Costa Sena Group (Hoffmann, 1983) is a marine metasedimentary sequence deposited above the metavolcanosedimentary Pedro Pereira Group (Carvalho, 1982; Fogaça et al., 1984), the latter containing schist, metaultramafic rocks and banded iron formation. Originally, the Costa Sena Group was divided in the Barão do Guaicuí and the Bandeirinha formations. However, the stratigraphic position of the latter has since been changed to the base of the Espinhaço Supergroup – which will be discussed in the section dedicated to this unit. The **Barão do Guaicuí Formation** (Fogaça et al., 1984) is essentially formed by schist, quartzite, banded iron formations, metaconglomerate, complemented by acid metavolcanic rocks dated at ca. 2049 ± 16 Ma (Machado et al., 1989). Left with a single formation confirmed within it, the Costa Sena Group is currently in a challenging conceptual stratigraphic situation. Chaves et al. (2012) proposed a demotion of the Pedro Pereira

Group to the status of a formation to be placed as the basal unit of the Costa Sena Group (Figure 11). This, in turn, extended the problem to the Rio Paraúna Supergroup, which would then be composed of a single group. A tentative inclusion of the Serra da Serpentina Group in the Rio Paraúna Supergroup was discussed by Rolim (2016) through the correlation with the Costa Sena Group. However, proper studies are required to solve this matter in the future.

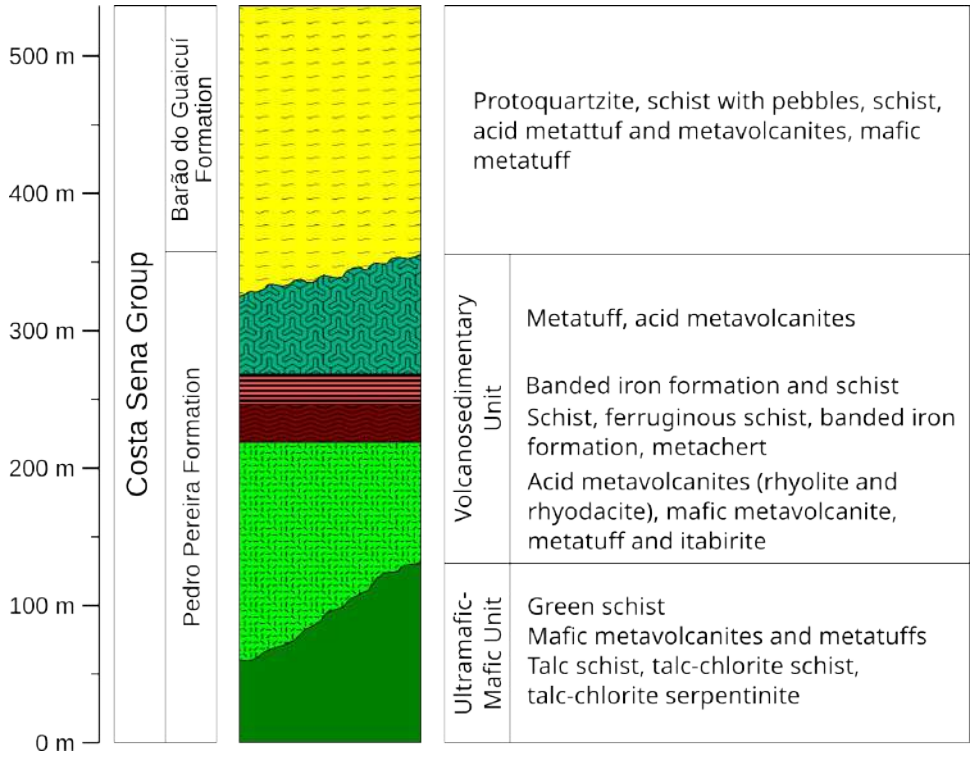

Figure 11. Stratigraphic column of the Costa Sena Group, elaborated according to the definitions of Fogaça et al. (1984) and the reviewed proposal of Chaves et al. (2012).

3.4.3. Statherian and Calymmian riftings, the Serra de São José Group and the Espinhaço Supergroup

The Espinhaço Basin has a long, discontinuous depositional history ranging between the Statherian Period and the Ectasian-Stenian limit (Machado et al., 1989; Chemale Jr. et al., 2011, 2012; Santos et al., 2013). Sedimentation in the basin occurred in continental rift systems affecting the São Francisco-Congo continent, nucleated in the Statherian and reactivated in the Calymmian, failing to achieve the passive margin stage (Martins-Neto, 1998; Danderfer-Filho et al., 2009; Pedrosa-Soares and Alkmim, 2011; Santos et al., 2020).

The Statherian openings were accompanied by episodes of magmatism that originated the **Borrachudos** and **Conceição do Mato Dentro** suites. These are, respectively, granitic and rhyolitic (Dorr and Barbosa, 1963; Knauer, 1990; Fernandes et al., 1994; Oliveira, 2002; Magalhães, 2019). Crystallization was dated between 1.75 and 1.69 Ga (Brito-Neves et al., 1979; Machado et al., 1989;

Fernandes, 2001; Gomes et al., 2020), an age considered to be the maximum, for the Espinhaço system. A hematitic phyllite, first described by Moraes and Guimarães (1930), dated at ca. 1.75 to 1.70 Ga (Machado et al., 1989; Knauer, 1990; Dussin and Dussin, 1995; Dussin, 2000; Bezerra-Neto, 2016) is also attributed to this stage. Its original composition and alteration history are still matters of debate. Considering an original basalt protholith, Knauer and Schrank (1993) and Chaves and Knauer (2020) posed that this rock results from a paleosoil developed over the rock, while Cabral et al. (2012) suggested boron-potassium-rich metasomatism from basinal fluids. Alternatively, Bezerra-Neto (2016) interpreted that the phyllite originated from a lamproitic protholith.

The rocks deposited in the southern segment of the Espinhaço Basin were first identified by Pflug (1965, 1968) and classified by Schöll and Fogaça (1979) in the original definition of the Espinhaço Supergroup, then composed of eight formations from bottom to top: São João da Chapada, Sopa-Brumadinho, Galho do Miguel, Santa Rita, Córego dos Borges, Córrego da Bandeira, Córrego Pereira and Rio Pardo Grande.

Dussin et al. (1984) divided the southern Espinhaço Supergroup in the Diamantina (São João da Chapada, Sopa-Brumadinho and Galho do Miguel formations) and Conselheiro Mata (Santa Rita, Córego dos Borges, Córrego da Bandeira, Córrego Pereira and Rio Pardo Grande formations) groups. Knauer (1990) opted to keep the São João da Chapada and Sopa-Brumadinho formations grouped as the Guinda Group, but listed the Galho do Miguel Formation as a standalone unit.

Until Chemale Jr. et al. (2012) and Santos et al. (2013) brought to light detrital zircon U-Pb ages to back the addition of the Bandeirinha Formation (Fogaça et al., 1984), originally placed in the Costa Sena Group, at the base of the Espinhaço Supergroup, its stratigraphic position was object of thorough debate (Knauer, 1990; Martins-Neto, 1998; Almeida-Abreu and Renger, 2002; Chemale Jr. et al., 2011; Lopes-Silva and Knauer, 2011). The U-Pb age results led Chemale Jr. et al. (2012) to significantly overhaul the stratigraphy of the Espinhaço Supergroup. These authors excluded the São João da Chapada Formation from the Diamantina Group, leaving it, as well as the Bandeirinha Formation, as standalone basal units deposited in a Statherian continental rift (the Lower Espinhaço Basin). The Diamantina and Conselheiro Mata groups represent deposition after the Calymmian rifting (the Upper Espinhaço Basin), with the former corresponding to the rift and first sag stages and the latter, to the final sag phase (Figure 12).

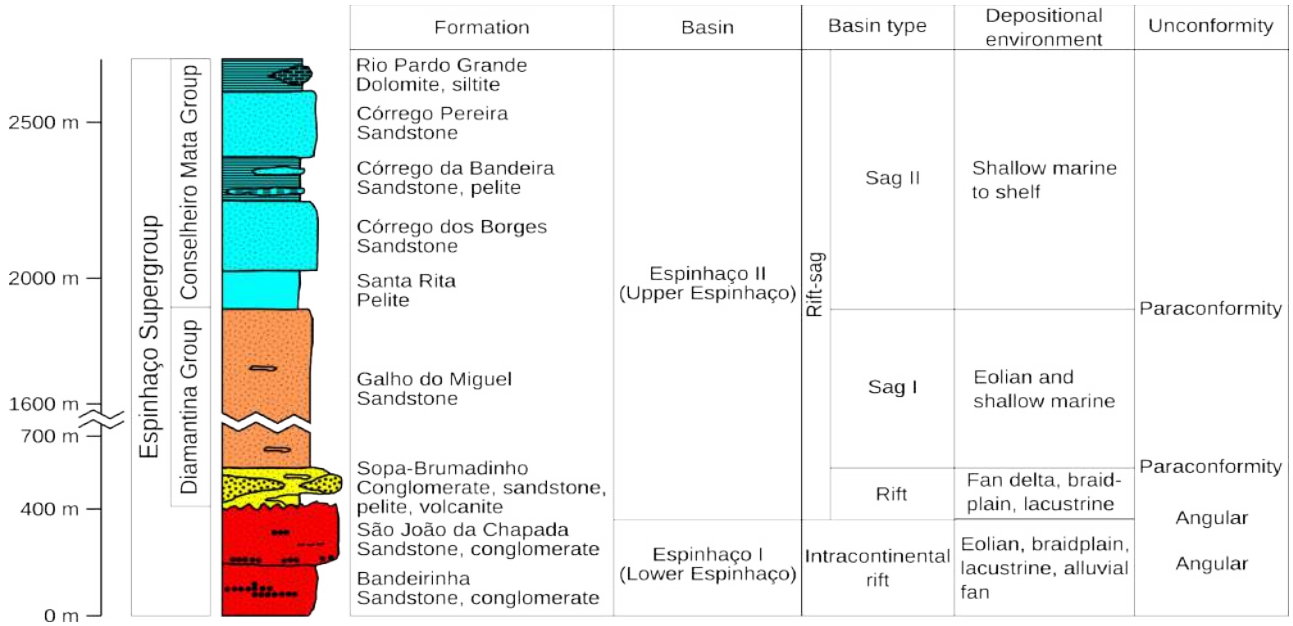

Figure 12. Stratigraphic column of the Espinhaço Supergroup in the region of Diamantina, after Martins-Neto (1998) and Chemale Jr. et al. (2012).

The work by Chemale Jr. et al. (2012), as well as studies in several other Proterozoic basins in the Brasília Belt, the São Francisco Craton, the Araçuaí-West Congo Belt and the Congo Craton, prompted Alkmim and Martins-Neto (2012) to classify the many different depositional stages in the compartments in first order sequences. The Espinhaço Supergroup was taken as reference, with the Bandeirinha and São João da Chapada formations belonging to the Espinhaço I Sequence, and the Diamantina and Conselheiro Mata groups placed in the Espinhaço II Sequence.

The classic descriptions and stratigraphic divisions of the Espinhaço Supergroup were made in the region of Diamantina, and are the most referenced definitions in studies addressing this unit. However, within the scope of our work, it is also worth mentioning the Itapanhoacanga Formation (Almeida-Abreu et al., 1989), a member of the Mesoproterozoic Serra de São José Group (13), defined by Rolim (2016) in the region of Conceição do Mato Dentro. In similar fashion to the Meloso Formation and the Costa Sena Group, the Serra de São José Group has never been described in our study area, but has been identified in the Serpentina Range. Moreover, two of its formations (Lapão and Itapanhoacanga) have been correlated to the Bandeirinha and São João da Chapada formations (respectively), leading to suggestions of inclusion of the Serra de São José Group in the Espinhaço Supergroup (Dussin, 1985; Rolim, 2016; Rolim et al., 2016) as the representative of the sedimentation of the Statherian rift system in its southeastern sector (10), a notion that we will adopt henceforth. Particularly for the Itapanhoacanga Formation, there are detrital zircon U-Pb ages available (Rolim et al., 2016). Being it a correlative of rocks – or proper members – of the Espinhaço

Supergroup, this makes it possible to evaluate its affinity with the rocks found in Serra do Cipó and its vicinities.

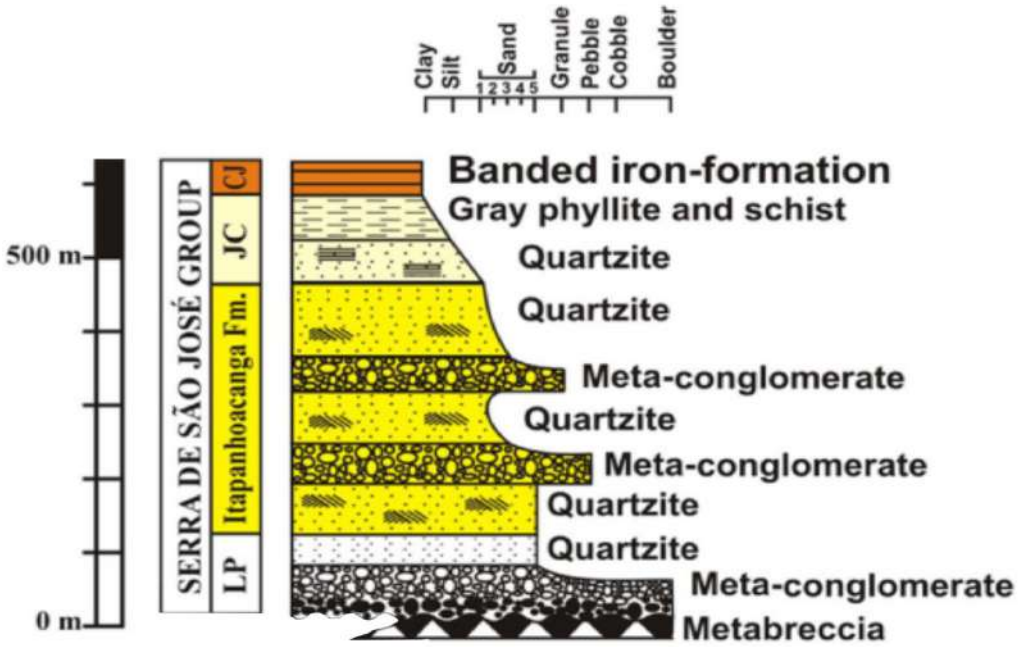

Figure 13. Stratigraphic column of the Serra de São José Group in the region of Conceição do Mato Dentro (Rolim et al., 2016).

3.4.3.1. Espinhaço I Sequence

The Espinhaço I Sequence contains the record of the Lower Espinhaço Basin (Alkmim and Martins-Neto, 2012; Chemale Jr. et al., 2012; Santos et al., 2013). As discussed, we adopt the proposals advocating for the inclusion of the Serra de São José in the Espinhaço Supergroup (Rolim, 2016; Rolim et al., 2016).

In the region of Diamantina, the Espinhaço I Sequence is mostly siliciclastic, and composed by two units from base to top, as follows:

The **Bandeirinha Formation** (Fogaça et al., 1984) is divided in a basal member composed by fine-grained, pure or micaceous quartzite grading to fine-grained schist, followed by the Olaria Member, formed by medium to thick-grained quartzite, and the Natureza Member, containing polymictic, matrix-supported metaconglomerate (Silva, 1993). The quartzites of this unit are distinctly reddish due to iron oxide coating, being interpreted as red beds (Lopes-Silva and Knauer, 2011). The Bandeirinha Formation was deposited, initially, in a braided fluvial system and later in a marine fan environment (Martins-Neto, 1998; Uhlein et al., 1998).

The **São João da Chapada Formation**, an alluvial-fan sequence divided in four levels: A, B, C and D (Pflug, 1968; Schöll and Fogaça, 1979). Level A is composed by polymictic metabrecchia and metaconglomerate, level B contains hematitic phyllite, level C is formed by quartzite-phyllite

intercalations, and level D is a fining-upward succession of quartzite and phyllite. Level D corresponds to the former Datas Member of the Sopa-Brumadinho Formation, reclassified by Chemale Jr. et al. (2011). The hematitic phyllite, whose origin is still matter of debate, may represent a stage of volcanic contribution to the deposition of the São João da Chapada Formation.

The Serra de São José Group in the region of Conceição do Mato Dentro significant chemical metasedimentary deposits. Currently, it is composed by the four following formations, from base to top:

A) The **Lapão Formation** (Rolim et al., 2016) contains metaconglomerate and medium to coarse-grained quartzite. The metaconglomerate clasts are mostly constituted by rocks from the underlying Serra do Sapo Formation

B) The **Itapanhoacanga Formation** (Almeida-Abreu et al., 1989), comprising thick packages of deep-marine fan quartzite, often ferruginous and sericitic. Intercalations of schist and matrix-supported metaconglomerate also occur, with the coarser levels becoming finer and less frequent upper within the unit, giving place to scattered pebbles and coarse-grained quartzite.

C) The **Jacém Formation** (Almeida-Abreu et al., 1989) is a monotonous fine to medium-grained white quartzite with parallel laminations defined by sericitic levels. Rarely, phyllite and schist layers cover the quartzite.

D) The **Canjica Formation** (Rolim et al., 2016) is a discontinuous sequence of banded iron formations, seldom interleaved with lenticular bodies of schist, phyllite and quartzite.

3.4.3.2. Espinhaço II Sequence

After the first rifting pulse in the Statherian, the system was reactivated in the Calymmian Period. The sediments deposited in the resulting basin (Upper Espinhaço) form the Espinhaço II Sequence, registering the rift and sag phases of this process. It is divided in the Diamantina and Conselheiro Mata Groups (Dussin et al., 1984; Chemale Jr. et al., 2012, 2012).

The Diamantina Group was deposited during the mechanical subsidence and the transition to the sag stage of the Calymmian rifting of the Upper Espinhaço Basin. Its constituents are described in the following items.

A) The **Sopa-Brumadinho Formation** (Pflug, 1965, 1968; Schöll and Fogaça, 1979), registers the rift stage of the Espinhaço II Sequence, separated from the São João da Chapada Formation by an angular unconformity (Santos et al., 2013). With fluvial origin, this formation is divided in three members (Mourão, 1995; Knauer, 2007; Chemale Jr. et al., 2011). The Caldeirões Member is made of heterogeneous quartzite (micaceous, pure, ferruginous) with thick metaconglomerate lenses. The Campo Sampaio Member is composed of intercalations of quartzite, phyllite and metasiltstone, with metabrecchia lenses. On a similar stratigraphic level to the Campo Sampaio Member, the Rio Preto Unit is constituted by intercalations of fine quartzite and schist with varying contents of carbonates and phosphate. Hematitic phyllite is also found in the Sopa-Brumadinho Formation, both in concordant and discordant positions.

B) The **Galho do Miguel Formation** (Pflug, 1968; Schöll and Fogaça, 1979), marking the transition between the rift and the sag phases of the Espinhaço II Sequence. This unit is composed by a thick package of pure, medium to fine-grained quartzite with few occurrences of micaceous quartzite or metasiltstone, deposited in an aeolian environment subject to episodes of marine transgression (Dussin et al., 1987).

The Conselheiro Mata Group, in turn, was completely deposited in the context of thermal subsidence and marine advance over the Upper Espinhaço Basin, marked by transgressive-regressive cycles (Dupont, 1995; Martins-Neto, 1998, 2000). It is divided the following units, identified by Pflug (1968) and Schöll and Fogaça (1979), as follows:

A) The **Santa Rita Formation** marks the first marine transgression over the continental platform of the Upper Espinhaço Basin. It is composed by two metapelite and phyllite facies separated by a barrier island quartzite.

B) The **Córrego dos Borges Formation** represents a sea-level regression, with deposition of micaceous and pure quartzite on the shoreline and associated dune systems.

C) The **Córrego da Bandeira Formation** is formed by a succession of metarhythmite and quartzite, corresponding to an advance of the sea over the basin.

D) The **Córrego Pereira Formation** contains metaarkose and pure quartzite from rivers and beach surf systems, marking a second progradation of the shoreline.

E) The **Rio Pardo Grande Formation** is composed by metapelite and dolomitic marble. It marks the end of the sedimentary record of the Espinhaço Supergroup as a final sea-level rise.

3.4.4. Tonian and Cryogenian rifting and the Macaúbas Group

From its onset to the establishment of the Adamastor Ocean, the Macaúbas Basin evolved in three stages (Pedrosa-Soares and Alkmim, 2011; Pedrosa-Soares et al., 2011; Kuchenbecker et al.,

2015). The first was an Early Tonian rifting pulse (Rift I) that was interrupted still in continental medium. It was accompanied by bimodal magmatism with formation of the **Pedro Lessa Suite** (Knauer, 1990), composed of metadiabase and metagabbro, the granitic **Salto da Divisa Suite** (Silva et al., 2008), and the **Pedra Preta Amphibolite** (Gradim, 2012). This magmatism was dated between 914 and 876 Ma (Machado et al., 1989; Silva et al., 2008; Menezes et al., 2012), estimated to be the duration of this stage. The second phase (Rift II) began at the Tonian-Cryogenian limit, with the establishment of a second rifting pulse that eventually opened a limited oceanic basin, the third stage (Drift) around ca. 645 Ma (Peixoto et al., 2015; Amaral et al., 2020).

The sedimentary register of the basin is the Macaúbas Group (Schöll, 1972; Karfunkel and Karfunkel, 1976; Karfunkel et al., 1985; Pedrosa-Soares et al., 1992). Each tectonic phase is represented by a particular set of faciological associations. Plus, the Rift II stage coincided in time with the Snowball Earth glaciation (Hoffman et al., 1998), in the Cryogenian, meaning that, besides recording different moments of the tectonic history of the basin, the Macaúbas Group also contains pre-glacial, glacial and post-glacial sequences (Karfunkel and Hoppe, 1988; Noce et al., 1997; Pedrosa-Soares et al., 2011; Babinski et al., 2012; Alkmim et al., 2017; Castro et al., 2019; Souza et al., 2019). This prompted Kuchenbecker et al. (2015) to propose a division of the Macaúbas Group in Lower, Middle and Upper sections (Figure 14)

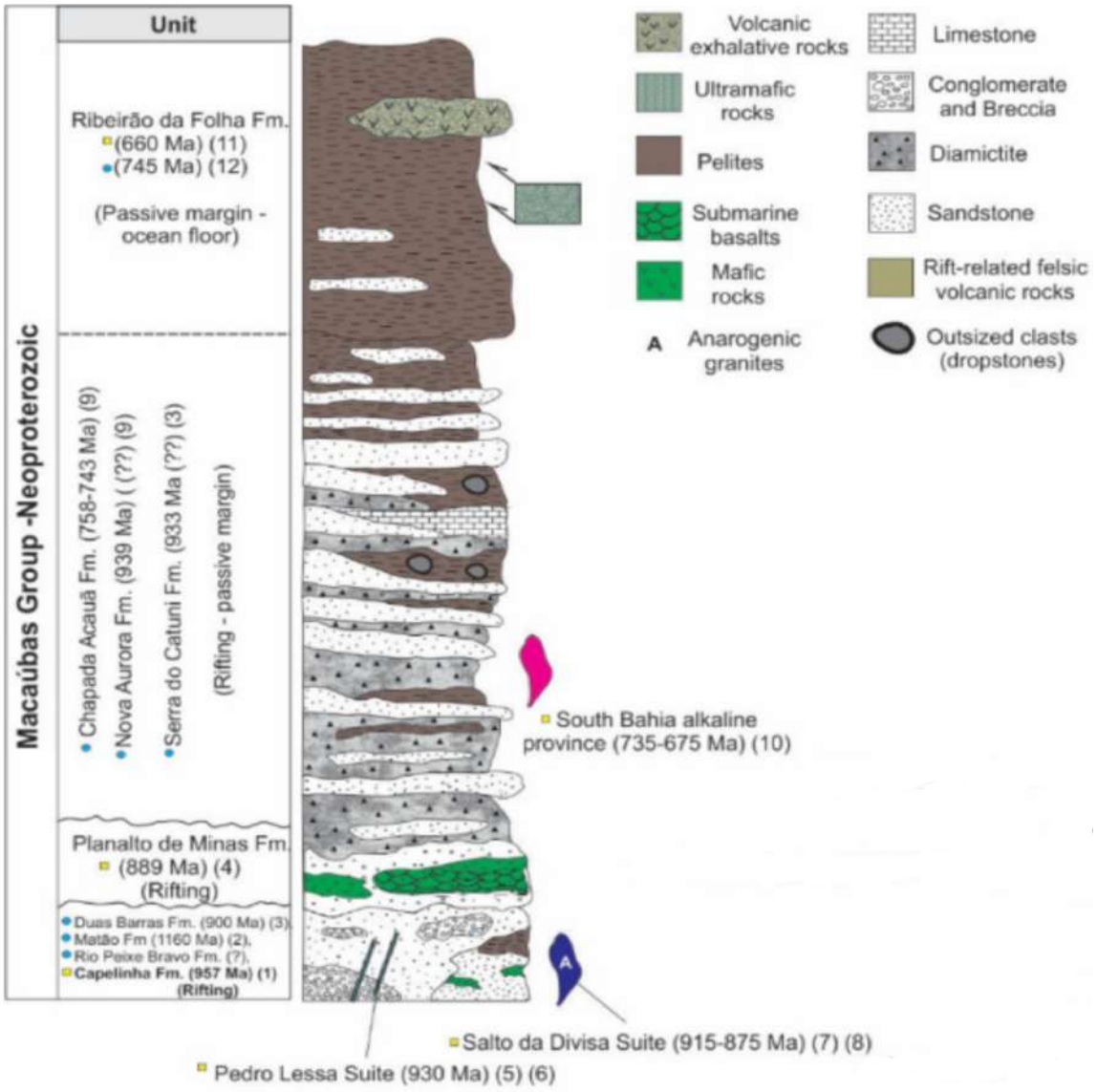

Figure 14. Stratigraphic column of the Macaúbas Group (Castro et al., 2019, modified from Pedrosa-Soares et al., 2007, 2008, and Babinski, 2012).

The Lower Macaúbas Sequence, constrained between 900 and 750 Ma (Kuchenbecker et al., 2015), contains continental to shallow marine units (**Capelinha** and **Matão-Duas Barras formations**). Its deposition was followed by a hiatus and erosion that lasted until the Cryogenian rifting, when sedimentation of Middle Macaúbas Sequence began. This section, deposited in glaciomarine settings (Karfunkel and Hoppe, 1988; Uhlein et al., 2007; Pedrosa-Soares et al., 2011), is formed by diamictite, tillite, varvite, as well as various quartzites and metapelites (**Serra do Catuni**, **Nova Aurora** and **Lower Chapada Acauã formations**). The Upper Macaúbas Sequence represents the evolution of the Macaúbas rift to a passive margin complex, marked by continental shelf sandstone and pelite (**Upper Chapada Acauã Formation**), as well as distal platform and ocean floor deposits of turbidite, chert, banded iron formations and limestone (**Ribeirão da Folha**

Formation). Mafic and metaultramafic rocks occur associated with the Ribeirão da Folha Formation, and are interpreted as tectonically dismembered remnants of ophiolite complexes (Pedrosa-Soares et al., 1992, 1998, 2001; Queiroga et al., 2007; Queiroga, 2010; Peixoto et al., 2015; Amaral et al., 2020).

3.4.5. Bambuí Group

The Bambuí Group (Costa and Branco, 1961) is the most extensive sedimentary cover of the São Francisco Craton. After various contributions (Oliveira, 1967; Braun, 1968; Schöll, 1973), it was divided by Dardenne, (1978), in the central region of Minas Gerais, in the Jequitaí, Sete Lagoas, Serra de Santa Helena, Lagoa do Jacaré, Serra da Saudade and Três Marias formations, deposited over the course of five complete transgressive-regressive cycles (Martins and Lemos, 2007; Uhlein et al., 2017). A conglomerate facies originally defined as a basal facies of the Sete Lagoas Formation was later dismembered, re-classified as the Carrancas Formation (Tuller et al., 2008) – a vision challenged by Delpomdor et al. (2020) – and positioned at the base of the Bambuí Group, concluding what is currently its most widespread stratigraphic column (Figure 15).

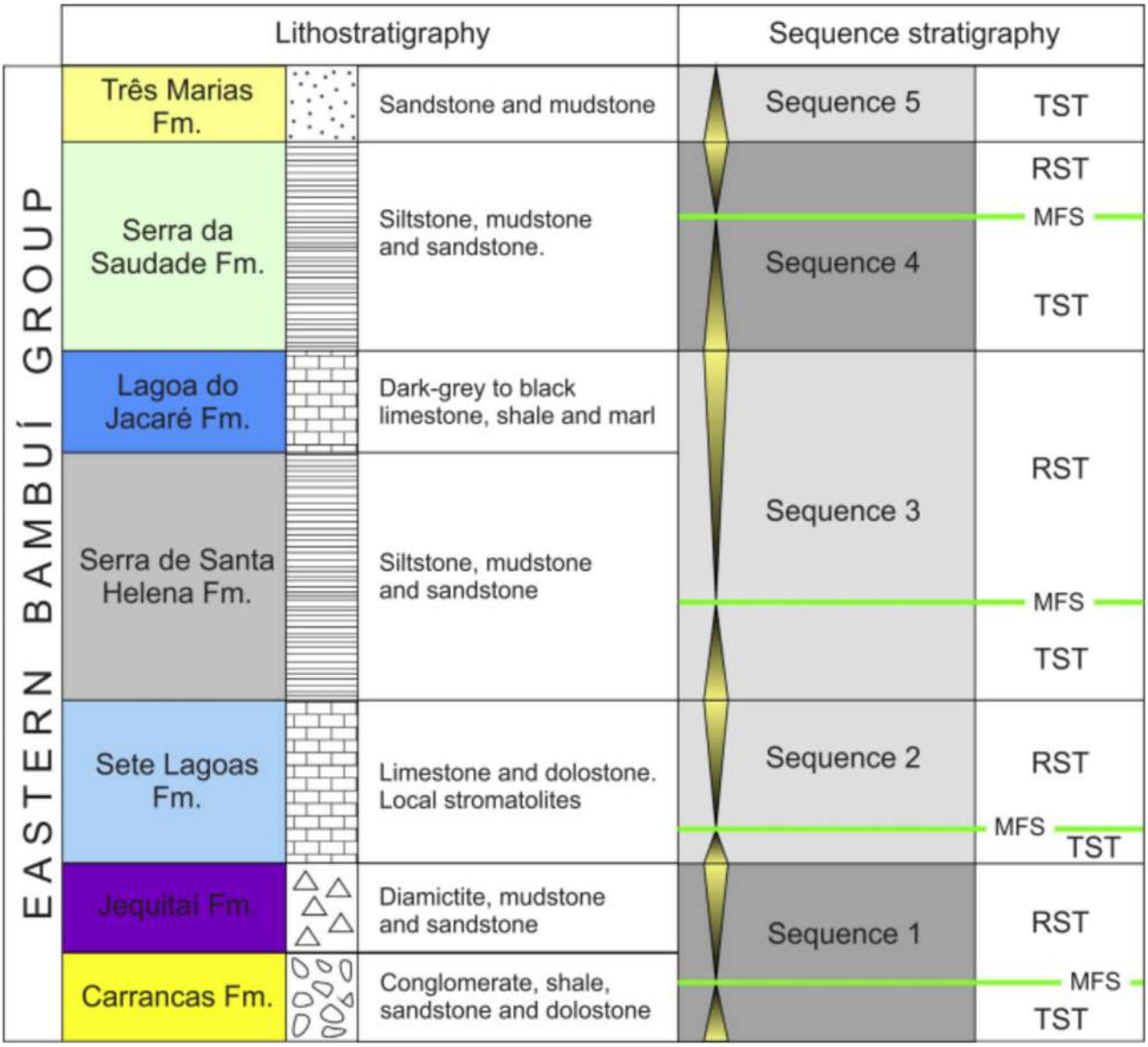

Figure 15. Litho and sequence stratigraphy of the Bambuí Group (Uhlein et al., 2017).

The **Carrancas Formation** (Costa and Branco, 1961; Tuller et al., 2008) typically contains conglomerate and pelitic rocks. Originally considered to have been deposited under glacial conditions over the continent (e.g. Romano and Knauer, 2003; Sgarbi et al., 2003; Rocha-Campos et al., 2011), recent petrographic and isotopic evidence now support origin from debris and mud flows in a lagoon or restricted marine free from glacial influence for this unit (Vieira et al., 2007; Tuller et al., 2010; Uhlein et al., 2012). The **Jequitaí Formation** (Oliveira and Leonardos in Isotta et al., 1969) is mainly composed of massive diamictite, deposited in a foreshore setting capped by ice (Isotta et al., 1969; Karfunkel and Hoppe, 1988; Rocha-Campos et al., 1996; Uhlein et al., 1998, 1999, 2011). Caxito et al. (2012) suggested that sedimentation occurred during the Marinoan Glaciation (~635 Ma), meaning that the Carrancas Formation is, thus, a pre-glaciaal unit (Uhlein et al., 2016). These two basal

formations of the Bambuí Group represent continental or transitional deposits, and are topped by a series of marine platform facies that ends with a final regression to transitional and continental environments.

The **Sete Lagoas Formation** (Costa and Branco, 1961) is the first sequence deposited after the rise of the advance of the sea over the Bambuí Basin. It is formed, at its base, by cap carbonates vinculated to the post-Marinoan Glaciation period (Caxito et al., 2012; Alvarenga et al., 2014). The remaining of this unit is composed by two successive shallowing upward transgressive sequences. The first contains dolostone and limestone with frequent sedimentary structures caused by the action of waves (the Pedro Leopoldo Member), and the second is formed by limestone (often stromatolitic) intercalated with pelites (the Lagoa Santa Member). A depositional hiatus separates the basal rocks from the middle and top sections (Uhlein et al., 2016; Perrella et al., 2017). The **Serra de Santa Helena Formation** (Oliveira, 1967; Dardenne, 1978) is constituted by a thick package of silty-clayish rhythmite indicating an expressive marine transgression and establishment of a low-energy, deep marine environment over the carbonatic platform. Occasional limestone or fine sandstone mark periods of higher agitation (Uhlein et al., 2004; Lima et al., 2007; Iglesias and Uhlein, 2009). The **Lagoa do Jacaré Formation** (Oliveira, 1967; Dardenne, 1978), composed by kilometric limestone lenses amidst a pelitic substrate, marks a period of marine regression and a environmental change into a high-energy carbonate platform that imprinted several structures into the rock, such as hummocky cross-beddings, intraclasts and oolites (Uhlein et al., 2004; Lima et al., 2007; Iglesias and Uhlein, 2009). Another marine transgression and the setting of a deep water environment occasionally disturbed by storms or turbidity currents. The sedimentary result is the **Serra da Saudade Formation** (Dardenne, 1978), a sequence of pelite and rhythmite, at times interleaved with greywacke, sandstone and calcirudite with frequent hummocky cross-bedding. A greenish phosphatic pelite (verdete) is characteristic of this unit (Uhlein et al., 2004; Lima, 2005; Iglesias and Uhlein, 2009). Closing the Bambuí Group, the **Três Marias Formation** (Braun, 1968; Dardenne, 1978) is composed by polymictic conglomerate at is base, followed by arkose, sandstone and siltstone, representing a significative marine regression, with establishment of a storm-influenced platformal environment succeeded by deltaic and fluvial systems (Costa, 1978; Chiavegatto, 1992; Lima, 2005).

The areas of occurrence of the Carrancas and Jequitaí formations are relatively small, and dwarfed by the voluminous space occupied by the remaining rocks of the Bambuí Group. Frequently, the local basal units of the group are the Sete Lagoas and Serra de Santa Helena formations (Costa and Branco, 1961; Paiva-Filho and Ponçano, 1972; Rocha-Campos and Hasui, 1981; Karfunkel and Hoppe, 1988; Cukrov et al., 2005; Romano, 2007; Vieira et al., 2007; Tuller et al., 2008, 2010; Romano et al., 2014).

Deposition of the Bambuí Group, according to most works (a premise we take up on in the present thesis), took place entirely in a foreland basin associated with the development of the Ediacaran-Cambrian orogens surrounding it (Chang et al., 1988; Pimentel et al., 2001; Martins-Neto et al., 2001; Martins-Neto, 2009). Based on seismic data, Romeiro-Silva and Zalán (2005) and Zalán and Romeiro-Silva (2007) proposed an initial intracratonic setting lasting until the sedimentation of the Lagoa do Jacaré Formation, only then changing into a foreland environment, but this interpretation is not compatible with the geochronological data available.

3.4.6. Jequitaí-Macaúbas – one ice blanket for two tectonic cribs

The Jequitaí Formation and the Macaúbas Group are correlated, having been deposited under influence of the same glaciation, and the former has even been listed as a member of the latter (Karfunkel and Karfunkel, 1976; Karfunkel and Hoppe, 1988). With areas of occurrence restricted to the eastern southeastern São Francisco Craton, the Jequitaí Formation was later reallocated into the Bambuí Group (Dardenne, 1978; Uhlein et al., 2011), being separated from the Macaúbas Group, which has occurrences limited to the Araçuaí Belt and registers a precursory basin of the Araçuaí-West Congo Orogen (Pedrosa-Soares et al., 1992, 1998, 2001; Pedrosa-Soares and Alkmim, 2011).

Yet, the correlation between the units has stood and was further detailed (Figure 16). Initially, the Jequitaí Formation was believed to be a continental facies of the glacial system, and the Macaúbas Group would be its marine representative (Isotta et al., 1969; Karfunkel and Karfunkel, 1976; Karfunkel and Hoppe, 1988). This interpretation was later changed. The Jequitaí Formation is now understood as a transitional unit, with continental facies at the base giving place to shallow marine sediments at the top (Rocha-Campos et al., 1996; Uhlein et al., 1998, 1999, 2011; Martins-Neto and Hercos, 2002; Cukrov et al., 2005), while the correlating sedimentation in the Macaúbas Group corresponds to deeper marine settings (Uhlein et al., 1998, 1999; Pedrosa-Soares et al., 2001, 2011).

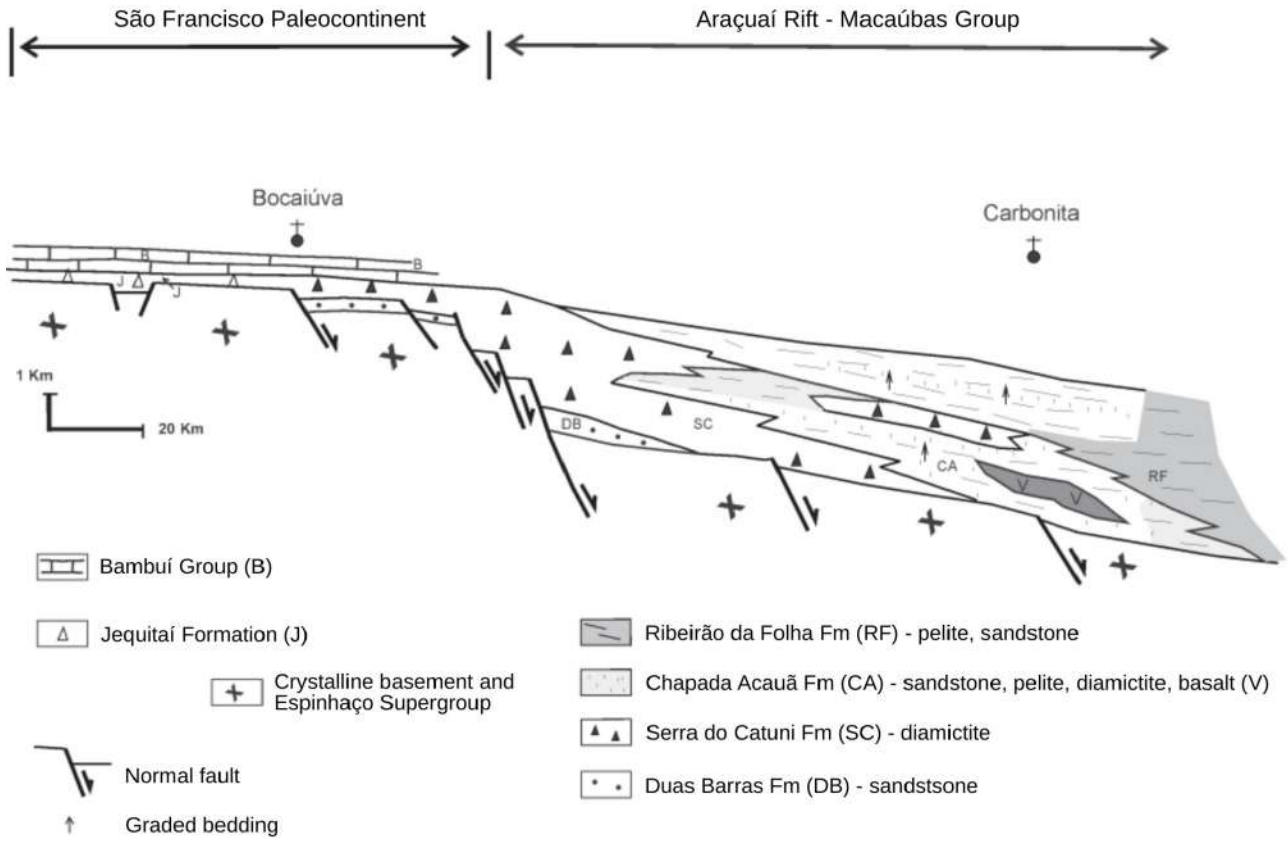

Figure 16. Lateral correlation between the Jequitaí Formation and the Macaúbas Group in central Minas Gerais (Uhlein et al., 2007).

3.5. Old and new questions

Even though the São Francisco Craton and the Southern Espinhaço Range are among the most thoroughly studied regions in South America, many questions regarding their geological past remain.

In recent times, the hypothesis of the Araçuaí-West Congo Orogen as product of intracontinental deformation (Trompette, 2000) has been revisited, questioning the existence of the Adamastor Ocean and proposing a hot-orogen model (Meira et al., 2015; Cavalcante et al., 2019; Vauchez et al., 2019; Fossen et al., 2020; Konopásek et al., 2020). Though evidence of ophiolitic sequences and tectonic models have been brought by numerous works (Pedrosa-Soares et al., 1992, 1998, 2001; Aracema et al., 2000; Queiroga et al., 2007; Queiroga, 2010; Pedrosa-Soares and Alkmim, 2011; Peixoto et al., 2015; Degler et al., 2018; Amaral et al., 2020; Caxito and Alkmim, 2023), contestations raise pertinent questions regarding the geometry, kinematics and duration of the closure of the oceanic basin.

Another point that has re-emerged from recent data is the temporality of the continental collisions that formed West Gondwana. Trindade et al. (2003, 2006), Tohver et al. (2010, 2012) and Tohver and Trindade (2014) posed that the amalgamation of the Amazonas and Rio Apa did not occur until the Cambrian Period, after several blocks had already been accreted to the megacontinent (in the

Ediacaran). However, a plethora of geotectonic and geochronological data support the completion of the formation of West Gondwana in the Ediacaran (Pisarevsky et al., 2008; Cordani et al., 2009, 2013; Pimentel et al., 2011; Amaral et al., 2012; Meira et al., 2015; Paula-Santos et al., 2015). Still, U-Pb age results show that sedimentation of the Bambuí Group spans from 635 to 524 Ma (Caxito et al., 2012; Moreira et al., 2020; Tavares et al., 2020), including 550 Ma ages for the Sete Lagoas Formation, the first carbonatic sequence of the group (Paula-Santos et al., 2015). K-Ar ages from the interior of the northern portion of the São Francisco Craton record deformation between 630 and 470-460 Ma (Süssenberger et al., 2014), that is, persisting well into the Cambrian and Ordovician period. Furthermore, paleontological and chemostratigraphical evidence (Warren et al., 2014; Paula-Santos et al., 2017) point to a possible marine connection between the Bambuí basin and other epicontinental seas in the Cambrian Period (e.g. the Nama Sea in the Kalahari Craton, among others) that were unaccounted for. While the this does not suggest the existence of an ocean to be closed at that time, a hypothesis that might be overpast, it means that foreland sedimentation mechanisms were active in the São Francisco for longer than anticipated.

As debate rages on, De Toni et al. (2023) hypothesized the Adamastor Ocean as a back-arc oceanic basin driven by the collisions between the São Francisco-Congo paleocontinent and other continental cores (the Nico Perez Terrane and the Río de la Plata Craton) to the west. This, in turn, requires better understanding of the chronology of the passive margin stage of the Macaúbas Basin.

Solutions for these geotectonic puzzles can only come from refinements to the extant models. That is true both for the São Francisco-Congo convergence, specifically, and for the behavior of the continental blocks during the amalgamation of West Gondwana.

The substance of this thesis dwells on the second point, that is, the imprints left by the Araçuaí Orogeny in the foreland region. Here, we bring data relating to the stratigraphic, structural and temporal relationships between the Southern Espinhaço Range and the São Francisco Craton in their interaction zone.

4. THE CRATON-OROGEN BORDER IN SERRA DO CIPÓ AND VICINITIES – RESULTS AND REVIEW

In this chapter, we present the result of our geological mapping and characterization of Serra do Cipó and its vicinities, dividing descriptions of the geognostic state of the area in items addressing its stratigraphy, structural geology, metamorphism and tectonic evolution. As we do so, we compare our observations with those made in previous works with our own, evidencing points we found coherent with our study and points that called for a conceptual review.

Stratigraphic and structural aspects of the area vary spatially in such a way that it was divided in two tectonic domains divided by the Espinhaço Front (Figure 17). The western compartment corresponds to the foreland region of the São Francisco Craton, often referred to here as the Foreland Domain, while the terrane to the east pertains to the marginal fold-and-thrust system of the Araçuaí Orogen, addressed here as the Fold-and-Thrust Domain. This domain is composed by the fold-and-thrust belt that integrates the Southern Espinhaço Range, locally known as the Cipó Range.

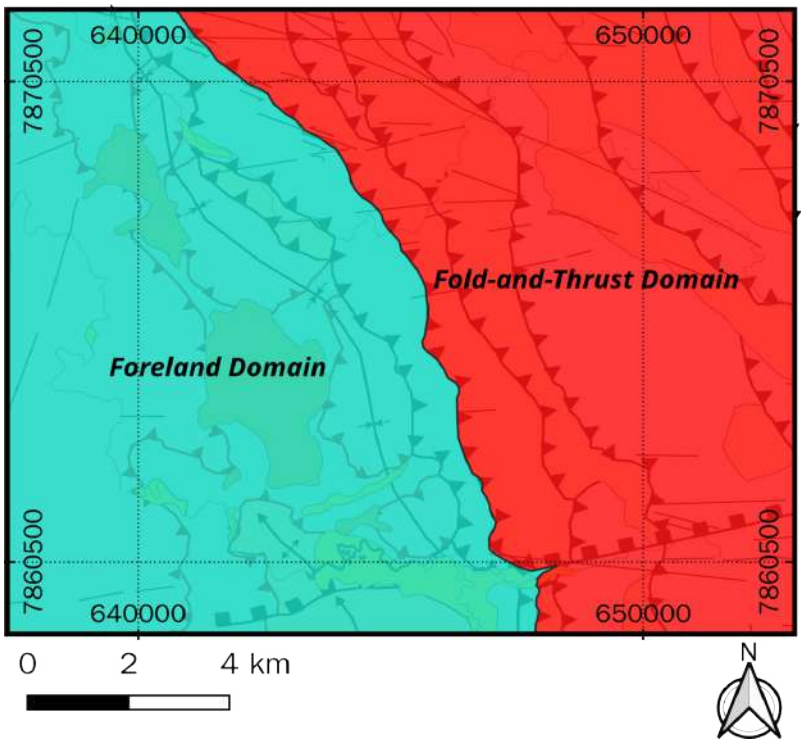

Figure 17. Tectonic compartmentalization of the region of Serra do Cipó.

4.1. Previous studies

In regional surveys, Serra do Cipó and its surroundings were first mapped in the 1970's at 1:100,000 scale by Schöll and Souza (1970 in Oliveira et al., 1997), and at 1:250,000 scale by Schöll (1972), and later by Oliveira et al. (1997), in the sphere of the Espinhaço Project, and Ribeiro (2010), under the Sete Lagoas-Abaeté Project, again at 1:100,000 scale in both cases. Magalhães (1988),

Marshak and Alkmim (1989) and Uhlein (1991) also contemplated the area, among others, in broad structural approaches of the São Francisco Craton.

A number of local-scale works were aimed specifically at the region of Serra do Cipó, addressing various of its geological aspects. Silva et al. (2007), Bakir et al. (2016) and Chierici et al. (2021) worked on the geological cartography and stratigraphy. In nearby areas, similar studies have also contributed for the definitions of contacts and stratigraphic correlations (Dussin, 1983; Karfunkel et al., 1991; Oliveira and Torres, 2014; Victoria and Moy, 2014). In turn, with structural scope, Oliveira (1994) and Taufner et al. (2021) studied the style and mechanisms of the deformation that affected the area.

4.2. Methods

We defined our target area between the coordinates UTM 23K 653000-637400 E and 78590000-7872000 N (using the datum Sirgas2000), covering 202.80 km². With that established, we proceeded to remote sensing, to help both planning campaigns and refine contact and structure traces on the resulting map. During the campaigns, we described petrographic aspects of the rocks exposed in the region, with greater attention to the structural elements. After facing incongruencies between our observations and the extant maps and stratigraphic models, we converted our interpretations into a local map, presented at 1:25,000 scale. Samples collected during the outings were dedicated to the series of analyses described in this and the following chapters. All samples collected for structural analysis and EBSD were oriented before being taken out from the outcrops.

4.3. Field work

Field work consisted of preparative stages, campaigns and post-field data treatment and analyses. In total, 165 rock outcrops and expositions were described, and samples were taken from 90 points (Table 2). Based on our observations, we made adjustments to the extant geological models of the area, such as maps and cross-sections. The reinterpreted geological map that resulted from the work and representative cross-sections of the study area are annexed to this thesis in Appendices A and B, and a map locating outcrops and sampling points comes in Appendix C.

Table 2. Field sampling summary.

Type of sample	Points sampled	Total of samples
Rock – not-oriented	20	28
Rock – oriented	56	61
Quartz vein (concordant with tectonic foliation)	25	32
Quartz vein (discordant with tectonic foliation)	1	1

4.4. Stratigraphy

The stratigraphy that we interpreted for the region of Serra do Cipó (Figure 18.a) is composed, from base to top by the Espinhaço Supergroup, represented by the São João da Chapada (Espinhaço I Sequence), Galho do Miguel, Santa Rita, Córego dos Borges (Espinhaço II Sequence) formations; the Pedro Lessa Suite; the Bambuí Group, represented by the Sete Lagoas and Serra de Santa Helena formations; and unconsolidated detrital and alluvial Cenozoic deposits. Each tectonic compartment has its own stratigraphic column, that is, we did not identify any occurrence of any stratigraphic unit in both domains. In the Foreland Domain, the São João da Chapada occurs to the south, as a rigid basement to the Bambuí Group, and to the north as a tectonic wedge lodged between the Sete Lagoas and Serra de Santa Helena formations (Figure 18.b). The stratigraphic sequence of the Fold-and-Thrust Domain is composed mainly by the Galho do Miguel, Santa Rita and Córrego dos Borges formations. At the heights of the Cipó Range, metamafic intrusive bodies attributed to the Pedro Lessa Suite cut through the Espinhaço Supergroup (Figure 18.c).

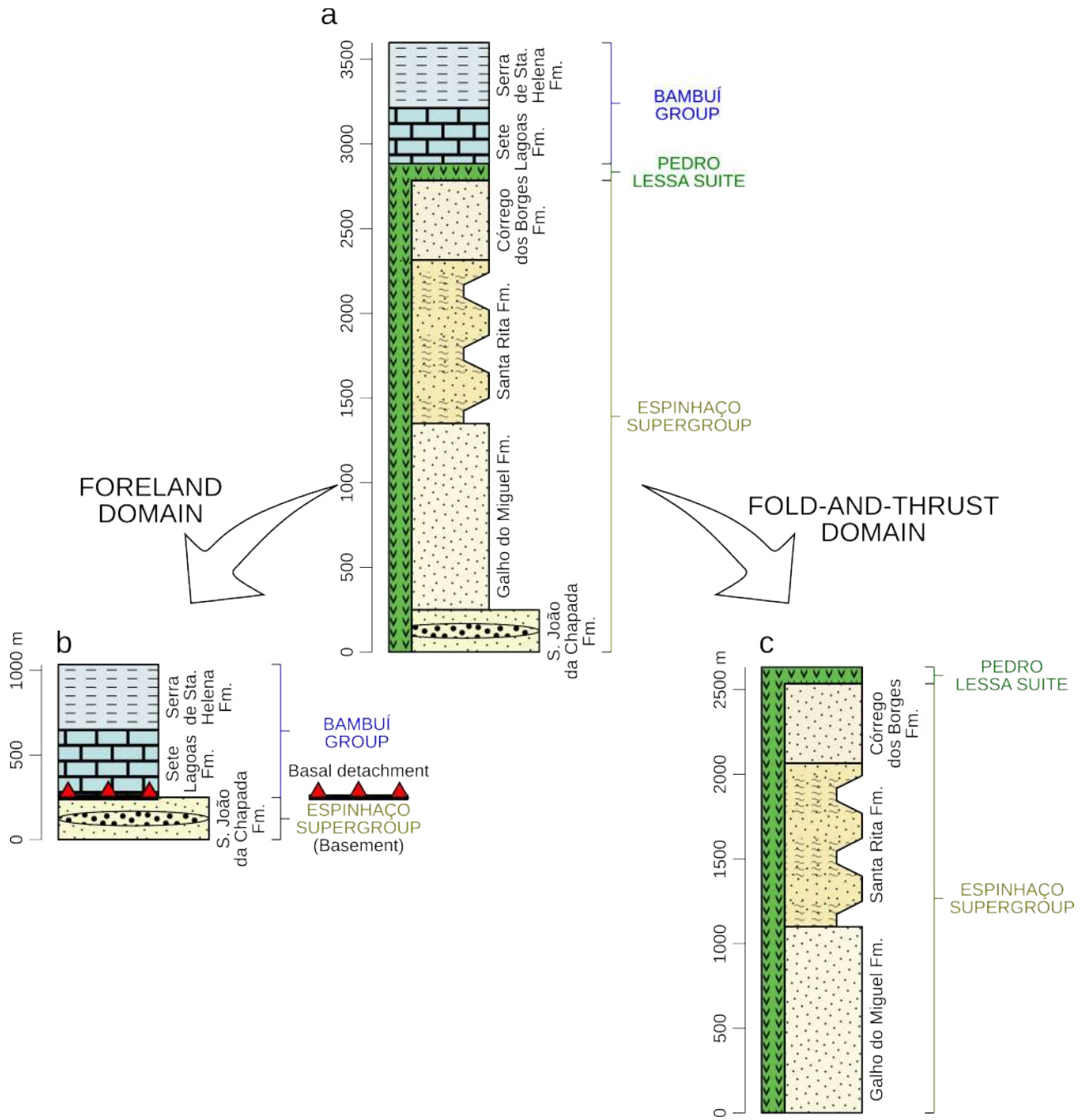

Figure 18. Stratigraphy of the region of Serra do Cipó, according to this work. a) Complete sequence; b) Stratigraphy of the Foreland Domain; c) Stratigraphy of the Fold-and-Thrust Domain.

We present here a reviewed stratigraphic column for the craton-orogen limit in the region of Serra do Cipó. It is relevant to stress The following items characterize the rock units identified in this study. Rather than following a simple global base-to-top sequence, we divide descriptions by tectonic domain, starting with the Fold-and-Thrust Domain and finishing with the Foreland Domain.

4.4.1. Fold-and-Thrust Domain

4.4.1.1. Espinhaço II Sequence – Galho do Miguel Formation

The Galho do Miguel Formation in the thickest unit found in the Cipó Range, reaching up to 1120 m. It occurs to the eastern portions of the study areas, always bordering the Santa Rita Formation, with thrusts at the base, which have topographic expression under the form of scarps (Figure 19.a), and normal contacts at the top. The Galho do Miguel is composed by its most characteristic facies: a pure, white, very well selected quartzite, with alternating fine-grained and medium-grained laminae (Figure 19.b). Medium-sized cross-bedings indicating varying directions of aeolian transport and ripple marks are common throughout the areas of occurrence of this unit (Figure 19.c, d). Tectonic foliation is sub-parallel to bedding surfaces, though discrete and poorly marked due to scarcity of mica or stretched quartz grains as markers.

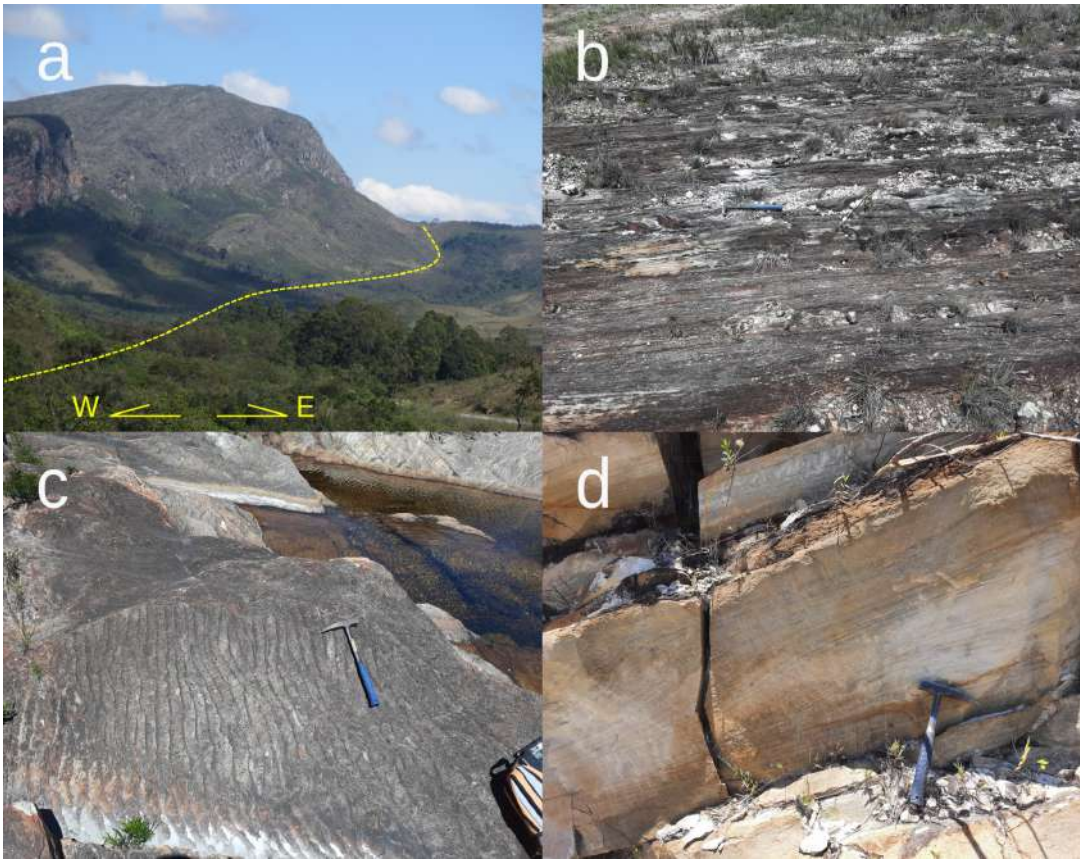

Figure 19. The Galho do Miguel Formation atop the Cipó Range: a) Scarps marking tectonic contacts with the Santa Rita Formation (view towards S); b) Laminated structure; c, d) Sedimentary structures – ripple marks (c) and cross-beddings (d).

4.4.1.2. Espinhaço II Sequence – Santa Rita Formation

The Santa Rita Formation marks the local termination of the Fold-and-Thrust Domain and the Espinhaço Front at the border with the São Francisco Craton, being thrusted over the Sete Lagoas Formation at the base of the Cipó Range. The Santa Rita Formation occurs interleaved with the Galho

do Miguel and Córrego dos Borges formations. The basal contacts are either normal, with the Galho do Miguel Formation, or thrusts faults, with the Córrego dos Borges Formation, while top contacts are invariably marked by thrusts. Thickness is about 980 m, probably due to a significative tectonic thickening of the original sequence, attributed to internal reverse shear zones, mesoscopic faults, duplexing and folding. With exception to the steep hillside of the Espinhaço Front, areas of occurrence of this unit usually have flat topography where the rocks are richer in clay and mica minerals (Figure 20.a), with scales of rock protruding upwards where proportion of quartz increases (Figure 20.a, b). Such scaly outcrops are typical of the Santa Rita Formation in the area. Gullies are common features in this unit, reaching metric depths and up to tens of meters in extension (Figure 20.c).

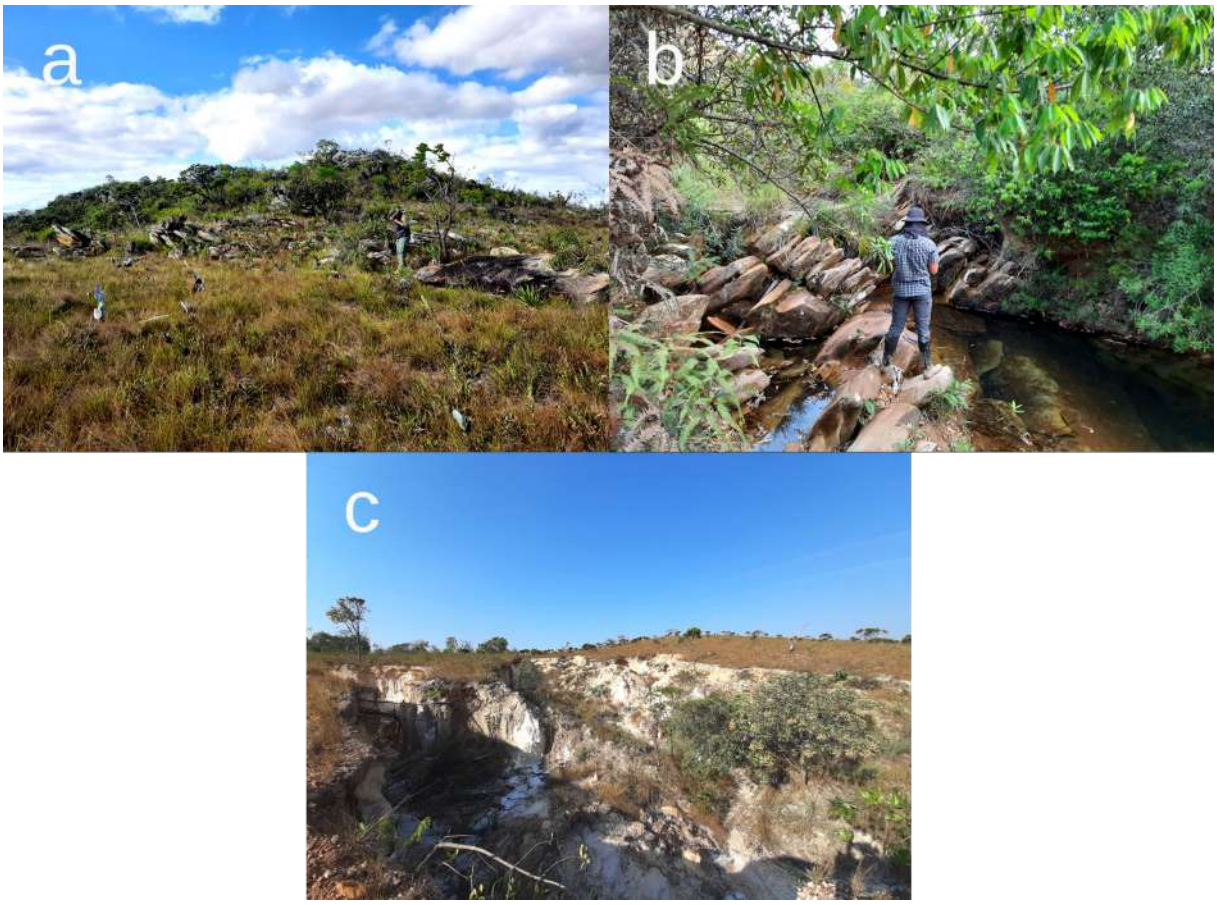

Figure 20. Forms of occurrence and features of the Santa Rita Formation at the heights of the Cipó Range: a) Flat topography on occurrence of phyllite interrupted by scaly protrusions of quartzitic levels; b) Detail of quartzitic scales protruding on outcrop; c) Gully developed on fine-grained succession.

The Santa Rita Formation is composed by a white, impure and fine-grained sericitic quartzite, containing milli-centimetric gray or green phyllitic layers. In the immediate vicinities of the Espinhaço Front, the rock contains significant content of clasts composed by microcline. Bedding-parallel foliation (phyllitic or schistose) and quartz veins, as well as S-C surfaces marking reverse

shear bands are widespread throughout this unit (Figure 21.a), with occasional occurrence of quartz rods and tension gashes. The texture of the rocks gradually changes from clastic (Figure 21.b) to mylonitic (Figure 21.c) as shear bands are approached, where the color of the rock also turns to dark gray. In the areas less disturbed by strain, sedimentary structures such as cross-beddings and ripple marks are common (Figure 21.d). Occasionally, the layers acquire a rhythmic aspect, with millimetric to centimetric thicknesses. Veins are usually found at or near the contact between quartzitic and phyllitic layers (Figure 21.e). Though sericite is the most prevalent mica phase, chlorite, biotite are also observed as accessories and constituting foliation surfaces. Tourmaline is also present, growing over the finer-grained portions adjacent to quartz veins alongside a number of opaque minerals (21.f).

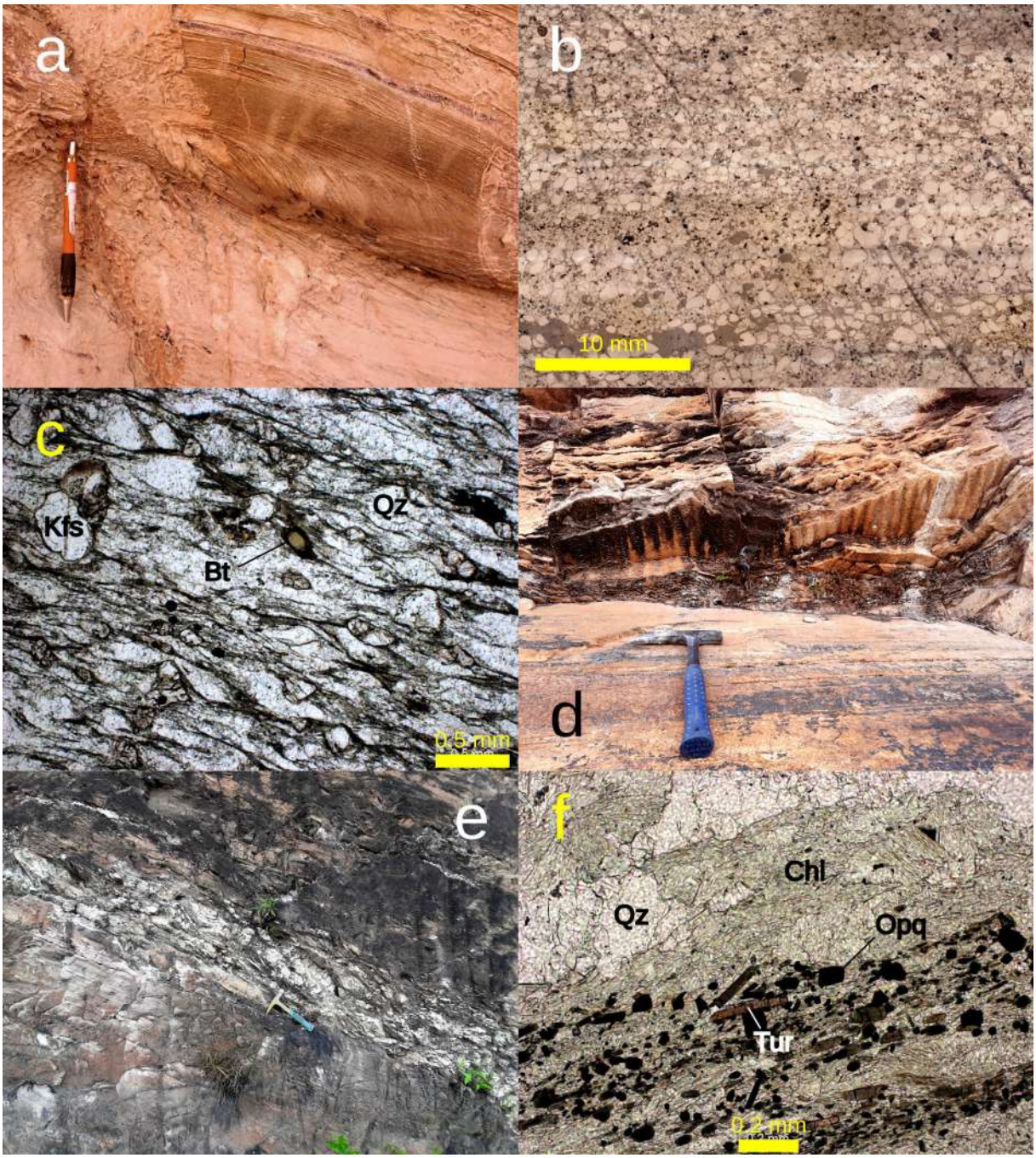

Figure 21. Features of the Santa Rita Formation: a) Quartzite with S-C foliation; b) Photomicrography showing clastic and laminated texture; c) Photomicrography showing development of mylonitic texture; d) Ripple marks; e) Outcrop cut by stretched quartz veins parallel to the tectonic foliation; f) Photomicrography showing development of tourmaline and opaque minerals adjacent to quartz vein.

4.4.1.3. Espinhaço II Sequence – Córrego dos Borges Formation

Mapped by Oliveira et al. (1997) on the northern border of the study area, the Córrego dos Borges is a tectonic sheet lodged within two instances of the Santa Rita Formation. It is formed by a white-grayish quartzite with millimetric sericitic levels. Metric intercalations of pure, recrystallized

quartzite are also present. We did not have access to the areas of occurrence of this unit. Based on the geological and topographic cartography, we estimate a thickness of the order of ~477 m.

4.4.1.4. Pedro Lessa Suite

A small sill and set of apophyses of foliated metadiabase occurs lodged in a contact between the Galho do Miguel and Santa Rita formations. These are representatives of the Pedro Lessa Suite in the Cipó Range. We found only one exposition of the rock in the study area, in a severely weathered state, with relics being composed of brown or purple clayish material (Figure 22). Fresh remnants amount for very little of the total volume, showing black color and aphanitic or fine-phaneritic texture. The attitudes of the apophyses and of the internal schistosity of the metadiabse are concordant to those of the contact, beddings and tectonic foliation surfaces of the host rocks.

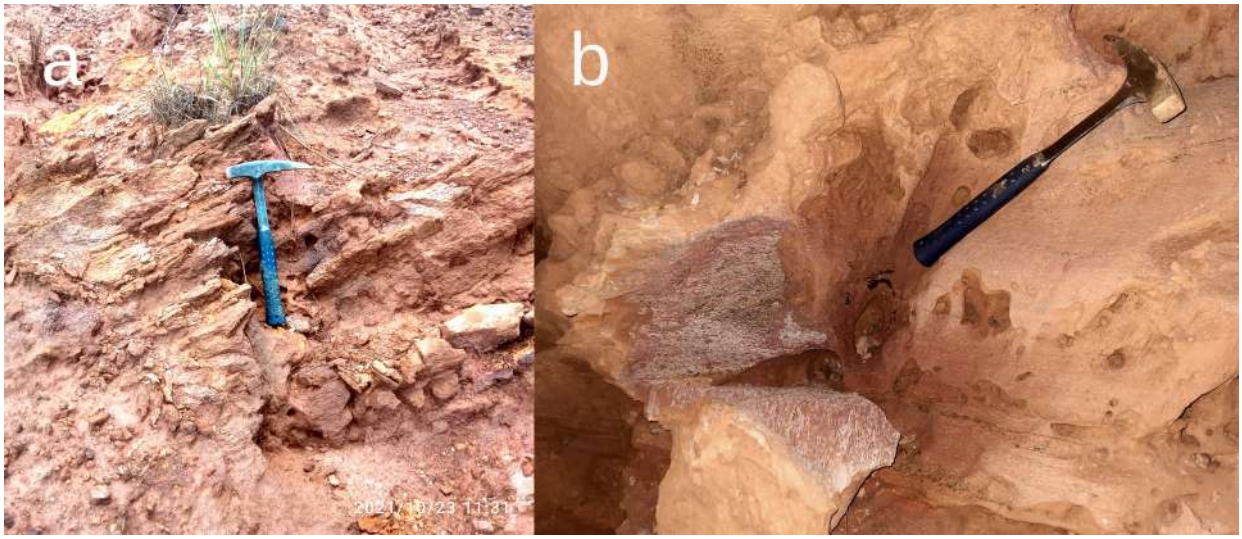

Figure 22. The Pedro Lessa Suite is poorly exposed in the region of Serra do Cipó. The single outcrop of the unit is severely weathered (a, b), with fresh remnants as rare occurrences.

4.4.2. Foreland Domain

4.4.2.1. Espinhaço I Sequence – São João da Chapada Formation

The São João da Chapada Formation occurs in two areas of the Foreland terrane. In an exposition in the southern limit of the study area, it is practically undeformed, sitting exposed in a structural window below a detachment surface that separates it from the Sete Lagoas Formation. This occurrence of the São João da Chapada Formation includes a very well known outcrop situated on the riverbed of the Cipó River, under a bridge on the access road to Serra do Cipó, at the coordinates UTM 23K 642662 E, 7860649 N). For this reason, this area will be referred to here as the Cipó River Window. In this structural window, the São João da Chapada is composed by an impure, poorly selected, beige or white quartzite, at times with conglomeratic aspect and well-preserved ripple marks

(Figure 23.a) and small to medium cross-beddings. Grains are sub-rounded to sub-angular (Figure 23.b), ranging from medium to coarse sand granulometry. In the remaining area of the structural window, significant matrix-supported oligomictic metaconglomeratic (Figure 23.c) and minor metadiamictitic (Figure 23.d) lenses are also contained within the quartzitic package, with rounded sub-rounded, sub-angular and angular clasts sizing between granule and cobble composed by quartzite or quartz. Tectonic foliation is present and sub-parallel to bedding surfaces, but weakly marked due to low mica content in the rocks and low degree of development.

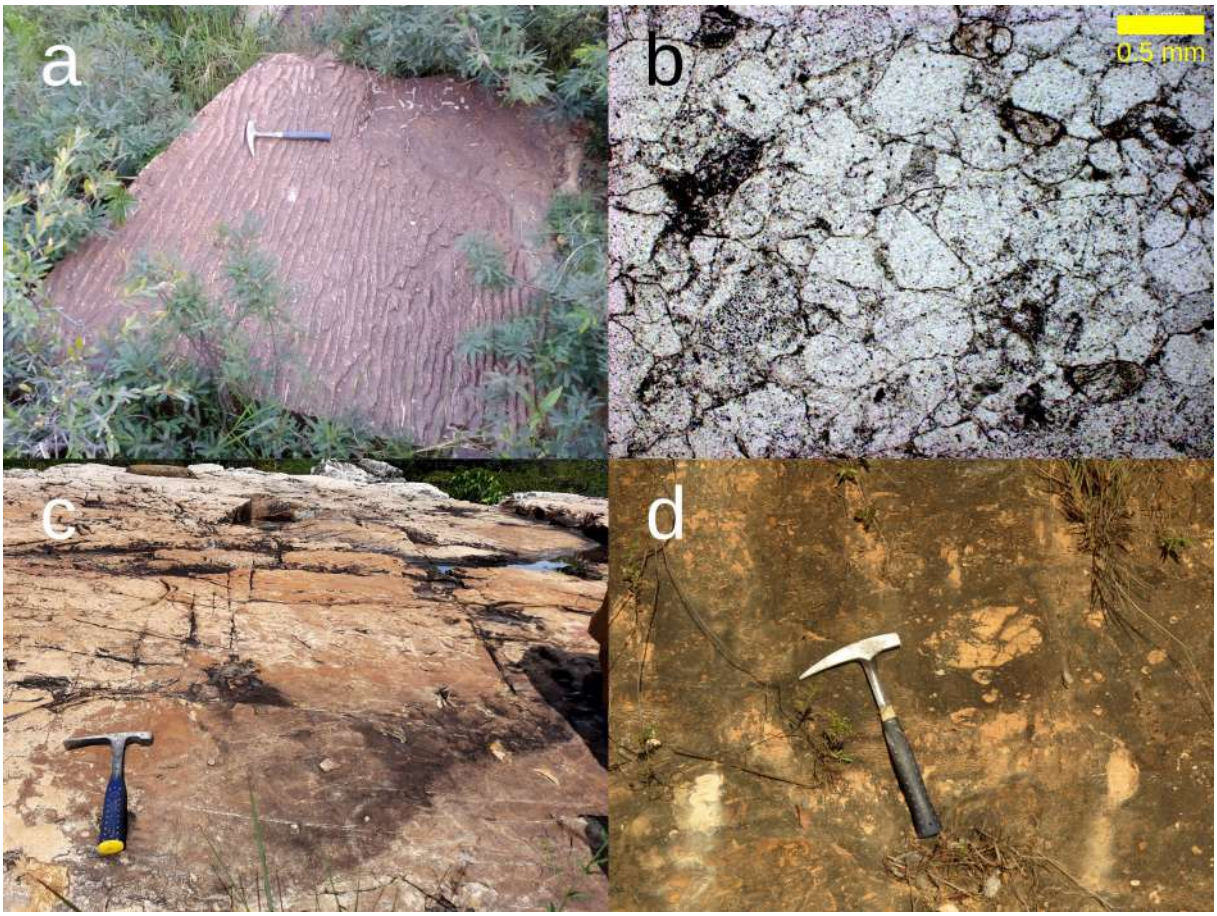

Figure 23. The São João da Chapada Formation in the Cipó River Window: a) Well-preserved ripple marks; b) Poorly selected granulometry and clasts with sub-rounded to sub-angular shape; c) Metaconglomeratic lens; d) Metadiamictitic lens.

In the center-north portion of the study area, the São João da Chapada unit occurs in the form of a 250 m-thick tectonic sheet wedged between the contact between the Sete Lagoas and Serra de Santa Helena formations. The local topography is characterized by a valley excavated by the Parauninha River, with the São João da Chapada wedge situated on the western bank. For this reason, we also refer to this area as the Parauninha Wedge. We interpret this sheet as the result of the top of the São João da Chapada Formation splintering westwards out of the otherwise undeformed sequence that forms the local rigid basement to the Bambuí Group, and experiencing dynamic recrystallization.

Within the sheet, three facies occur. At the base comes a white, coarse-grained and poorly selected quartzite, with millimetric brownish levels. This lithotype contains a metric lenticular body of foliated oligomictic metaconglomerate (Figure 24.a, b) with a coarse-grained, poorly selected matrix. The tectonic foliation in this area is more developed than in the structural window to the south. It becomes phyllitic or schistose and acquires an anastomosed aspect surrounding coarse clasts (Figure 24.c). The quartzite is topped by a metadiamictite with fine-grained, poorly selected matrix. Expositions in general are weathered, occurring in troughs, gulches and ravines.

Figure 24. The São João da Chapada Formation in the Parauninha Wedge: a, b) Weathered exposition of metaconglomerate in ravines; c) Photomicrography showing stretched clasts and anastomosed schistosity; d) Weathered exposition of metadiamictite.

The thickness of this unit has been determined as at least 250 m, based on the top and bottom contacts of the Parauninha Wedge. However, we cannot affirm that the entire package of the São João da Chapada Formation was thrusted into the wedge. Hence, 250 m is the minimum value of thickness to be considered for this unit. Based on our data, it is not possible to estimate how much deeper the

contact between the São João da Chapada and the underlying rocks (whether the crystalline basement or another supracrustal unit) in the Cipó River Window is.

4.4.2.2. Bambuí Group – Sete Lagoas Formation

The Sete Lagoas Formation occupies most of the central strip of the study area, arranged in a corridor-like manner. It is also the foreland unit bordering the Espinhaço Front, where it is overridden by the Santa Rita Formation. At its easternmost areas of occurrence, the Sete Lagoas Formation is involved in the advance of the fold-and-thrust front, forming either internal thrusts or being heaved above the Serra de Santa Helena Formation. In such cases, the limestone forms rugged protrusions (Figure 25) in the topography that reach up to 1000 m of altitude. In the remaining of the Foreland Domain, relief is relatively smooth and flat, ranging between 800 and 900 m altitudes. Aside from the aforementioned thrust contacts, this unit sits between a basal and a top detachments, in contact with the São João da Chapada and the Serra de Santa Helena formations, respectively. Thickness of this formation is estimated at approximately 490 m, but we estimate that it may be increased up to 730 m near the interface with the Espinhaço Front due to folding and hinge zone thickening.

Figure 25. A hill composed by limestone of the Sete Lagoas Formation protruding from the surface in the immediate vicinities of the Espinhaço Front.

The Sete Lagoas Formation is carbonatic, constituted either by grainy limestone or medium-grained marble. The rocks are layered, mostly composed by thicker (centi or decimetric) white to

light beige horizons, with thinner (milli or centimetric) brown, gray and black levels and millimetric intercalations of greenish marl (Figure 26.a). Calcite veins are also common, both concordant with the layered structure or cutting through the strata. Occasionally, small cross-beddings are present (Figure 26.b). The limestone is composed mainly of calcite and quartz in varying proportions in each layer, with sericite, chlorite, phlogopite and opaque minerals as secondary components (Figure 26.c). The marl levels have the same mineralogical constitution, but mica minerals are the primary fraction, with chlorite accounting for the greenish hue. Due to the difference in the contents of mica, the limestone packages show no to poorly marked spaced cleavage, while the marl films are strongly foliated.

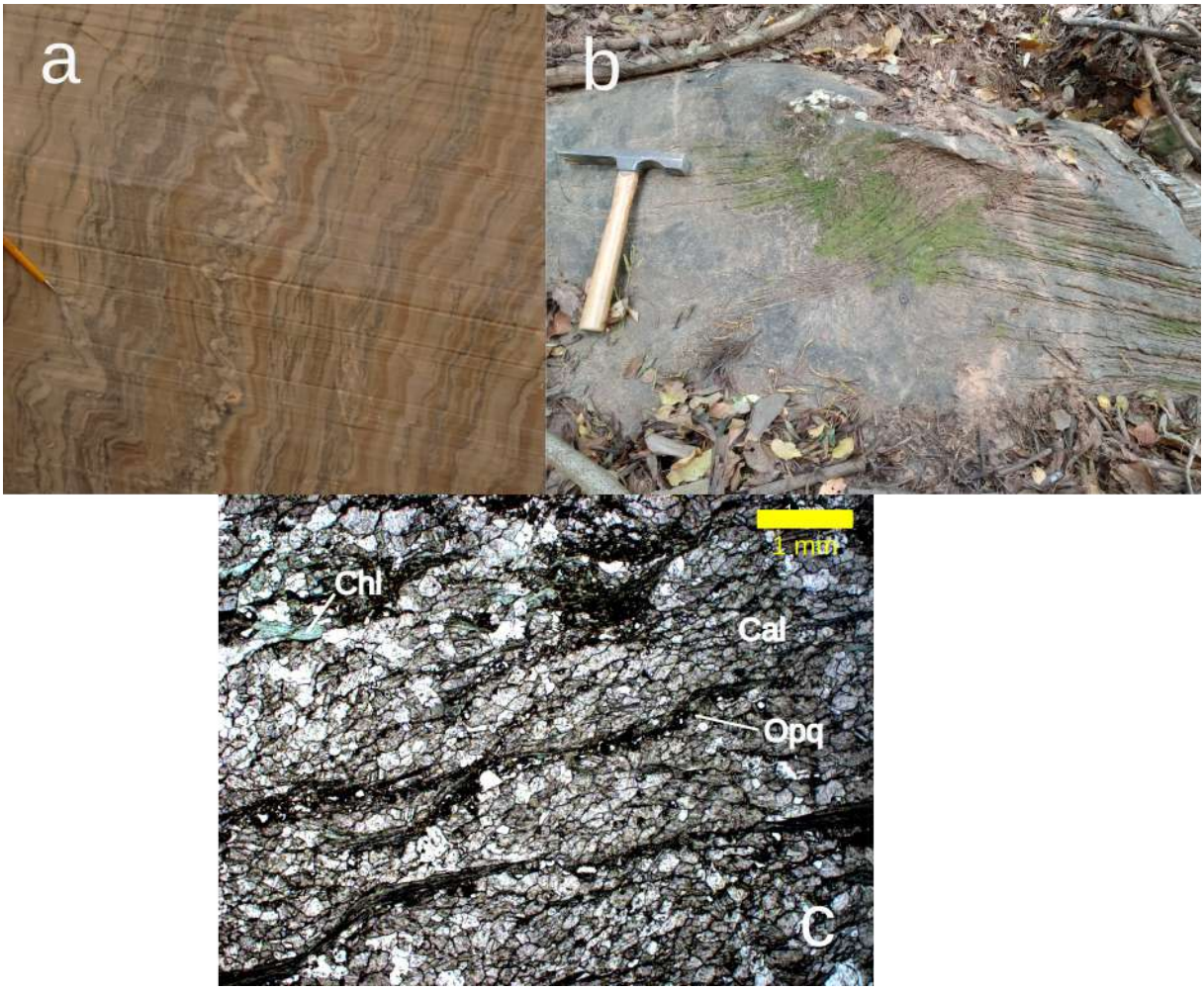

Figure 26. Petrographic aspects of the Sete Lagoas Formation in the region of Serra do Cipó: a) A sequence of folded limestone (beige, gray, white and brown) and marl layers; b) Cross-bedding in limestone; c) Photomicrography of a foliated calcitic limestone with domainial slate cleavage formed by chlorite and opaque minerals.

4.4.2.3. Bambuí Group – Serra de Santa Helena Formation

The youngest lithological unit in the region of Serra do Cipó is the Serra de Santa Helena Formation, a foreland sequence at least 470 m thick (limited by the topography). It occupies the entire

western portion of the study area, as well as central hilltops, where topography is smooth and altitudes range between 900 and 1000 m. This unit is often exposed profoundly weathered, in which case it has a flaky aspect with orange, beige (Figure 27.a), red and purple colors. Fresh outcrops exhibit gray siltstone or metasiltstone, or gray-white rhythmite or metarhythmite, where gray bands are composed by silt and white mica and the white bands contain quartzous silt (Figure 27.b). Slate cleavage is pervasive and mostly parallel or sub-parallel to the bedding, but also occurs at oblique positions when developed along axial surfaces of folds. The Serra de Santa Helena Formation is only found atop the Sete Lagoas Formation, mostly separated by a detachment surface, except for its easternmost limits, where it forms the footwall of a thrust system, hauled under the carbonatic rocks.

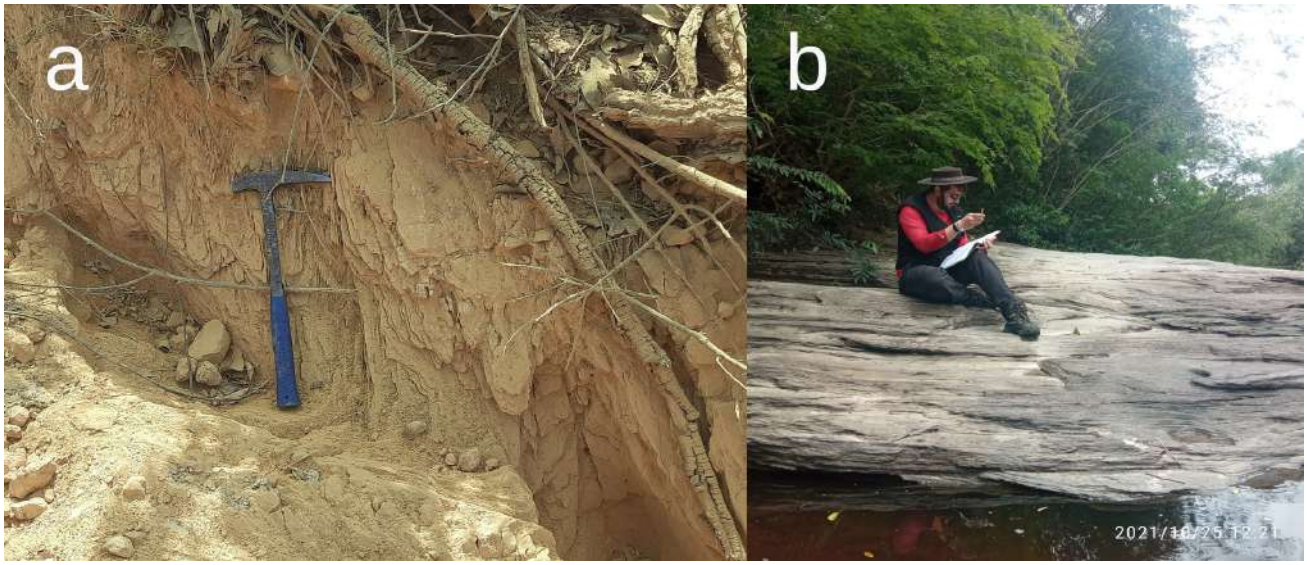

Figure 27. The Serra de Santa Helena in the region of Serra do Cipó: a) Weathered outcrop with flaky aspect, representative of the most common form of occurrence of the unit; b) Fresh outcrop preserving the rhythmic structure and evidencing the slate cleavage.

The Serra de Santa Helena Formation also hosts at least two different generations of quartz veins. The older veins are sub-parallel to the bedding surfaces and were involved in the folding, faulting and shearing of that affected the unit (Figure 28.a). The younger veins are sub-vertical and cut through the whole set of rocks and structures at outcrop scale (Figure 28.b).

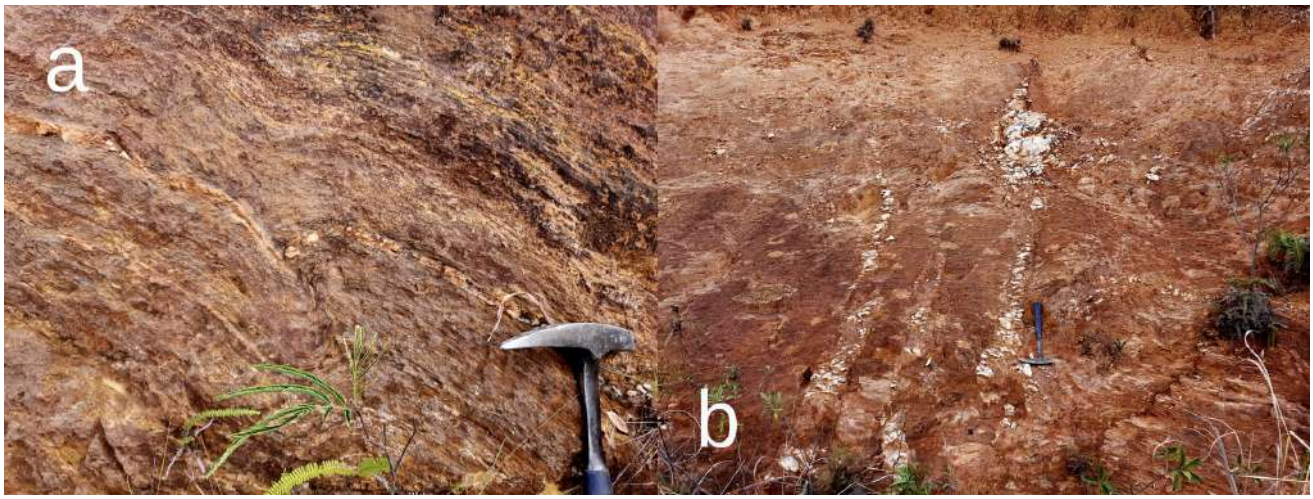

Figure 28. Veins in the Serra de Santa Helena Formation: a) Quartz vein sub-parallel to the sedimentary layers involved in rupturing and fault-related folding alongside the rest of the package; b) Sub-vertical quartz vein cutting through the entire sedimentary sequence and previous structures.

4.5. Structural Geology

The structural framework of the region of Serra do Cipó follows the tectonic division derived from the advance of the Araçuaí fold-and-thrust belt over the São Francisco Craton. Tectonic foliation and stretch lineations have relatively constant attitudes throughout the area, but, due to the regional tectonic compartmentalization and rheological properties, the collection of structures in each domain is different from the other. Moreover, there are differences in the way such structures are distributed between the various stratigraphic units of the study area.

Naturally, the major set of thrusts and associated folds that establish the fold-and-thrust belt dominates the regional structural framework (Figure 29). At mesoscopic scale, thrusts and shear bands are the most prominent structures of the Fold-and-Thrust Compartment, with subordinate tight folds. Normal faults are also present, with rarer occurrences. In the Foreland Compartment, outcrops often exhibit tight, isoclinal and recumbent folds that extend down to microscopic level, with subordinate shear bands. Tectonic foliation is more pervasive in the Fold-and-Thrust compartment, acquiring the aspect of schistosity, whereas components are often not visible in the Foreland Compartment, where these structures are mostly present as slate cleavage. Crenulation cleavage is also occasionally present in outcrops of the foreland. Stretch lineations and kinematic indicators invariably indicate an east-to-west vergence with little to no strike-slip component.

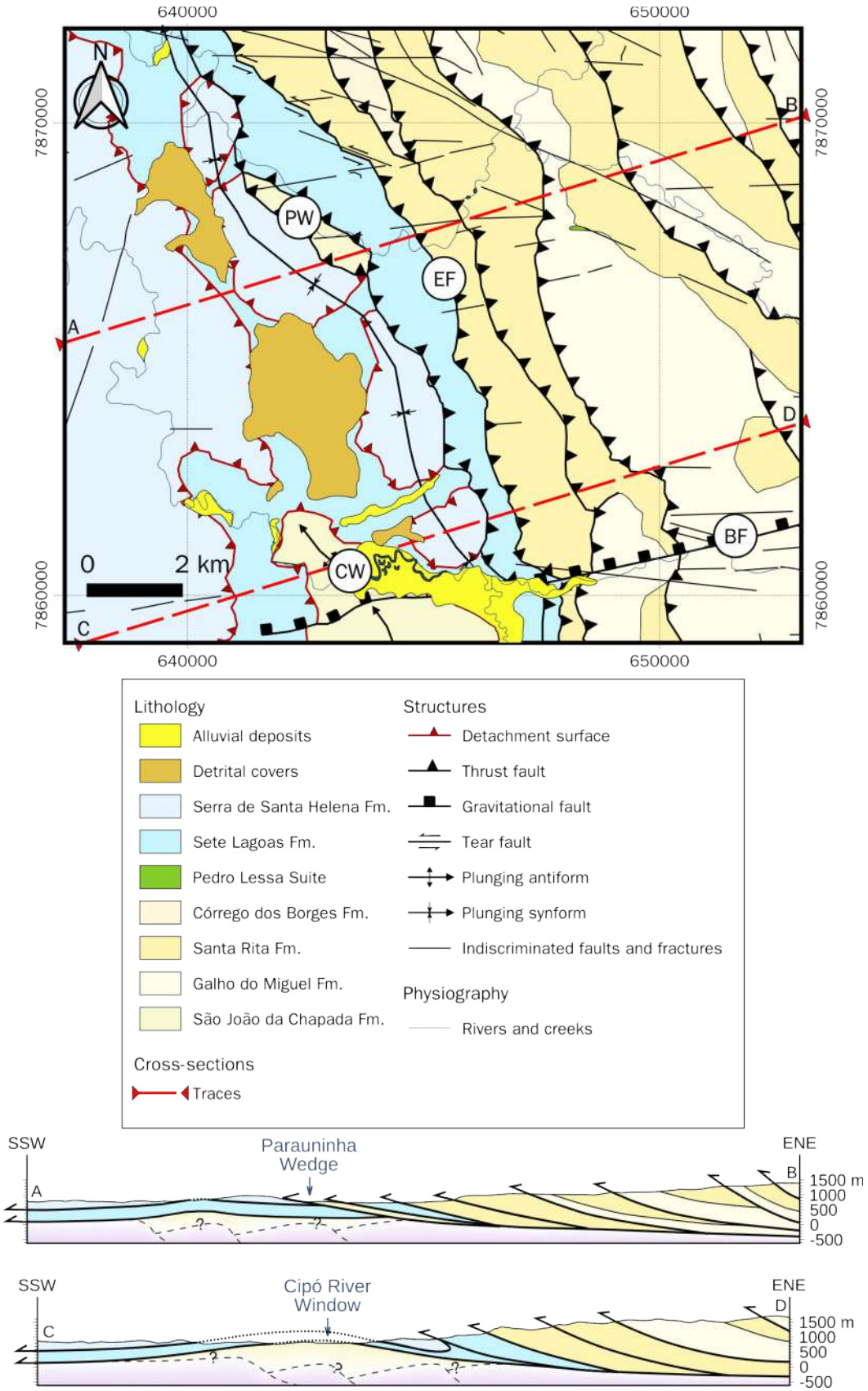

Figure 29. Geologic map and cross-sections from the study area, with locations of points of interest: EF – Espinhaço Front; PW – Parauninha Wedge; CW – Cipó River Window; BF – Bocaina Fault (vertical scale equal to horizontal scale).

We characterize structures in this section starting with beddings, tectonic foliations, lineations and kinematic indicators, then moving on to faults, folds and shear zones.

4.5.1. Beddings and sedimentary structures

Bedding surfaces are marked by granulometric variations, often accompanied by changes in the mineral contents and color of the rock. Sedimentary structures such as ripple marks and cross-beddings also serve as indicators of bedding limits, as well as geopetal indicators.

Beddings are predominantly subhorizontal, with low dips towards east, with a mean attitude of N18ºW/19ºNE (Figure 30.a). In the Foreland Domain, dips overall are gentler and towards east (mean N18ºW/7NE; Figure 30.b), with instances of west-dipping surfaces, but west-verging folds are more common in this compartment, also causing beds to dip steeply towards west or, when overturned, towards east. Bedding attitudes are more consistent in the Fold-and-Thrust Domain and proximal foreland areas, with angles ranging between 20º and 40º along N25-30ºW strikes (mean N18ºW/29ºSE; Figure 30.c). Sub-horizontal and west-dipping surfaces occur in mesoscopic folds, on short limbs of vergent folds. In rare occasions, short limbs may be overturned, showing high dips to the east.

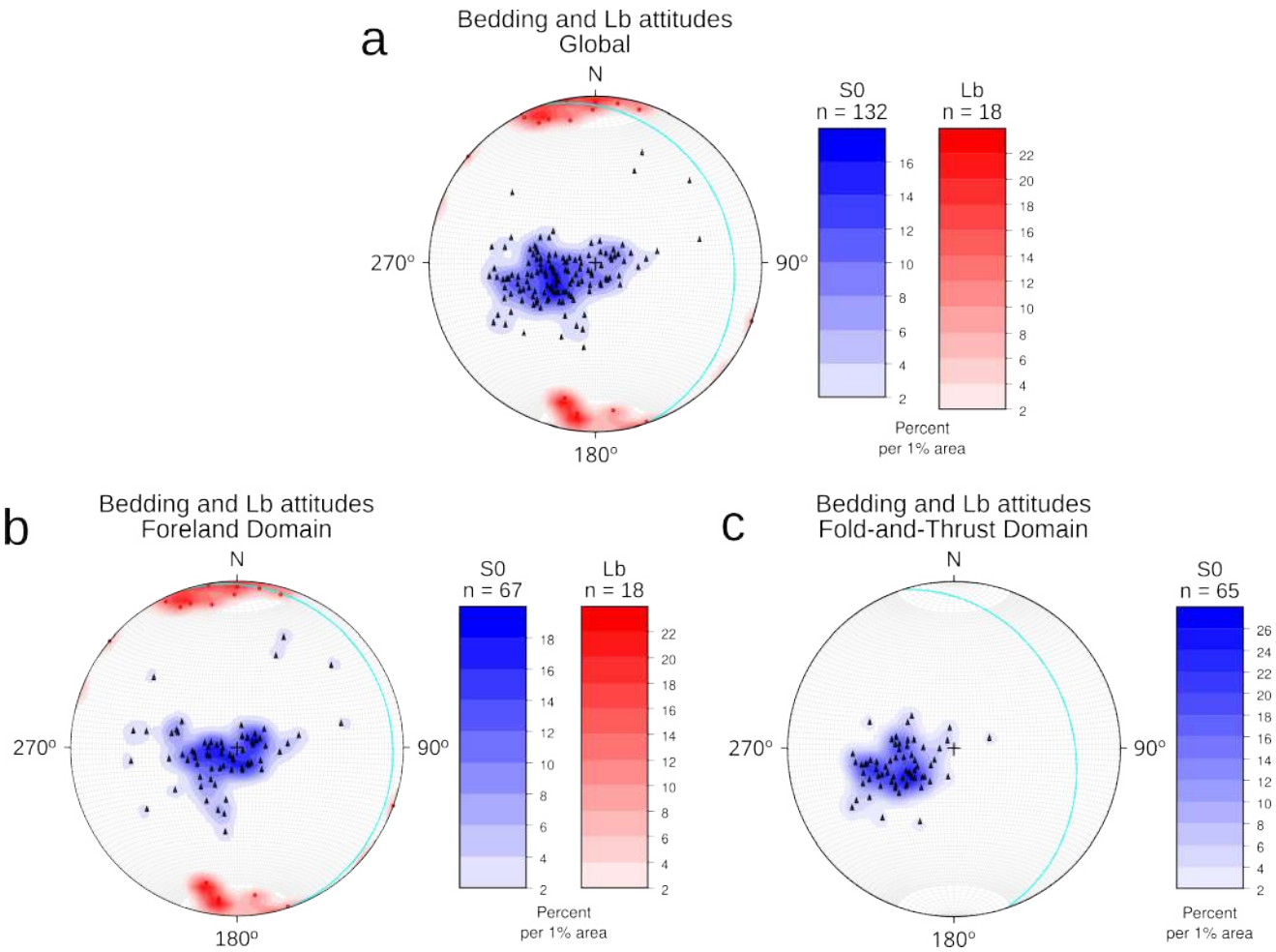

Figure 30. Stereographic projection of bedding and L_b attitudes from the region of Serra do Cipó: a) Global plot; b) Plot of attitudes from the Foreland Domain; c) Plot of attitudes from the Fold-and-Thrust Domain. Light blue great circles indicate the mean bedding attitude.

4.5.2. Tectonic foliations and lineations and associated structures

All local lithological units exhibit tectonic foliation marked by oriented mica or prismatic minerals. In the Fold-and-Thrust Domain, mica is often visible marking these surfaces at outcrop scale. In the Foreland Domain, the most evident tectonic foliation surfaces in the Serra de Santa Helena is a ubiquitous slate cleavage sub-parallel to the bedding. Occasionally, crenulation cleavage is also present in this unit. In the Sete Lagoas Formation, marl levels show a schistose aspect, while the limestone is poorly if not foliated.

Foliation attitudes consistently show moderate dip angles towards the east quadrant (mean N17ºW/25ºNE). Trends follow mostly N-S to N25ºW directions, but deflections of up to N45ºW were observed (Figure 31.a), mostly in the center-north portion of the area. On average, dips are gentler in the Foreland Domain than in the Fold-and-Thrust Domain (N22ºW/17ºNE *vs*. N16ºW/34ºNE; Figure 31.b, c).

Two superimposed sets of foliations are present, which is more discernible in the Fold-and-Thrust compartment, where structures of the first set are parallel to sub-parallel to the bedding, and structures of the second set form dip slightly more steeply or occur as S-C structures. In the Foreland area, the younger planes are not well marked, except in cases where crenulation cleavage or re-foldings are present. However, in terms of attitudes, the foliations of both sets are very close – at times, sub-parallel –, probably due to successive coaxial stages of folding or progressive deformation, and we group attitudes alluding to both sets of structures as S_n. The difference becomes evident in few outcrops where the older structures are affected by folding with the younger structures at the position of the axial surface. Near faults and shear bands, foliation becomes mylonitic, denoting west-verging reverse kinematic.

There are two main sets of linear structures in the study area. The first is composed by stretch lineations (L_n), made up by elongated or oriented crystals (e.g. mica, quartz, tourmaline), developed on the surfaces of the main tectonic foliation (S_n). Invariably, these lineations are downdip or sub-parallel to the maximum slope of foliation (mean N85ºE/29ºNE; Figure 31.a), representing the predominance of thrusting in the deformation system. That is true for both local tectonic compartments (mean N84ºE/23ºNE for the Foreland Domain and N84ºE/29ºNE for the Fold-and-Thrust Domain; Figure 31.b, c).

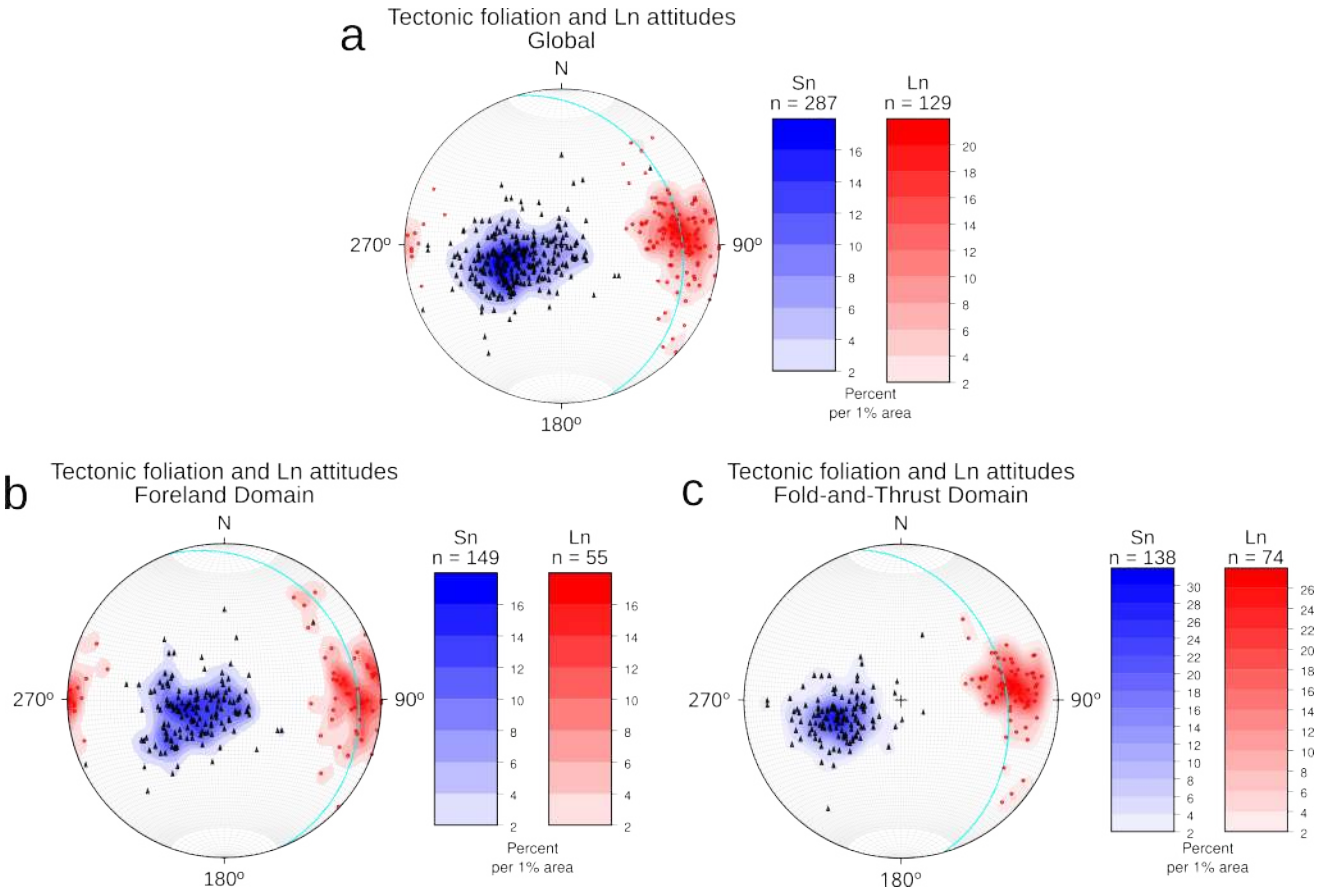

Figure 31. Stereographic projection of S_n (poles and mean plane) and L_n attitudes from the region of Serra do Cipó: a) Global plot; b) Plot of attitudes from the Foreland Domain; c) Plot of attitudes from the Fold-and-Thrust Domain. Light blue great circles indicate the mean attitudes of the tectonic foliation.

The second set of linear structures comprises bedding-clevage intersections (L_{int}) and crenulation axes. These lines are sub-horizontal with gentle NNE-N plunges (mean N9ºW/1ºSE) that are parallel to the regional fold axes and are therefore classified as b-axis lines, or L_b (Figure 30).

4.5.3. Veins

Quartz veins are common in both domains, particularly in the Santa Rita and Serra de Santa Helena formations. In the Fold-and-Thrust Domain, the presence of veins is accompanied by an increase in the size of mica and development of schistose texture, as well as growth of tourmaline and opaque minerals on the mica-rich levels of the rocks (e.g. Figure 21.f). Thicknesses are usually millimetric or centimetric, with rare instances of thicker (decimetric) veins.

With exception of the sub-vertical veins of the Serra de Santa Helena Formation (Figure 28.b), quartz veins are concordant with the first set of tectonic foliation, and are affected by the regional deformation and development of the second set of foliation surfaces. Folds and boudinage occur in

veins in both compartments, as well as asymmetries influenced by shear zones (Figure 28.a; Figure 32).

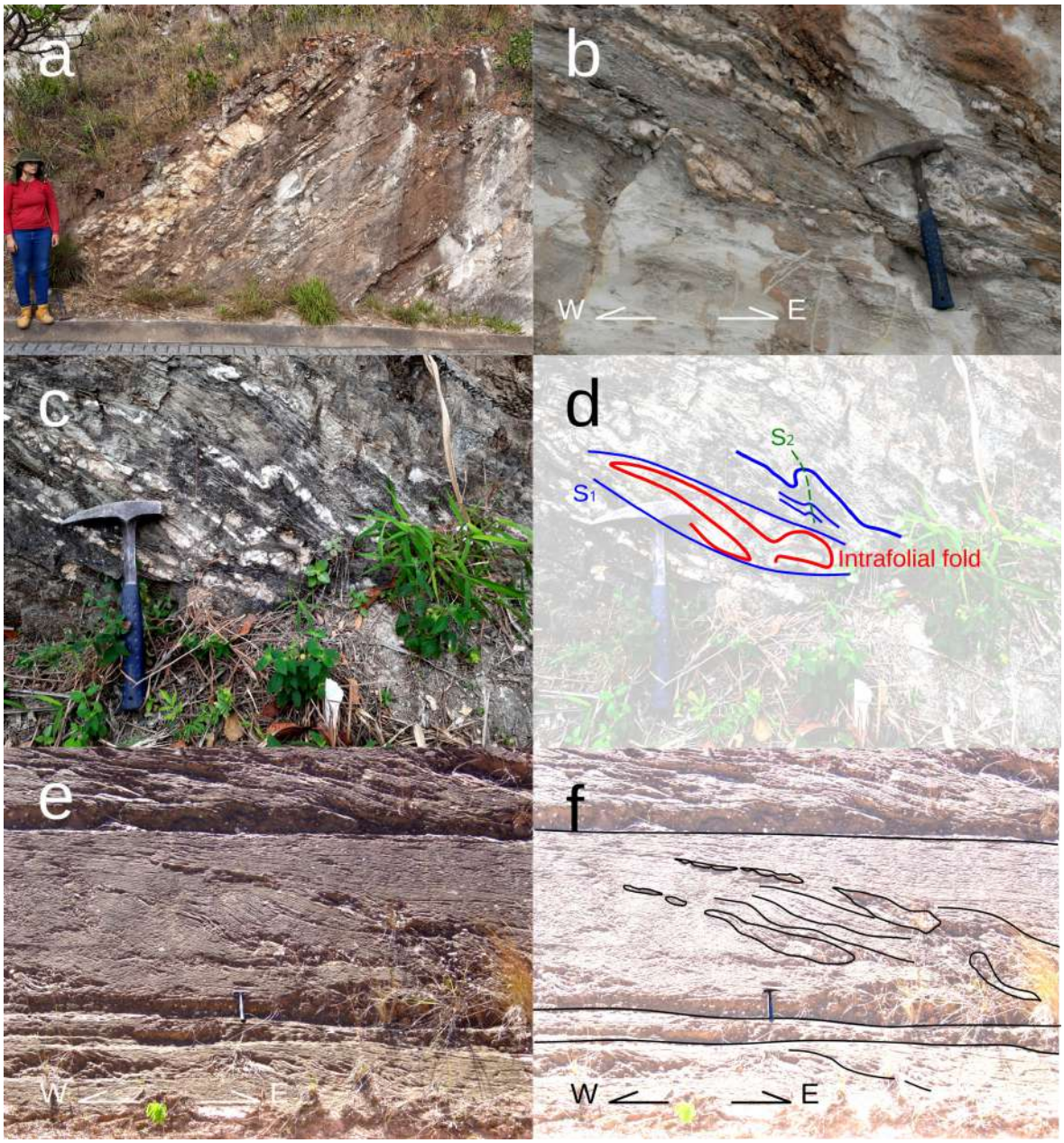

Figure 32. Occurrences of quartz veins in the region of Serra do Cipó: a) Concordant with the first set of tectonic foliation; b) Asymmetric (σ-type) boudin in outrcrop of the Santa Rita Formation; c, d) Folded quartz vein in the Santa Rita Formation and respective sketch; e) Sheared quartz vein in the Serra de Santa Helena Formation.

Calcite veins are exclusive to the Sete Lagoas Formation, and occur in two positions: concordant with the beddings, in which case the veins at times are affected by structures such as folds and shear zones together with the primary structures (Figure 33.a) or concordant with structures such as faults, when veins cut through the sedimentary layers (Figure 33.b).

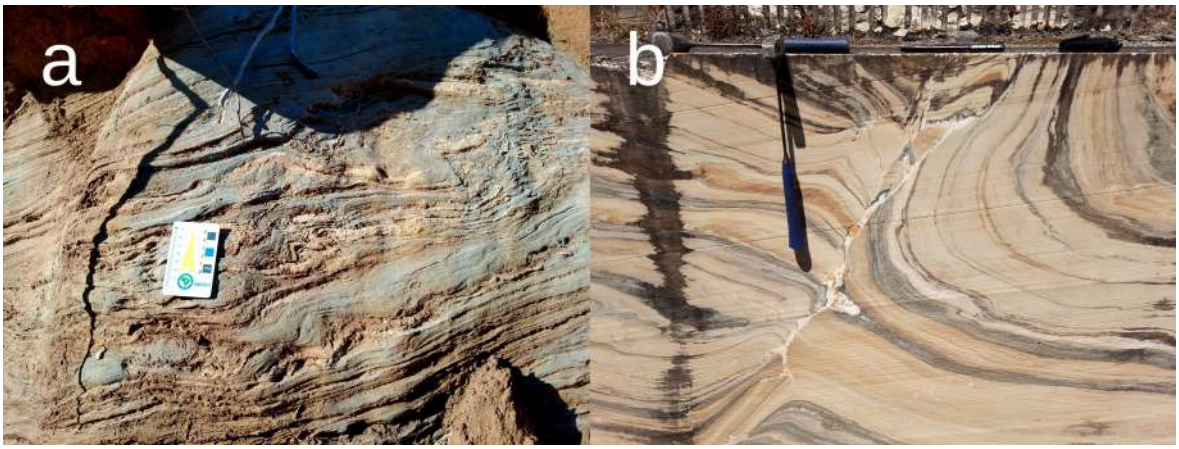

Figure 33. Calcite veins in the Sete Lagoas Formation: a) Vein parallel to the sedimentary layers, affected by asymmetric fold with the rest of the package; b) Vein parallel to reverse fault cutting through the sedimentary layers.

4.5.4. Reverse faults and shear zones

4.5.4.1. Reverse structures

The most important structural features in the region of Serra do Cipó is a major system of west-verging NNE-SSW-trending reverse faults, which extend beyond the southern and northern boundaries of the study area. These are the structures that characteristically define the craton-orogen transition with the Espinhaço-Bambuí (in this case, between the Santa Rita and Sete Lagoas formations) inversion, and are connected with the remainder of the Southern Espinhaço Espinhaço thrust system. Aside from the craton-orogen border, the thrusts mark tectonic inversions within the Fold-and-Thrust Domain, and reach further west of the boundary and into the Foreland Domain, causing reverse faulting of the Sete Lagoas Formation, at times propelling this unit over the São João da Chapada and Serra de Santa Helena formations, and generating the tectonic sliver that wedges the São João da Chapada into the Bambuí Group (Figure 29).

The system of thrusts is structured in an imbricated fan stemming out of a regional basal detachment (Figure 29). We estimate that the dips of the thrust fronts increase from west to east from 8º to 35º towards the east quadrant. These attitudes are also concordant with the average dips of the tectonic foliation.

Thrusts and reverse shear bands are also common at mesoscopic and microscopic scale. Displacements along theses structures are centimetric at most. The texture of rocks turns progressively more mylonitic nearer these structures, with development of a series of kinematic indicators, such as S-C foliation, asymmetric stretched veins, boudins, tension gashes and recrystallization tails (Figure 32.b, e, f; Figure 33; Figure 34).

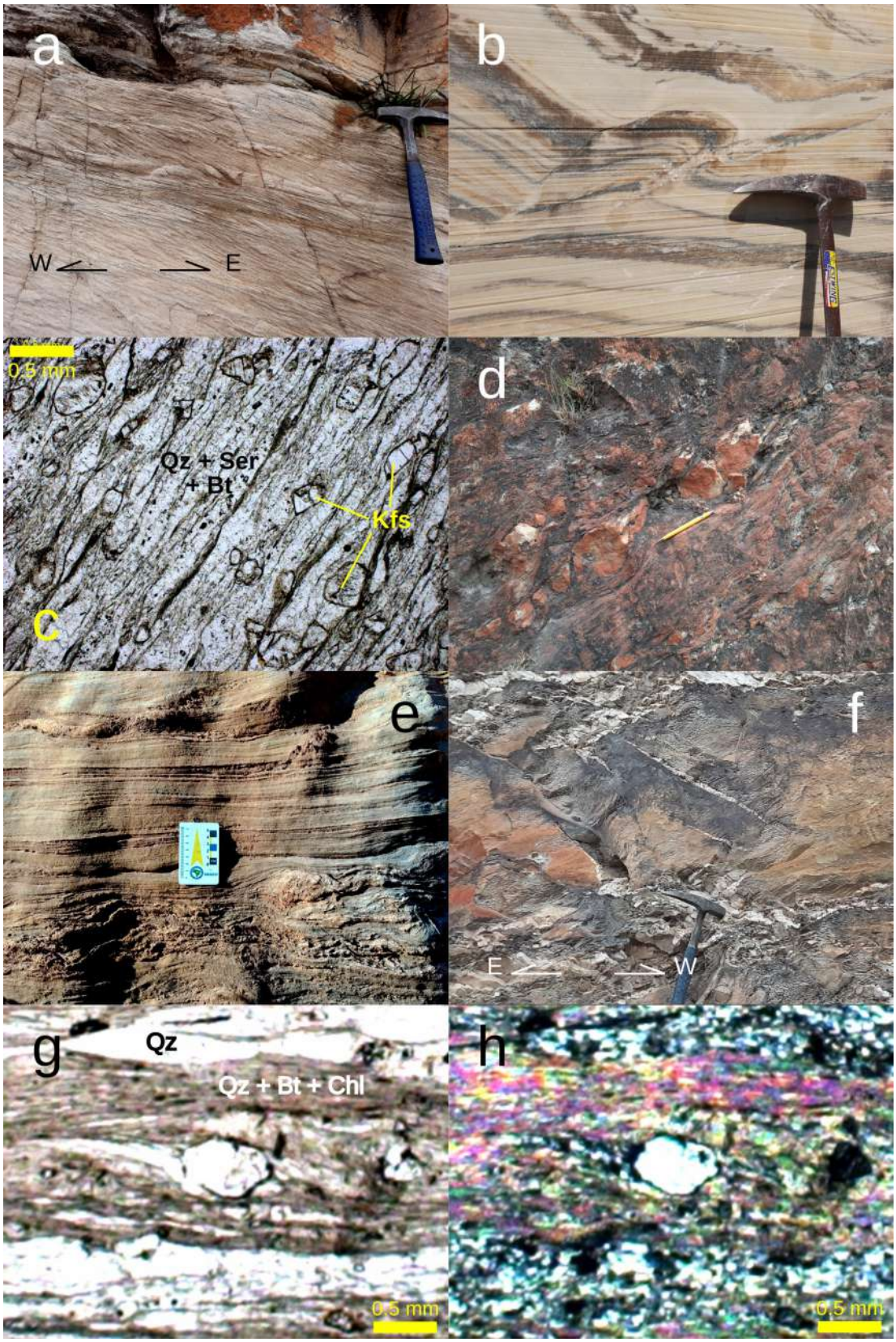

Figure 34. Mesoscopic and microscopic reverse structures and texture from the region of Serra do Cipó: a) Reverse shear band in the Santa Rita Formation; b) Fault system in the Sete Lagoas Formation; c) Mylonitic quartzite of the Santa Rita Formation; d) Asymmetric (σ-type) boudinage in quartz vein of the Santa Rita Formation; e) Strecthed (σ-type) calcite vein in the Sete Lagoas Formation; f) Tension gashes associated with shear zone in the Santa Rita Formation; g, h) Recrystallization tail (σ-type) in quartz grain in sample from the Santa Rita Formation.

4.5.4.2. The Bambuí Group detachments

Most of the basal contacts of the units of the Bambuí Group in the region of Serra do Cipó are marked by flat detachments. It is our understanding that the detachment between the São João da Chapada (Espinhaço Supergroup) and Sete Lagoas (Bambuí Group) formations corresponds also to the regional detachment from which the thrust faults of the regional thrust system of the Espinhaço Front splay out. The Serra de Santa Helena Formation, in turn, is also separated from the Sete Lagoas Formation by a flat basal detachment.

4.5.5. Folds

In general, fault-related folds are the most common in the study area, associated with the reverse faults and shear zones (Figure 34.b; Figure 35).

Figure 35. Reverse fault and associated fold in limestone of the Sete Lagoas Formation.

In the Fold-and-Thrust Domain, mesoscopic folds are common in the Santa Rita Formation, whose organization in quartz-rich and mica-rich layers, often with presence of quartz veins results in stronger competence contrasts. The homogeneity of the rocks of the Galho do Miguel Formation, in turn, does not offer favorable conditions to the occurrence of small-scale folding.

Mesoscopic folds become more frequent nearer the inversion Santa Rita-Sete Lagoas inversion. Centimetric to decimetric, tight to isoclinal folds occur, affecting beddings, foliation surfaces and veins. These structures are highly asymmetric, with shorter and longer limbs indicating vergence to the west (Figure 32.c, d). Thickened hinge zones, ruptured limbs, intrafolial folds and boudinage of

the limbs are usually associated to these structures. There is also observable development of a second set of foliation surfaces, which dip with moderate angles towards east, at higher angles than or sub-parallel to the previous foliation. Other common fold structures in the Fold-and-Thrust Compartment are very gentle undulations of beddings, foliation and quartz veins. These folds do not cause perceptible variations in bedding or vein thickness.

In the Foreland Domain, gentle, regional-scale anticline-syncline system affecting the main foliation (S_n) encompasses all the lithological units of the compartment (the São João da Chapada, Santa Rita, Sete Lagoas and Serra de Santa Helena formations), being truncated to the east by the Espinhaço Front (Figure 29). The strike of the axial surface of this structure is parallel to the trend of the regional thrust system (NNW-SSE), and the fold axis is sub-horizontal with a gentle plunge towards NNW. Following an original proposal by Oliveira (1994), we pose that the folds of the syncline were exacerbated to the east, along the limit with the Espinhaço Thrust System, due to the rheological properties and contrasts of the rocks involved in the process.

Both formations of the Bambuí Group exhibit folds that range from microscopic to decametric dimensions. In the Sete Lagoas Formation, folds range from microscopic to decametric dimensions (Figure 36.a, b). Closer to the Espinhaço Front, the position of axial surfaces varies greatly, from recumbent to moderately inclined (Figure 36.b, c, d). Folds in this context are usually closed to tight, with parasitic folds associated. Instances of isoclinal and sheath folds, as well as fold interference patterns are also present (Figure 36.c, d, e, f).

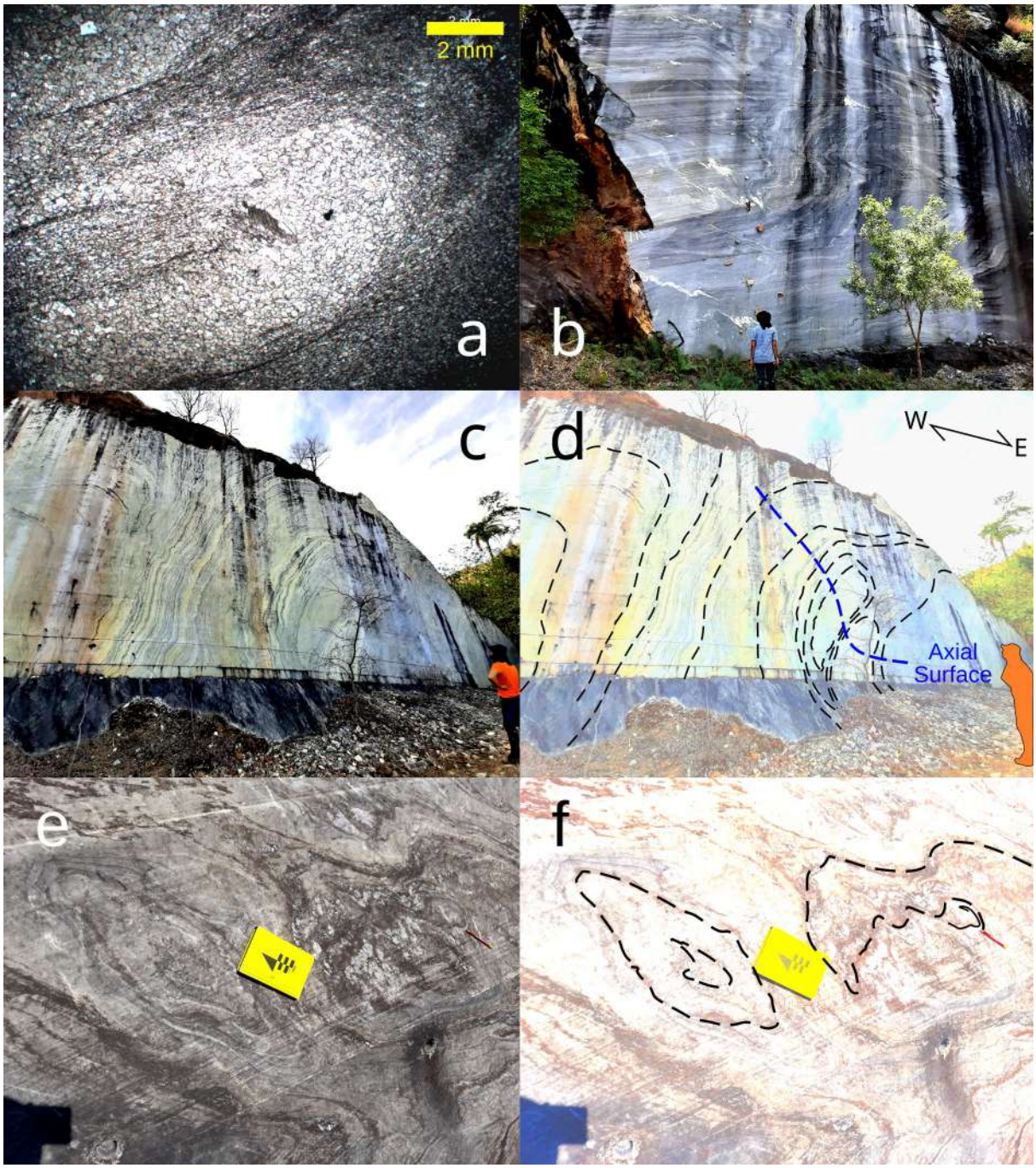

Figure 36. Folds of the Sete Lagoas Formation: a) Photomicrography of isoclinal fold; b) Closed and isoclinal recumbent folds; c, d) Inclined closed, tight and sheath folds with respective sketch; e, f) Boomerang and loop interference patterns and respective sketch.

As distance to the Espinhaço Front increases, recumbent tight and isoclinal folds with thickened hinge zones become prevalent in the Sete Lagoas Formation. Beddings in the limbs and axial surfaces are sub-horizontal, gently dipping towards east or west, as plunge fold axes. This is particularly visible at point HJ 162 (UTM 23K 641914 E/7862034 N; Figure 37.a, b).

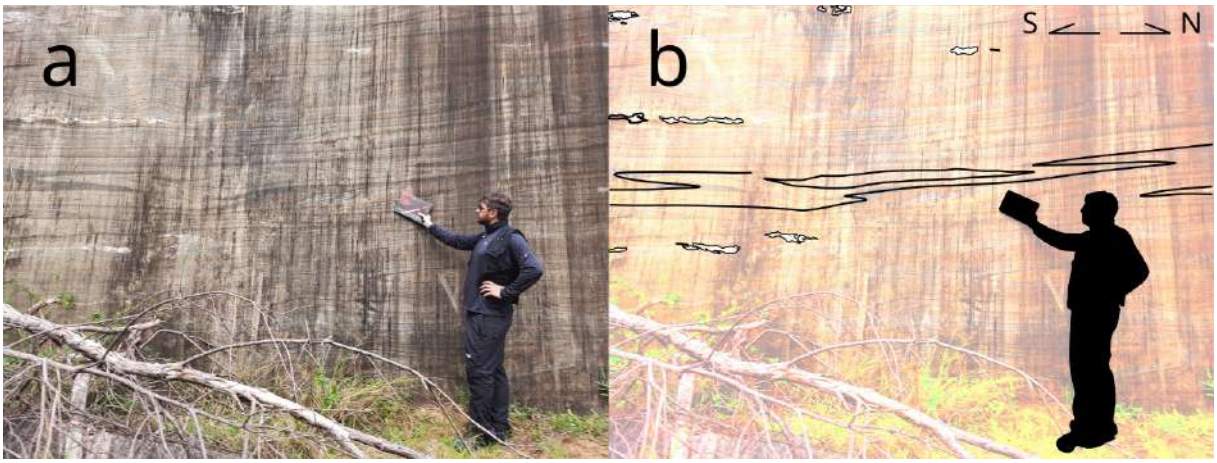

Figure 37. Recumbent folds in limestone of the Sete Lagoas Formation (a) and respective sketch (b).

Regardless of the geometry of the structures, the attitudes of axial surfaces follow the regional trend of NNW-SSE strikes and dips towards east with low to moderate angles. Kinematic indicators and fold asymmetries are also coherent with the global trend of movement towards west. Fold axes are sub-horizontal, plunging towards NNW or N. Subordinate reverse faults shear zones are associated with these structures (Figure 34.b), with centimetric to decimetric reverse downdip displacements, as well as fractures filled with calcite veins.

Folds in the Serra de Santa Helena Formation show the same strike and vergence towards west as the regional patterns. Most prominently, expositions contain metric to decametric, west-verging similar folds with sub-horizontal axes (Figure 38). Bedding-parallel slate cleavage is involved in the folding of the layers, and at times cut by a posterior set of cleavage surfaces at the position of the axial surfaces. Few outcrops also exhibit crenulation, in which case crenulation surfaces dip steeply towards east and axes are sub-horizontal, following N-S trends. All these structures are commonly interrupted and dragged by reverse shear zones that dip gently (< 20º) to east and reach decimetric thicknesses (Figure 32.e, f). This configuration indicates the occurrence of duplex sequences, which have been described in previous works (Magalhães, 1988; Oliveira, 1994). There are minor occurrences of centimetric kink bends and east-dipping reverse faults with discrete displacement.

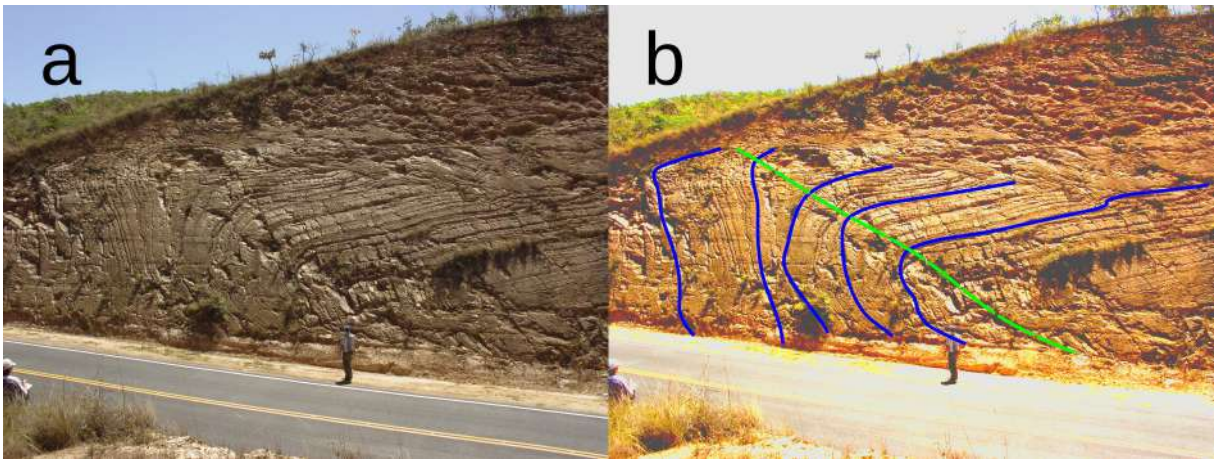

Figure 38. Asymmetric, west-verging fold in the Serra de Santa Helena Formation (a) and respective sketch (b).

4.5.6. Minor normal faults

Normal faults are rare. Few occurrences of structures of this nature are present in the Santa Rita Formation. When present, these structures cut through the entire set of reverse structures (Figure 39).

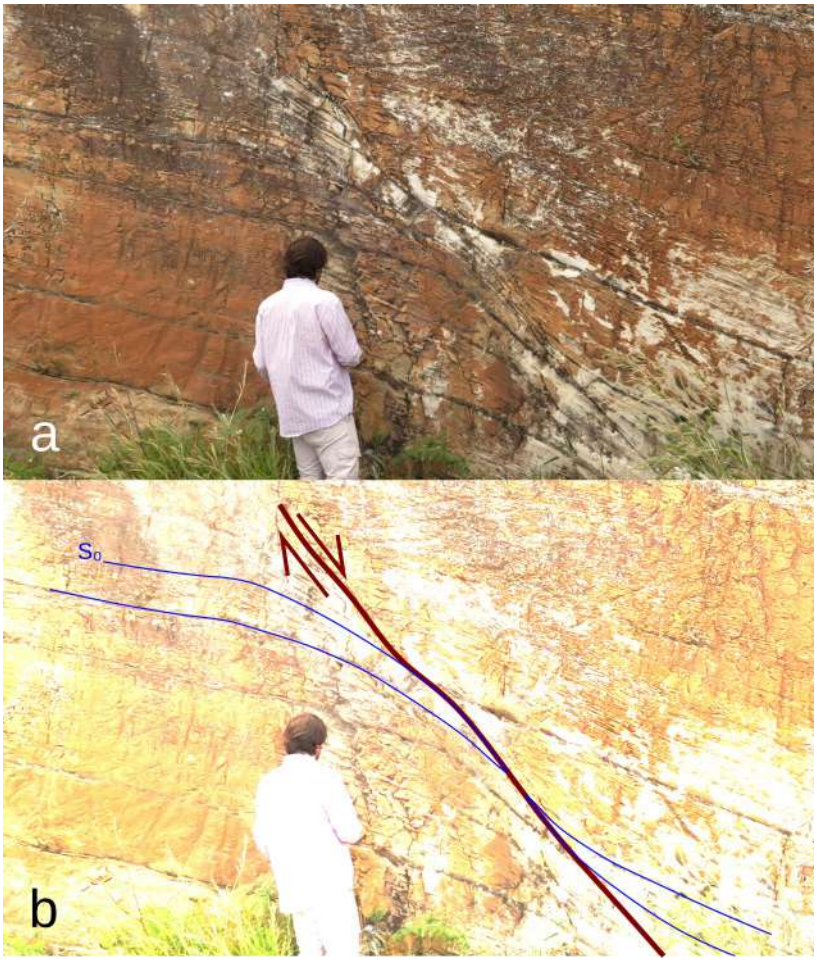

Figure 39. Photo (a) and sketch (b) of normal fault cutting through beds and tectonic foliation in the Santa Rita Formation.

4.5.7. The Bocaina Fault

An E-W-trending, sub-vertical fault cuts through the entire regional set of structures at the southern end of the study area, forming a prominent linear structure known as Cipó Fault (Schöll and Souza, 1970 apud Oliveira et al., 1997) or Bocaina Lineament (Oliveira, 1994). We propose here the adoption of the term Bocaina Fault, corroborating displacement along the surface and avoiding the repetitive coinage of the “Cipó” lexicon, already used for the local river system, hill range and urban district.

Three different models have been put forward for this structure in previous works. Schöll and Souza (1970 apud Oliveira, 1997) described it as a tear fault connecting two segments of the Espinhaço Front, formed at an *AC* position, considering the principal axes of the regional strain system. Oliveira (1994) suggested that the fault was originally a transfer fault that preceded the Espinhaço-Bambuí inversion, and later acted as a tear fault during the Brasiliano Cycle, with minor sinistral strike-slip displacement. Finally, Oliveira et al. (1997) interpreted the apparent lateral movement of the structure as an effect of erosion, and raised the hypothesis of gravitational dislocation along the surface, which was maintained by Silva et al. (2007), who proposed abatement of the block to the south of the fault.

Here, we maintain the interpretation of the Bocaina Fault as a normal. However, contrary to Silva et al. (2007), we propose abatement of the northern block, based on reference provided by the contacts between the São João da Chapada and Sete Lagoas formations, which are disposed in a gentle anticline in the Foreland Domain. Through a basic geometric reconstruction of the anticline along the fault surface using chevron and concentric styles for the fold flanks to estimate the location of pre-faulting contiguous points (Figure 40), we calculate the displacement around approximately 125 m.

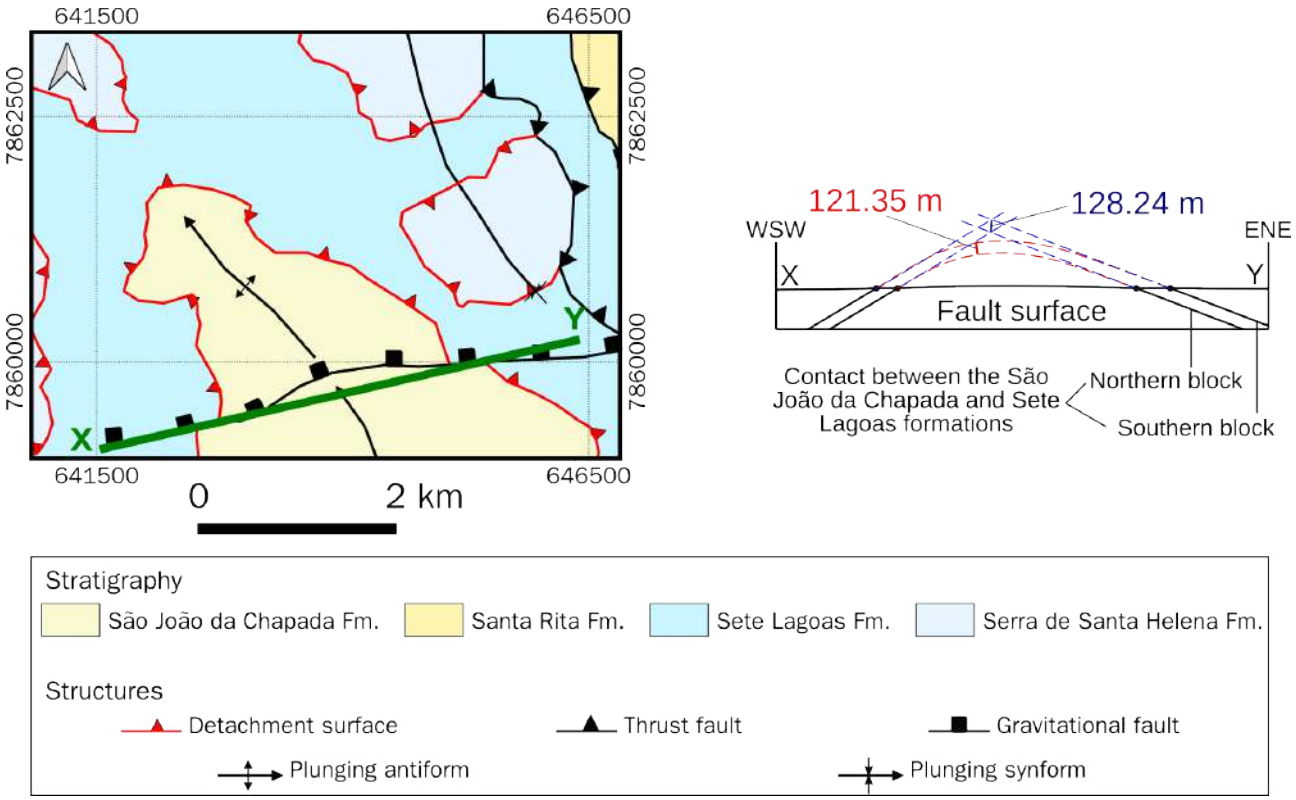

Figure 40. The Bocaina Fault: a) Simplified map excerpt. Neogene covers and physiography were excluded to show the continuity of the structure; b) Basic reconstruction and measure of displacement based on estimated contiguous points.

5. THE ESPINHAÇO SUPERGROUP IN THE REGION OF SERRA DO CIPÓ – DETRITAL ZIRCON U-PB AGES

Stratigraphic concerns arose over the course of this work. For the Bambuí Group, our data were coherent with descriptions and classifications from previous studies. However, for the quartzitic and metaconglomeratic rocks, the extant models would not fit the actual lithotypes found during the campaigns. In order to clarify this matter, we carried out U-Pb dating of detrital zircons, and compared the results with those from other works using the same methodology not only for units previously suggested as possible classification for rocks of the study area, that is, the Espinhaço Supergroup, the Macaúbas Group and the Jequitaí Formation (Schöll, 1972; Oliveira, 1994; Oliveira et al., 1997; Silva et al., 2007; Ribeiro, 2010; Bakir et al., 2016, p. 201; Chierici et al., 2021), but also for the Meloso Formation (Rolim et al., 2016), a unit defined in nearby regions, and the Barão do Guaicuí Formation of the Costa Sena Group (Fogaça et al., 1984), one of its correlatives. This enabled an evaluation of the affinity of the age-spectra of our samples with those from the considered units.

5.1. U-Pb dating and the LA-ICP-MS method

Zircon ($ZrSiO_4$) occurs in appreciable amount in many different kinds of rocks, and contains trace amounts of uranium and thorium, but little to no lead. Its isotopic blocking temperature is also high, in the order of 800 ºC. This makes this mineral an excellent resource for radiometric dating based on the decay of uranium and thorium to lead. A U-Pb age is a composition of analyses of three decay systems: ^{238}U-^{206}Pb, ^{235}U-^{207}Pb and ^{232}Th-^{208}Pb, which contributes to its precision (Metzger and Krogstad, 1997; Bowring and Schmitz, 2003; Dickin, 2005; Pickhardt et al., 2005; Schoene, 2014).

For igneous rocks, zircons register the age of crystallization of magma and successive crystallization stages, for the case of zoned crystals, but it is the application of radiometric dating to detrital zircons that is interesting for the purpose of this thesis.

Another important characteristic of zircon is its high mechanical and chemical resistance to alteration, weathering and erosion. This means that this mineral may resist several erosion-transport-deposition cycles. The collection of detrital zircon U-Pb ages in sedimentary and metasedimentary rocks are important tools for the determination of the maximum sedimentation age and for the evaluation of sedimentary provenance and the contribution share of each source-areas (Feng et al., 1993; Stern and Berman, 2001; Bowring and Schmitz, 2003; Dickin, 2005; Allègre, 2008; Kröner et al., 2014; Schoene, 2014).

Among the several methods for dating zircons, we used the laser ablation – inductively coupled plasma – mass spectrometry (LA-ICP-MS). In this method, under high vacuum conditions, a sample

is converted to the plasma state and transported through an electromagnetic field that scatters the various ions according to their mass. These ions hit a mass detector that then determines the composition of the sample. For U-Pb dating, the age (**t**) of the sample is obtained based its contents of the radioactive (^{238}U, ^{235}U and ^{232}Th) and radiogenic (^{206}Pb, ^{207}Pb and ^{208}Pb) isotopes, all normalized by its content of the stable isotope ^{204}Pb (or common lead), through the equations

$$\left(\frac{^{206}Pb}{^{204}Pb}\right)=\left(\frac{^{206}Pb}{^{204}Pb}\right)_0+\left(\frac{^{238}U}{^{204}Pb}\right)\left(e^{(\lambda_{238}t)}-1\right), \quad \textbf{Equation 2}$$

$$\left(\frac{^{207}Pb}{^{204}Pb}\right)=\left(\frac{^{207}Pb}{^{204}Pb}\right)_0+\left(\frac{^{235}U}{^{204}Pb}\right)\left(e^{(\lambda_{235}t)}-1\right), \quad \textbf{Equation 3}$$

and

$$\left(\frac{^{208}Pb}{^{204}Pb}\right)=\left(\frac{^{208}Pb}{^{204}Pb}\right)_0+\left(\frac{^{232}Th}{^{204}Pb}\right)\left(e^{(\lambda_{232}t)}-1\right), \quad \textbf{Equation 4}$$

where λ_{238}, λ_{235} and λ_{232} are the decay constants of Pb_{238}, U_{235} and Th_{232}, respectively, and the terms with the subscript index 0 refer to the ratio of the radiogenic lead isotopes over common lead. In zircons, such values are usually negligible (Feng et al., 1993; Fryer et al., 1993; Pickhardt et al., 2005; Schoene, 2014; Schaltegger et al., 2015). Moreover, these equations can be read as linear systems in ^{206}Pb/^{204}Pb *versus* ^{238}U/^{204}Pb, ^{207}Pb/^{204}Pb *versus* ^{235}U/^{204}Pb and ^{208}Pb/^{204}Pb *versus* ^{232}Th/^{204}Pb spaces. The closing age of the system (**t**) is a factor of the slope of each equation, and may be found solving the equations for **t**. After manipulation of each equation, this is made by

$$t_{238}=\frac{1}{\lambda_{238}}\ln\left[1+\left(\frac{^{206}Pb}{^{238}U}\right)\right], \quad \textbf{Equation 5}$$

$$t_{235}=\frac{1}{\lambda_{235}}\ln\left[1+\left(\frac{^{207}Pb}{^{235}U}\right)\right], \quad \textbf{Equation 6}$$

and

$$t_{232}=\frac{1}{\lambda_{232}}\ln\left[1+\left(\frac{^{208}Pb}{^{232}Th}\right)\right]. \quad \textbf{Equation 7}$$

In this chapter, we present our analyses of U-Pb ages in detrital zircons from quartzitic rocks from the region of Serra do Cipó. We studied samples from both the Foreland and Fold-and-Thrust domains of the study area (Figure 41). The analyses were executed with the objective of re-evaluating the local stratigraphy and increase the reliability of the discussions regarding the evolution of the area.

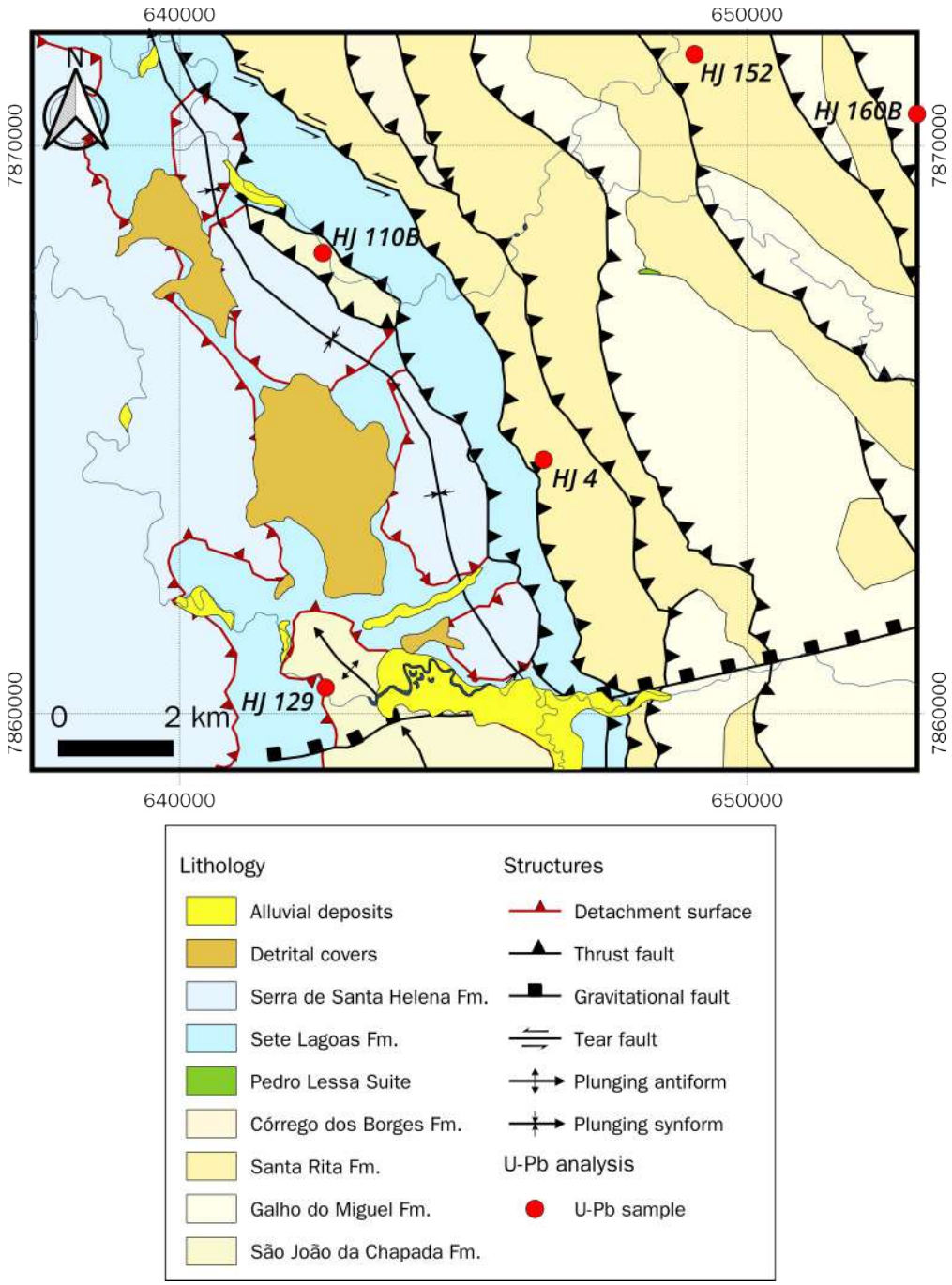

Figure 41. Location of the samples taken from the region of Serra do Cipó for detrital zircon U-Pb dating.

5.2. Practical and analytical procedures

5.2.1. Our work

Zircon grains were obtained from each sample using conventional gravimetric, density and magnetic (Frantz) separation techniques at the Geochronological Research Center of the Institute of Geoscience of the University of São Paulo (CPGeo-IGC-USP). Next, the concentrates were mounted in epoxy resin and polished. Each mount was then analyzed by cathodoluminescence (CL) coupled with a scanning electron microscope (SEM) under 15kV acceleration voltage so as to reveal

morphological and structural features inside the grains, which guided the selection of the most appropriate points for U-Pb analyses, avoiding fractures and areas that may have experienced Pb loss during the course of geologic time. Finally, dating was carried out at the CPGeo-IGC-USP in a Finnigan Neptune ICP-MS coupled with a laser excimer Analyte Excite (193nm). Each analysis consisted of 40 sequential 1-second measurements – 10 without laser activation for determination of white noise and 30 under laser ablation, which was performed with a 20μm spot diameter, 0.89J/cm2 fluence, 6Hz frequency and 6mJ intensity. The ablated material was carried by Helium at a 0.300L/min rate. The standards GJ-1 and Pleosovic were used as reference for quality control of the measurements. Results with a discordance above 10% were discarded.

Concordia curves and histograms were built using Isoplot 4.15 (Ludwig, 2008), while kernel probability distribution charts were plotted using a spreadsheet toolkit by Gehrels (2011). For that, we used the $^{207}Pb/^{206}Pb$ ages obtained for our samples.

5.2.2. Establishing a regional database of U-Pb detrital zircon ages

In addition to the results obtained in this work, we also compiled $^{207}Pb/^{206}Pb$ detrital zircon ages from several studies on rocks from the Meloso Formation (Rolim et al., 2016), the Barão do Guaicuí Formation (Santos, 2015), the Espinhaço Supergroup (Chemale Jr. et al., 2012; Santos, 2015; Santos et al., 2013, 2015; Rolim et al., 2016; Silveira, 2017; Oliveira et al., 2019), the Macaúbas Group (Martins et al., 2008; Chemale Jr. et al., 2012; Peixoto, 2013; Kuchenbecker et al., 2015; Castro et al., 2019, 2020; Souza et al., 2019; Amaral et al., 2020; Oliveira et al., 2021) and the Jequitaí Formation (Rodrigues, 2008), units that have either been suggested as possible classification options for rocks in the study area or that have been described in the vicinities. For one sample from Kuchenbecker et al. (2015) of the Chapada Acauã Formation (Macaúbas Group), $^{207}Pb/^{206}Pb$ ages were not available, and we used $^{235}U/^{206}Pb$ Ages.

We used a second spreadsheet toolkit by Gehrels (2011) to plot multiple detrital zircon U-Pb age kernel probability density (KPD) curves for comparison between the age spectra of our samples with the remaining units considered in this work.

5.2.3. Kolmogorov-Smirnov test

All the data – from our samples and compiled from other works – were submitted to the Kolmogorov-Smirnov (KS) test, a non-parametric statistical test that determines the probability that different samples come from the same original population (the null hypothesis), using a third spreadsheet toolkit by Gehrels (2011). The null hypothesis is rejected for cases where the test result is equal to or lower than 0.05, based on a 95% confidence level.

We adopted three different approaches to the compiled data for this test, comparing our samples to: i) each sample of each work; ii) the overall data for each lithological formation from each work; and iii) grouped ages of different works for each lithological formation within reasonable spatial correspondence. Results may not be representative for sample sizes under 30. For our purposes, that means less than 30 U-Pb zircon ages per sample. We only maintain such cases in our analyses for the Barão do Guaicuí Formation (23 zircon ages; Santos, 2015) and the Meloso Formation (28 and 21 zircon ages; Rolim et al., 2016) formations, because more robust age data for these units are not available.

5.2.4. Multidimensional Scaling

Multidimensional Scaling (MDS) provides a visual aid for understanding the dissimilarity between samples. MDS builds an n vs. n (where n is the total number of samples considered) dissimilarity matrix is built and turns it into an abstract two-dimensional cartesian space, where each sample is plotted as a point. In this study, MDS was performed based on the results of the KS tests, using IsoplotR (Vermeesch, 2018).

5.3. Results

Detrital zircons from five samples, HJ 4, HJ 110B, HJ 129, HJ 152 and HJ 160B (Table 3), from the Serra do Cipó area were dated via the U-Pb method. Complete results may be found in Appendix D. The zircon grains recovered from the samples are usually well rounded, indicating that the sediment matured during transport (Figure 42). The most prevalent U-Pb age sets in the samples are Orosirian-Rhyacian (2.0-2.2 Ga) or Neoarchean (2.6-2.9 Ga). Both sets have significant presence in samples HJ 4 and HJ 152, while Orosirian-Rhyacian zircons are largely predominant in samples HJ 110B, HJ 129 and HJ 160B. The youngest zircons in each sample are of Calymmian age, except for sample HJ 160B, whose youngest zircon is from the Orosirian Period (Figure 42, Table 4).

Table 3. List of samples from the study area sent for detrital zircon U-Pb dating.

Sample	Coordinates (UTM 23K)		Rock
	E	N	
HJ 4	646417	7864461	Quartzite
HJ 110B	642523	7868109	Meta-paraconglomerate
HJ 129	642575	7860454	Quartzite
HJ 152	649077	7871612	Quartzite
HJ 160B	653213	7870558	Quartzite

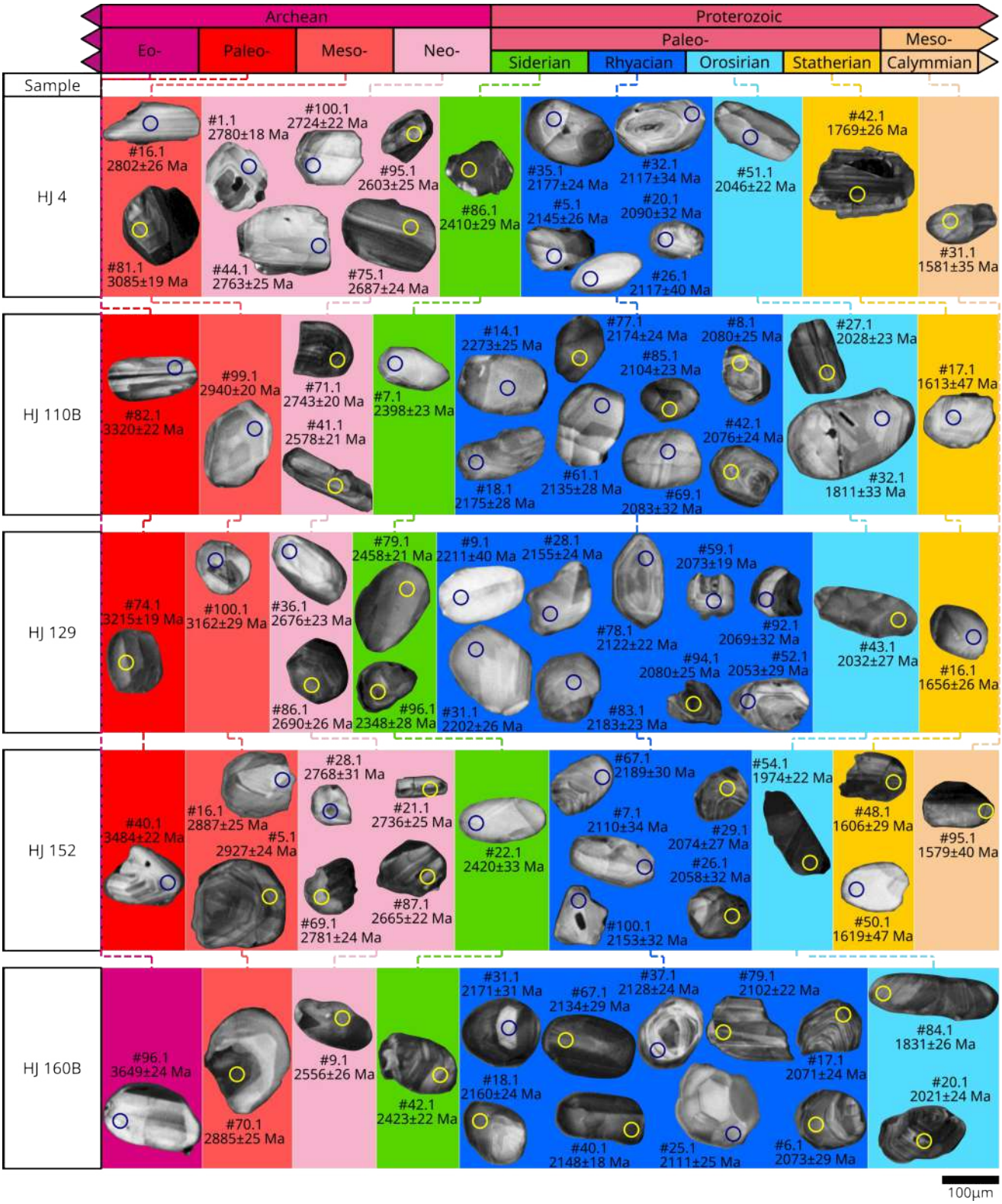

Figure 42. Representative zircon U-Pb age distribution in the samples of this study.

Table 4. Youngest zircon and main age population sets of the analyzed samples.

Sample	Youngest zircon (Ma)	Main sets (Ga)
HJ 4	1580 ± 21	1.6-1.7; 2.0-2.2; 2.6-2.8
HJ 110B	1613 ± 47	2.0-2.2; 2.5-2.9
HJ 129	1656 ± 26	2.0-2.2; 2.4-2.7
HJ 152	1579 ± 40	1.6-1.8; 2.0-2.2; 2.3-2.4; 2.6-2.9
HJ 160B	1831 ± 26	2.0-2.2; 2.4; 2.7-2.9

5.3.1. Sample HJ 4

Sample HJ 4 comes from the base of the main thrust of the Espinhaço system, where the Espinhaço Supergroup units are thrusted over the Bambuí Group. It is mainly an impure, white to pinkish, poorly selected, foliated quartzite with alternating fine-grained and coarse grained layers marking the bedding, as well as ripple marks and cross-beddings. Milimetric, green-gray micaceous (mainly white mica and chlorite) levels are often found between sandy layers, indicating former presence of clay. Millimetric to centimetric shear bands and S-C foliation are found throughout the whole extension of the quartzite expositions, always indicating reverse movement towards west.

From this sample, 96 zircon grains were analyzed, 52 of which yielded concordant U-Pb age data. The grains are subhedral to anhedral, with diameters ranging from 120 to 330 μm. The most abundant populations are Orosirian-Rhyacian, with 18 grains (~35% of the total), and Neoarchean, with 21 grains (~40% of the total), while the youngest zircon dates from the Calymmian (1580 Ma) and is part of a population with six other grains from the Statherian-Calymmian periods (Figure 43).

5.3.2. Sample HJ 110B

Sample HJ 110B was collected from a metaconglomerate in the valley excavated by the Parauninha River. It integrates the Parauninha Wedge, a tectonic sheet where the São João da Chapada (Espinhaço Supergroup), the local rigid basement, is thrusted into the Bambuí Group. The rock is oligomictic, counting with angular to well-rounded pebbles and cobbles composed of white, fine-grained quartzite and white vein quartz, randomly scattered, that is, without imbrication or preferred orientation. The matrix is poorly selected, composed by chlorite, biotite, K-feldspar and quartz. It is mostly formed by coarse sand, but also by granules and finer fractions. Schistosity is observed in the matrix as planar structures that change into an anastomosing aspect enveloping clasts.

From this sample, 94 zircon grains, with 78 providing concordant U-Pb age data. The grains are mostly well-rounded and anhedral, with diameters between 100 and 140 μm.The youngest zircon has a Calymmian age of 1613 Ma, followed by a further 2 grains of Statherian age (1737 Ma and 1780

Ma) and one Late Orosirian zircon (1811 Ma). Orosirian-Rhyacian zircons are lagely predominant in this sample, with 58 grains (~74% of the total) dating from those periods (Figure 43).

5.3.3. Sample HJ 129

Sample HJ 129 was extracted from an outcrop on the riverbed of the Cipó River. It is a little to undeformed quartzite with a yellowish hue. Bedding is marked by granulometric variation, ripple marks and cross-beddings, and the grains are spherical and well-rounded. The rock is mostly medium-grained, not very well selected, but with granulometry consistently varying between fine and medium sand. Finer levels tend to be better selected than the coarser ones.

For this sample, 73 concordant U-Pb ages were obtained, each coming from individual zircon grains, out of a total of 100. The grains are subhedral to anhedral, ranging from 120 to 220 μm in diameter. The most significant zircon population in this sample is Orosirian-Rhyacian (50, or ~70% of the total). A single Calymmian (1656 Ma) zircon stands out on its own, with the next youngest zircons already belonging to the Orosirian-Rhyacian population (Figure 43).

5.3.4. Sample HJ 152

Sample HJ 152 was collected from an outcrop at the heights of the Espinhaço Range. It is a quartzite with a distinctive light to dark gray color, composed mostly by recrystallized quartz and fine white mica. The texture is strongly mylonitc, deflecting around porphyroclasts – usually K-feldspar, but also quartz. The granulometry may have been significantly reduced due to mylonitization and most sedimentary characteristics have been masked with the development of fine, deformed matrix, but porphyroclasts are fine to medium-sized grains of sand.

In this sample, 48 individual grains of zircons provided concordant U-Pb ages, out of a total of 96. Zircons are subhedral and usually well-rounded, with diameters between 100 and 300 μm. The youngest zircon dates to 1579 Ma and is part of a 4-grain Calymmian population. The most abundant populations are Orosirian-Rhyacian and Neoarchean, with 17 (~35%) and 14 (~29%) grains, respectively (Figure 43).

5.3.5. Sample HJ 160B

Sample HJ 160B was collected from an outcrop at the highest local point of the Espinhaço Range in the study area, regionally known as the Alto Palácio Hill. It is a pure, very well selected bimodal quartzite, with layers alternating between fine-grained and fine-to-medium grained. Medium and large cross-beddings are common, as are ripple marks. Tectonic foliation formed by aligned white

mica crystals may be present, but the content of these minerals is low, making this structure not very evident or pervasive.

From this sample, 98 zircon grains were dated, concordant U-Pb ages being obtained from 68. Zircons are anhedral, well-rounded and have mostly high sphericity, with good diameter selection, sizing between 120 and 310 μm. Unlike the remaining samples, whose youngest zircons date to the Calymmian period and which contain Statherian grains, the youngest zircon in sample HJ 160B is Orosirian (1831 Ma). It stands out on its own, but it can be understood as part of the Orosirian-Rhyacian zircon population, the most prevalent in the sample, with 53 grains, which makes up approximately 78% of the total (Figure 43).

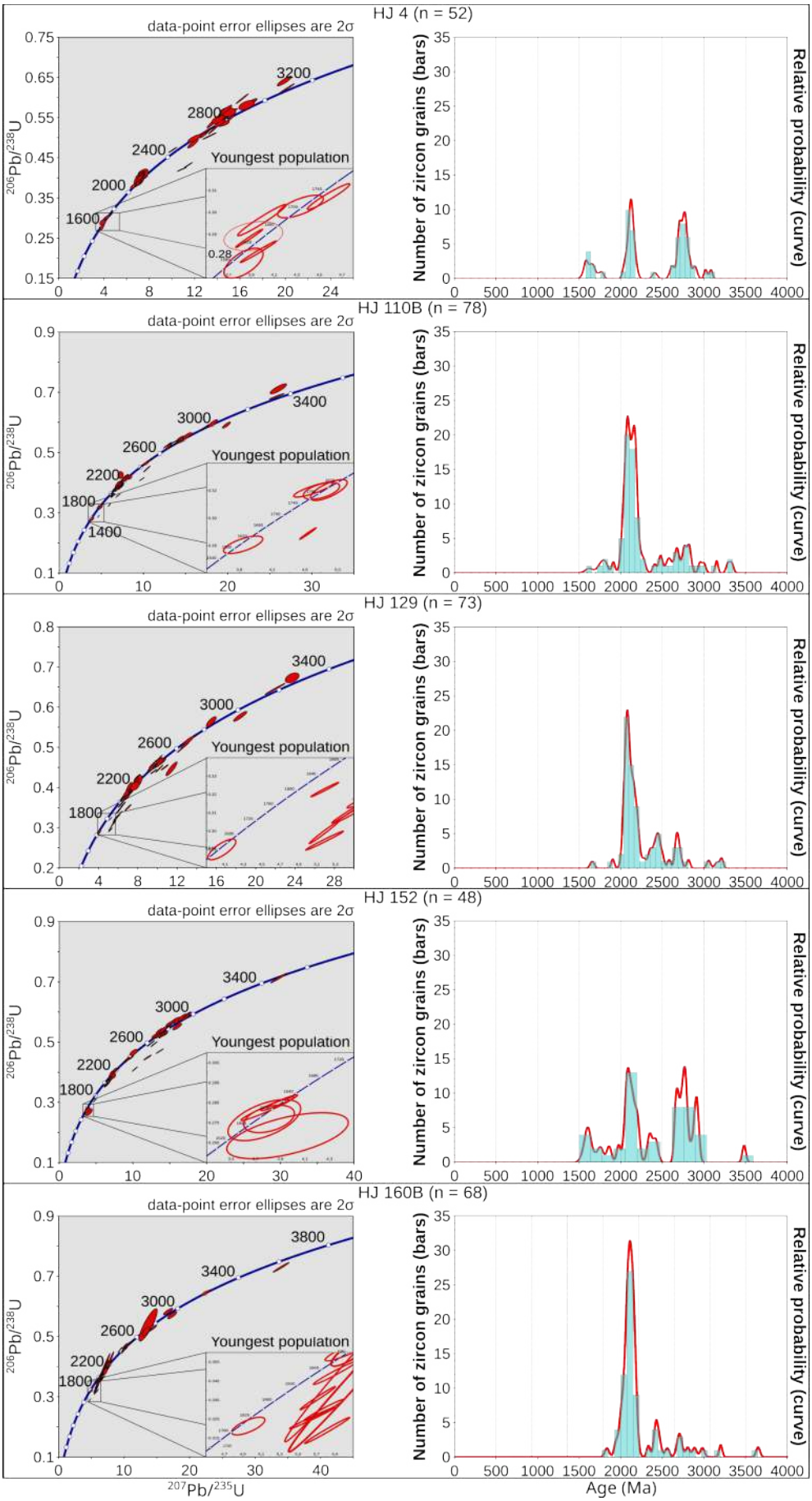

Figure 43. Concordia curves (left) and $^{207}Pb/^{206}Pb$ detrital zircons U-Pb age frequencies (right) for the analyzed samples.

5.4. Discussion

5.4.1. Lithological affinities and classification

Our results were compared with detrital zircon U-Pb age data available from recent papers and academic theses addressing the Meloso Formation and the Costa Sena Group, the Espinhaço Supergroup, the Macaúbas Group and the Jequitaí Formation, i.e., units from the Southern Espinhaço Range and vicinities that have been suggested as candidates for the lithological classification of the rocks from the region of Serra do Cipó, or with known nearby occurrences (case of the Meloso Formation and the Costa Sena Group). Statistical analyses of all the considered data are presented in the form of kernel probability density (KPD) diagrams with indication of youngest zircons, cumulative frequency charts, Kolmogorov-Smirnov tests and Multidimensional Scaling (MDS) diagrams. For the Sopa-Brumadinho Formation (Espinhaço Supergroup), we separated the data from works at its type locality (Santos et al., 2013; Santos, 2015; Silveira, 2017) and from a different location, Extração (Chemale Jr. et al., 2012). It is important to stress that these statistical results are related with the source areas age patterns and with the sediment transport process for the detrital zircon grains, being useful but not definitive for discriminating specific lithostratigraphic units.

The youngest detrital grain age criterion (Table 4) does not provide sufficient substance to solve the classification problem. By this criterion, all that may be posed is that samples HJ 4, HJ 110B, HJ 129 and HJ 152 cannot belong to pre-Espinhaço sequences, i.e., to the Meloso Formation and the Costa Sena Group. The same criterion does not preclude sample HJ 160B from belonging to a pre-Espinhaço unit.

Light is shed over the matter when the detrital U-Pb age distribution curves (Figure 44, Figure 45) and statistical analyses are brought forward – the complete tables containing the results of the KS tests are given in Appendix E. Our samples show strong Orosirian-Rhyacian and Neoarchean age peaks, strongly compatible with the Espinhaço Supergroup. The older sequences do not have so prominent peaks of this age, while the younger ones (Macaúbas-Jequitaí) do, but also show significant populations of Calymmian to Tonian ages, which are absent in our samples.

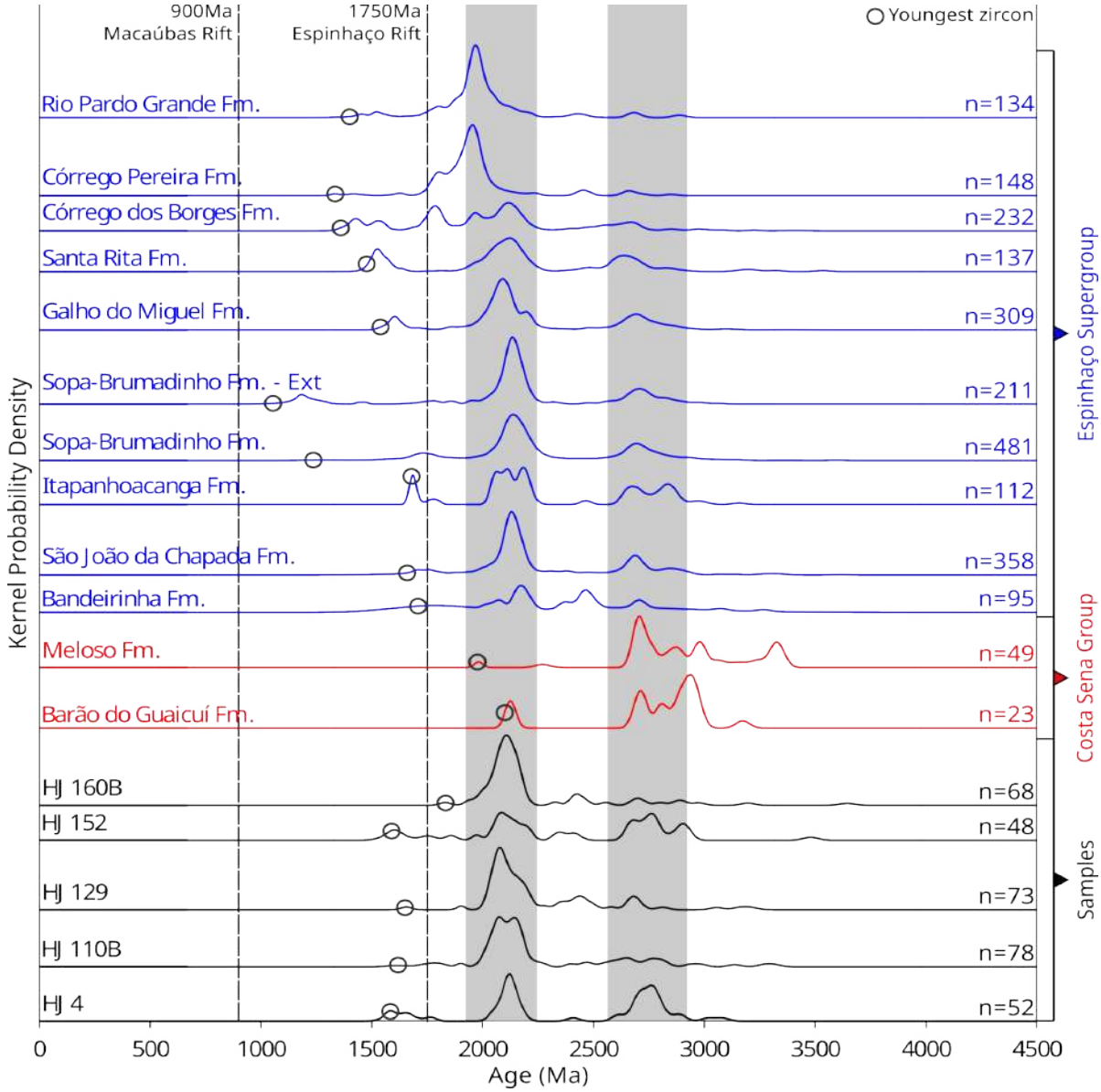

Figure 44. Stacked kernel probability density (KPD) curves of our samples and samples from the Barão do Guaicuí Formation, the Meloso Formation and the Espinhaço Supergroup. Gray circles indicate the age of the youngest zircons.

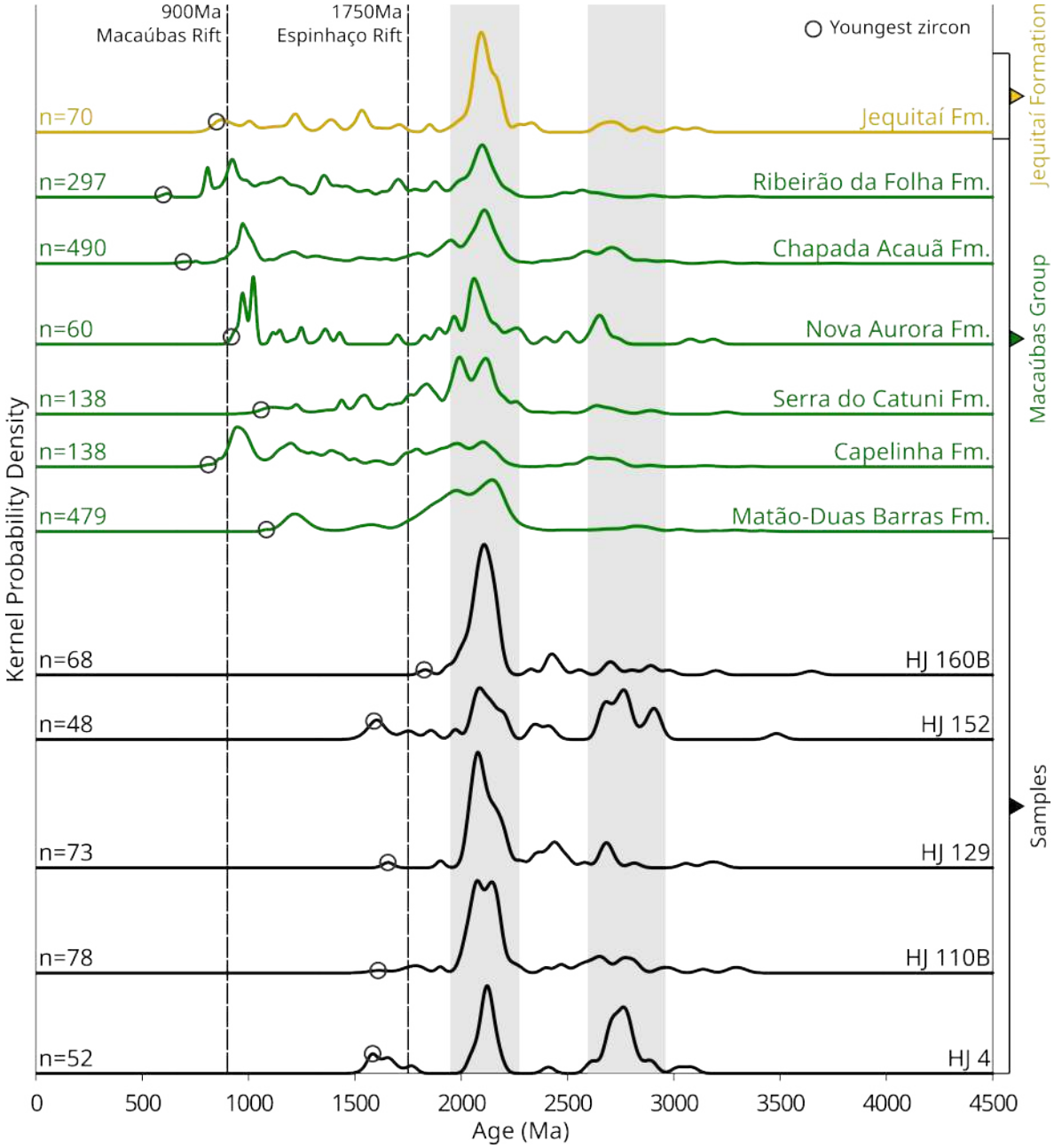

Figure 45. Stacked kernel probability density (KPD) curves of our samples and samples from the Macaúbas Group and the Jequitaí Formation. Gray circles indicate the age of the youngest zircons.

Indeed, the results of the KS test (Table 5) show that the age distribution in our samples are statistically compatible only with a number of formations of the Espinhaço Supergroup, namely the Itapanhoacanga, São João da Chapada, Sopa-Brumadinho, Galho do Miguel and Santa Rita formations, i.e., only for these units the test does not reject the hypothesis that our samples and the samples from these units analyzed in previous studies come from the same original population.

Table 5. Kolmogorov-Smirnov test results for detrital U-Pb ages of our samples *versus* the compiled database. Values in bold and blue represent cases where the null hypothesis (that the samples and the considered units come from the same original population) is not rejected, while values in red correspond to results where the null hypothesis is rejected.

Sample/Unit		p-value vs. samples				
		HJ 4	**HJ 110B**	**HJ 129**	**HJ 152**	**HJ 160B**
	HJ 4	-	0.009	0.001	**1.000**	0.001
	HJ 110B	0.009	-	**0.985**	0.042	**0.926**
	HJ 129	0.001	**0.985**	-	0.011	**0.584**
	HJ 152	**1.000**	0.042	0.011	-	0.009
	HJ 160B	0.001	**0.926**	**0.584**	0.009	-
Costa Sena Affinity	Barão do Guaicuí Fm. (Santos, 2015)	0.001	0.000	0.000	0.001	0.000
	Meloso Fm. (Rolim et al., 2016)	0.000	0.000	0.000	0.000	0.000
Espinhaço Affinity	Bandeirinha Fm. (Chemale Jr. et al., 2012; Santos et al., 2013)	0.027	0.011	0.034	**0.179**	0.001
	São João da Chapada Fm. (Chemale Jr. et al., 2012; Santos et al., 2013; Santos, 2015; Silveira, 2017; Oliveira et al., 2019)	0.011	**0.090**	**0.183**	**0.057**	0.042
	Itapanhoacanga Fm. (Rolim et al., 2016)	**0.393**	**0.104**	0.019	**0.501**	0.009
	Sopa-Brumadinho Fm. (Santos et al., 2013; Santos, 2015; Silveira, 2017)	0.009	**0.300**	**0.292**	**0.057**	0.013
	Sopa-Brumadinho Fm. – Extração (Chemale Jr. et al., 2012)	0.004	**0.628**	**0.314**	0.008	**0.379**
	Galho do Miguel Fm. (Chemale Jr. et al., 2012; Santos et al., 2015)	0.000	**0.961**	**0.622**	0.001	**0.494**
	Santa Rita Fm. (Chemale Jr. et al., 2012; Santos et al., 2015)	0.002	**0.159**	0.030	0.025	**0.126**
	Córrego dos Borges Fm. (Chemale Jr. et al., 2012; Santos et al., 2015)	0.000	0.000	0.000	0.000	0.000
	Córrego Pereira Fm. (Chemale Jr. et al., 2012; Santos et al., 2015)	0.000	0.000	0.000	0.000	0.000
	Rio Pardo Grande Fm. (Chemale Jr. et al., 2012; Santos et al., 2015)	0.000	0.000	0.000	0.000	0.000
Macaúbas-Jequitaí Affinity	Matão-Duas Barras Fm. (Martins et al., 2008; Chemale Jr. et al., 2012; Souza et al., 2019; Oliveira et al., 2021)	0.000	0.000	0.000	0.000	0.000
	Capelinha Fm. (Castro et al., 2019; Amaral et al., 2020)	0.000	0.000	0.000	0.000	0.000
	Serra do Catuni Fm. (Kuchenbecker et al., 2015; Oliveira et al., 2021)	0.000	0.000	0.000	0.000	0.000
	Nova Aurora Fm. (Kuchenbecker et al., 2015)	0.000	0.000	0.000	0.004	0.000
	Chapada Acauã Fm. (Kuchenbecker et al., 2015; Castro et al., 2020)	0.000	0.000	0.000	0,000	0.000
	Ribeirão da Folha Fm. (Peixoto, 2013; Amaral et al., 2020)	0.000	0.000	0.000	0.000	0.000
Jequitaí Formation (Rodrigues, 2008)		0.000	0.005	0.002	0.000	0.003

This is further expressed on the cumulative age frequency chart (Figure 46) and the MDS dispersion (Figure 47). These diagrams distinguish three affiliation sets, defined by: i) Samples from the Barão do Guaicuí and Meloso formations (the Costa Sena Affiliation Group); ii) Samples from the Espinhaço Supergroup from its base up to the Santa Rita Formation (the Espinhaço Affiliation Group); and iii) samples from the remaining Upper Espinhaço Supergroup, the Macaúbas Group and the Jequitaí Formation (the Macaúbas-Jequitaí Affiliation Group). The affinity between the

Mesopretorozoic Upper Espinhaço units and the Neoproterozoic Macaúbas Group and Jequitaí Formation is a curious feature that encourages further studies. It is possible that the same or similar areas – at different moments in time – were the source of sediments (and, thus, detrital zircons) for these rocks. We also clarify that a p-value that passes the test for a unit-sample pair does not mean that said unit is necessarily the correct lithological classification for said sample or that said unit is necessarily present in the study area. Rather than interpreting valid p-values specifically to each unit-sample pairing, it is more sensible to consider the affiliation groups that emerged through these analyses. With these sets defined, all our samples fall into or closer to the Espinhaço Affinity Group.

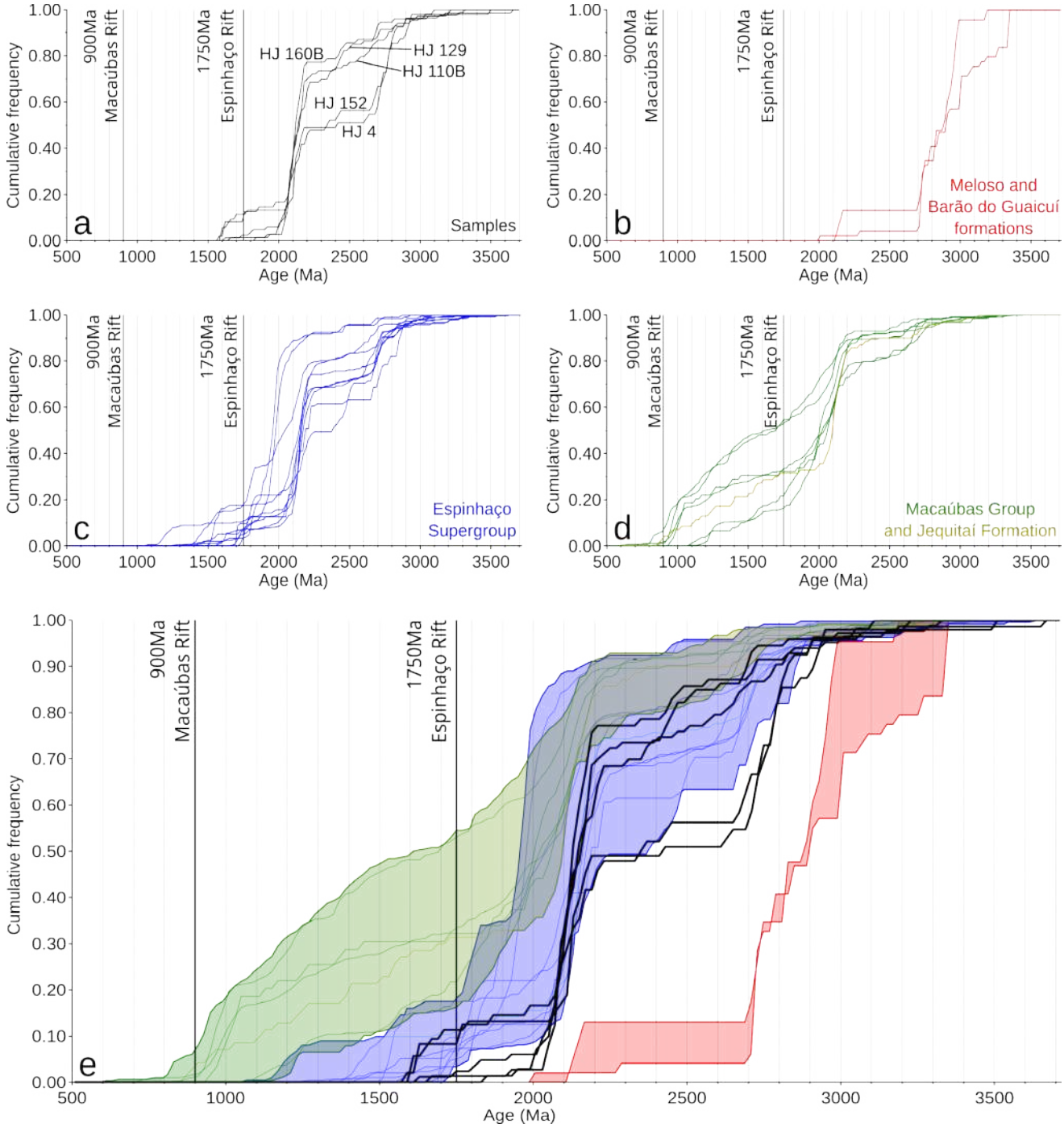

Figure 46. Cumulative frequency charts of detrital zircon U-Pb ages for the samples in this study (a) ages compiled for the Meloso and Barão do Guaicuí formations (b), the Espinhaço Supergroup (c), the Macaúbas Group and the Jequitaí Formation (d), and a superposition of all the age spectra (e).

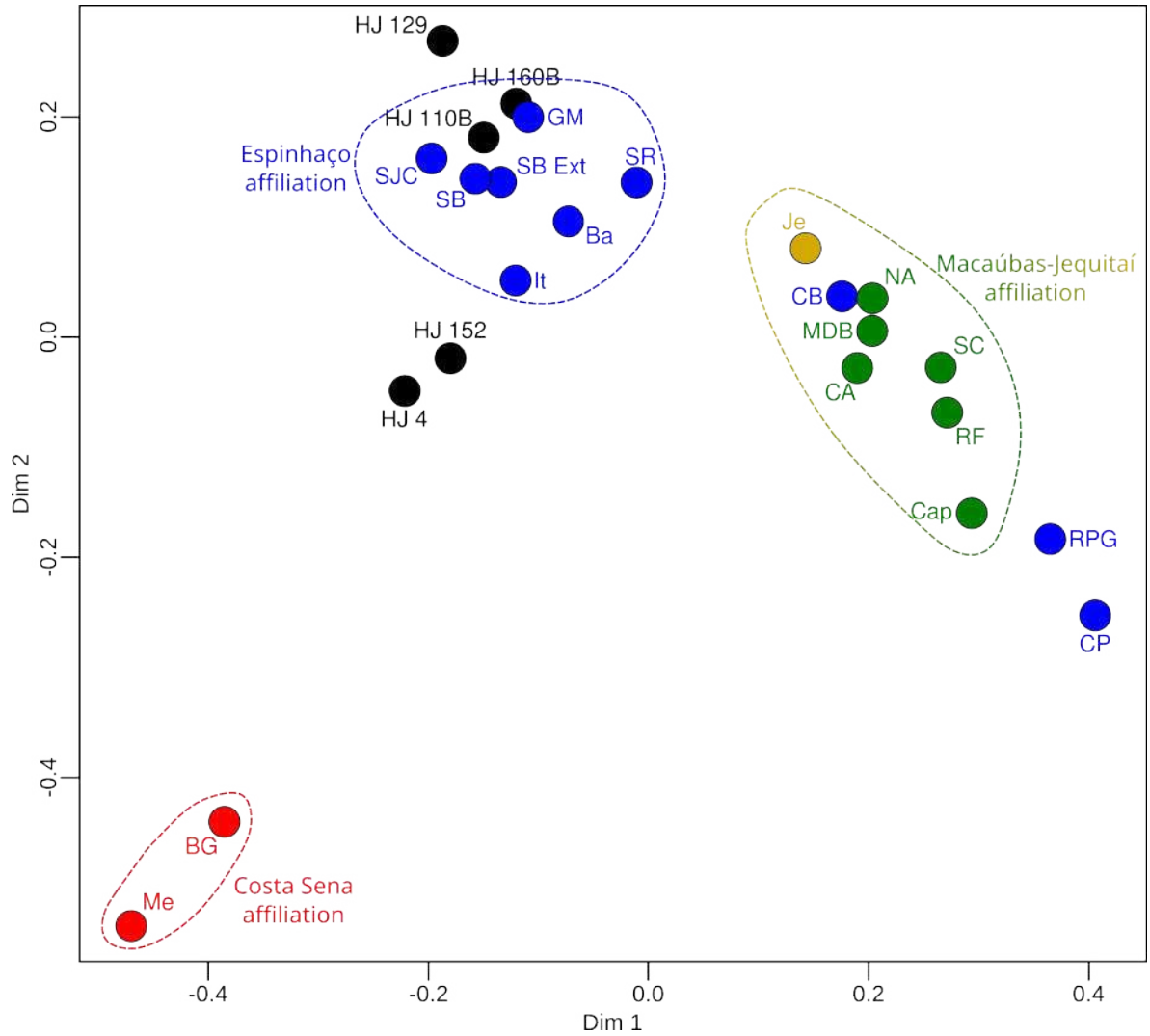

Figure 47. Multidimensional Scaling distribution and grouping of samples of this study and compiled data from other works.

These considerations constrain the possible classification candidates to the São João da Chapada Formation (Espinhaço I Sequence), or the Sopa-Brumadinho, Galho do Miguel, Santa Rita and Córrego dos Borges formations (Espinhaço II Sequence). In the next sessions, we will discuss our interpretations for each sample.

5.4.1.1. Sample HJ 4

The rocks at the base of the Espinhaço Front have been mapped in previous works into the Conselheiro Mata Group (Schöll, 1972), the Macaúbas Group (Oliveira, 1994; Oliveira et al., 1997; Ribeiro, 2010) or the São João da Chapada Formation (Chierici et al., 2021). Sample HJ 4, collected in this context, is a poorly-selected quartzite interbeded with milimetric micaceous levels, compatible with a sub-surf plataformal environment. The KS and MDS analyses do not support the previous classification into the Macaúbas Group. The youngest zircon population and the petrographic features

of the rock make its interpretation as part of the São João da Chapada, Itapanhocanga or Sopa-Brumadinho formations infeasible, being most likely part of the Conselheiro Mata Group, of which it may be classified as one of the coarser members of the Santa Rita Formation. This means that the rocks thrusted over the Bambui Group at the craton-orogen limit in the central zone of the study area belong to the Espinhaço Supergroup.

It is noteworthy that the KS test p-value result for the sample HJ 4 *versus* sample HJ 152 (Table 5) is rounded up to 1.000 up to the fifth decimal plate, suggesting that both are very likely to have originated from the same original population.

5.4.1.2. Sample HJ 110B

The rocks in the Parauninha Wedge (Chapter 4, item 4.4.2.1) have been previously described as belonging to the Macaúbas Group, and interpreted either as a structural window (Oliveira, 1994), a normal stratigraphic sequence (Oliveira et al., 1997), or a klippe (Ribeiro, 2010). Here, we reinterpreted this area as a tectonic sheet lodged amidst rocks of the Bambui Group, in the foreland region west of the main Espinhaço Thrust Front. Coming from the wedge, sample HJ 110B is an oligomictic matrix-supported metaconglomerate. The distribution pattern of detrital zircon U-Pb ages of this sample is not compatible with what has been observed for the Macaúbas Group, suggesting an older deposition. The faciological features of this sample are more compatible with the São João da Chapada and the Sopa-Brumadinho formations. Between these candidates, the youngest zircon criterion (1613 ± 47 Ma) points more likely to the São João da Chapada Formation.

5.4.1.3. Sample HJ 129

The Cipó River Window (Chapter 4, item 4.4.2.1), original context of sample HJ 129, has been formerly considered part of the Macaúbas Group (Oliveira, 1994; Oliveira et al., 1997; Ribeiro, 2010), the Jequitaí Formation (Schöll, 1972) or the Espinhaço Supergroup (Marshak and Alkmim, 1989). The association of meta-paraconglomerate and quartzite with ripple marks and cross-beddings points to alluvial or fluvial sedimentation characteristic of either the São João da Chapada Formation or the Sopa-Brumadinho Formation. Mono or oligomictic, matrix-supported conglomerates are more common in the São João da Chapada Formation, given its context of an alluvial fan deposited during the mechanical subsidence stage of the Espinhaço Rift, while the Sopa-Brumadinho conglomerates are mostly polymictic, clast-supported and bear well-rounded clasts, typical of riverbeds. This makes the São João da Chapada Formation a more appropriate classification for sample HJ 129. The undeformed state of the rock strengthens the interpretation of the area as a structural window, the

quartzite and meta-paraconglomerate being the local rigid basement of the remaining units found in the study area.

Thus, we do not support the map by Oliveira (1994) and subsequent works (Oliveira et al., 1997; Ribeiro, 2010) that place these rocks in the Macaúbas Group, or the work by Schöll (1972), who mapped them into the Jequitaí Formation. Rather, we believe that the model proposed by Marshak and Alkmim (1989) is closer to the reality, suggesting a classification in the Espinhaço Supergroup, and add detail to that by proposing the São João da Chapada Formation as its plausible representative in the area.

5.4.1.4. Sample HJ 152

Sample HJ 152 comes from the immediate vicinities of a shear zone parallel to the major thrust system, in an area previously mapped as Santa Rita Formation (Oliveira, 1994; Oliveira et al., 1997; Ribeiro, 2010) at the heights of the Cipó Range. Although more strongly deformed and recrystallized, its mineralogy and sedimentary aspects allows to characterize it as a quartz-pelitic rock with sand-sized clasts composed by K-feldspar or quartz. These characteristics, alongside the detrital zircon age pattern of the sample as shown by the KS and MDS tests, particularly by the affinity between this sample and sample HJ 4 (Figure 44, Figure 45, Figure 46, Figure 47, Table 5), are consistent with the interpretation as Santa Rita Formation.

5.4.1.5. Sample HJ 160B

The region of Alto Palácio, where sample HJ 160B was collected, has been considered in previous geological maps as an area of occurrence of the Galho do Miguel Formation (Oliveira, 1994; Oliveira et al., 1997; Ribeiro, 2010). Sample HJ 160B has distinctive attributes from its sedimentary facies, as the mineralogical purity, well-selected fine to medium granulometry and structures such as large cross-beddings and ripple marks. These features are typical of aeolian environment, making the Galho do Miguel Formation indeed a suitable classification for this sample. This interpretation is supported by results found in the KS test and MDS, and not precluded by the age of the youngest zircon (1831 ± 26 Ma).

5.4.2. Possible areas of sedimentary provenance

All our samples have Rhyacian-Orosirian (2.0-2.2 Ga) zircons as the most prominent populations, also with relevant contribution from Neoarchean (2.5-2.9 Ga) zircons. It is reasonable to assume, thus, that primary sources of these detrital grains were constantly available during the sedimentation of the Espinhaço Supergroup in the southern SER.

The Cipó Range is adjacent, to the south and west, to several Neoarchean TTG basement blocks (e.g. Belo Horizonte, Bação, Betim) and to the Rio das Velhas Greenstone Belt (~2.7 Ga). The Guanhães Block, to the east, and the Gouveia Complex, to the north, also contain rocks dating from the Neoarchean (Peixoto et al., 2015; Barrote et al., 2017).

Rhyacian to Orosirian granite magmatism also occurred in these blocks (Grochowski et al., 2021), and high-grade metamorphic units of the same age (e.g. the Juiz de Fora, Pocrane and Mantiqueira complexes) are basement inliers in the Araçuaí Orogen (Fonte-Boa, 2017; Cutts et al., 2018; Degler et al., 2018; Kuribara et al., 2019). The Mineiro belt, in the southern São Francisco Craton, represents a crustal segment of the 2.47–2.00 Ga known by its Siderian and Rhyacian juvenile rocks (Teixeira et al., 2022). All these units are potential sources for the main detrital age sets of the Espinhaço Supergroup.

Statherian and Calymmian magmatism in the São Francisco Craton and the Araçuaí Orogen are associated with the rifting pulses responsible for opening the the Espinhaço Basin. Most probably, the Borrachudos (1688 Ma) and Conceição do Mato Dentro (1750 Ma) suites are the sources of the Statherian zircons. Calymmian-age volcanism has been described in intermediate lava flows in the Bomba Formation (1589 Ma), Northern Espinhaço Range (Danderfer-Filho et al., 2009; Santos et al., 2020), and in basic amphibolite lenses (1529-1096 Ma) cutting the Pocrane Complex in what is now located in the crystalline core of the Araçuaí Orogen (Fonte-Boa, 2017). Basic rocks usually have low zircon content, making the Bomba Formation a less likely and distal source of Calymmian zircons in our samples.

Few Eo, Paleo and Mesoarchean zircons are present. Most notably, only a single Eoarchean zircon (3649 ± 24 Ma) was found in our samples, in the Galho do Miguel Formation. All this suggests that it is probable that crust of these ages was exposed to provide sediments to the Espinhaço Supergroup. These grains also could have been inherited by the younger suites during emplacement, and then eroded into the basin.

Eoarchean detrital zircons also have been found in other works addressing the Espinhaço Supergroup (Chemale Jr. et al., 2012; Santos et al., 2015), the Macaúbas Group (Kuchenbecker et al., 2015) and the Iron Quadrangle (Hartmann et al., 2006), which could point to the presence of primary Eoarchean basement during the deposition of the Espinhaço Supergroup. Yet another possibility is that the Eoarchean zircon originated from a more distant area, the Gavião Block, Northern Espinhaço Range, where Oliveira et al. (2020) and Moreira et al. (2022) dated gneisses at 3.65 Ga. Finally, for the Paleo-Mesoarchean zircons, primary sources could be found in the Santa Bárbara Complex (3210 Ma) or the Mineiro Belt (3219 Ma), in the Iron Quadrangle (Lana et al., 2013).

It is an important reminder that the units listed here are the closest to Serra do Cipó, but sedimentary agents may transport grains several thousands of kilometers away from their source areas.

5.5. Conclusion

The Espinhaço thrust Front in the Cipó Range is marked by a direct contact between the Espinhaço Supergroup over the Bambuí Group. The pre-Bambui outcroping units show an affinity with the Upper and Lower Espinhaço sequences, both in the Foreland and the Fold-and-Thrust Compartments. Petrographic aspects as well as detrital zircon U-Pb age values and distribution patterns do not support the presence of pre-Espinhaço units or of the younger Macaúbas Group and Jequitaí Formation in the region. Our studies also promote significant changes to the spatial distribution of the stratigraphic units in the area. Therefore, this review brings significant alterations to previous maps, especially those by Karfunkel et al. (1991), Oliveira (1994), Oliveira et al. (1997), Ribeiro (2010) and Chierici et al. (2021). We bring back the proposal by Schöll (1972) and Marshak and Alkmim (1989) regarding the distribution of the Espinhaço Supergroup.

Statistical analysis (kernel probability distribution, Kolmogorov-Smirnov Test and Multidimensional Scaling dispersion) coupled with the study of sedimentary facies and petrography suggest the correlation of the outcroping units in the area with the São João da Chapada, Sopa-Brumadinho, Galho do Miguel and Santa Rita formations of the Espinhaço Supergroup.

Thus, our data endorses the craton-orogen boundary in the area is marked by the tectonic inversion of the Espinhaço Supergroup over the Bambuí Group, and that the Macaúbas Group was either completely eroded, detached by the thrust fault system or was not deposited at all in the region.

In the foreland compartment, the São João da Chapada Formation is found practically exempt of deformation in the Cipó River structural window, acting as the local stratigraphic rigid basement, separated by detachments from the Bambuí Group, which was deformed during the tectonic events of the Brasiliano-Pan African Orogeny. The remaining occurrences of the Espinhaço Supergroup are all restricted to the Fold-and-Thrust Domain – wedged into the Bambuí Group (a second occurrence of the São João da Chapada Formation) or in the Southern Espinhaço Range (Galho do Miguel and Santa Rita formations).

The basement of the São Francisco Craton and the Araçuaí Orogen (e.g. the Belo Horizonte, Gouveia and Pocrane complexes, the Guanhães Block, the Rio das Velhas Supergroup) is the most likely primary source of zircons for the rocks in the study area, for the case of the Archean and Paleoproterozoic zircons, whereas the Mesoproterozoic zircons most likely originated from the igneous suites generated during the rifting events that opened the Espinhaço basin (e.g. the

Borrachudos and Conceição do Mato Dentro suites). However, specific sedimentary provenance studies could shed more light over this matter.

6. STRAIN ANALYSIS IN SERRA DO CIPÓ: SHAPE PREFERRED ORIENTATION AND ELLIPSOID RECONSTRUCTION

Strain analysis is a way to quantify the deformation that rocks of an area have experienced by the determination of numeric parameters. Such attributes are calculated using the shape, position, size and orientation of structural elements present in a rock. This numeric description also enables comparison between the deformation of different regions. Strain analysis depends on the kinds of strain markers devisable on the fabric of a rock, that is, objects whose pre-deformational shapes are known or can be reliably estimated. If there are enough structures to distinguish between different stages over the course of the deformation, a progressive system or the occurrence of separate events may be described. Otherwise, an initial setting can be inferred from the final product, that is, the structural elements imprinted on the rock, but intermediate stages cannot be interpreted based solely on strain analyses. (Ramsay and Huber, 1983; Twiss and Moores, 2007; Ragan, 2009; Davis et al., 2012).

Here, we aim to characterize the finite state of strain of the region of Serra do Cipó. For that, we applied the Shape Preferred Orientation method (Launeau and Cruden, 1998; Launeau and Robin, 2003).

6.1. The Shape Preferred Orientation (SPO) method and strain ellipsoid reconstruction

In this study, we use clastic quartz grains from metasandstones as strain markers. For that, we applied the Shape Preferred Orientation (SPO) method (Launeau and Cruden, 1998; Launeau and Robin, 2003). In an SPO analysis, individual grains (**j**) are computationally identified on a binary (black and white) raster image of a sample based on sequential presence or absence of black pixels. Based on the shape of the grain, an inertia tensor ($\mathbf{M_j}$) is calculated. A mean inertia tensor (**M**) is then obtained, combining all individual tensors on the image. The eigenvalues and eigenvectors of **M** correspond, respectively, to the length and orientation of the axes of the tensor on the plane of the image.

The first parameters to be calculated are the coordinates of the center of each grain, based on its area (**A**) and the coordinates of all the pixels (**i**) that compose it on the image, through

$$x_c = \frac{1}{A}\sum_i x_i \qquad \textbf{Equation 8}$$

and

$$y_c = \frac{1}{A}\sum_i y_i. \qquad \textbf{Equation 9}$$

These values are sufficient for the determination of $\mathbf{M_j}$:

$$M_j = \begin{bmatrix} m_{xxj} & m_{xyj} \\ m_{xyj} & m_{yyj} \end{bmatrix}, \quad \textbf{Equation 10}$$

where

$$m_{xxj} = \frac{1}{A} \sum_i (x_i - x_c)^2, \quad \textbf{Equation 11}$$

$$m_{xyj} = \frac{1}{A} \sum_i (x_i - x_c)(y_i - y_c), \quad \textbf{Equation 12}$$

and

$$m_{yyj} = \frac{1}{A} \sum_i (y_i - y_c)^2. \quad \textbf{Equation 13}$$

After all the **N** individual inertia tensors have been calculated, the global tensor, that is, the shape preferred orientation, is obtained by

$$M = \frac{1}{N} \sum_j M_j = \frac{1}{N} \begin{bmatrix} \sum_j m_{xxj} & \sum_j m_{xyj} \\ \sum_j m_{xyj} & \sum_j m_{yyj} \end{bmatrix}. \quad \textbf{Equation 14}$$

If an approximately symmetric shape and isotropic distribution can be assumed for the grains of the rock, as well as a passive behavior during strain, the mean inertia tensor resulting from this analysis can be interpreted as the finite strain ellipsis for the section of the rock displayed on the image. If the results of at least three different sections of the same sample are combined, it is possible to interpolate the entire finite strain ellipsoid of the deformation system that affected the point where the sample was collected (Launeau and Robin, 2005).

6.2. Practical and analytical procedures

A total of seven samples (Figure 48, Table 6) were analyzed through three different, (near-)perpendicular thin sections, each from cuts made as close as possible to the estimated orientation of the principal sections of the strain ellipsoid, that is, the XY, XZ and YZ sections (Figure 49.a, b). For the graphic analyses, we digitized individual grains on each thin section (Figure 49.c, d) and had them run through the SPO2003 software (Launeau and Robin, 2003) to obtain the mean grain shape and inertia tensor (Figure 50.a, b), and used the resulting ellipsis parameters – shape ratio and rake – to calculate the finite strain ellipsoid (Figure 50.c, d) of each sample using the software Ellipsoid2003 (Launeau and Robin, 2005). The graphic output of the software represents the shape and anisotropy of the ellipsoids using a TP' chart, where T is the shape parameter (T < 0 meaning prolate shape, T = 0 meaning plane strain and T > 0 meaning oblate shape) and P' is an anisotropy parameter, ranging from 1 to infinity (Jelinek, 1981). The software also provides the Flinn's k

parameter (Flinn, 1965), which we call to when making reference to ellipsoid shapes and strain regimes (k < 1 meaning oblate shape, k= 1 meaning plane strain, and k > 1 meaning prolate shape).

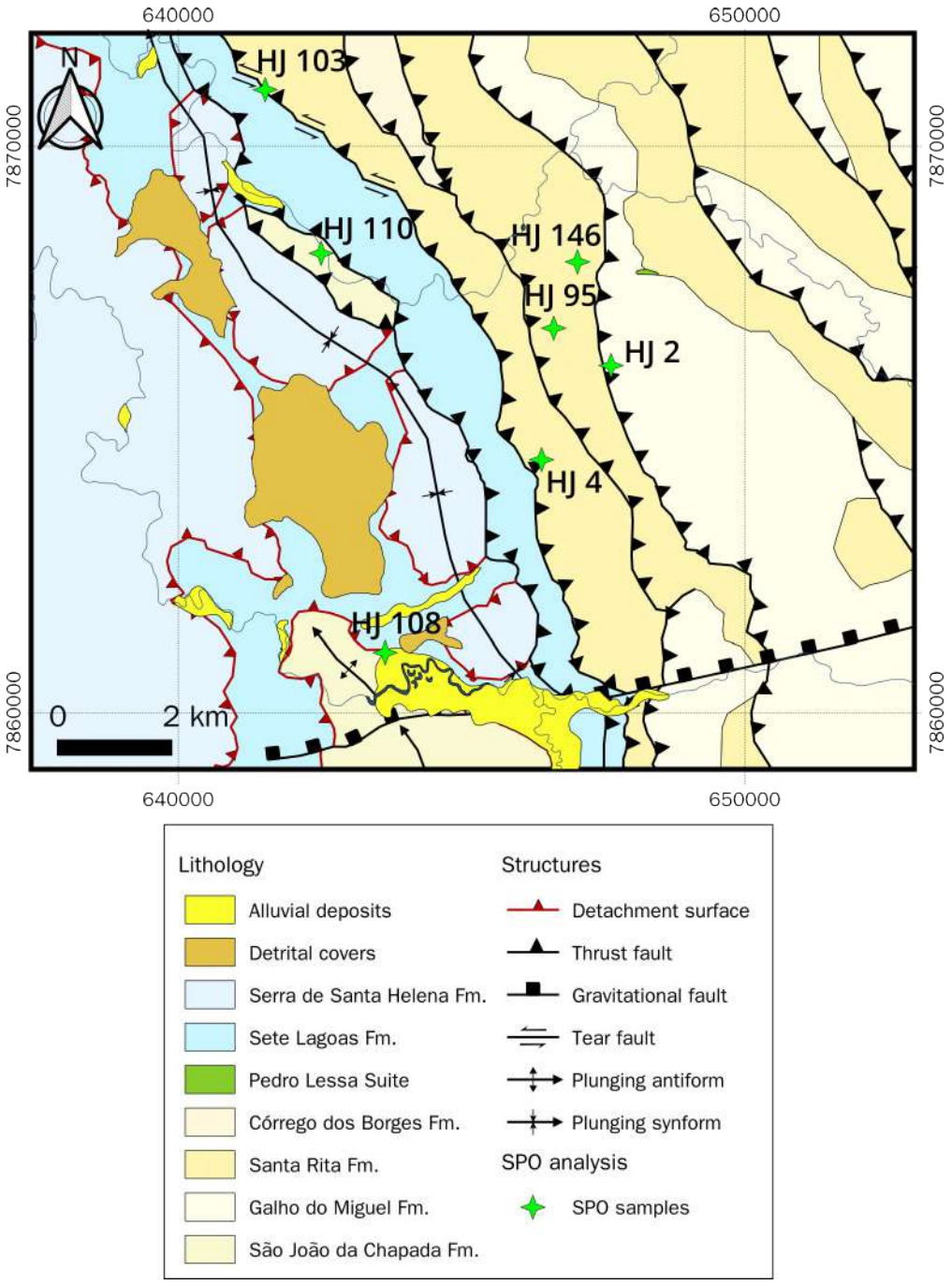

Figure 48. Location of the samples used for SPO analysis in the study area.

Table 6. Location, orientation, classification, type and context of the samples used in SPO analysis.

Sample	Coordinates (UTM 23K)		Section Orientation (Dip direction/Dip)			Unit	Rock	Context
	E	N	A	B	C			
HJ 2	647643	7866126	247/67	158/79	64/25	Santa Rita Fm	Quartzite	Mid-sequence in Fold-and-Thrust Domain
HJ 4	646417	7864461	269/74	181/81	65/21	Santa Rita Fm	Quartzite	Base of the Espinhaço Front
HJ 95	646630	7866786	106/80	176/57	23/31	Santa Rita Fm	Quartzite	Mid-sequence in Fold-and-Thrust Domain
HJ 103	641535	7871000	224/37	297/85	40/50	Santa Rita Fm	Quartzite	Base of the Espinhaco Front
HJ 108	643654	7861060	224/62	303/85	60/21	São João da Chapada Fm	Quartzite	Structural window (rigid basement)
HJ 110	642523	7868109	257/70	168/74	29/26	São João da Chapada Fm	Meta-paraconglomerate	Tectonic sheet
HJ 146	647050	7867958	255/44	158/80	75/47	Santa Rita Fm	Quartzite	Thrust in Fold-and-Thrust Domain

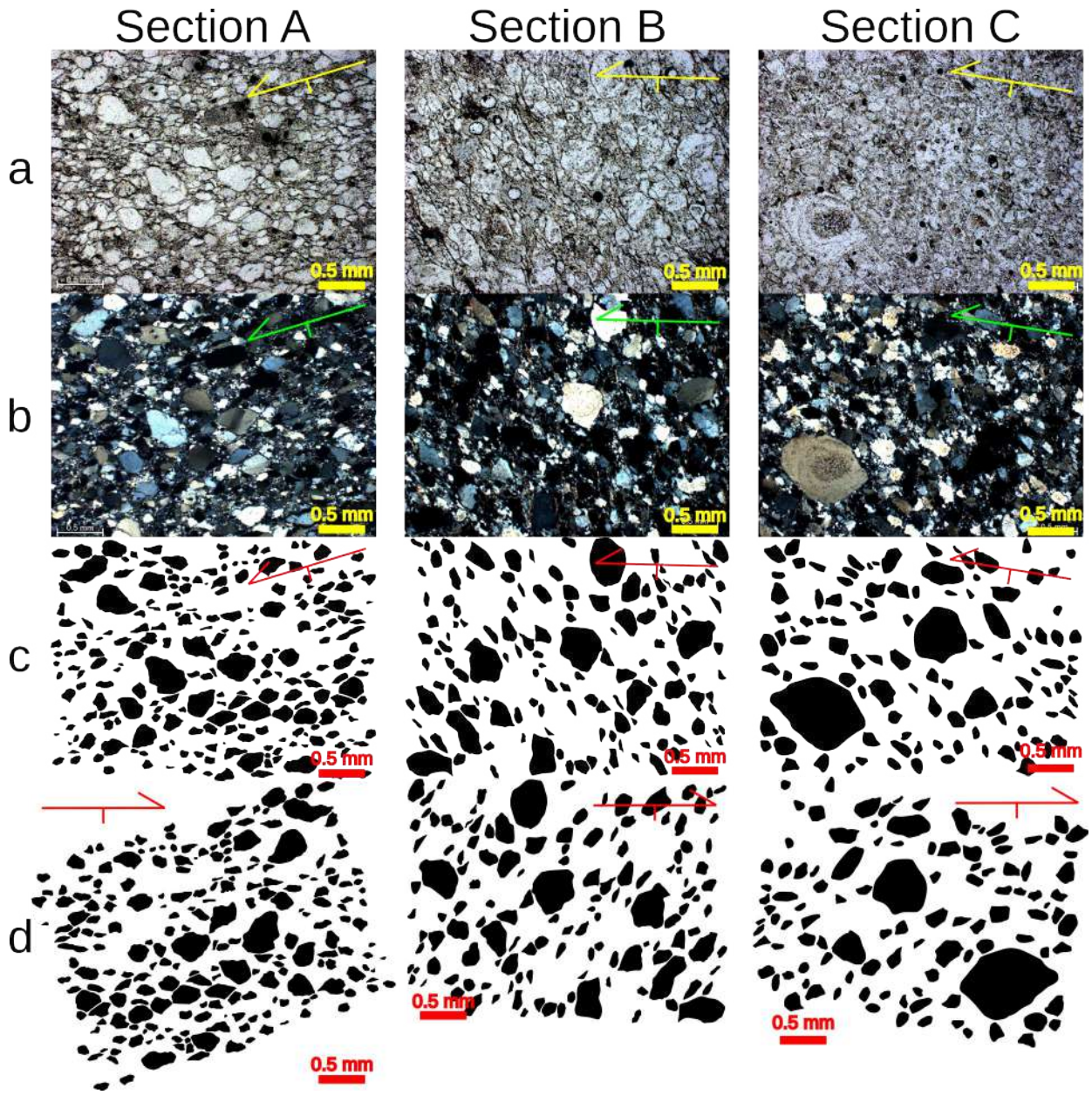

Figure 49. Sample preparation for SPO analysis (example of sample HJ 103): Photomicrographies under uncrossed (a) and crossed (b) polarizers, and corresponding binary figures of digitized grains for graphic analysis before (c) and after (d) adjustment of the orientation mark according to the right hand rule.

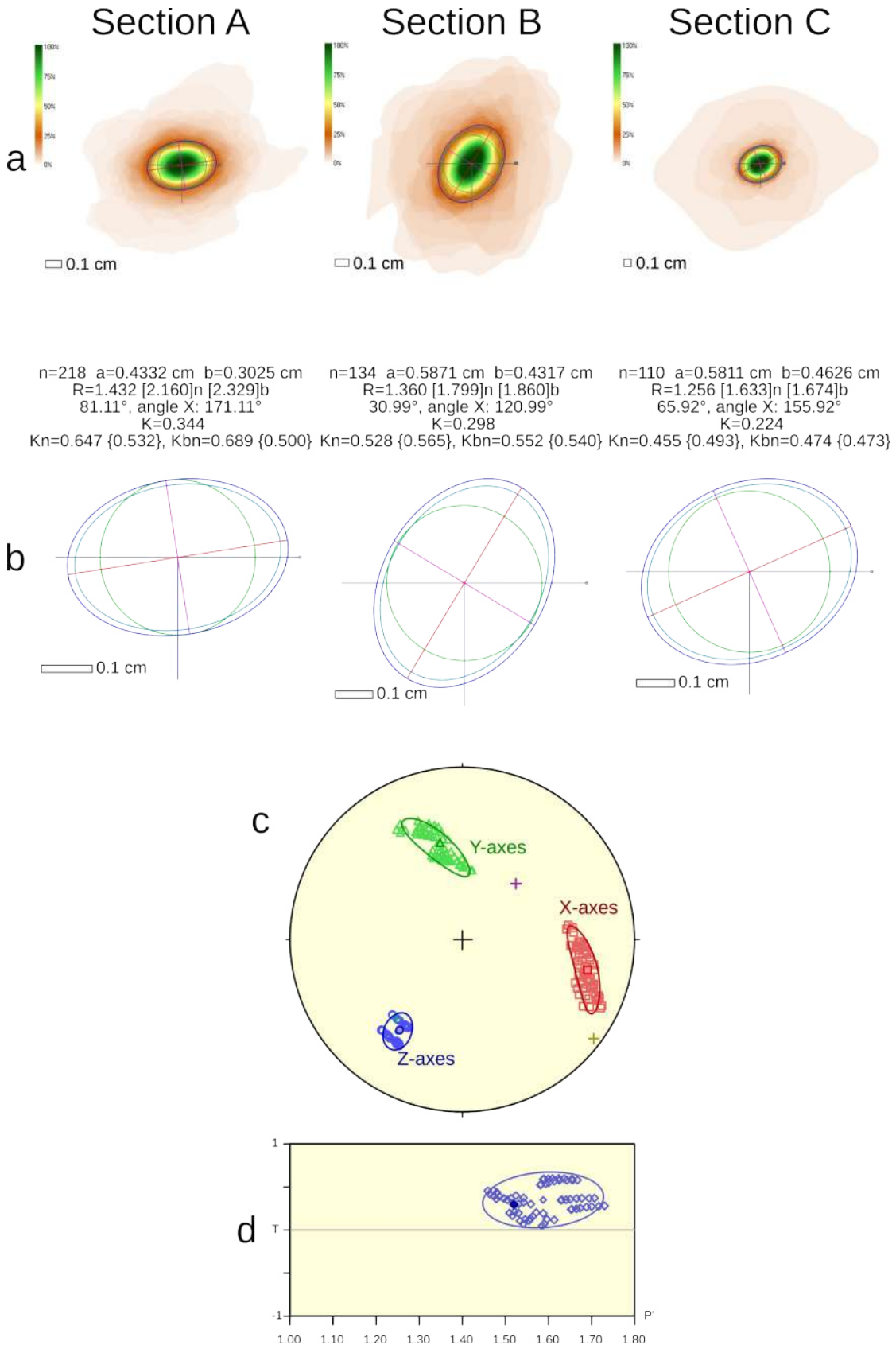

Figure 50. Results of a SPO analysis of a sample (example of sample HJ 103): a) Mean shapes of all objects analyzed; b) Mean inertia tensors; c) Orientation of the X, Y and Z axes of the calculated strain ellipsoid; d) TP' chart for the calculated ellipsoid.

6.3. Results

6.3.1. Samples

6.3.1.1. HJ 2

Sample HJ 2 was collected in the Santa Rita Formation, in the heights of the Cipó Range. It is composed by a white, fine-grained quartzite intercalated by millimetric phyllitic or schistose layers. Centimetric reverse, west-vergent shear bands are widespread in its original outcrop, and the texture of the rock is strongly mylonitic. The foliation and stretch lineation are defined both by recrystallized clasts and metamorphic mica.

6.3.1.2. HJ 4

Sample HJ 4 was taken from the Santa Rita Formation at the base of the Main Espinhaço Thrusts, close to its tectonic inversion with the Bambuí Group in the central portion of the study area. This sample is a foliated coarse-grained quartzite with well-preserved cross-beddings and ripple marks. At this point, a normal fault crosses through the sedimentary layers and tectonic foliations of a previous stage.

6.3.1.3. HJ 95

Another sample from the Santa Rita Formation at the heights of the Cipó Range, sample HJ 95 is an impure, fine-grained quartzite containing anastomosed tectonic foliation sub-parallel to the orientation of the bedding surfaces. The quartz grains are usually stretched or recrystallized, forming σ-type shapes that indicate reverse movement towards west.

6.3.1.4. HJ 103

This sample was also collected from the Santa Rita Formation at the Espinhaço Front in the northern portion of the study area. It is a white, medium-grained quartzite containing coarser grain fractions. The grains are usually elongated and forming sigmoidal shapes, indicating reverse, west-verging movement. The mica content in this sample is low, but enough for the development of a well-marked cleavage that deflects around the clastic fraction, forming an anastomosed texture.

6.3.1.5. HJ 108

Sample HJ 108 comes from the São João da Chapada, in the Cipó River Window, near the contact with the Sete Lagoas Formation. This sample is formed by a practically undeformed white, medium-grained and poorly selected quartzite, in which grains are mostly sub-angular or sub-rounded. The tectonic foliation is poorly developed and has a slightly higher dip than the beddings.

6.3.1.6. HJ 110

Sample HJ 110 comes from the other area of exposition of the São João da Chapada Formation in the region of Serra do Cipó, the Parauninha Wedge. It is composed by an olygomictic matrix-supported meta-paraconglomerate. The clasts are composed by quartz or fine-grained quartzite. The matrix is extensively foliated and formed by coarse, poorly selected sand. Stretched and elongated grains and clasts form φ or reverse σ indicators, and the foliation envelops the grains in an anastomosed aspect.

6.3.1.7. HJ 146

This sample was taken from the vicinities of a west-verging thrust in the Santa Rita Formation at the heights of the Cipó Range. It is composed by a medium-grained, poorly selected and foliated quartzite that experienced dynamic recrystallization with recrystallized or stretched quartz grains as reverse kinematic indicators. The foliation is composed both by oriented mica and recrystallized quartz of the fine-grained matrix.

6.3.2. SPO analysis

We applied the Shape Preferred Orientation (SPO) method (Launeau and Cruden, 1998; Launeau and Robin, 2003) to obtain the strain axes and reconstruct the finite strain ellipsoid of seven oriented samples from the study area. We selected samples where passive behavior could be assumed for the strain markers – in this study, individual quartz grains – during strain and where textural features were devisable enough for graphic recognition.

The ellipsoid shapes and respective parameters (Table 7, Table 8, Figure 51) obtained are mostly oblate, except for sample HJ 146, which shows a near plane-strain and slight prolate shape (Flinn's $K = 1.037 \pm 0.868$). The intensity of deformation (R_f) is given by the ratio between the X and Z axes. R_f ranges from 1.320 to 1.784 for the flattening cases, while the constriction case shows a much higher value: 2.942. Long axes (X) are sub-horizontal to low-plunging, with azimuths fluctuating between ~NE and ~ESE. Intermediate axes (Y) are sub-horizontal and trend mostly around the NNW-SSE direction. Finally, short axes (Z) are high-plunging to subvertical with a SW trend (52).

Table 7. Mathematical parameters of the strain ellipsoids calculated for each sample.

Sample	n[a]	Axial lengths			$\sqrt{\widetilde{F}}^b$	Flinn's k	R_f	Format
		X	Y	Z				
HJ 2	696	1.142 ± 0.013	1.110 ± 0.012	0.789 ± 0.006	8.2%	0.073 ± 0.055	1.449 ± 0.023	Oblate
HJ 4	965	1.123 ± 0.032	1.046 ± 0.033	0.851 ± 0.038	3.1%	0.343 ± 0.307	1.320 ± 0.088	Oblate
HJ 95	730	1.234 ± 0.057	1.065 ± 0.064	0.762 ± 0.042	3.8%	0.422 ± 0.325	1.622 ± 0.139	Oblate
HJ 103	1088	1.220 ± 0.056	1.054 ± 0.052	0.779 ± 0.040	5.0%	0.473 ± 0.376	1.568 ± 0.133	Oblate
HJ 108	568	1.194 ± 0.089	1.035 ± 0.059	0.811 ± 0.047	5.0%	0.606 ± 0.676	1.475 ± 0.181	Oblate
HJ 110	1484	1.286 ± 0.149	1.079 ± 0.108	0.724 ± 0.079	7.5%	0.452 ± 0.641	1.784 ± 0.363	Oblate
HJ 146	988	1.724 ± 0.252	0.990 ± 0.096	0.588 ± 0.052	3.3%	1.138 ± 0.868	2.942 ± 0.656	Prolate

[a]n: total amount of grains identified on the section images used to reconstruct the strain ellipsoid.

[b] $\sqrt{\widetilde{F}}$: incompatibility index between the elliptical parameters fed for the strain ellipsoid calculations and the resulting geometric shape. Indexes up to 10% are considered acceptable.

Table 8. Spatial orientation of the strain axes of the strain ellipsoids calculated for each sample.

Sample	X-axis		Y-axis		Z-axis	
	Trend	Plunge	Trend	Plunge	Trend	Plunge
HJ 2	40.7º ± 20.8º	14.5º ± 0.9º	133.8º ± 20.8º	11.8º ± 0.9º	261.3º ± 1.4º	71.1º ± 0.9º
HJ 4	58.5º ± 29.8º	31.5º ± 7.3º	151.6º ± 29.5º	4.6º ± 6.8º	247.6º ± 10.4º	57.8º ± 5.4º
HJ 95	109.7º ± 24.7º	0.9º ± 4.7º	19.6º ± 24.0º	3.0º ± 7.0º	221.7º ± 7.6º	87.4º ± 7.1º
HJ 103	103.2º ± 10.1º	27.0º ± 5.6º	344.8º ± 21.0º	42.8º ± 5.8º	215.1º ± 10.2º	35.0º + 5.8º
HJ 108	40.2º ± 24.8º	11.0º ± 10.6º	131.6º ± 24.7º	6.7º ± 6.4º	253.2º ± 11.1º	77.3º ± 6.0º
HJ 110	83.3º ± 42.4º	26.7º ± 12.9º	347.5º ± 42.0º	11.3º ± 5.8º	237.7º ± 14.3º	60.6º ± 2.5º
HJ 146	103.5º ± 7.4º	30.2º ± 3.0º	3.6º ± 7.7º	16.4º ± 2.7º	249.0º ± 3.8º	54.7º ± 2.5º

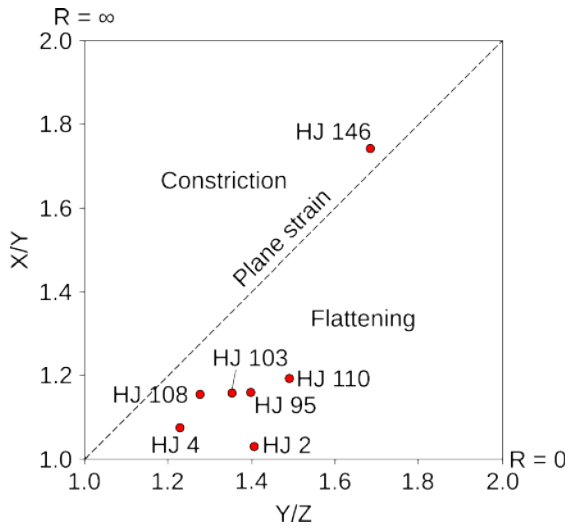

Figure 51. Flinn diagram for the samples from Serra do Cipó.

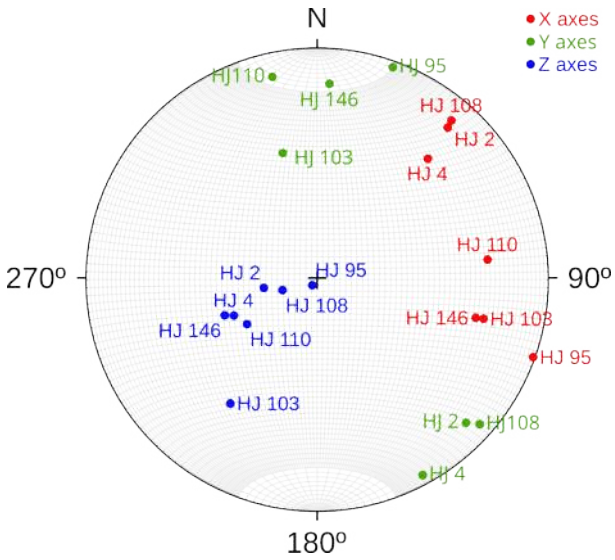

Figure 52. X, Y and Z axes attitudes of the strain ellipsoid calculated for each sample from Serra do Cipó.

6.4. Discussion

The results show X strain axes oriented along NE or SE trends and plunging to the eastern quadrant, providing theoretical foliations (flattening planes, or XY sections) dipping towards east (Figure 53), as well as sub-vertical Z strain axes. This configuration is coherent with the orientation, nature and kinematics of the syn-tectonic structures observed in the field (e.g. tectonic foliation and stretch lineations, as well as with an orogenic setting, thus holding conformity with previous local surveys (Magalhães, 1988; Oliveira, 1994) and the regional structural and tectonic framework and the evolution models described for the Southern Espinhaço Range.

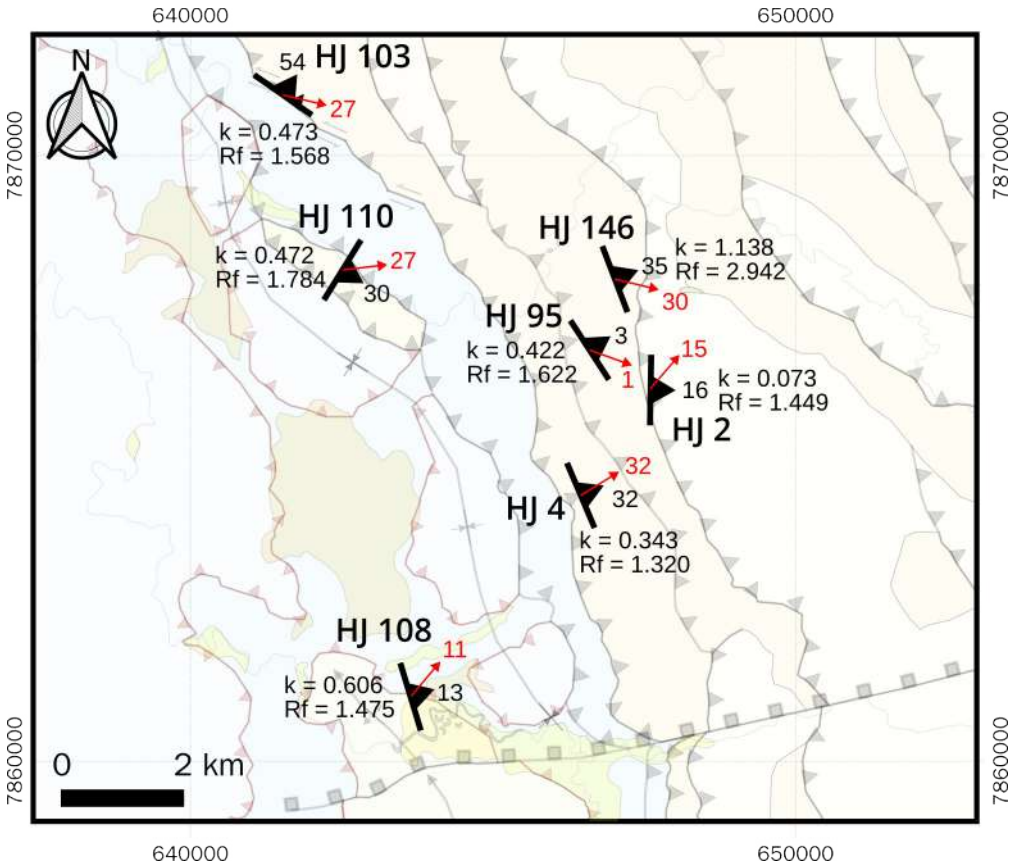

Figure 53. Spatial distribution of ellipsoid parameters of the samples from the study area: XY sections (theoretical foliations), X-axes (red lineations), Flinn's k and shape ratio (R_f).

The total strain (R_f) values range mostrly between 1.320 and 1.784, with a 2.942 obtained for a strongly mylonitic sample taken from a shear zone. A study of the same nature was performed in the Southren Espinhaço Range by Cordeiro (2008), but 40 km distant from the craton-orogen limit, with results between 1.5 and 2.0 on average, but with outliers surpassing 10.0 in shear zones. These extreme values are expected to be higher than ours, as the inner confines of the fold-and-thrust belt experienced more successive deformation increments than the marginal areas such as the region of Serra do Cipó.

The total strain calculated for sample HJ 108 (R_f = 1.475 ± 0.181) is not coherent with the interpretation of the São João da Chapada at its location as a rigid basement exposed in the Cipó River structural window. However, this site is very close to the contact with the overlying Sete Lagoas Formation, thus the measured strain probably reflects the strong deformation related to the basal detachment of the Bambuí Group.

The predominant oblate shapes of strain ellipsoids could be related either to a combination of simple and pure shear (Sanderson and Marchini, 1984; Fossen et al., 1994; Fossen and Tikoff, 1998),

or to a loss of volume by the sedimentary units along the flattening (XY) plane (parallel to the tectonic foliation) due to dehydration (Ramsay and Wood, 1973).

6.5. Conclusion

The southern extremes of the Southern Espinhaço Range were deformed during the Brasiliano Cycle. The thrust front was driven towards WSW, straight against the São Francisco Craton, resulting in a regional strain ellipsoid with sub-horizontal long and intermediate axes and a sub-vertical short axis. Though local factors have caused fluctuations of axes attitudes throughout the study area, the trend of reverse systems verging towards west is unwavering. Mostly, strain was accommodated by flattening, that is, with predominance of formation of planar (rather than linear) structures, with only one case of constriction (and formation of linear textures) having been observed.

7. DEFORMATION MECHANISMS IN SERRA DO CIPÓ – QUARTZ CRYSTALLOGRAPHIC AXES ELECTRON BACKSCATTER DIFFRACTION ANALYSIS

The fabric of a rock is controlled not only by the distribution of the various mineral phases present, but also by the crystallographic orientation of the minerals. A Lattice or Crystallographic Preferred Orientation (LPO or CPO), or texture, as it is usually called in Materials Science, is produced when deformation acts at the intracrystalline level, by mechanisms such as dislocation creep and mechanical twinning, resulting, for example, in minerals with undulose extinction (Passchier and Trouw, 2005). Many factors come into play together when an LPO pattern is imprinted on a rock (Mainprice and Nicolas, 1989; Schmid, 1994):

1. The active slip systems.
2. The ratio between the axes of the instantaneous strain ellipsoid.
3. The finite strain and flow pattern over the course of deformation.
4. The proportion of contribution of pure and simple shear (vorticity) in the system.
5. Grain bulging or grain boundary migration under dynamic recrystallization.
6. Growth (and its rate) of grains from solution.

Determining the individual contribution of each of these factors is challenging. Strain increments have the effect of increasing the number of crystalline defects, which makes the mineral phase less stable, while recovery and recrystallization mechanisms have the opposite effect, lowering the intracrystalline energy of the system (Cottrell, 1964; Trimby et al., 1998).

The Electron Backscatter Diffraction method analyzes the crystallographic orientation of the grains in a sample, helping to determine the mechanisms and even to estimate the conditions under which strain occurred. In this work, we applied this method to evaluate the orientation of the crystallographic [c] axes of quartz to further characterize the deformation of the study area.

In the region of Serra do Cipó, Taufner et al. (2021) used EBSD to analyze rocks of the Espinhaço Supergroup and the Sete Lagoas Formation. According to these authors, for samples from the Espinhaço Supergroup, a random texture of distribution of quartz crystallographic axes and few indicators of plastic behavior were observed, indicating that these rocks were deformed by dynamic recrystallization and pressure-dissolution and re-precipitation. In the limestones, coarse-grained calcite deformed by mechanical twinning and intracrystalline dislocations along the basal plane, while fine-grained calcite deformed by a combination of pressure-dissolution and diffusion, and dissolution slip.

7.1. The Electron Backscatter Diffraction (EBSD) method

The Electron Backscatter Diffraction method consists of placing a sample inside a vacuum chamber, emitting an electron beam at it and an having an electronic sensor detect the diffraction patterns of the emitted electrons caused by their interaction with the nuclei and electron clouds of atoms in the sample. Electrons deflect by the same angle form conical zones – the Kossel Cones – that are registered on the sensor as lines, or bands – the Kikuchi Bands. Each diffraction pattern produced by the sample-beam interaction forms a distinct pattern of Kikuchi Bands. The direction of crystallographic preferred orientation of the sample is marked by the intersections of the bands (Prior et al., 1999; Morales et al., 2007; Ahrenkiel, 2018; Padilha and Sandim, 2021).

7.2. But why quartz?

Quartz is one of the most abundant minerals on the continental crust, and the most abundant component of siliciclastic sedimentary and metasedimentary rocks. All samples analyzed in this thesis using the EBSD method are quartzitic. Hence, the response of quartz to the regional strain is representative for the whole rock, as demonstrated in past studies (e.g. Lister and Snoke, 1984; Schmid and Casey, 1986; Hirth and Tullis, 1992).

For quartz, the propagation of crystalline defects and slip systems are also intimately linked to the crystallographic plane and axes of the mineral, and vary according to the conditions of temperature, strain rate, differential stress and the presence of water in lattices or along grain boundaries (Passchier and Trouw, 2005). Table 9 summarizes the most characteristic mechanisms active in quartz according to the temperature condition.

Table 9. Deformation mechanisms of quartz by temperature range, after Tullis (1970), Barber and Wenk (1991), Hirth and Tullis (1992), Kruhl (1996), Dunlap et al. (1997), Okudaira et al. (1998), van Daalen et al. (1999), Stipp et al. (2002), and Passchier and Trouw (2005).

Temperature range	Mechanism
< 300 ºC	Brittle fracturing, pressure solution and transfer of material
300-400 ºC	Dislocation glide and creep, basal plane slip in the (c)<a> direction, bulging. Dauphiné twinning may also occur
400-500 ºC	Dislocation creep, prism {m}<a> slip, pressure solution, subgrain rotation, grain boundary migration
500-700 ºC	Grain boundary migration
> 700 ºC	Prism {m}<c> slip, basal <a> and prism <c> slip, rapid recovery

7.3. Practical and analytical procedures

We studied four quartzite samples from the region of Serra do Cipó, all belonging to the Espinhaço Supergroup (Figure 54, Table 10), to analyze the mechanisms active during deformation of the Foreland Domain (HJ 108), the Espinhaço Front (HJ 4 and HJ 103) and the Fold-and-Thrust

Domain (HJ 154). Samples HJ 4, HJ 108 and HJ 154 were cut as close as possible to the direction of the XZ section, that is, parallel to the stretch lineation and perpendicular to the tectonic foliation, while sample HJ 103 was cut closer to the YZ section, i.e., perpendicular to both these structures.

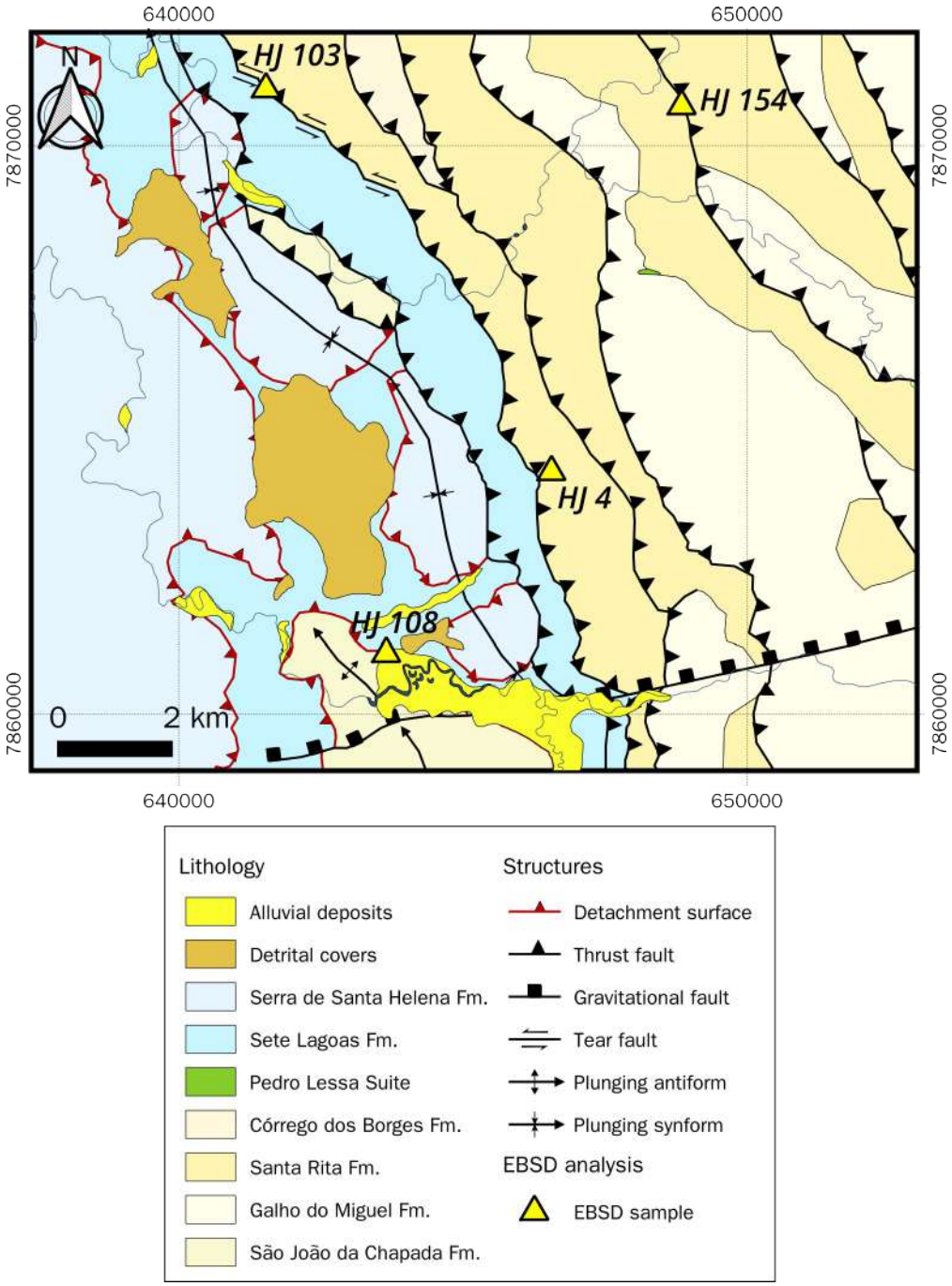

Figure 54. Location of the samples destinated for EBSD analysis in the study area.

Table 10. Location, orientation, classification, type and context of the samples used in EBSD analyses.

Sample	Coordinates (UTM 23K)		Section Orientation (Dip direction/Dip)	Lithological unit	Rock	Context
	E	N				
HJ 4	646417	7864461	181/81	Santa Rita Fm	Quartzite	Base of the Espinhaço Front
HJ 103	641535	7871000	224/37	Santa Rita Fm	Quartzite	Base of the Espinhaco Front
HJ 108	643654	7861060	224/62	São João da Chapada Fm	Quartzite	Structural window (rigid basement) – Foreland Domain
HJ 154	648857	7870700	214/88	Santa Rita Fm	Quartzite	Thrust fault – Fold-and-Thrust Domain

Thin sections 25 μm thick were elaborated from each sample, polished and finished with a 20 nm coloidal silica lapping for 3 hours. EBSD analyses were executed on a Thermo-Fei FEG450 scanning electron microscope coupled with a Velocity Plus TSL-EDAX EBSD camera, at the Center for Electron Microscopy of the Federal University of Paraná. Samples were positioned in the microscope at a 20º angle about the electron beam. The EBSD data were acquired in low vacuum conditions (60 Pa) using a 150 mA beam at a 20 nm distance and under a 20 kV acceleration voltage.

A coordinate system was attributed to the samples, aligning with the finite strain axes. The X axis, parallel to the stretching lineation, corresponds to the [100] direction, the Y axis, perpendicular to the stretching lineation and parallel to the tectonic foliation, corresponds to the [001] direction, and Z axis, normal to the foliation, corresponds to the [010] direction. Pole figures represent XZ sections for samples HJ 4, HJ 108 and HJ 154, and the YZ section for sample HJ 103.

To obtain inverse pole figures (IPFs), the weighted average of each point in the grain was utilized to avoid skewing towards larger grains. The resulting IPF plots depict the X direction of the sample ([100]) angled to the [c] axis, while the Z axis of the sample is parallel to the <a> axes.

7.4. Results

We separated granulometric fractions in our samples between small and large grains, establishing a diameter threshold of 100 μm. This is because this value seems to mark a limit in the distributions of the crystallographic axes of quartz, which may reflect different behaviours during deformation. Small grains are part of the rock matrix, while large grains are part of the clastic fraction.

7.4.1. HJ 4

Sample HJ 4 comes from the base of the Espinhaço Front. The quartzite of this sample has a well-preserved clastic texture (Figure 55.a), but presents tectonic foliation defined by mica and

oriented quartz. Small and large grains comprise similar proportions (approximately 58% and 42%, respectively) of the population of quartz grains in the sample (Figure 55.b).

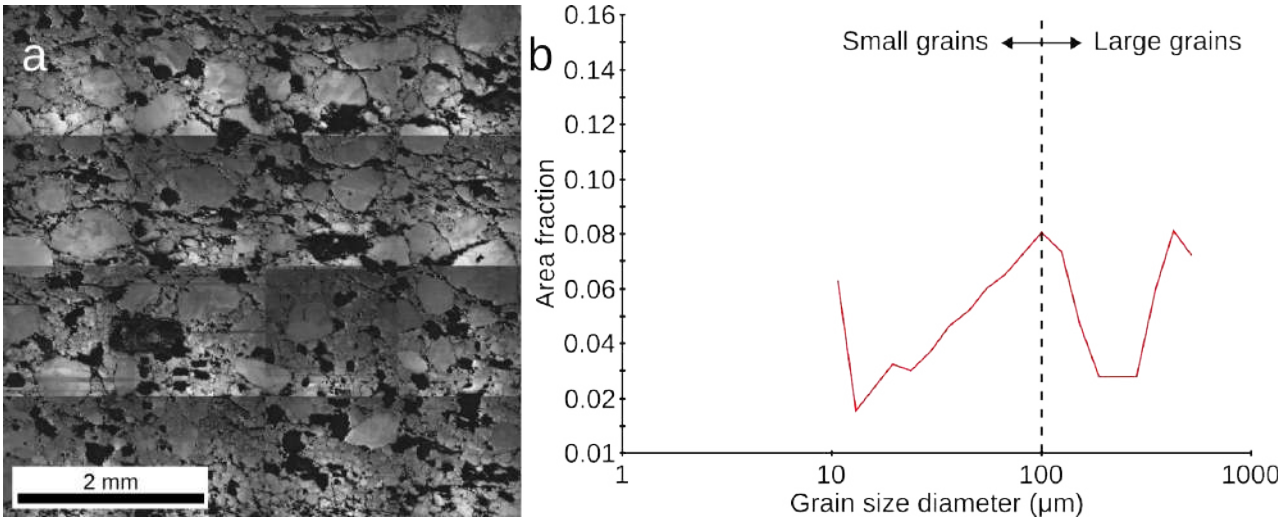

Figure 55. Clastic texture (a) and distribution of quartz grain diameters (b) of sample HJ 4.

The crystallographic orientations of the small grains fraction, corresponding to a population of grain size smaller than 100 μm, are distributed along the XY plane at an angle of approximately 20˚ to the X axis. The <a> axes ($[2\bar{1}\bar{1}0]$) are oriented along a single girdle that runs approximately in the N-S (Z) direction. This may suggest a [c] axis ([0001]) texture of prism [c] slip (Figure 56.a, c). However, such a texture is typically associated with high-temperature deformation, which is inconsistent with the mineral assemblage and microstructures in these rocks.

On the other hand, the texture (which refers to the crystallographic preferred orientation) of the larger grains (those larger than 100 μm) is quite different. The [c] axes are distributed along a broken girdle that is asymmetrically arranged in the NE-SW quadrant of the pole figure. This asymmetry suggests a reverse sense of shear consistent with the kinematic indicators observed in the field. On the other hand, the <a>-axes align obliquely to the X axis (Figure 56.b, c).

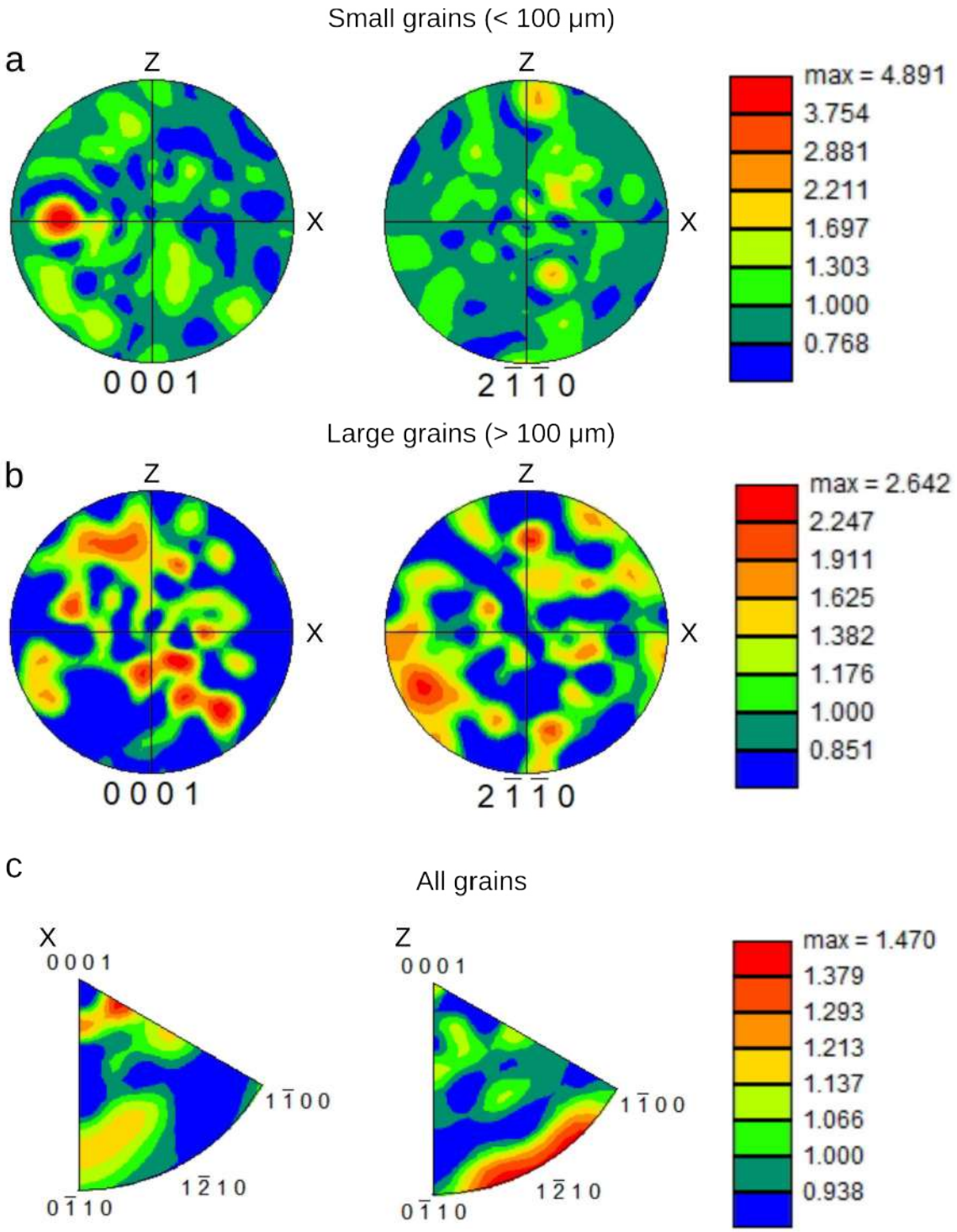

Figure 56. EBSD data from sample HJ 4: Pole figures – a) Small-grained fraction; b) Large-grained fraction – and inverse pole figure (c).

7.4.2. HJ 103

Sample HJ 103 was also collected at the Espinhaço Front. The microstructures show quartz contacts at times marked by bulging and more influence of shearing and recrystallization (Figure 57.a) than sample HJ 4, as well as more developed tectonic structures, i.e., foliation and lineation.

These structures are marked mainly by oriented or recrystallized quartz and mica in the matrix. Recrystallization structures are often asymmetric (σ-type), indicating reverse movement. Small grains represent approximately 74% of the quartz population in this sample, *versus* ~26% of large grains (Figure 57.b).

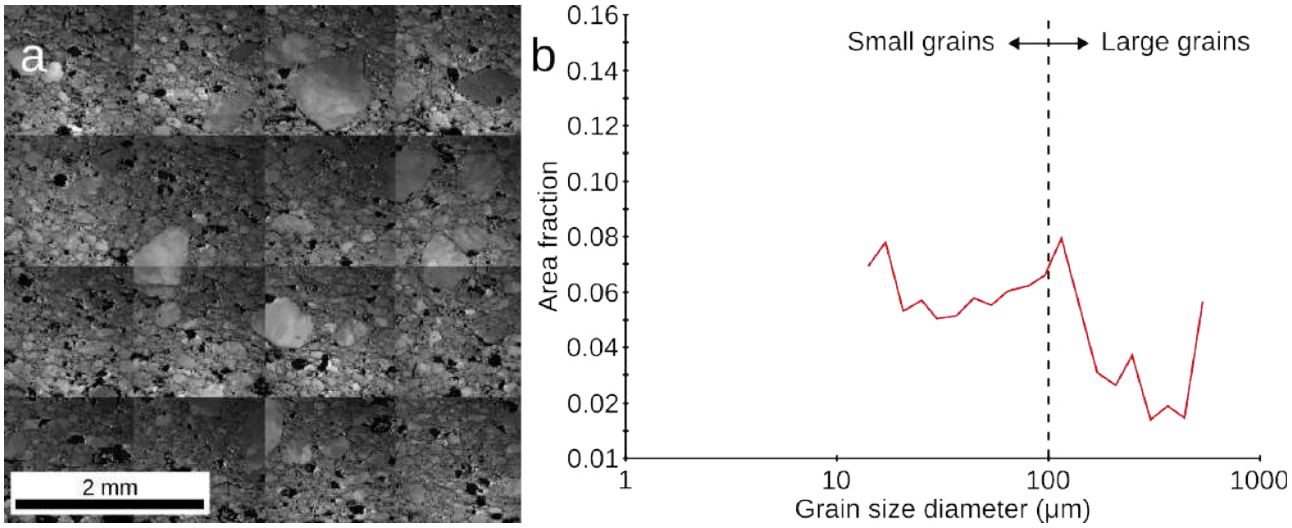

Figure 57. Recrystallized texture with porphyroclasts (a) and distribution of quartz grain diameters (b) of sample HJ 103.

There are two types of textures observed in sample HJ 103, for both the larger and the smaller fraction of the grains.

The first feature is marked by the distribution of the [c] axis in the rhomb position with secondary contribution of basal slip. This distribution is similar to that of a single asymmetric girdle that is slightly displaced from the N-S (Z) direction of the pole figure. This likely reflects a deviation from the XZ position during the cutting process. When the pole is near the foliation (the Z or [010] direction), [c] axis distribution becomes wider around Z, opening up at a large angle. The Z direction does not bisect this distribution, resulting in an asymmetry that indicates a dextral sense of shear (Figure 58.a, b).

A second texture emerges due to the alignment of [c] axes predominantly along the X axis of the sample, characteristic of oriented growth by precipitation after pressure dissolution. Additionally, there is a wide distribution of angles around the X direction. The <a> crystallographic axis for this texture is distributed around the Z direction of the sample (Figure 58.a, b).

The inverse pole figure illustrates the Z axis of the sample, exhibiting a broad distribution between the [c] and <a> axes. Similarly, the X direction displays an even wider spread, with the peak lying between the [c] and <a> axes (Figure 58.c).

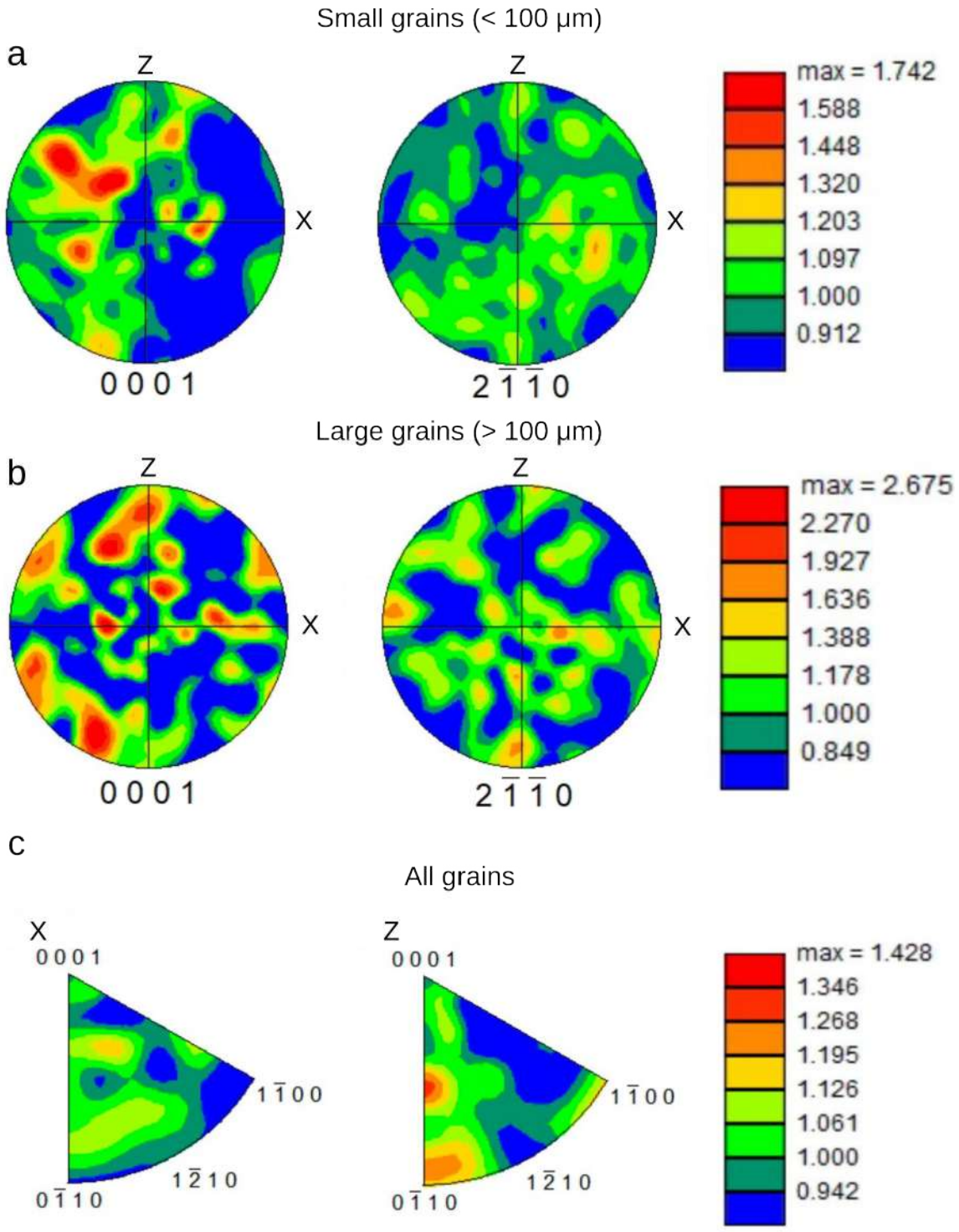

Figure 58. EBSD data from sample HJ 103: Pole figures – a) Small-grained fraction; b) Large-grained fraction – and inverse pole figure (c).

7.4.3. HJ 108

Sample HJ 108 originated from the Cipó River Window, close to the top contact, marked by the detachment that separates the São João da Chapada (base) and Sete Lagoas (top) formations (top). This is a sample of metasandstone with poorly selected and sub-angular to sub-rounded grains.

Tectonic foliation and lineation are poorly imprinted onto the fabric of the rock, which exhibits a well-preserved clastic texture (Figure 59.a). The structure of the rock is primarily composed of large grains (~69%), which form the framework, and smaller grains (~31%) occupy the gaps (Figure 59.b).

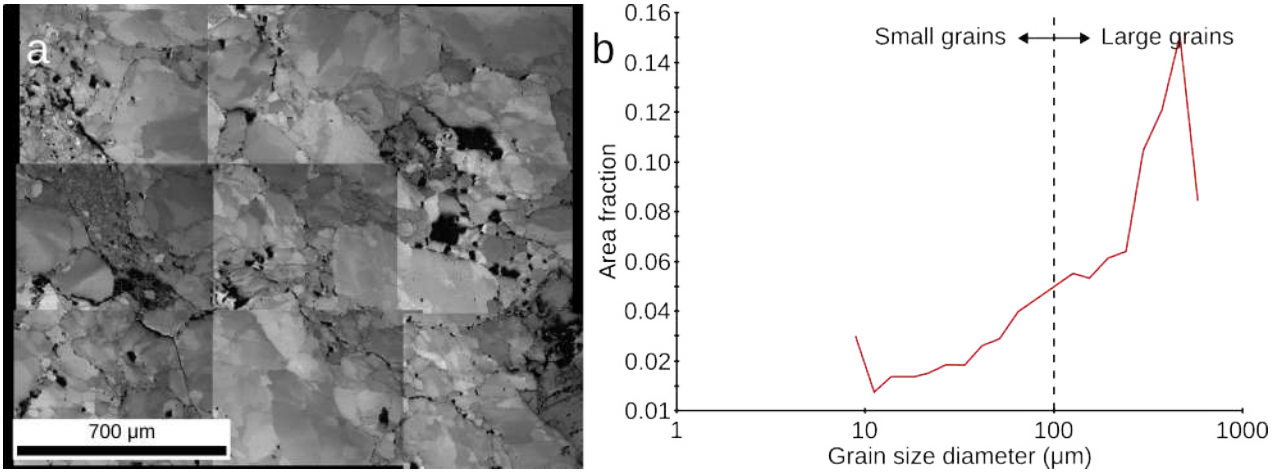

Figure 59. Clastic texture (a) and distribution of quartz grain diameters (b) of sample HJ 108.

Texture similarity exists across the two different granulometric classes. The [c] axes exhibit two distinct distributions in the pole figure (Figure 60.a, c): one distribution shows a concentration of [c] axes inclined towards the Z axis, spreading at an open angle, and another trend involves [c] axes aligning with the foliation plane (XY).

In the first case, [c] axis concentration corresponds to the alignment of the <a> axis, indicating activation of the rhomb <a> slip system. Conversely, [c] axes oriented towards the X direction suggest low-temperature conditions favoring oriented growth of quartz grains due to precipitation from dissolution at highly compressed sites. In this scenario, the <a> axis tends to be parallel or aligned with the Z axis.

The texture observed in the inverse pole figures supports these findings, showing both large and small grains at angles to the Z and X directions, along with their <a> axes alignments (Figure 60.b, d).

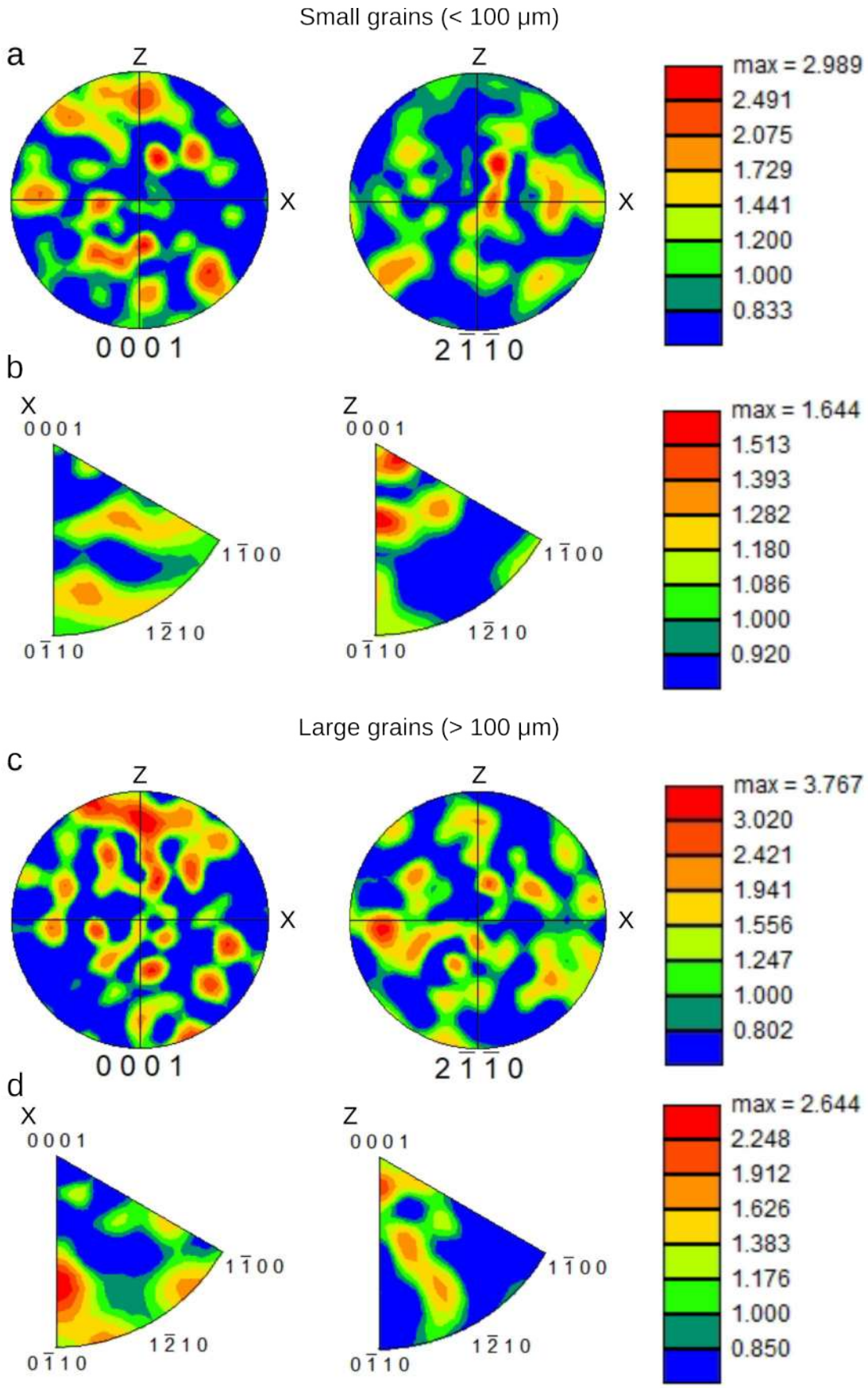

Figure 60. EBSD data from sample HJ 108: Small-grained fraction: a) Pole figure; b) Inverse pole figure; Large-grained fraction: c) Pole figure; d) Inverse pole figure.

7.4.4. HJ 154

Sample HJ 154 was collected in a reverse shear zone affecting the Santa Rita Formation, in the heights of the Cipó Range. The rock is a foliated quartzite with fine to medium-sized porphyroclasts of quartz and K-feldspar scattered amidst a fine matrix composed by recrystallized quartz and mica (Figure 61.a). The asymmetry of fabric elements denotes top movement towards west. Almost the entire population of quartz in the rock (over 99%) corresponds to the small-grained fraction of the matrix (Figure 61.b)

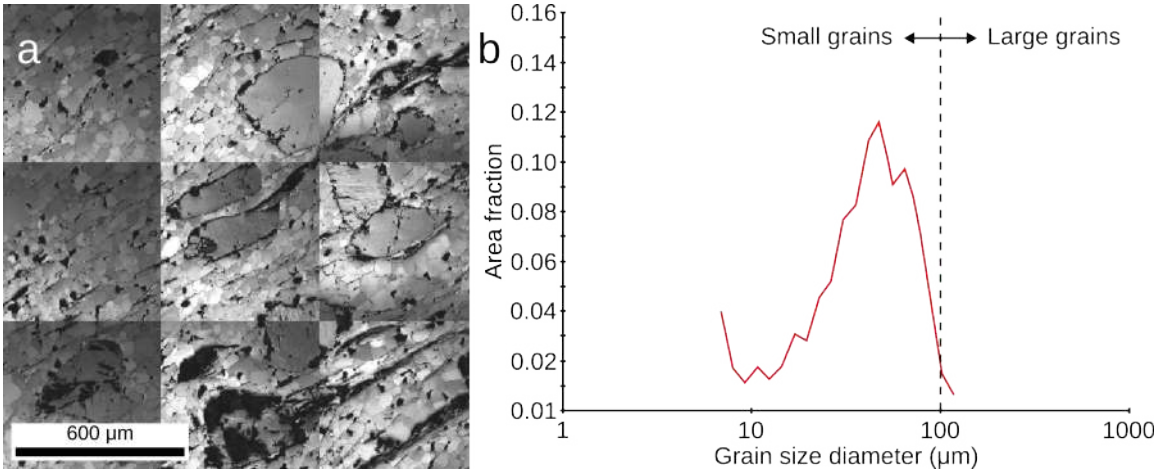

Figure 61. Mylonitic texture (a) and distribution of quartz grain diameters (b) of sample HJ 154.

Compared to the other samples, the grain size in sample HJ 154 is below the 100 µm threshold established to separate the small and large grain sizes.

Like the other samples, this sample HJ 154 has two types of textures (Figure 62). The [c] axes are in a position in the pole figures indicating a rhomb plane acting as a slip plane during deformation; the direction of slip is along <a>, as can be seen by the alignment of this <a> axis in the X direction.

The other texture arises from the orientation of the [c] axes close to the X direction and the <a> axes close to the Z axis. This suggests grain growth is controlled by the deformation, where quartz grains grow fast in the X-direction, that is, parallel to the stretch direction.

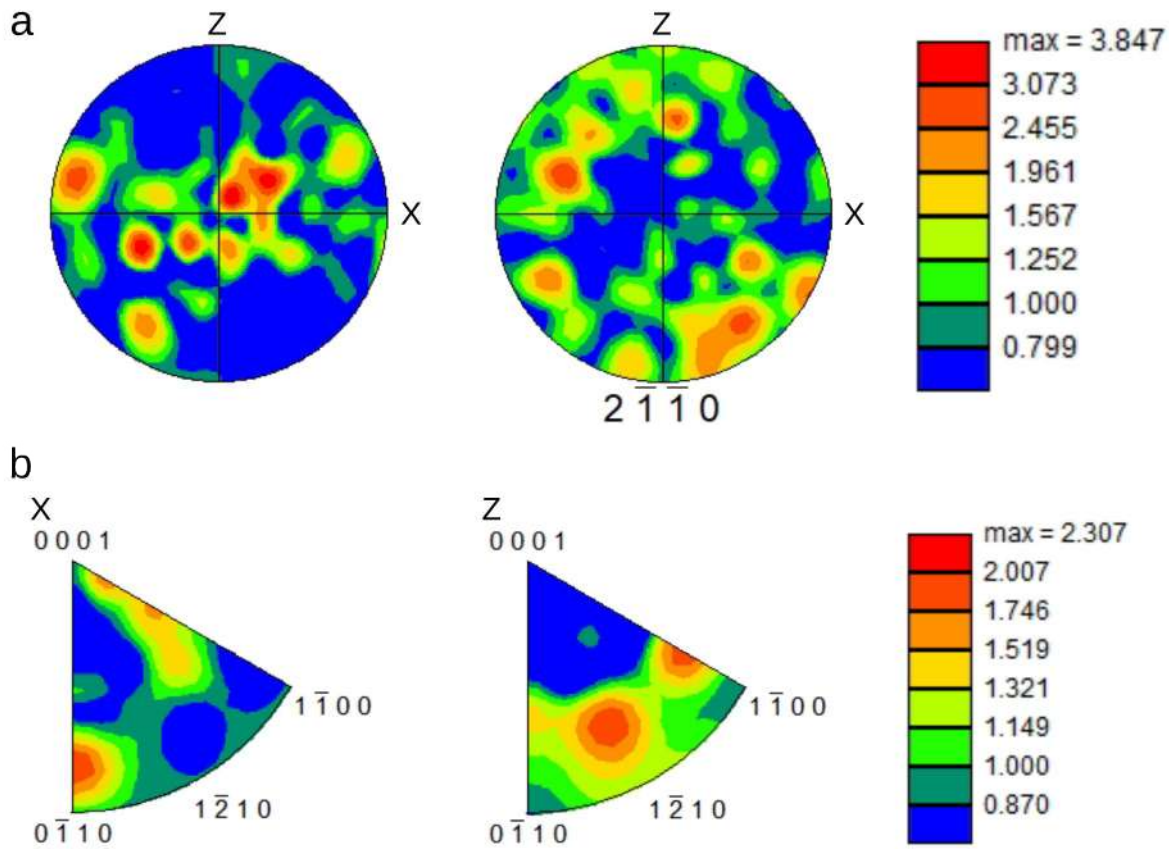

Figure 62. EBSD data from sample HJ 154: a) Pole figure; b) Inverse pole figure.

7.5. Discussion

The [c] axes of quartz are distributed at an angle between the Y and Z directions. This is usually interpreted as an activation of rhomb planes by dislocation glide during the deformation. The alignment of <a> axes parallel to the X axis of the sample, i.e., parallel to the mineral stretch lineation, is compatible with a slip system rhomb <a>. In all samples, this type of texture is present.

Conversely, a texture where [c] axes lie toward the X direction can be interpreted in two ways. One is where the temperature is high and activation of slip along the c-axis becomes possible. However, this is unlikely for the tectonic setting of Serra do Cipó. The second and most likely scenario is where quartz grains grow oriented along a fast-growth direction, which results in [c] axes parallel to X and the stretch lineation.

Therefore, we interpret that intracrystalline deformation of quartz in the study area was partitioned into two mechanisms that acted concomitantly: crystal-plastic dislocation glide with activation of rhomb <a> slip and limited climb, and controlled fast growth parallel to the stretching direction as a result of pressure-dissolution and re-precipitation (Table 11).

Table 11. Main intracrystalline deformation mechanisms in the samples from Serra do Cipó.

Sample	Tectonic Domain	Granulometric fraction	Main deformation mechanism
HJ 4	Fold-and-Thrust	< 100 μm	Pressure-dissolution and re-precipitation
		> 100 μm	Dislocation glide (rhombohedron)
HJ 103	Fold-and-Thrust	< 100 μm	Pressure-dissolution and re-precipitation
		> 100 μm	Dislocation glide (rhombohedron)
HJ 108	Foreland	< 100 μm	Dislocation glide (rhombohedron)
		> 100 μm	Dislocation glide (rhombohedron)
HJ 154	Fold-and-Thrust	-	Dynamic recrystallization/Pressure-dissolution and re-precipitation

By combining the crystallographic textures and deformation mechanisms – including weak basal slip activation – with the microstructures and mineral assemblages present in our samples, we estimate a temperature for deformation in a 300-450 ºC range, most likely within the 350-400 ºC interval.

In a previous study, Taufner et al. (2021) identified dynamic recrystallization and pressure-dissolution creep as the main intracrystalline deformation mechanism in a sample of quartzite from the Fold-and-Thrust Domain of the region of Serra do Cipó. The sample analyzed by these authors was collected from an outcrop where shear bands and mylonitic texture were well developed and a fine-grained matrix predominated, and showed quartz [c] axes strongly oriented in a great circle close to the direction of the X direction. This is akin to the behavior observed in sample HJ 154, which also comes from a strongly sheared outcrop, though the patterns obtained by Taufner et al. (2021) are not as strong as those observed in our study (Figure 63). This may indicate cooler conditions during deformation in comparison, but it is important to stress that the setting of samples HJ 4, HJ 103 and HJ 154 were close to major thrusts.

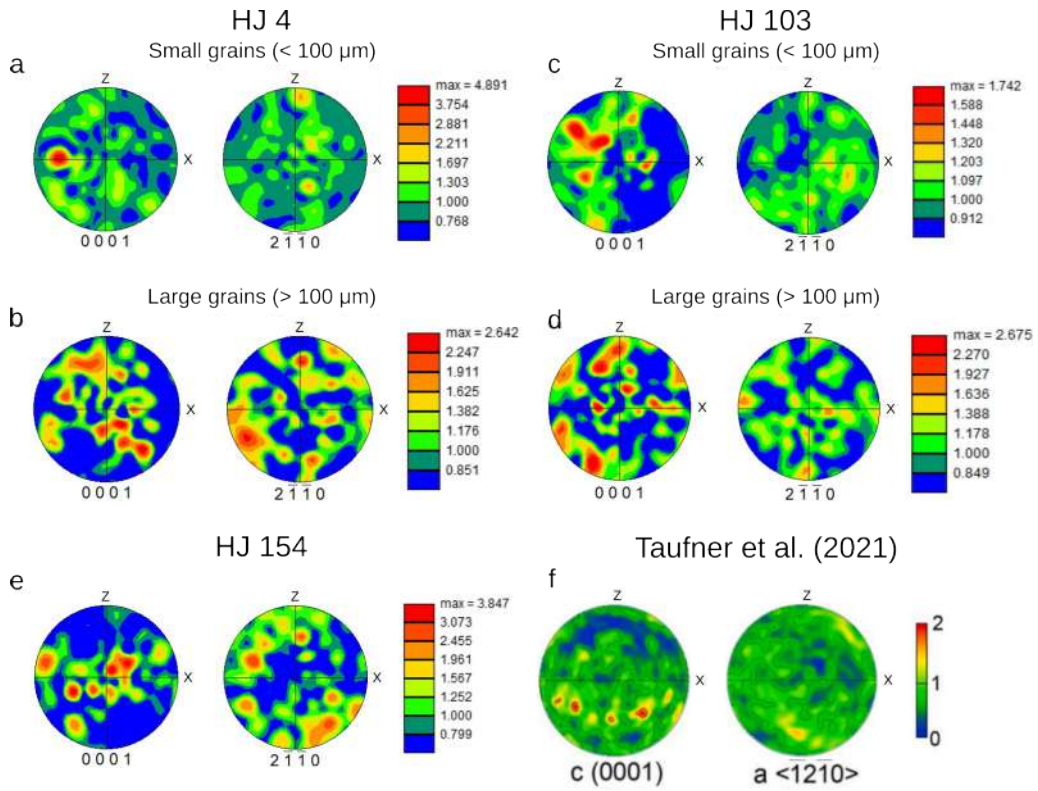

Figure 63. EBSD patterns obtained in quartzites from the Fold-and-Thrust Domain of the region of Serra do Cipó: a-e) This study; f) Taufner et al. (2021)

In the Foreland Domain, Taufner et al. (2021) studied the intracrystalline behavior of calcite from the Sete Lagoas Formation. In the limestone samples analyzed, a partition of deformation was observed. The coarse-grained calcite fraction accommodated strain through mechanical twinning and intracrystalline dislocations along the basal plane. In contrast, the fine grains of calcite were deformed by a combination of pressure-dissolution and diffusion or dissolution-slip. These regimes point to lower temperatures in the Foreland, which is coherent with the crystallographic texture of sample HJ 108 the only sample in this study exhibiting basal slip activation.

7.6. Conclusion

Quartzites from the craton-orogen transition in the region of Serra do Cipó register the deformation from the Araçuaí Orogeny, characterized by the presence of major west-verging structures. The abundance of quartz in the local rocks means that the behavior of this mineral during deformation is representative of the entire system. At intracrystalline scale, strain was accommodated by two main mechanisms: dislocation glide and pressure-dissolution and re-precipitation. Minor occurrences of bulging are also present. This possibly sets the temperature conditions between 350 and 400 ºC.

A partition of the preferred deformation mechanism seems to be stronger at a granulometric threshold of 100 μm. Both mechanisms are active regardless of the fraction, but dislocation glide predominates in the larger fraction, and pressure-dissolution and re-precipitation dominates in finer quartz grains.

In the tectonic compartment defined by the fold-and-thrust belt of the orogen, dislocation glide occurs most notably along the rhombohedral planes. While this is also true for the rocks from the foreland, in this sector dislocations on the basal system are also significant, indicating cooler conditions in comparison with the orogenic domain.

8. A P-T ASSESSMENT OF THE EMPLACEMENT OF CONCORDANT QUARTZ VEINS IN SERRA DO CIPÓ – A STUDY OF FLUID INCLUSIONS

As a mineral is formed, it may retain crystallographic defects that enable the entrapment of fluid (either liquid or gas) or solid phases in its structure. These inclusions can occupy significant volumes in a rock, often comparable to those of accessory minerals, highlighting the importance of their study for understanding the formation of the system as a whole (van den Kerkhof and Hein, 2001).

The analysis of fluid inclusions allows the determination of its composition, density and salinity. These attributes, in turn, can be used to calculate the physicochemical conditions (pressure and temperature) that prevailed during the entrapment of the inclusions within the mineral structure (Roedder, 1984).

Inclusions are divided into three types according to a temporal-genetic classification, which refers to the relative time of their entrapment in the mineral structure. Inclusions that were trapped during mineral growth are either primary, which occupy spaces in the mineral structure, or pseudo-secondary, which fill spaces generated by fractures. Secondary inclusions, conversely, are formed after the mineral growth, indicating different stages of geological processes (Roedder, 1984; Goldstein et al., 2003).

Microthermometry, a widely used technique involving cooling and heating of a sample to observe phase changes in the inclusions, marks the eutectic point of the solution (associated with its composition), the final-ice melting point (associated with its salinity and density) and the homogenization temperature (associated with the P-T conditions of its formation). Another method of fluid inclusion analysis is Raman spectroscopy, a technique that involves capturing photons from a restricted region of a sample illuminated by laser or X-rays, allowing the determination of the composition of a solution contained in a fluid inclusion (Randive et al., 2014). In this study, we analyzed fluid inclusions from the region of Serra do Cipó using microthermometry.

8.1. Practical and Analytical Methods

Six representative quartz vein samples were selected for fluid inclusion analysis: three from the Foreland Domain and three from the Fold-and-Thrust Domain (Figure 64, Table 12). All sampled veins are concordant with the tectonic foliation of the host rocks. Fluid inclusion petrography was carried out on 100 μm thick double-polished sections for recognition and mapping of the target inclusions. Microthermometric data (eutectic, final ice-melting, homogenization temperatures) were acquired using a Linkam THMS600 heating-cooling stage with a model T94 controller attached to an Olympus BX51 optical microscope at the Fluid Inclusion Laboratory of the Institute of Geoscience of

the University of São Paulo (LIF-IGc-USP). The stage was calibrated with the Merck MSP standard for high temperatures and Merck Signotherm for low temperatures.

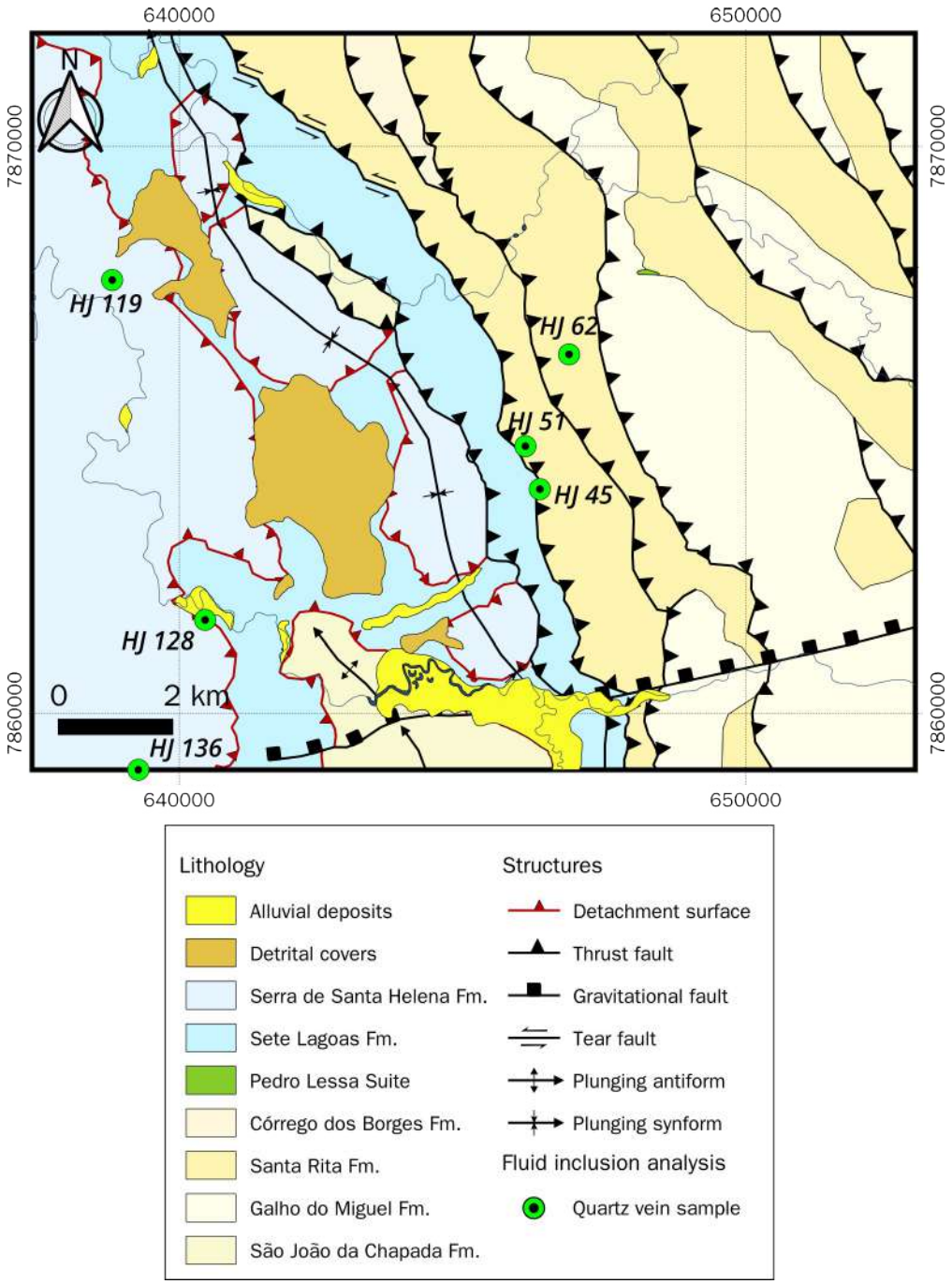

Figure 64. Location of the quartz samples destinated for fluid inclusion analysis in the study area.

Table 12. Location of the samples of quartz veins used in fluid inclusion analyses.

Sample	Location (UTM 23K)		Host rock
	E	N	
HJ 45	646369	7863947	Quartzite
HJ 51	646114	7864705	Quartzite
HJ 62	646885	7866327	Quartzite
HJ 119	638816	7867640	Siltstone
HJ 128	640457	7861637	Siltstone
HJ 136	639278	7857374	Siltstone

Salinities and densities were calculated with the package FLUIDS (Bakker, 2003), based on the models by Pitzer (1991) and (Archer, 1992), and the equation of state of Zhang and Frantz (1987). The isochoric curves were calculated using the package ISOC (Bakker, 2003), using the equation of state by Bodnar and Vityk (1994) and (Knight and Bodnar, 1989). We plotted estimations of lithostatic and hydrostatic pressure gradients for reference on the isochore charts, calculated using hypothetical geothermal gradients of 30-40 ºC/km, average rock density of 2.7 g/cm³ and water density of 1.0 g/cm³.

We deployed a series of statistical analyses to evaluate the microthermometric data and investigate potential differentiation of inclusion groups. The first group of methods consisted of Hartigan's Dip Test (Hartigan and Hartigan, 1985), which is a hypothesis test, as well as a non-parametric evaluation of uni and multimodality of modes by kernel smoothing and a non-parametric evaluation of population mixture. It was applied to the eutectic temperatures of each sample to verify whether two populations of inclusions were present. The second set of statistical analysis was used on the salinity values calculated for all the samples, to determine whether the inclusions from the Foreland and Fold-and-Thrust Domains belonged to the same original population (i.e., from the same original solution). For this, we used the non-parametric Shapiro-Wilk (Shapiro and Wilk, 1965) and Kruskal-Wallis (Kruskal and Wallis, 1952) normality tests. All statistical methods were executed on R (R Core Team, 2023). The package used for the Hartigan's Dip Test was created by Maechler (2023). For the uni-multimodal evaluation, we used the package Laplace's Demon (Statisticat, 2021). The charts for the evaluation of mixtures were created using the package Mixtools (Benaglia et al., 2009), using a bandwidth of 1.3 for all samples. The mixture analysis for sample HJ 136 was inconclusive, thus we created a second chart with a bandwidth of 1 to reduce bias in our estimation.

8.2. Results

8.2.1. General Description of Fluid Inclusions

All fluid inclusions are primary and biphasic, composed of an aqueous phase and a vapour phases. The volume of the vapour phases in the inclusions occupies mostly 1 to 5% of the total. The

dimensions of the inclusions range up to 50 µm, with few exceptions reaching 70 to 100 µm. The smallest inclusions are round, oblong, oval and triangular (Figure 65.a), while the larger ones (> 20 µm) also exhibit irregular shapes (Figure 65.b). Two modes of occurrence of inclusions were observed: random distribution and intragranular trails (Figure 65. c).

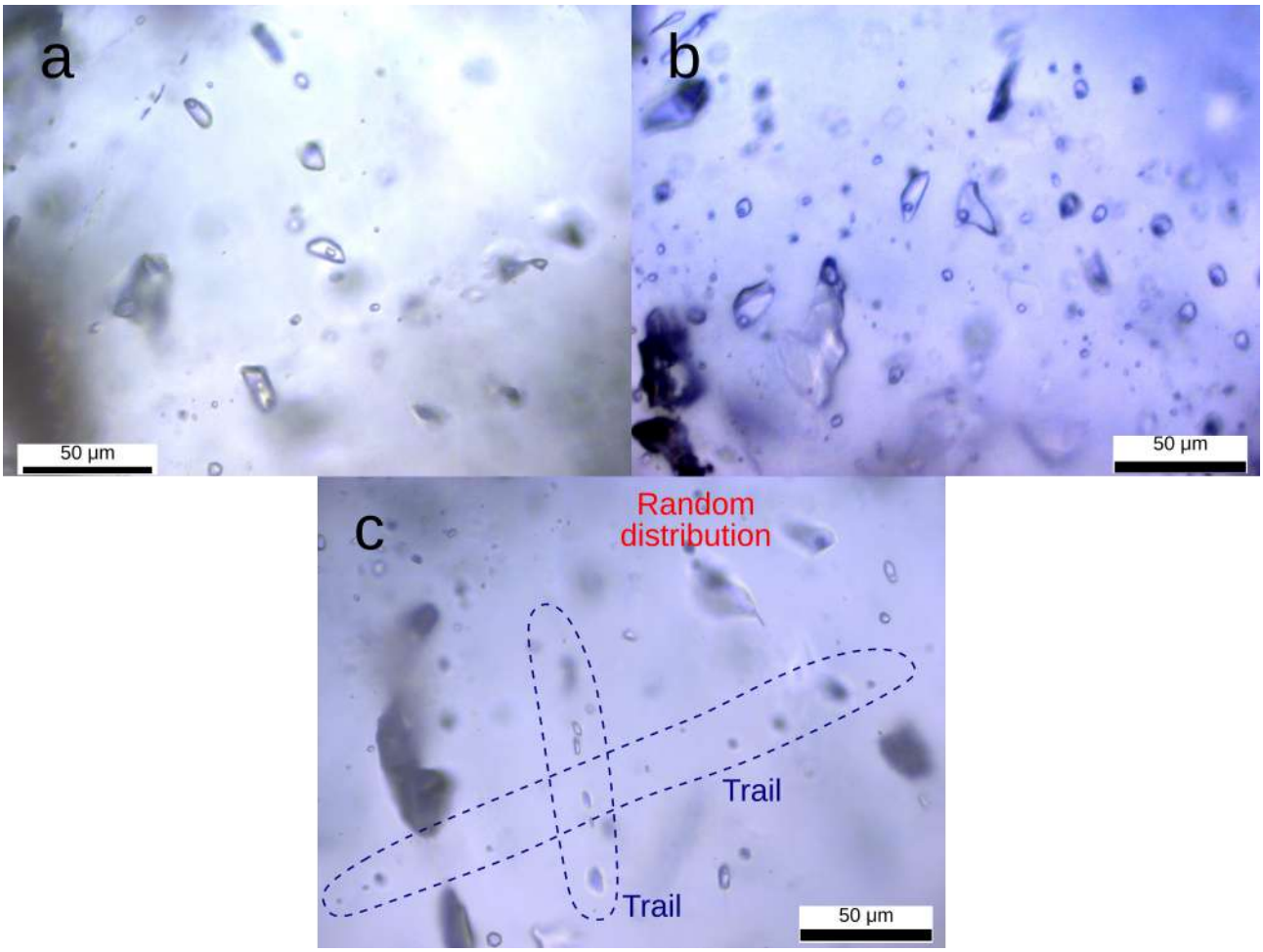

Figure 65. Smaller (< 20 µm) fluid inclusions have mostly regular shapes, while larger (> 20 µm) inclusions may develop irregular shapes – a) Photomicrography of sample HJ 62; b) photomicrography of sample HJ 127. Inclusions may be distributed randomly or in trails – c) Photomicrography of sample HJ 45.

8.2.2. Microthermometry

Results of the microthermometric analysis are summarized in Table 13, including values of density (ρ), volume of the vapour phase (V_{vap}), eutectic (T_{eut}), final-ice melt (T_{fim}) and homogenization (T_{hom}) temperatures, and salinity, as well as the salt systems estimated to be present in the inclusions. Inclusions are divided into two groups corresponding to the tectonic compartmentalization of the study area – the Fold-and-Thrust and Foreland domains.

Table 13. Result summary of the microthermometric analysis of the samples of this study.

Group	Samples	n	ρ (g/mL)	V_{vap} (%)	T_{eut} (ºC)	T_{fim} (ºC)	T_{hom} (ºC)	Salinity (Na Cl eq. wt%)	Salt systems
Fold-and-Thrust	HJ 45, HJ 51, HJ 62	346	0.833 to 1.003	1 to 22	-48.1 to -21.5	-7.8 to -0.4	95.7 to 224.6	0.233 to 11.648	H_2O-NaCl-$CaCl_2$ H_2O-NaCl-$FeCl_2$ H_2O-NaCl-$MgCl_2$
Foreland	HJ 119, HJ 128, HJ 136	304	0.913 to 0.984	1 to 30	-44.6 to -23.1	-6.0 to -0.1	100.1 to 196.4	0.233 to 8.812	

8.2.2.1. Eutectic temperatures

Eutectic temperatures range between -48.1 and -21.5 ºC (Table 13, Figure 66), indicating that the fluid inclusions from the region of Serra do Cipó are formed by fluids of the H_2O-NaCl-$CaCl_2$, H_2O-NaCl-$FeCl_2$ and H_2O-NaCl-$MgCl_2$ saline systems.

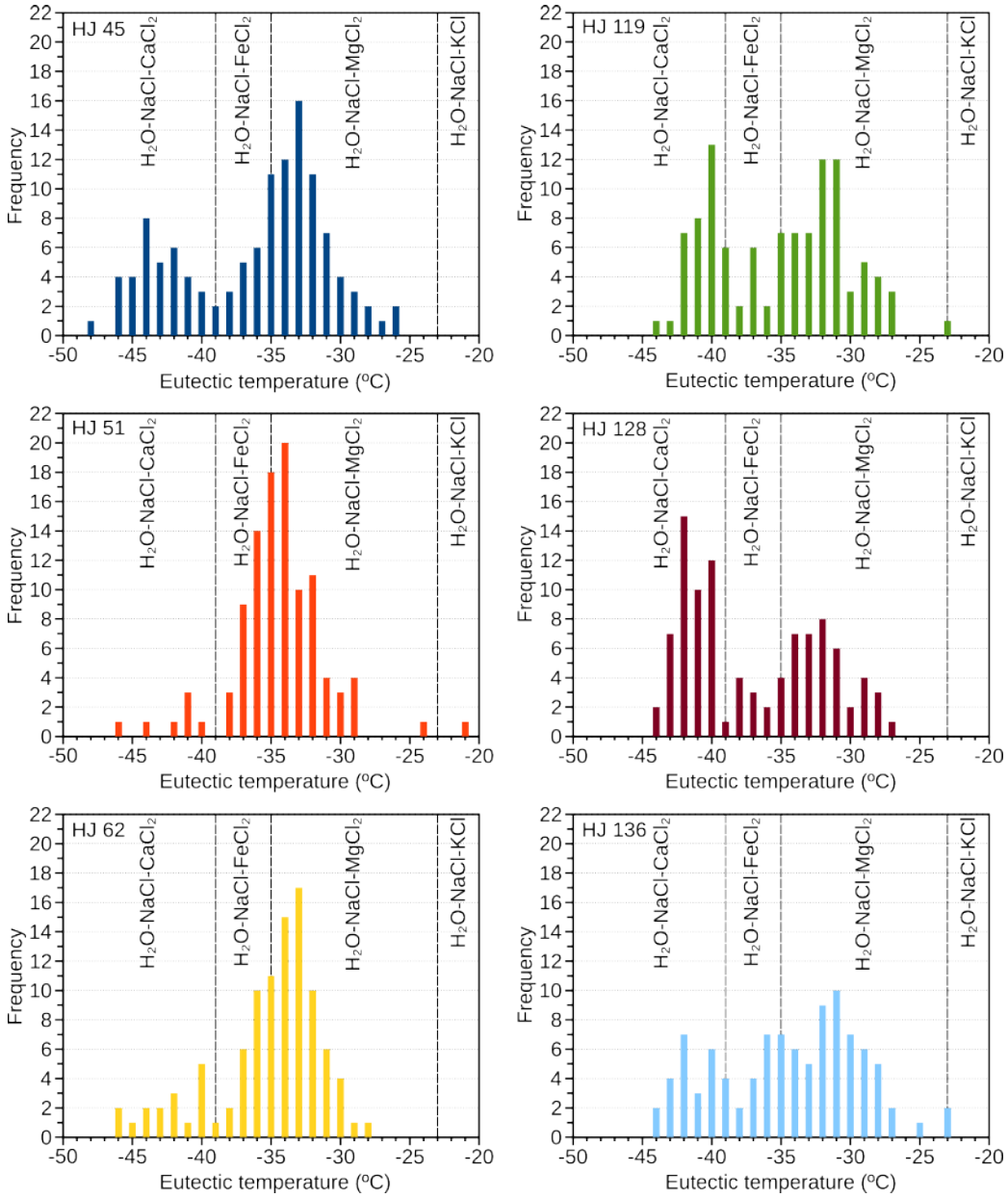

Figure 66. Distribution of eutectic temperatures in the samples of this study.

8.2.2.2. Final-ice melting temperatures and salinity

Final-ice melting temperatures range between -7.8 and -0.1 ºC (Table 13, Figure 67), corresponding to salinity values between 0.233 and 11.648 NaCl eq. wt% and densities between 0.833 and 1.003 g/mL. The distributions of final-ice melting temperatures and salinity values are bimodal. Even though both apparent groups have members in ranges more characteristic of the other, the populations as a whole are distinguishable: inclusions from the Fold-and-Thrust Compartment show lower final-ice melting points (and are thus denser and more saline), concentrating between approximately -4.04 and -5.77 ºC, while the ones from the Foreland area concentrate between -1.06 and -3.93 ºC.

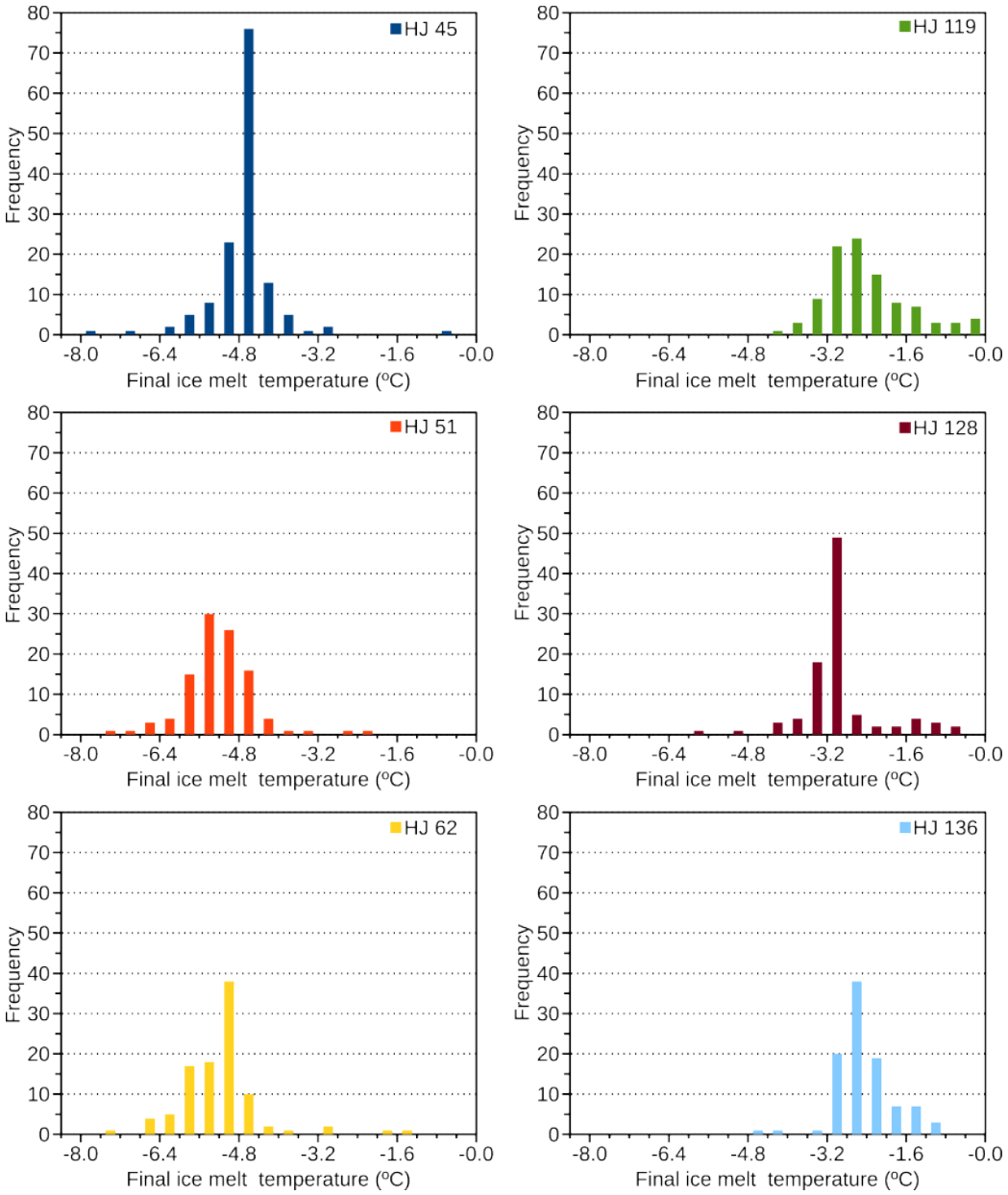

Figure 67. Distribution of final-ice melting temperatures in the samples of this study.

8.2.2.3. Homogenization temperatures

The distribution of homogenization temperatures is similar for inclusions of all samples. Results range between 95.7 and 224.6 ºC, concentrating mostly between 121.50 and 156.88 ºC (Figure 68).

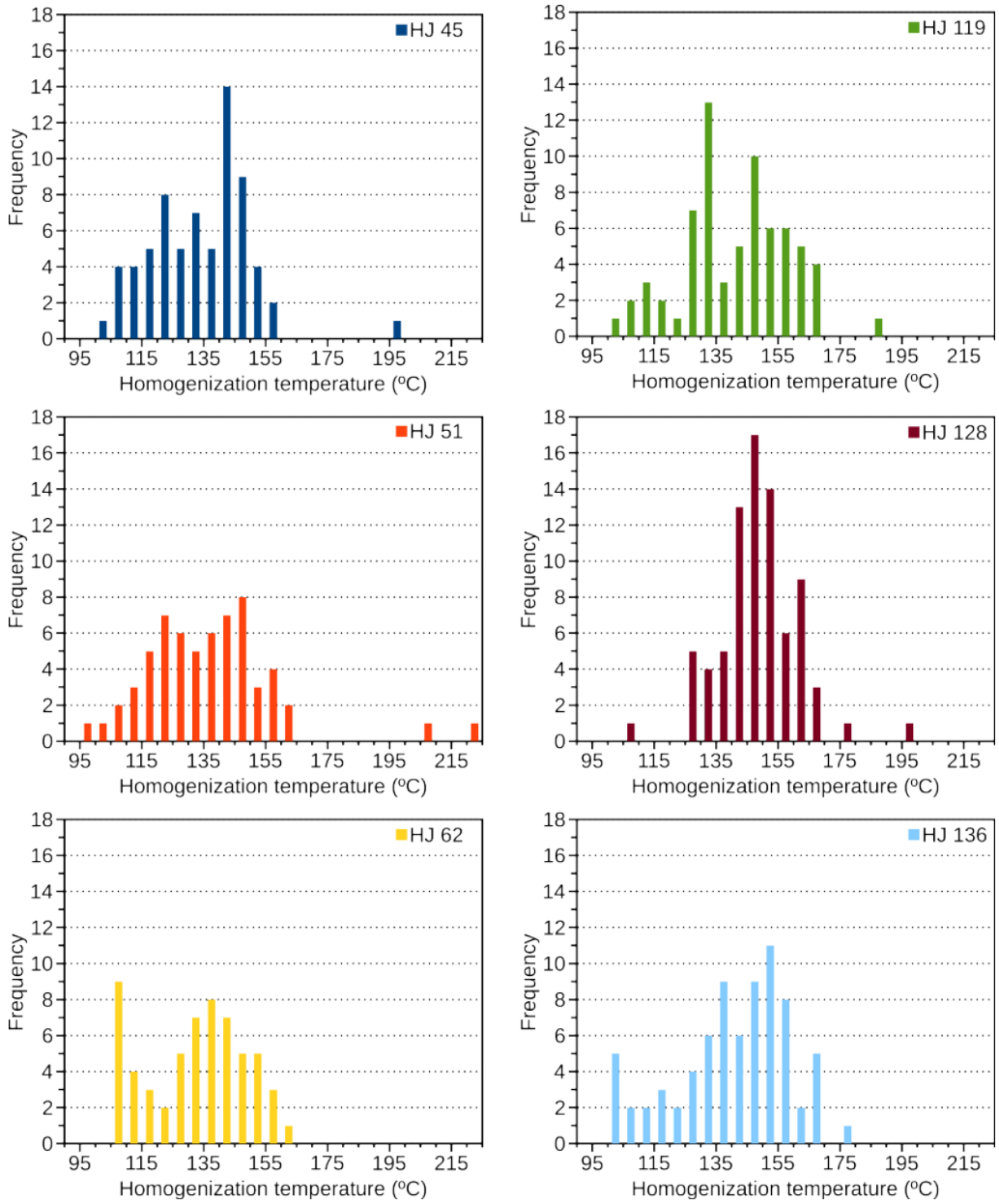

Figure 68. Distribution of homogenization temperatures in the samples of this study.

8.3. Discussion

8.3.1. Eutectic Temperatures

The presence of two apparent peaks in multiple eutectic temperature histograms (Figure 66) prompted us to run Hartigan's Dip Test and two non-parametric analyses (kernel modality and mixture evaluation) to verify statistically whether the distribution of eutectic temperatures in our

samples is unimodal (i.e., most likely a single population of fluid inclusions is present) or bimodal (i.e. most likely two different populations of fluid inclusions are present). For the Hartigan's Dip Test, the null hypothesis (H_0) is that the samples are unimodal. The results (Table 14) are ambiguous for samples HJ 45, HJ 62 and HJ 136. Particularly for sample HJ 136, the mixture evaluation was inconclusive. Sample HJ 51 is most likely unimodal, whereas samples HJ 119 and HJ 128 are most likely bimodal. The proportions of mixtures are given in Figure 69.

Table 14. Results of statistical analyses of the distributions of eutectic temperatures in the studied samples.

Sample	Hartigan's Dip Test (H_0: distribution is unimodal)		Mode kernel smoothing	Mixture evaluation		
				Result	Expected mean T_{eut}(ºC)	
	p-value	Result			If unimodal	If bimodal
HJ 45	0.349	H_0 is not rejected	Bimodal	Bimodal	-	-43.33; -33.70
HJ 51	0.962	H_0 is not rejected	Unimodal	Unimodal	-34.85	-
HJ 62	0.917	H_0 is not rejected	Bimodal	Bimodal	-	-42.55; -34.29
HJ 119	0.018	H_0 is rejected	Bimodal	Bimodal	-	-39.90; -32.30
HJ 128	0.036	H_0 is rejected	Bimodal	Bimodal	-	-41.14; -32.56
HJ 136	0.790	H_0 is not rejected	Bimodal	Uni or bimodal	-35.01	-38.89; -32.85

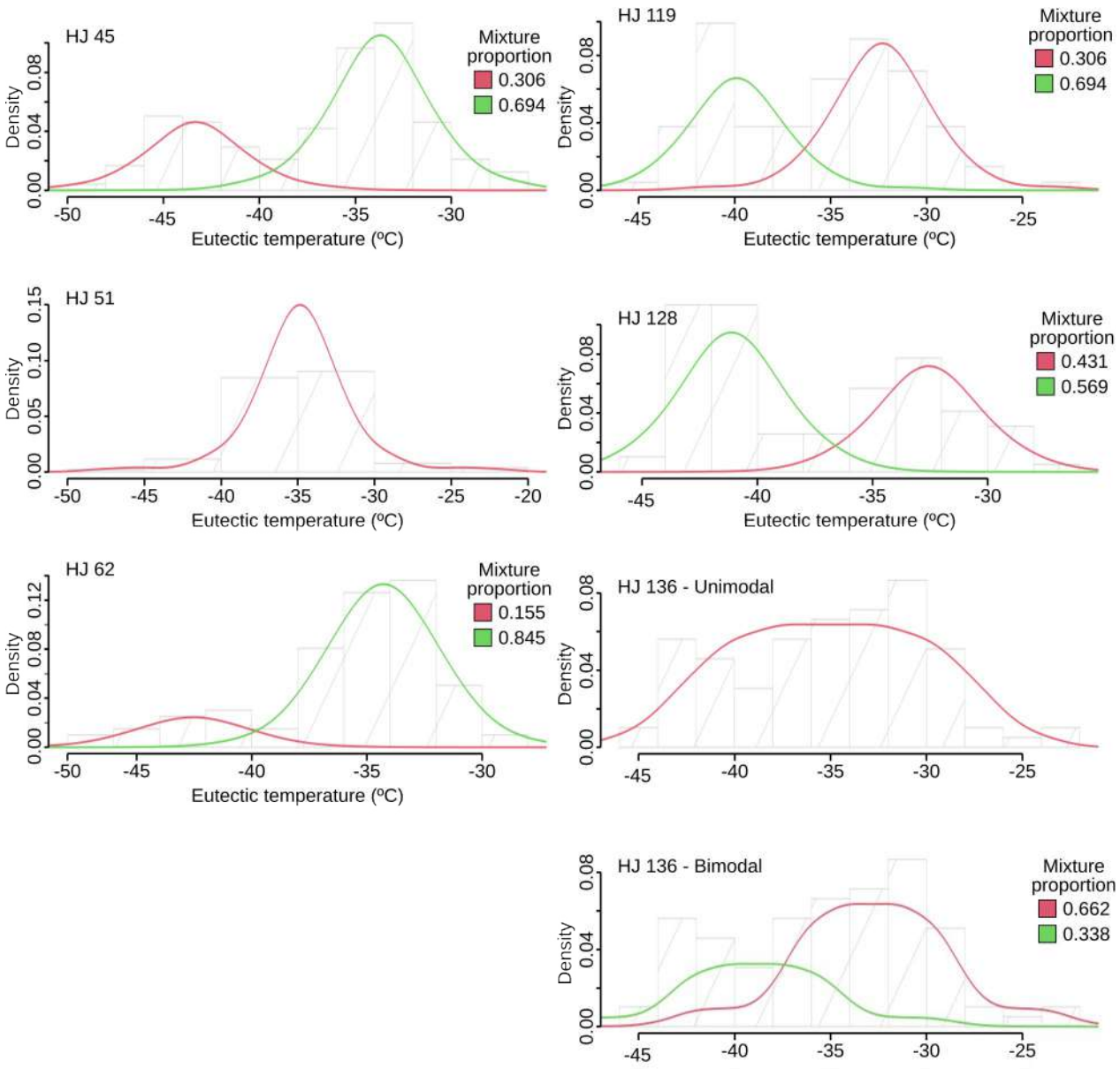

Figure 69. Proportions of mixtures estimated for the analyzed samples.

8.3.2. Salinity and the Formation of Inclusions

Like the distribution of final-ice melting temperatures (Figure 67), dispersions of salinity (Figure 70) are notably bimodal. One of the apparent groups encompasses the samples from the Fold-and-Thrust Domain (HJ 45, HJ 51 and HJ 62), whereas the samples from the Foreland Domain (HJ 119, HJ 128 and HJ 136) form the other group.

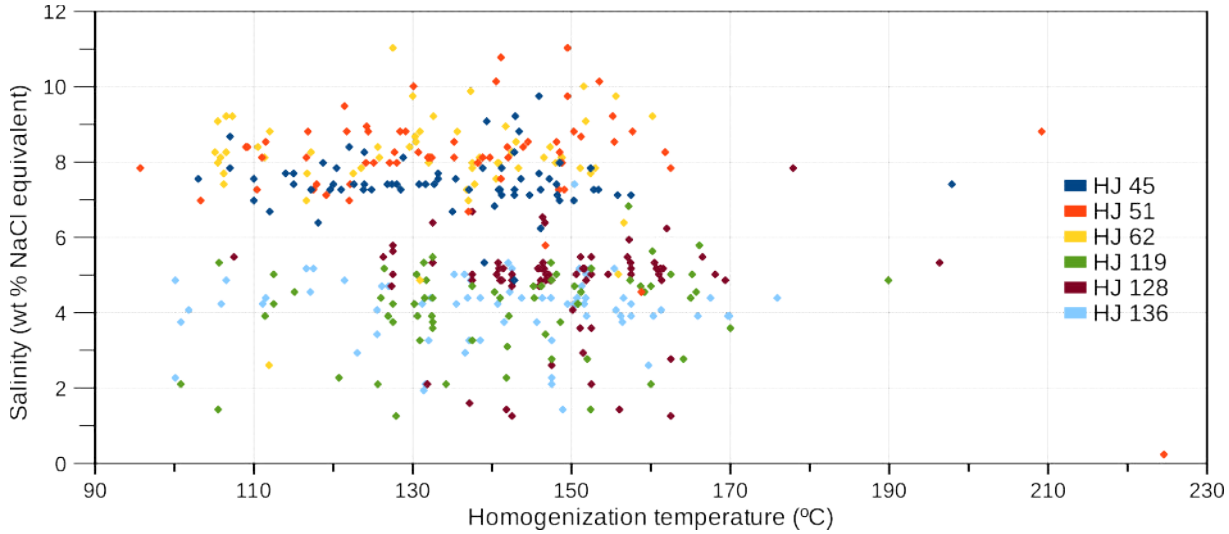

Figure 70. Dispersion of salinity values versus homogenization temperatures for the studied samples.

To evaluate this apparent division of fluid inclusions in groups, we ran Kruskal-Walis and Shapiro-Wilk tests with the null hypothesis (H_0) that the two groups belong to the same original population. For both tests, we obtained p-value << 0.001, a result that rejects H_0, indicating that the two groups of inclusions are statistically different. This is a strong indicative that the veins from each tectonic compartment (and respective fluid inclusions) originated from separate solutions.

8.3.3. Origin and Mixture of Fluids

The fluid inclusions in our samples are primary and formed by a mixture of fluids. The lack of correspondence between the inclusions from the Foreland and Fold-and-Thrust Domains suggest that, a regional circulation of fluid is unlikely, as it would have a homogenizing effect. Furthermore, other gaseous components typical of metamorphic fluids such as CO_2 and CH_4 (Crawford and Hollister, 1986) are absent. Thus, the fluids that originated the veins from the region of Serra do Cipó most likely originated from autochthonous solutions present in pores and discontinuities in the rocks and sediments at the moment of entrapment. The mixture indicated by our results could correspond, for example, to different contributions of meteoric water and basinal brines.

8.3.4. P-T Conditions

Using the homogenization temperatures measured and the density values calculated for the fluid inclusions in our samples, we obtained the isochoric curves depicted in Figure 71.

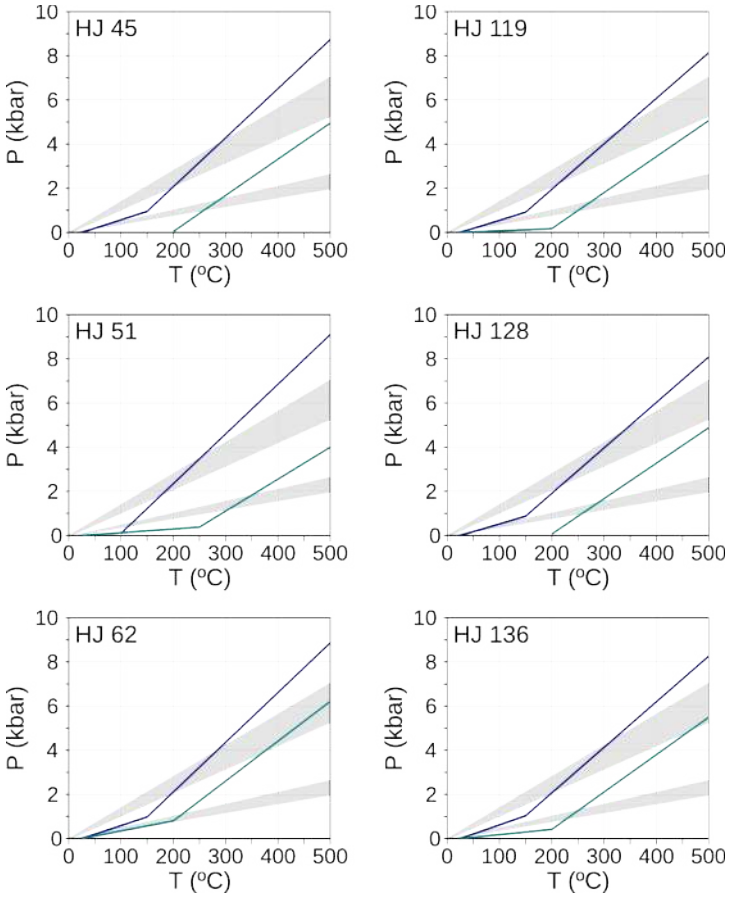

Figure 71. Isochores obtained for the studied samples.

8.4. Conclusion

In terms of composition, fluid inclusions contained in quartz veins from Serra do Cipó are biphasic (vapour and liquid phases), belong to the H_2O-NaCl-$CaCl_2$, H_2O-NaCl-$FeCl_2$ and H_2O-NaCl-$MgCl_2$ saline systems, with concentrations between 0.2 and 11.6 NaCl eq. wt%. Statistical analyses have demonstrated that the populations of inclusions from each of the local tectonic compartments (Foreland and Fold-and-Thrust) are distinct, suggesting separate origins. Furthermore, the data point towards the possibility of existence of multiple populations of inclusions contained in the same vein. Most probably, rather than a regional-scale circulation of metamorphic fluids, each group of inclusions was originated by intra-basinal fluids of restricted circulation, such as brines contained in the pores of sedimentary rocks and meteoric water, with limited contribution of water originated from the dehydration caused by the low-grade metamorphism that affected the region.

The P-T fields calculated based on the homogenization temperatures (95.7-224.6 ºC) offer insights into the environmental conditions prevailing during the entrapment of the inclusions, contributing to our understanding of the geological processes at play.

9. DATING THE BRASILIANO DEFORMATION IN SERRA DO CIPÓ – METAMORPHIC MICA K-AR AND *IN SITU* RB-SR AGES

One of the mysteries surrounding the São Francisco Craton and the Araçuaí Orogen is the temporality of the orogeny. With Cambrian ages being determined for the foreland sedimentation – the Bambuí Group (Warren et al., 2014; Paula-Santos et al., 2015; Moreira et al., 2020; Tavares et al., 2020), and for metamorphism in the northern São Francisco Craton (Süssenberger et al., 2014), it becomes a pressing matter that more data about the age of this tectonic cycle are brought to light.

Minerals of the mica group have blocking temperatures lower than that of zircons, on par with conditions characteristic to tectonic events. This makes these minerals poor choices for dating magmatic crystallization, but excellent candidates for dating metamorphic events (McSween et al., 2003; Dickin, 2005; Allègre, 2008).

Potassium is an important component of many minerals of the mica group. One of its natural isotopes, ^{40}K is radioactive and decays to ^{40}Ca by β-decay or ^{40}Ar by electron capture or electron capture associated with γ radiation. Each process has its own constant of decay (λ_β, λ'_e and λ_e, respectively), and the sum of all three constants gives the global constant of decay of ^{40}K ($\lambda_{K\text{-}Ar}$). Argon does not naturally enter the mineral structure of micas and, thus, K-Ar dating is based on the – sensible – premise that all the argon in a system is radiogenic (Kelley, 2002; Lee, 2015).

Rb-Sr dating is based on the decay of an isotope of Rubidium, ^{87}Rb, into an isotope of Strontium, ^{87}Sr, by β-decay, with a constant of decay $\lambda_{Rb\text{-}Sr}$). A difficulty for dating this geochronometer stems from the fact that both Rubidium and Strontium occur in trace amounts in micas. This is overcome using ratios considering the ^{86}Sr isotope, which is stable and not the product of decay of any isotope found in nature. ^{87}Sr and ^{86}Sr are just as likely to enter mineral structures, hence, $^{87}Sr/^{86}Sr$ tends to be the same for all minerals of a rock at the moment of crystallization, depending on the availability of each isotope. Rubidium and Strontium, however, enter minerals in different amounts and, thus, $^{87}Rb/^{86}Sr$ ratios are variable among the mineral phases. By extension, as ^{87}Rb decays to ^{87}Sr, the $^{87}Sr/^{86}Sr$ ratios, initially constant, will change after crystallization, because minerals with higher ^{87}Rb content will later contain more radiogenic ^{87}Sr. The concentration of ^{87}Sr is given by the initial amount of ^{87}Sr in the system ($^{87}Sr_0$), to which radiogenic ^{87}Sr is added by the decay of ^{87}Rb (McSween et al., 2003; Dickin, 2005).

Determining the closure age of a K-Ar or Rb-Sr isotopic system requires measurement of the parent (^{40}K or ^{87}Sr) and daughter ($^{40}Ar^*$ or ^{87}Rb) and, for the case of Rb-Sr dating, a stable isotope (^{86}Sr). For these methods, the resulting equations form linear systems where the closing age (**t**) is a factor in the slope (Wemmer, 1991; Clauer et al., 1995, 1997; McSween et al., 2003; Dickin, 2005), much like the case of U-Pb dating as described in Chapter 5. By similar processes of mathematical

manipulation, the equations that determine when the geochronometric systems K-Ar and Rb-Sr closed for the last time, respectively, are

$$t_{K-Ar} = \frac{1}{\lambda_{K-Ar}} \ln\left[1 + \left(\frac{\lambda_{K-Ar}}{\lambda_e + \lambda'_e}\right)\left(\frac{^{40}Ar^*}{^{40}K}\right)\right] \quad \textbf{Equation 15}$$

and

$$t_{Rb-Sr} = \frac{1}{\lambda_{Rb-Sr}} \ln\left\{1 + \left(\frac{^{(86)}Sr}{^{(87)}Rb}\right)\left[\left(\frac{^{87}Sr}{^{86}Sr}\right) - \left(\frac{^{86}Sr}{^{87}Sr}\right)_0\right]\right\}, \quad \textbf{Equation 16}$$

where $\left(\frac{^{86}Sr}{^{87}Sr}\right)_0$ is the ratio of ^{86}Sr and ^{87}Sr at the moment of crystallization, which can be estimated as the value at which a curve plotted on a $\left(\frac{^{86}Sr}{^{87}Sr}\right)$ *versus* $\left(\frac{^{86}Sr}{^{87}Rb}\right)$ intercepts the ordinate axis.

Here, we studied samples from the region of Serra do Cipó taken close to the craton-orogen border. Given the break-forward model of the propagation of the fold-and-thrust front over the foreland (Chapter 2), dating samples near the limit ensures that the results record the youngest stage of advance of the orogenic system. We took four samples samples from three different settings (Figure 72, Table 15): two in the Santa Rita Formation (Espinhaço Supergroup), as close as possible to the Espinhaço Front, and two in the Serra de Santa Helena Formation (Bambuí Group), the (meta-)sedimentary cover of the foreland area, one from a point close (900 m) to the thrust front and another at a greater distance (4800m), to evaluate possible geochronological gradients.

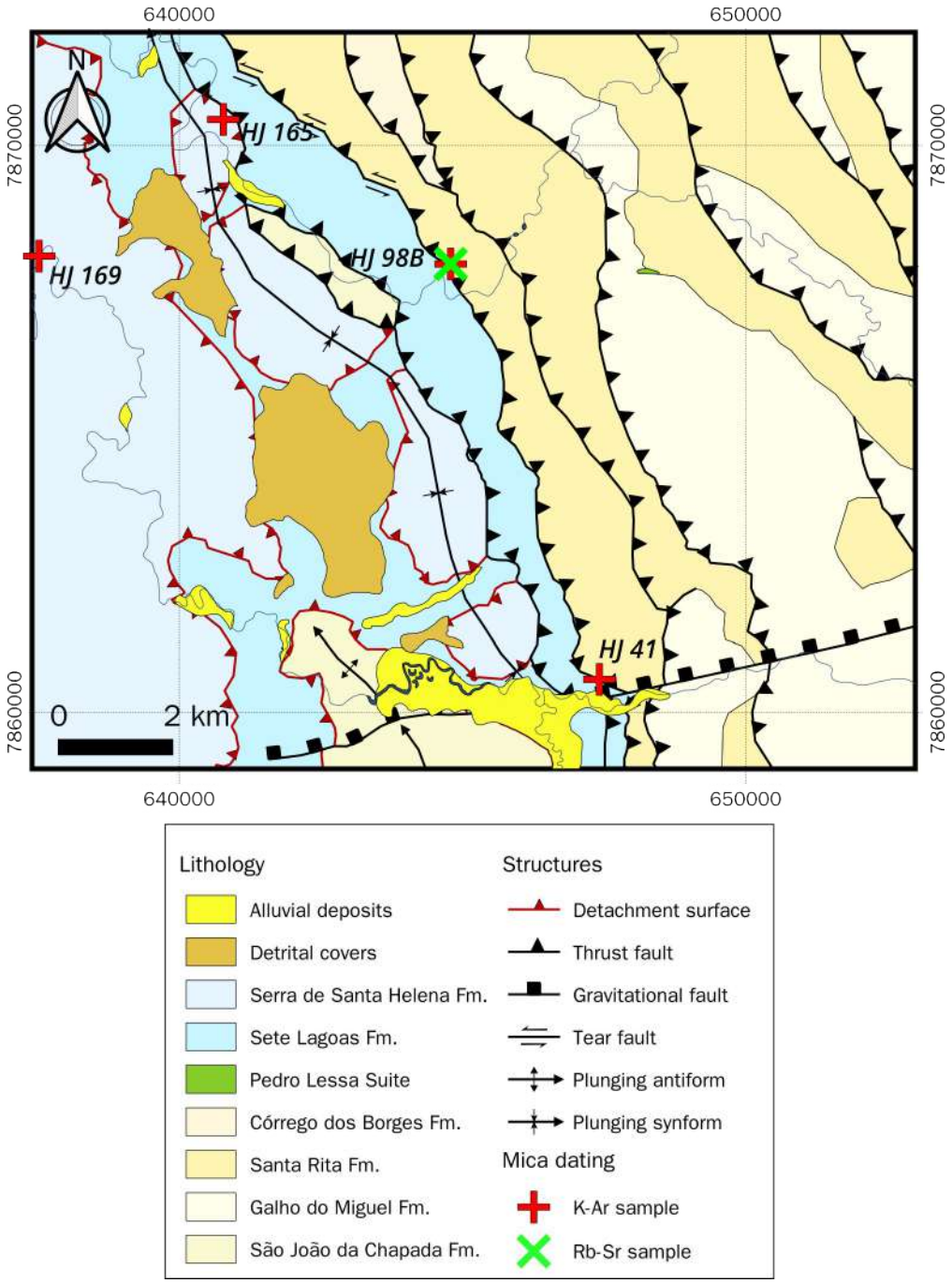

Figure 72. Location of the samples destinated for K-Ar and *in situ Rb-Sr* dating in the study area.

Table 15. Original location, classification and context of the samples dated by the K-Ar and in situ Rb-Sr methods.

Sample	Coordinates (UTM 23K)		Rock	Stratigraphic unit	Context
	E	N			
HJ 41	647421	7860580	Ultra-mylonitic quartzite	Santa Rita Formation	Espinhaço Front
HJ 98B	644794	7867906	Quartzite	Santa Rita Formation	Espinhaço Front
HJ 165	640779	7870459	Metapelite	Serra de Santa Helena Formation	Craton, 900 m from Espinhaço Front
HJ 169	637525	7868046	Pelite	Serra de Santa Helena Formation	Craton, 4800 m from Espinhaço Front

9.1. Practical and analytical procedures

9.1.1. K-Ar dating of fine mica fractions

All procedures regarding K-Ar dating were executed at the Laboratory of Isotopes of the Geoscience Centre of the Georg-August University Göttingen.

9.1.1.1. Sample preparation and Illite Crystallinity (IC) measurement

We used 2 to 3 kg of rock material from each sample to process the separation of the fine mineral fractions < 2 and < 0.2 µm for K-Ar age and Illite Crystallinity (IC) determinations. The rocks were crushed and ground in a shatter (vibration) mill for 10 to 20 seconds and split into sizes < 63 and > 63 µm. Fractions < 63 µm were used to extract the clay fractions < 2µm by settling in Atterberg cylinders. A second < 2µm fraction was obtained the same way, and then used to separate fractions < 0.2 µm in an ultra-centrifuge (Wemmer, 1991). All these fine fractions were examined by X-ray diffraction (XRD) to determine IC and mineralogical composition.

All X-ray data were produced by step scan on an XRD-Eigenmann Orion Komet P2 diffractometer. A Cu-Anode was used, powered with a 40 mA current under a 40 kV acceleration voltage. For the identification of clay minerals, scans were executed on the < 2 µm fraction between 3 and 35°2Θ at 0.020° steps, each step scanned for 2 seconds. per step. One measurement was performed per fraction. IC was determined using the software RayfleX Analyze, by XRD Eigenmann. A total of 151 points were scanned between 7 and 10° 2Θ, using a step size of 0.020°2Θ and an integration time of 4 seconds. The receiving slit was 0.3 mm wide, with a divergence slit of 1.265 mm (0.5°). The value of IC is marked by the peak width at half height of the 10-Å peak of the diffraction profile. All samples were investigated in duplicates (A and B) and in air-dried and glycolated status to detect expandable layers of smectite-type minerals. For the identification of clay minerals,

IC-values are given in Δ°2ΘCuKα and classified based on the classic Kübler Index (Kübler, 1967) and the newly proposed CIS scale of Warr (2018), which uses reference samples for interlaboratory standardization. Both scales lead to the same interpretation, the difference residing in the numeric values attributed to the cristallinity ranges. For the different stages of very-low-grade metamorphism, the following correlations to mineral facies is appropriate:

1. Diagenetic zone – zeolite facies (< 200 ºC);
2. Anchizone – prehnite-pumpellyite facies, plus pumpellyite-actinolite facies (200-300 ºC);
3. Epizone – incipient greenschist facies (> 300 ºC).

9.1.1.2. Analytical procedures for K-Ar dating

Argon isotopic composition was measured in a stainless-steel extraction and purification line coupled to a Thermo Scientific ARGUS VI™ noble gas mass spectrometer operating in static mode. The amount of radiogenic ^{40}Ar was determined by isotope dilution, using a highly enriched ^{38}Ar spike from Schumacher, Bern (Schumacher, 1975). The spike was calibrated against the biotite standard HD-B1 (Fuhrmann et al., 1987). Age calculations were based on the constants recommended by the IUGS quoted in Steiger and Jäger (1977). Presence of potassium (K_2O) was determined in duplicate by flame photometry using a BWB-XP flame photometer. The samples were then dissolved in a mixture of HF and HNO_3, according to the technique of Heinrichs and Herrmann (1990). Analytical error for the K-Ar age calculations is given with a 95% confidence level (2σ). Details of argon and potassium analyses for the laboratory in Göttingen are given in Wemmer (1991).

9.1.2. In Situ *Rb-Sr dating of mica*

In situ Rb-Sr dating was performed at the John de Laeter Centre, Curtin University. Rb and Sr isotope contents were measured in a RESOlution 193 nm ArF excimer laser with a Laurin Technic S155 sample cell coupled to an Agilent 8900 triple quadrupole mass spectrometer in MS/MS mode using the $N_2O_{(g)}$ as reaction gas in the collision cell to enable measurement of rubidium and strontium isotopes (Cheng et al., 2008; Zack and Hogmalm, 2016; Hogmalm et al., 2017). The analytical conditions for Rb–Sr are summarized in Table 16 following the method described elsewhere (Olierook et al., 2020; Liebmann et al., 2022; Ribeiro et al., 2023). Data reduction was performed in Iolite 4 (Paton et al., 2011) using an in-house data reduction scheme adapted from Redaa et al. (2021). Rb–Sr isochrons and ages were calculated using the maximum likelihood model in IsoplotR (Vermeesch, 2018) with the ^{87}Rb decay constant of Villa et al. (2015). Ages and uncertainties are presented at 2 standard error from the mean (2 SE), with error propagation and error correlation following Rösel and Zack (2022). Inverse Rb–Sr isochrons are used to minimize the extreme error correlation following Li and Vermeesch (2021). Rb-Sr isotopic dataset from reference materials and unknowns are presented in Appendix F.

Table 16. Analytical conditions for *in situ* acquisition of Rb and Sr isotopes in muscovite.

***In situ* Rb-Sr dating settings**	
Mass spectrometer	Agilent 8900 ICP-MS
Laser system	ASI RESOlution
Wavelength (nm)	193
Repetition rate (Hz)	5
Laser fluency ($J.cm^{-2}$)	2.5
Ablation time (s)	60
Spot size (µm)	64
He flux rate ($ml.min^{-1}$)	320
He carrier gas ($l.min^{-1}$)	0.32
Ar carrier gas ($l.min^{-1}$)	1.0
N_2 addition ($ml.min^{-1}$)	1.2
Reaction gas (collision cell)	30% N_2O in He

$^{87}Sr/^{86}Sr$ and $^{87}Rb/^{86}Sr$ ratios were drift-corrected and calibrated against NIST610 ($^{87}Sr/^{86}Sr$ = 0.709699 ± 0.000018, $^{87}Rb/^{86}Sr$ = 2.389 ± 0.005; Woodhead and Hergt, 2001). Matrix correction of drift-corrected $^{87}Rb/^{86}Sr$ was applied to mica analyses using a fractionation factor obtained from a pressed powder tablet of phlogopite Mica-Mg that was analysed interspersed with the unknowns, assuming a crystallization age of 519.4 ± 6.5 Ma and $^{87}Sr/^{86}Sr_0$ of 0.72607 ± 0.00070 (as described by Hogmalm et al., 2017). Mica-Mg isotopic data yielded an anchored-isochron date of 519 ± 2 Ma (MSWD = 0.9, N = 88), consistent with reference values. Unknowns were additionally bracketed with in-house biotite reference material CK001 (422 ± 6 Ma; Kirkland et al., 2007), which yielded an isochron age of 418 ± 9 Ma (MSWD = 0.2, N = 25).

9.2. Results

9.2.1. Samples

9.2.1.1. HJ 41

Sample HJ 41 was taken from the Santa Rita Formation close to the Espinhaço Front in the southern portion of the study area. It is composed by a fine-grained, laminated quartzite with high mica content. The schistosity and stretch lineations are strongly marked in this sample. The rock as a whole has ultra-mylonitic texture and is structured as a series of undulated flat surfaces with sigmoidal geometry indicating west-verging movement of the top successions.

9.2.1.2. HJ 98B

This sample was also collected from the Santa Rita-Sete Lagoas inversion, but further north from sample HJ 41 along the strike of the Espinhaço Front. The rock in this location is a poorly

selected, medium-grained foliated quartzite containing millimetric phyllitic and schistose flasers. The outcrop from which sample HJ 98B comes is cut by several quartz veins parallel to the tectonic foliation. Adjacent to the veins, the rock becomes schistose, with an important growth of hydrothermal minerals (e.g. tourmaline). The sample was taken in such a context.

9.2.1.3. HJ 165

Sample HJ 165 belongs to the Serra de Santa Helena Formation, and was collected at a point at approximately 900 m distant of the Espinhaço Front in the northern end of the study area. This rock a foliated metarhythmite formed by millimetric interleaved gray, micaceous layers and white, quartzous levels.

9.2.1.4. HJ 169

Sample HJ 169 also comes from the Serra de Santa Helena Formation, but was collected in the northwestern corner of the study area at approximately 4800 m from the Espinhaço Front. This rock is a gray metapelite with well-marked slate cleavage parallel to the bedding and gently undulated due to crenulation.

9.2.2. X-Ray Diffraction

Quartz and muscovite are the most dominant minerals in our samples from Serra do Cipó. Other important mineral phases that occur as accessories are chlorite, K-feldspar and albite. Trace amounts of hematite, kaolinite and calcite were also identified (Table 17).

Table 17. Semi-quantitative mineralogical constitution of the samples analyzed by X-ray diffraction. The symbol +++ denotes a mineral that is one of the principal components of the rock; ++ means an abundant mineral; + means a mineral found in trace amounts; and - means that the mineral is absent in the considered sample.

Sample	Mineral							
	Quartz	Musc/Ill.	Albite	K-Feldspar	Chlorite	Kaolinite	Hematite	Calcite
HJ 41	+++	++	-	+	-	-	-	-
HJ 98B	+	+++	?	-	-	+	+	-
HJ 165	+++	++	++	-	++	-	-	-
HJ 169	+++	++	++	-	++	-	-	+

9.2.3. Illite Crystallinity (IC)

The differences between the IC measured in air-dried and glycolated conditions in our analyses are not significant (Figure 73), meaning smectite-type minerals can be ruled out from the composition of the fine mica fractions from our samples. Raw IC values vary between 0.163 and 0.221 Δ°2ΘCuKα, providing index ranges of 0.185-0.231 (Kübler Index) and 0.249-0.302 (CIS Index).

Regardless of the classification index adopted, these results indicate Epizonal conditions, or a temperature of 300 ºC or above for the system.

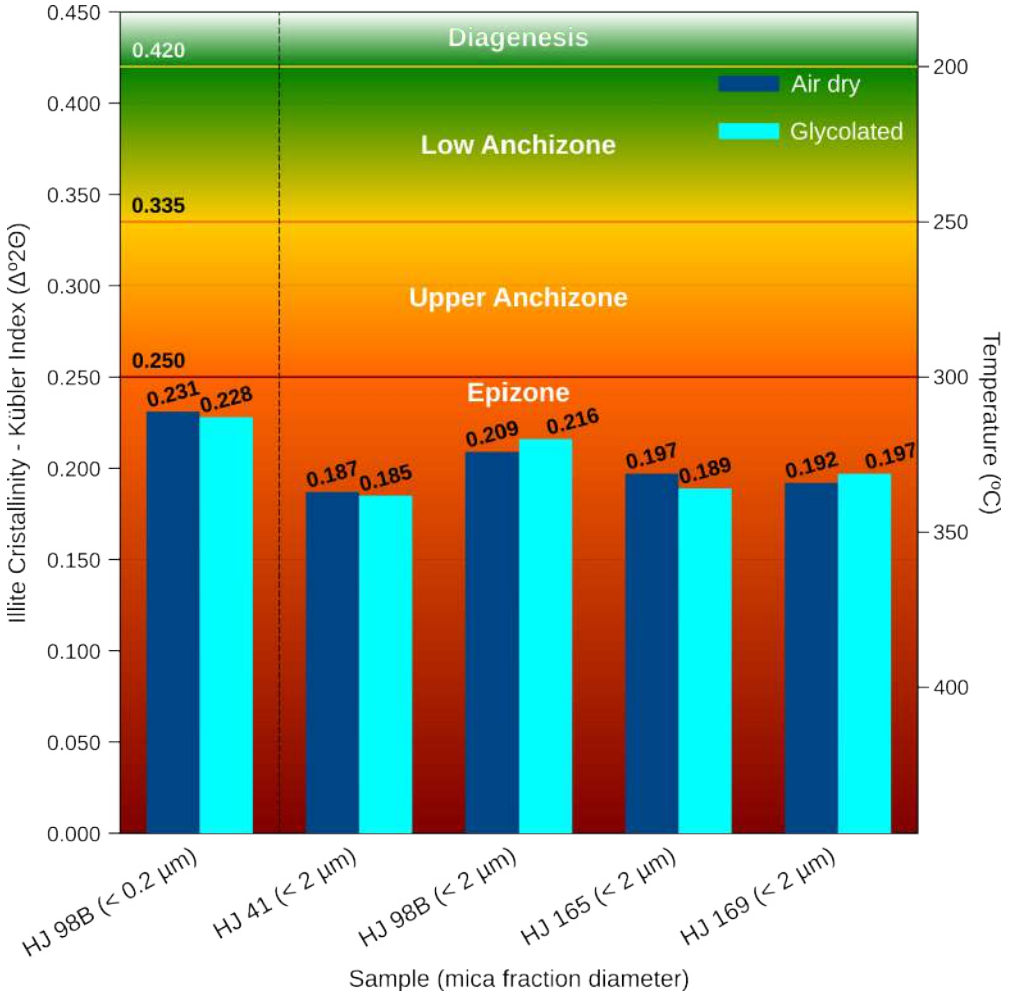

Figure 73. Illite Crystallinity for our samples and environmental conditions respective to Kübler Indexes.

9.2.4. K-Ar dating

Fractions of muscovite < 2 µm were retrieved from all four samples sent for analyses, but fractions under 0.2 µm could be obtained only from sample HJ 98B. The K-Ar ages yielded by < 2 µm mica range from 456.1 ± 8.6 to 510.3 ± 5.3 Ma, while the age calculated for the < 0.2 µm fraction was 432.6 ± 7.5 Ma (Table 18).

9.2.5. In situ *Rb-Sr dating*

In situ Rb-Sr dating was executed on a total of 58 points of muscovite on a thin section of sample HJ 98B, from the base of the Espinhaço Front. The data pairs (Appendix F) are distributed very close along the line on the $^{87}Sr/^{86}Sr$ vs. $^{87}Rb/^{86}Rb$ diagram (Figure 74) calculated for the system. The slope of the line gives a closure age of 548.8 ± 17.1 Ma (Table 18).

Table 18. K-Ar and in situ Rb-Sr ages obtained for the studied samples.

Sample	*In situ* Rb-Sr age (Ma)	K-Ar age (Ma)	
		< 2 µm fraction	< 0.2 µm fraction
HJ 41	-	456.1 ± 8.6	-
HJ 98B	548.8 ± 17.1	476.2 ± 7.5	432.6 ± 7.5
HJ 165	-	495.8 ± 9.3	-
HJ 169	-	510.3 ± 5.3	-

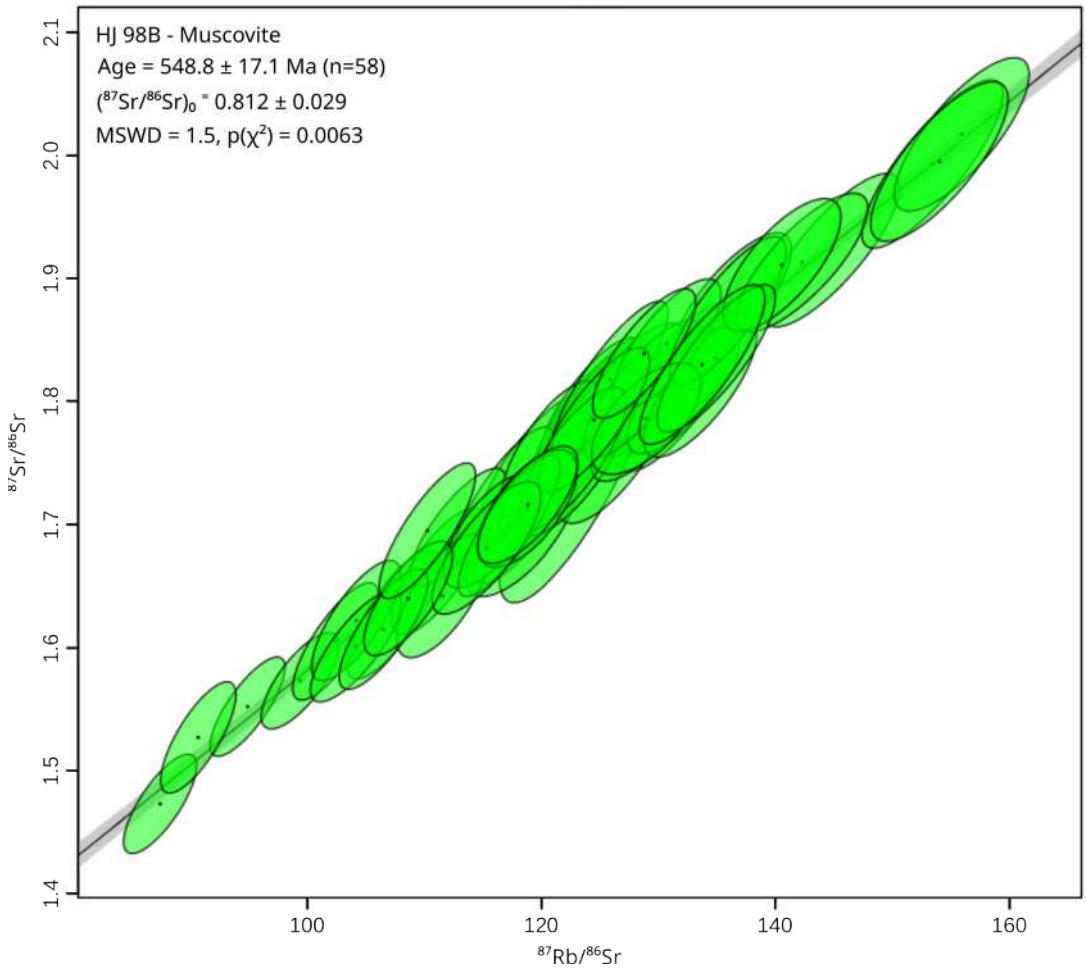

Figure 74. $^{87}Sr/^{86}Sr$ vs. $^{87}Rb/^{86}Rb$ chart and respective linear regression and age from in situ Rb-Sr dating of sample HJ 98B.

9.3. Discussion

All Illite Crystallinity indexes indicate that our samples experienced high epizonal conditions (300 ºC or above). Thus, we can safely discard influence of detrital mica, that is, we can consider detrital information as having been reset, and consider the K-Ar ages as actual regional cooling stages following the metamorphic peak.

Samples from the Serra de Santa Helena Formation (HJ 165 and HJ 169) yielded Cambrian-Ordovician metamorphic/deformational cooling ages, about 510.3-495.8 Ma, which are consistent with depositional ages determined for the Bambuí Group, which spanned from 635 to 524 Ma (e.g.

Pimentel et al., 2011; Warren et al., 2014; Paula-Santos et al., 2015, 2017; Pimentel, 2016; Kuchenbecker et al., 2020; Moreira et al., 2020; Tavares et al., 2020; Caxito et al., 2021). Samples from the Santa Rita Formation (HJ 41 and HJ 98B) yielded similar ages, about 500-433 Ma, indicating that the orogenic activity lasted until the Ordovician or even the Silurian. Sample HJ 98B also has an *in situ* Rb-Sr age of 548 Ma, which we interpret as the age of the metamorphic peak. Combined, these ages suggest a cooling history about 116 Ma long (Figure 75).

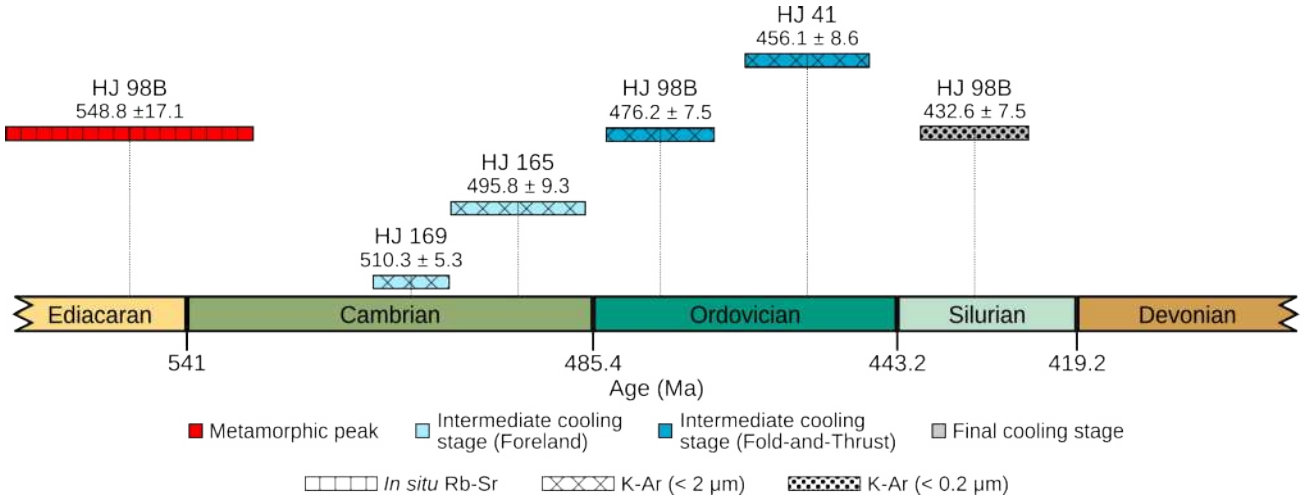

Figure 75. Metamorphic peak and cooling stages of the region of Serra do Cipó indicated by radiometric dating of mica.

9.4. Conclusion

Results show that, while the metamorphism related to the Brasiliano-Pan African Cycle peaked around the Ediacaran-Cambrian limit (548.8 ± 17.1 Ma) in the region of Serra do Cipó, it took about 116 Ma for the system to cool down to effectively close the metamorphic system of muscovite (432.6 ± 7.5 Ma). Coupled with stratigraphic and structural evidence, this suggests that the region remained tectonically active well into the Cambrian and Ordovician periods, and perhaps up to the Mid Silurian Period.

10. FURTHER DISCUSSIONS

While the previous chapters were written as independently from one another as possible, geologic processes are not isolated phenomena. Thus, there is a number of discussions that emerge from putting together the results obtained and the interpretations made so far. The purpose of this chapter is to delve into various points that combine data from two or more of the previous chapters.

10.1. Stratigraphic compartmentalization of the region of Serra do Cipó

Our stratigraphic column of the region of Serra do Cipó (18) is significantly different from the one by Oliveira et al. (1997; Figure 76.a), whose model is the most influential since the time of its proposal. This stratigraphic review was deemed necessary based on field observations, and is supported by detrital zircon U-Pb age data (Chapter 5).

We do not recognize the Macaúbas Group at all in the area, attributing rocks previously placed in this unit to the São João da Chapada and Santa Rita formations. Our stratigraphic observations regarding the presence, distribution and division of the Bambuí Group are coherent with the previous models. We could not traverse areas classified into the Córrego dos Borges Formation and, therefore, maintain this unit in the column, after the model by Oliveira et al. (1997), with minor alteration to contact traces based on remote sensing.

In this sense, the pioneering stratigraphy by Schöll (1972) classified rocks either into the Basal Espinhaço Supergroup or the Conselheiro Mata Group (Figure 76.b), a model with stronger correspondence with our own. However, this author also proposed the presence of the Jequitaí Formation for metadiamictites, metaconglomerates, and coarse-grained quartzites of the area, which we discard, again suggesting placement in the São João da Chapada Formation.

A new proposal for the craton-orogen interface was posed by Chierici et al. (2021; Figure 76.c), rejecting the presence of the Macaúbas Group and classifying the quartzitic rocks of the Fold-and-Thrust Domain into the São João da Chapada and Sopa-Brumadinho formations. Once more, our field observations and laboratory analyses do not support the proposed model. The area studied by these authors was smaller than ours and did not contemplate siliciclastic rocks in the Foreland Domain.

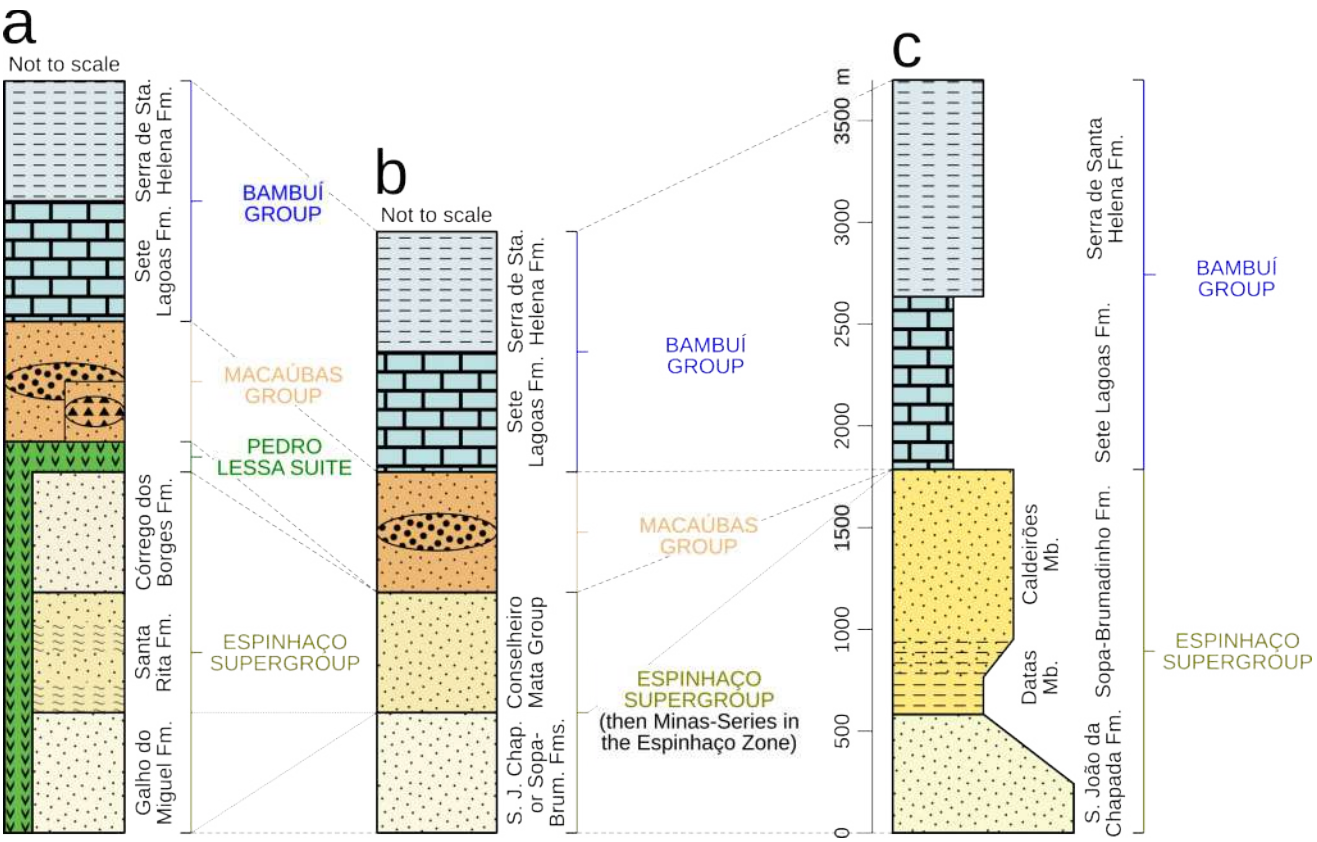

Figure 76. Stratigraphic columns of the region of Serra do Cipó according to past proposals by: a) Oliveira et al. (1997); b) Schöll (1972); c) Chierici et al. (2021).

10.2. P-T-t conditions during deformation

There were no previous studies dedicated specifically to the determination of metamorphic conditions along the Espinhaço Front. Estimations for the study area and neighboring regions are based on petrographic analyses of mineral associations. The most important mineral assemblages described for rocks of the study area in previous works are quartz + sericite + chlorite in siliciclastic rocks; calcite + quartz + sericite + phlogopite in carbonatic rocks; and albite + chlorite + epidote + amphiboles from the tremolite-actinolite series in metamafic rocks (Oliveira et al., 1997; Bakir et al., 2016). We observed the same mineral assemblages during our work, but, for the siliciclastic successions of the Fold-and-Thrust Domain, we also recognized incipient metamorphic biotite as one of the mineral phases at equilibrium composing tectonic foliation surfaces, thus expanding the paragenesis to quartz + sericite + chlorite + biotite. This corroborates previous observations from the region of Lapinha da Serra, approximately 15 km north of Serra do Cipó (Oliveira and Torres, 2014). All these associations define low-grade metamorphism peaking at the greenschist facies, and the appearance of biotite defines a metamorphic gradient with an increase in temperature from west to east, that is, from the foreland to the fold-and-thrust belt. Furthermore, biotite requires higher

temperatures to form in metamorphic conditions than chlorite, meaning that previous estimates underestimated the metamorphic conditions that affected the region.

Combining the mineral assemblages described for the rocks from the study area, the distribution of quartz [c] axes and microcrystalline deformation mechanisms identified with EBSD analyses, the isochores obtained from the fluid inclusion data (Figure 71) and illite crystallinity (Figure 73), we can estimate a more restrict P-T field for the Ediacaran-Cambrian tectonism that affected Serra do Cipó and its vicinities (Figure 77). To the original isochores, we added an inferior thermal limit given the illite crystalinity indexes in our samples, which point to epizonal conditions, that is, temperatures above 300 ºC. Furthermore, the EBSD results suggest limit temperatures between 300 and 450 ºC for the occurrence of dislocation glide with basal and rhombohedral slip activation as observed in the analyzed samples. The presence of metamorphic biotite in the Fold-and-Thrust Domain allows us to define a lower limit given by its reaction curve, while its absence in a paragenesis containing chlorite indicates the upper limit in the Foreland Domain. The resulting intervals were 385-450 ºC and 2.8-8.0 kbar for the Fold-and-Thrust Domain and 300-411 ºC and 1.7-6.0 kbar for the Foreland Domain.

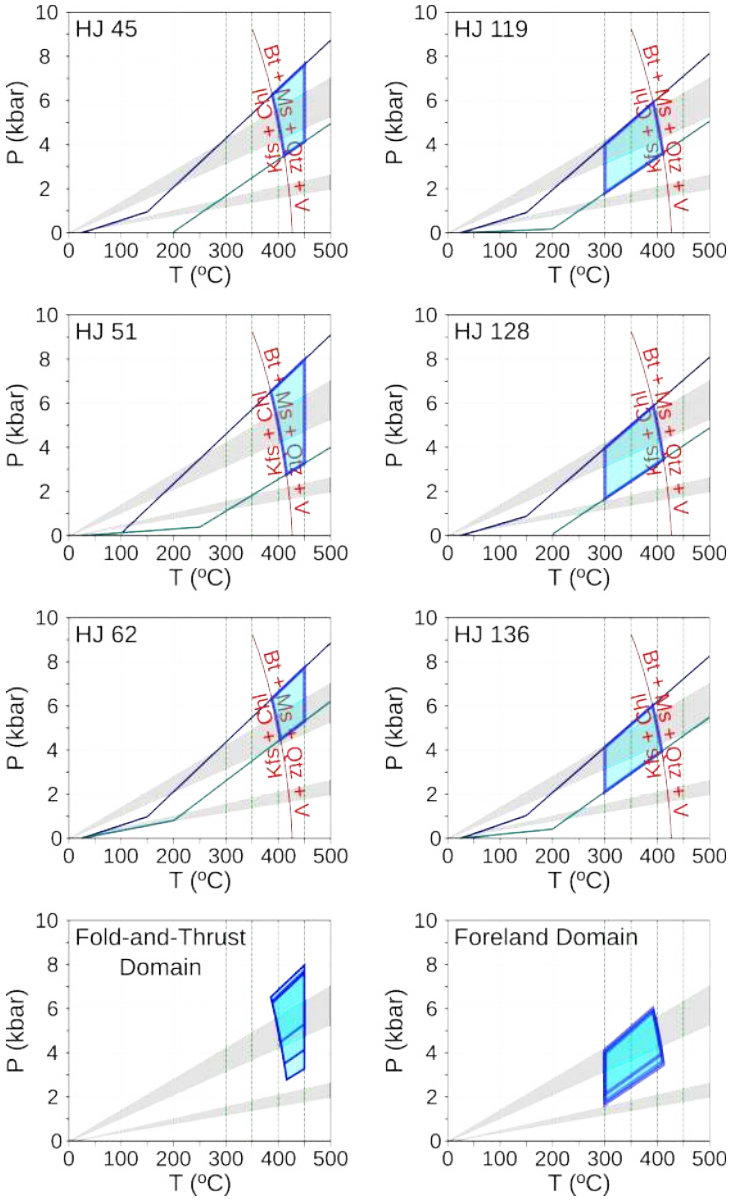

Figure 77. P-T fields determined for the region of Serra do Cipó. Formation of biotite based on Bucher and Grapes (2011)

As there are no other P-T-t results or estimates from the marginal fold-and-thrust belt of the Araçuaí Orogen, the only available data refer to inner orogenic domains. The extant results from these areas point to greenschist to amphibolite conditions.

To the north of the Guanhães Block, between the Minas Novas Transpressive Corridor and the Chapada Acauã Shear Zone, Queiroga et al. (2016) identified garnet-bearing assemblages in the Capelinha Formation (Macaúbas Group), interpreted as the product of crystallization during the collisional stage that formed the regional foliation around 570 Ma. For this event, geothermobarometric analyses revealed a clockwise P-T trajectory where temperature increased from 500 to 620 ºC and pressure decreased from 8.0 to 4.5 kbar. Th-U-Pb dating of homogeneous monazites revealed a period of recrystallization around 490-480 Ma, associated to a tectonothermal

event associated with the orogenic collapse, constraining the youngest time limit for metamorphic processes in the Araçuaí Orogen.

In the region of Piranga, southeastern end of the Quadrilátero Ferrífero, affected by deformational processes related to the final stages of the Brasiliano Orogeny, Queiroz et al. (2019) studied schists previously classified into the Neoarchean Rio das Velhas Supergroup, shown by U-Pb dating to belong to younger units (the Sabará or Itacolomi groups, or even the Espinhaço Supergroup). Pseudosection modeling indicated that metamorphism reached amphibolite facies with P-T values of 630-650 ºC and 6.9-7.2 kbar, and chemical monazite ages of ca. 500 Ma point to recrystallization or resetting in the Cambrian Period.

U-Pb dating of igneous zircons from collisional granites led Silva et al. (2011) to propose that the collisional stage for the internal domain of the Araçuaí ended at ca. 560 Ma. The 570 Ma ages obtained by Queiroga et al. (2016) and the 548.8 Ma ages obtained in our study are consistent with the dissipation of heat from the crystalline core to the orogenic margins from this stage.

A tectonothermal reactivation around the Cambrian-Ordovician boundary (~480 Ma) in the Araçuaí Orogen has been associated with decompression caused by the collapse of the orogenic buliding (Alkmim et al. 2006). Queiroga et al. (2016) and Queiroz et al. (2019) associated the 490-480 Ma and 500 Ma ages obtained in their study, respectively, to this event. Despite having K-Ar ages dating to this period, we have not identified evidence of a Cambrian-Ordovician thermal reactivation in the region of Serra do Cipó. Hence, our interpretation for the study area is of a long cooldown stage spanning around 116 Ma, from the metamorphic peak in the Late Ediacaran up until the Mid Silurian. Samples from the foreland reached blocking temperatures for < 2 μm muscovite as soon as 38.5 Ma after the metamorphic peak, whereas the fold-and-thrust belt only reached such conditions 72.6 Ma after the metamorphic peak. This indicates faster cooling of the foreland, which is coherent with the geotectonic context, as the fold-and-thrust belt naturally experiences more tectonic and thermal activity. The same might apply to the second cooling stage, but we could not retrieve < 0.2 μm mica fractions from the samples from the foreland to make this estimation (Figure 78).

As is the case of sample HJ 98B, sample HJ 41 was also collected at the base of the Espinhaço Front, but is approximately 20.1 Ma younger (456.1 ± 8.6 Ma *versus* 476.2 ± 7.5 Ma). This may indicate that the thrust system was active until the Cambrian-Ordovician transition. The age result of the < 0.2 μm mica fraction of sample HJ 98B also reveal that tectonic activity in the region lasted way into the Paleozoic Era. The final closure of the K-Ar system, occurred at 432.6 ± 7.5 Ma, evidence that the Espinhaço Front was possibly still active in the Mid Silurian.

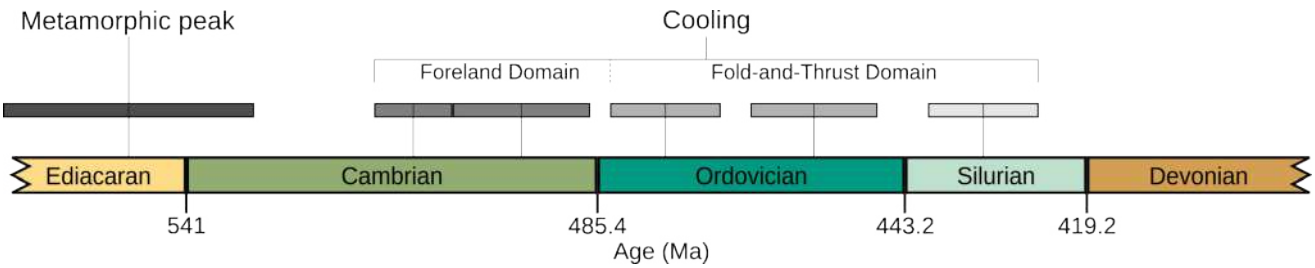

Figure 78. Age of metamorphism and cooling period of the region of Serra do Cipó.

10.3. Tectonic and structural evolution

Compared to previous works (Magalhães, 1988; Marshak and Alkmim, 1989; Oliveira, 1994; Oliveira et al., 1997; Silva et al., 2007; Ribeiro, 2010; Oliveira and Torres, 2014; Victoria and Moy, 2014; Bakir et al., 2016; Chierici et al., 2021), our structural data attest to the coherence of the Espinhaço Front in the region of Serra do Cipó in the overall context of the Southern Espinhaço Range fold-and-thrust system. A plethora of kinematic indicators (S-C foliation, sigmoidal porphyroclasts, tension gashes, fault-related folds, asymmetric fold limbs, stretch lineations, etc) corroborate thrusts from east to west along the major faults. However, our stratigraphic revision causes some natural incompatibilities, such as the limits of the fold-and-thrust belt, which cascades to the role and interpretation of the Bocaina Fault.

10.3.1. The Parauninha conundrum – a window? A klippe? A sheet?

Most structural observations made here are befitting with the available data regarding the region of Serra do Cipó (Magalhães, 1988; Marshak and Alkmim, 1989; Uhlein, 1991; Oliveira, 1994; Oliveira et al., 1997; Silva et al., 2007; Ribeiro, 2010; Bakir et al., 2016; Chierici et al., 2021; Taufner et al., 2021). However, we propose a new interpretation of the nature of the occurrences of siliciclastic rocks in contact with the Sete Lagoas Formation in the central-north portion of the study area, in the valley of the Parauninha River. The three previous works that also contemplated this location propose three different models for the area. Oliveira (1994) posed that the siliciclastic rocks belong to the Macaúbas Group and are exposed in a structural window, below the Sete Lagoas Formation, and that all the stratigraphic sequence is involved in a major-scale anticline (Figure 79.a). Oliveira et al. (1997) had a similar interpretation, but mapped the contact as normal between the same units (Figure 79.b). Ribeiro (2010), on the other hand, drastically changed this model, mapping this area as a tectonic protrusion stemming from the Main Espinhaço Thrust, occurring as a klippe that heaved the Macaúbas on top of the Sete Lagoas Formation (Figure 79.c).

Our data, however, do not support any of these proposals. First, the detrital zircon U-Pb age results indicate that the siliciclastic rocks in this location most likely belong the São João da Chapada

Formation (Espinhaço Supergroup). Furthermore, the fabric of the rocks shows significant tectonic features, such as mylonitic texture, reflecting involvement in the deformation that affected the region. The distribution of lithotypes in the area shows that the São João da Chapada Formation is below the Sete Lagoas Formation, at its eastern limit, and above the Serra de Santa Helena Formation, at the western boundary. The structural trends, the attitudes of beddings and tectonic foliation and the kinematic indicators all point to the occurrence of west-verging reverse movement. This setting is more consistent with a tectonic sheet of the top of the São João da Chapada Formation being lodged between the two local representatives of the Bambuí Group (Figure 79.d). The proposals both by Oliveira (1994) and Oliveira et al. (1997) do not contemplate the occurrence of the stratigraphic inversion observed in the area or the deformed state of the siliciclastic rocks, and none of our structural data suggest structures suggest a process of ejection of a klippe into a cratonic terrane as proposed by Ribeiro (2010), which would require local changes in the distribution of strain axes that would cause the formation of east-verging backthrusts and other structures with vergences opposed to the regional trend.

We therefore put forward the third model presented in the stratigraphic description of the São João da Chapada Formation. As the Espinhaço Front advanced over the São Francisco Craton, the propagation of thrusts to the foreland caused the top of the São João da Chapada Formation to splinter upwards and westwards, wedging a part of this sequence into the overlying sequences of the Bambuí Group.

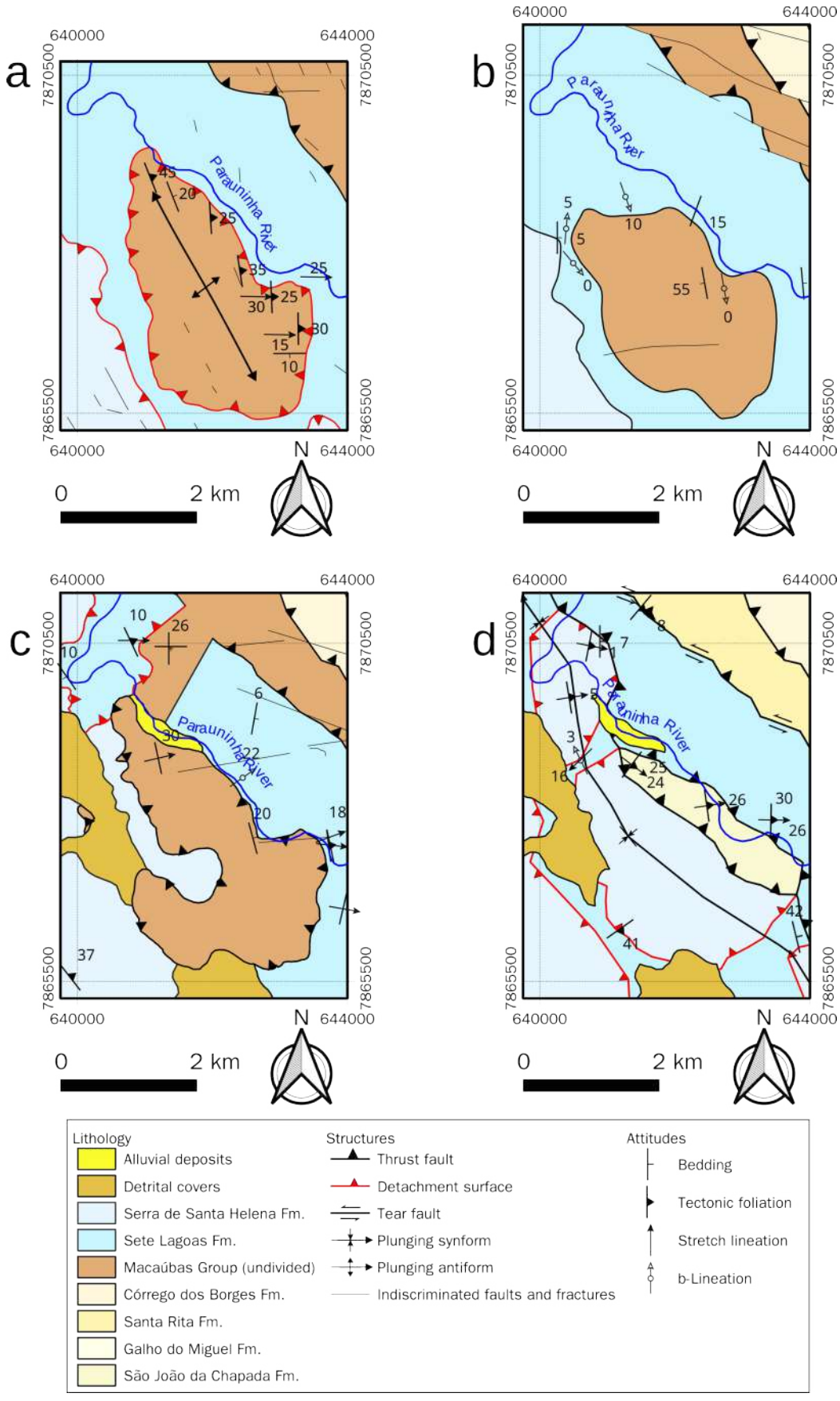

Figure 79. Interpretations of the siliciclastic rocks from the valley of the Parauninha River. a) Oliveira (1994); b) Oliveira et al. (1997); c) Ribeiro (2010); d) This Work. All color schemes for rocks and structures were adapted to the standards used in this work to facilitate comparison.

10.3.2. The Bocaina Fault

The Bocaina Fault follows a trend nearly perpendicular to the orientation of the Espinhaço thrust system. A structure in such a disposition could be – and has been – interpreted as a transfer fault, as proposed by Oliveira (1994). However, our interpretation of the Bocaina Fault as a normal fault, after Oliveira (1994) and Silva et al. (2007), and our stratigraphic-tectonic revision of the outlines of the Espinhaço Front is incompatible with this structure as a transfer fault. Rather, we pose that the Bocaina Fault is posterior and unrelated to the Brasiliano Orogeny and, contrary to the proposal by Silva et al. (2007), we propose abatement of the northern block. However, we do not possess enough information to establish when exactly in time the faulting occurred.

10.3.3. Thin-skinned or thick-skinned tectonics

We follow the previous model proposed by Marshak and Alkmim (1989) that suggests that the Espinhaço Thrust System is arranged as an imbricated fan. According to these authors, the thrusts reach all the way down to the crystalline basement, that is, the deformation occurred in a thick-skinned regimen. We follow this model in this study, but, contrary to these authors, we deem a thin-skinned style more likely for the local evolution of the Espinhaço Front. However, reliable determination of whether the crystalline basement was involved or not during the local deformation during the Brasiliano-Pan African Orogeny would require data that we do not possess (e.g. sub-surface investigation).

10.3.4. The Brasiliano Orogeny – the Espinhaço Front as a Coulomb wedge

The structural framework of the region of Serra do Cipó encompasses several indicators of progressive deformation, such as the successive sets of tectonic foliations, sub-parallel not only to each other, but also to quartz veins (which would originally form perpendicularly to the stretching direction). Shear bands and S-C structures are pervasive at mesoscopic and microscopic scales, showing successive deformation increments and displacements that are centimetric at most. On the other hand, the major thrusts and associated structures point to episodes of expressive deformation pulses. In our interpretation, this incremental-episodic mechanism indicates that the structural arrangement of the Espinhaço Front is the result of its evolution as a Coulomb wedge that was active from the onset of the Brasiliano-Pan African Orogeny until the Mid Silurian (432.6 ± 7.5 Ma, age of the youngest cooling stage), driven by the orogenic lateral spread and the buoyancy of the crustal roots. Progressive deformation would cause the wedge to thicken and, reaching the critical taper condition, a thrust front would form and mark a new moment of advance of the Fold-and-Thrust Domain over the São Francisco Craton. Concomitantly, the Foreland Domain would also deform in

response to the tectonic activity in the adjacent compartment, with the deformation of the Bambuí Group, the development of the detachments and the overarching syncline-anticline system.

As far as these structures are concerned, our interpretation does not require separate pulses or mechanisms for the nucleation of structures. In this sense, we diverge from the bi-phasic model proposed by Magalhães (1988) and Oliveira (1994). These authors proposed two separate coaxial stages of deformation, where the first (D_1) would correspond to the nucleation of the mesoscopic structures (shear bands, asymmetric folds) and the formation of the detachment surfaces in the foreland, and the second (D_2) would be the moment when major thrusting, regional-scale folds and crenulation would occur.

The nucleation of normal structures are not mentioned in the works by Magalhães (1988) and Oliveira (1994). However, our interpretation of the system as a Coulomb wedge model also encompasses gravitational structures such as the ones observed in the Santa Rita Formation. The normal faults would be formed as a response to supercritical topographic slopes, adjusting the surface to suitable conditions. It is noteworthy, however, that normal faults are always the youngest structures in their areas of occurrence, not showing evidence of reactivation or interference with posterior increments of reverse deformation. Alternatively, the sub-vertical quartz veins of the Serra de Santa Helena Formation point to a posterior extensional stage, which could have been set due to an alleviation of the orogenic pressure or orogenic collapse, which would also account for the formation of normal faults in the system.

11. CONCLUSIONS

The region of Serra do Cipó is divided in two tectonic compartments, each with its own stratigraphy. To the East lies a segment of the Southern Espinhaço Range, the marginal fold-and-thrust belt of the Araçuaí Orogen. This compartment is almost completely composed by rocks of the Espinhaço Supergroup (the Galho do Miguel, Santa Rita and Córrego dos Borges formations), cut by limited metamafic dikes of the Pedro Lessa Suite. To the west lies the foreland region of the São Francisco Craton, where the Bambuí Group (with the Sete Lagoas Formation at the base and the Serra de Santa Helena Formation at the top) was deposited concomitantly with the building of the adjacent orogenic system, having the São João da Chapada Formation (Espinhaço Supergroup) as a local rigid basement.

Our stratigraphic model is supported by detrital zircon U-Pb ages, and represents a significant change from the most recent proposal (Chierici et al., 2021) and the current most widespread interpretations of the area (Oliveira, 1994; Oliveira et al., 1997; Ribeiro, 2010), with a callback to a pioneering work (Schöll, 1972). However, previous models suggested the existence of the Macaúbas Group or the Jequitaí Formation in the area, which we reject. In this sense, we also bring back a member of the Espinhaço Supergroup as the local basement, as suggested by Marshak and Alkmim (1989).

The Espinhaço Front marks the craton-orogen limit, where the Santa Rita Formation is thrusted over the Sete Lagoas Formation. Together with a series of major west-verging thrusts affecting both tectonic compartments, the Espinhaço Front is the most prominent structural feature in the area, connecting with the rest of the thrust system of the Southern Espinhaço Range to the north and to the south. The Fold-and-Thrust Domain is characterized by a series of tectonic inversions of the Galho do Miguel, Santa Rita and Córrego dos Borges formations, and west-verging mesoscopic reverse shear bands and asymmetric folds complement the main structural framework. In the Foreland Domain, a regional-scale system of detachments, deformation and associated folding affects all stratigraphic units. A tectonic sliver of the São João da Chapada Formation is wedged between the and the Sete Lagoas and Serra de Santa Helena formations, having splintered upwards during the Brasiliano-Pan African Orogeny. Otherwise, in the Cipó River Window, the São João da Chapada Formation is slightly deformed or not deformed at all. A detachment surface separates it from the Sete Lagoas Formation, which is also detached from the top unit, the Serra de Santa Helena Formation. Low angle thrust faults and shear zones are widespread throughout the Bambuí Group, with subordinate overturned mesoscopic folds.

Two sub-parallel sets of tectonic foliations are pervasive in all stratigraphic units of the area. These structures are also generally sub-parallel or form tight angles with the primary bedding

surfaces, but there are instances where first set of foliation is crenulated or (together with beddings) involved in folding, having the younger foliations positioned at the axial plane. Aside from these occasional structures, the tectonic foliations dip consistently with gentle to moderate degrees towards east.

Strain analyses showed that the long (X) axes are sub-horizontal, with gentle plunges fluctuating in the eastern quadrants, and that flattening was the preferred regime for the accomodation of strain, consistent with the attitudes of the local stretching lineations and the development of tectonic foliation in the area. EBSD analyses of the disposition of quartz crystallographic axes suggested dislocation glide with rhomb <a> slip activation and dissolution and re-precipitation were the main mechanisms at intracrystalline level. Dislocation glide dominated in the coarser fractions of rocks (> 100 μm), while dissolution and re-precipitation was more active in finer grians (< 100 μm).

The study of fluid inclusions revealed that each tectonic compartment contains its own population of inclusions. This suggests that, a regional circulation of fluids – which would have a homogenizing effect – was unlikely, and that the local quartz veins most probably originated from intra-basinal fluids trapped in the pores of the sediments, with limited contribution of water from metamorphic dehydration.

We propose that the fold-and-thrust belt evolved as a Coulomb wedge driven by the tectonic forces generated by the lateral spread and the buoyancy of the crustal roots in the orogenic core. In this context, rather than a poly-phasic evolution, the region of Serra do Cipó experienced progressive deformation, which caused crustal thickening until the system reached a critical taper condition, when a new thrust would cause the advance of the orogenic front onto the foreland, and the process would repeat itself until the orogenic activity ceased and the isostatic equilibrium was re-established. This model comprises the nucleation of nearly all structures observed in the area: tectonic foliations, faults, folds, shear zones, and is coherent with the kinematic indicators present.

Normal faults observed in the Fold-and-Thrust Domain may be linked to the supercritical topographic conditions established during the evolution of the wedge. Alternatively, these structures may be related to a posterior alleviation of the tectonic pressures, a stage when other extensional features such as sub-vertical veins from the Foreland Domain were formed.

The formation of the E-W-trending Bocaina Fault occurred after the Brasiliano-Pan African Orogeny and is probably unrelated to this event. The fault is normal, with abatement of the northern block estimated at approximately 125 m.

For the advance of the fold-and-thrust belt over the foreland, we estimate that deformation occurred between 385-450 ºC and 2.8-8.0 kbar in the Fold-and-Thrust Domain and between 300-411 ºC and 1.7-6.0 kbar in the Foreland Domain. Moreover, the system was active from the establishment

of the Brasiliano-Pan African Orogeny, reaching metamorphic peak at ca. 548.8 Ma, near the Ediacaran-Cambrian limit. K-Ar age data indicate that the region then experienced a 116 Ma-long continuous cooldown deep into the Eopaleozoic. The final deformation stages associated with the crystallization of very fine mica reached the Mid Silurian (432.6 Ma).

REFERENCES

Ahrenkiel, S.P., 2018, Kikuchi diffraction: Rapid City, South Dakota School of Mines and Technology, 8 p., doi:10.15036/arerugi.42.1140.

Alkmim, F.F., 2004, O que faz de um cráton um cráton? O Cráton do São Francisco e as revelações almeidianas ao delimitá-lo, *in* Mantesso-Neto, V., Bartorelli, A., Carneiro, C.D.R., and Brito-Neves, B.B. eds., Geologia do continente sul-americano: evolução da obra de Fernando Flávio Marques de Almeida, São Paulo, Beca, p. 17–35.

Alkmim, F.F., Brito-Neves, B.B., and Alves, J.A.C., 1993, Arcabouço tectônico do Cráton do São Francisco: uma revisão (J. M. Dominguez & A. Misi, Eds.): Salvador, SBG-BA/SBG-SE/SGM/CNPq, 45–62 p.

Alkmim, F.F., Kuchenbecker, M., Reis, H.L.S., and Pedrosa-Soares, A.C., 2017, The Araçuaí Belt, *in* Heilbron, M., Cordani, U.G., and Alkmim, F.F. eds., São Francisco Craton, Eastern Brazil: Tectonic genealogy of a miniature continent, Handel, Springer, Regional Geology Reviews, p. 255–276.

Alkmim, F.F., Marshak, S., Pedrosa-Soares, A.C., Peres, G.G., Cruz, S.C.P., and Whittington, A., 2006, Kinematic evolution of the Araçuaí-West Congo Orogen in Brazil and Africa: nutcracker tectonics during the Neoproterozoic assembly of Gondwana: Precambrian Research, v. 149, p. 43–64, doi:10.1016/j.precamres.2006.06.007.

Alkmim, F.F., and Martins-Neto, M.A., 2001, A bacia intracratônica do São Francisco: arcabouço estrutural e cenários evolutivos, *in* Pinto, C.P. and Martins-Neto, M.A. eds., Bacia do São Francisco - Geologia e recursos naturais, Belo Horizonte, SBG-MG, p. 9–30.

Alkmim, F.F., and Martins-Neto, M.A., 2012, Proterozoic first-order sedimentary sequences of the São Francisco craton, eastern Brazil: Marine and Petroleum Geology, v. 33, p. 127–139, doi:10.1016/j.marpetgeo.2011.08.011.

Alkmim, F.F., Pedrosa-Soares, A.C., Noce, C.M., and Cruz, S.C.P., 2007, Sobre a evolução tectônica do Orógeno Araçuaí-Congo Ocidental: Geonomos, v. 15, p. 25–43.

Allègre, C.J., 2008, Isotope Geology: Cambridge, Cambridge University Press, 512 p., doi:10.1017/CBO9780511809323.

Almeida, F.F.M., 1967, Diferenciação tectônica da Plataforma Brasileira, *in* XXIII Congresso Brasileiro de Geologia, Salvador, Anais, v. 1, p. 29–46.

Almeida, F.F.M., 1977, O Cráton do São Francisco: Revista Brasileira de Geociências, v. 7, p. 349–363.

Almeida, F.F.M., Brito-Neves, B.B., and Carneiro, C.D.R., 2000, The origin and evolution of the South American platform: Earth Science Reviews, v. 50, p. 77–111, doi:10.1016/S0012-8252(99)00072-0.

Almeida, F.F.M., Hasui, Y., Brito-Neves, B.B., and Fuck, R.A., 1981, Brazilian structural provinces: an introduction: Earth-Science Reviews, v. 17, p. 1–29, doi:10.1016/0012-8252(81)90003-9.

Almeida-Abreu, P.Â., Knauer, L.G., Hartmann, M.B., Vieira-dos-Santos, M.L.V., Abreu, F.R., Schrank, A., and Pflug, R., 1989, Estratigrafia, faciologia e tectônica do Supergrupo Espinhaço na região de Serro-Conceição do Mato Dentro, Minas Gerais, Brasil: Zentralblatt für Geologie und Paläontologie Teil I, v. 5–6, p. 857–873.

Almeida-Abreu, P.Â., and Renger, F.E., 2002, Serra do Espinhaço Meridional: um orógeno de colisão do Mesoproterozóico: Revista Brasileira de Geociências, v. 32, p. 01–14, doi:10.25249/0375-7536.20023210114.

Alvarenga, C.J.S., Santos, R.V., Vieira, L.C., Lima, B.A.F., and Mancini, L.H., 2014, Meso-Neoproterozoic isotope stratigraphy on carbonates platforms in the Brasilia Belt of Brazil: Precambrian Research, v. 251, p. 164–180, doi:10.1016/j.precamres.2014.06.011.

Amaral, L.S.S., Caxito, F.A., Pedrosa-Soares, A.C., Queiroga, G.N., Babinski, M., Trindade, R.I.F., Lana, C.C., and Chemale Jr., F., 2020, The Ribeirão da Folha ophiolite-bearing accretionary wedge (Araçuaí Orogen, SE Brazil): new data for Cryogenian plagiogranite and metasedimentary rocks: Precambrian Research, v. 336, p. 105522, doi:10.1016/j.precamres.2019.105522.

Amaral, W.S., Santos, T.J.S., Wernick, E., Nogueira-Neto, J.A., Dantas, E.L., and Matteini, M., 2012, High-pressure granulites from Cariré, Borborema Province, NE Brazil: Tectonic setting, metamorphic conditions and U-Pb, Lu-Hf and Sm-Nd geochronology: Gondwana Research, v. 22, p. 892–909, doi:10.1016/j.gr.2012.02.011.

Aracema, L.W., Neves, A.C., Ferreira, J.C.H., Pedrosa-Soares, A.C., Lobato, L.M., and Noce, C.M., 2000, Novas evidências de remanescentes oceânicos na Faixa Araçuaí: as rochas meta-ultramáficas de São José Da Safira: Geonomos, v. 8, p. 55–61.

Araújo, A.L.B., Barbosa, D.M.D., Rosa, P.A.S., and Roncato, J., 2020, Caracterização geológica-estrutural da conexão Araçuaí - São Francisco na área-tipo da Formação Rio Pardo Grande (Supergrupo Espinhaço, Minas Gerais): Geonomos, v. 28, p. 25–46.

Babinski, M., Pedrosa-Soares, A.C., Trindade, R.I.F., Martins, M.S., Noce, C.M., and Liu, D., 2012, Neoproterozoic glacial deposits from the Araçuaí Orogen, Brazil: age, provenance and correlations with the São Francisco craton and West Congo belt: Gondwana Research, v. 21, p. 451–465, doi:10.1016/j.gr.2011.04.008.

Bakir, B.F., Maia, B.S., Franco, D.S., and Ersinzon, F., 2016, Mapeamento geológico em escala 1:25.000 a sul de Cardeal Mota, Serra Do Cipó - Mg [Graduation Project]: UFMG, 256 p.

Barber, D.J., and Wenk, H.R., 1991, Dauphiné twinning in deformed quartzites: Implications of an in situ TEM study of the α-β phase transformation: Physics and Chemistry of Minerals, v. 17, p. 492–502, doi:10.1007/BF00202229.

Barbosa, J.S.F., and Sabaté, P., 2004, Archean and Paleoproterozoic crust of the São Francisco Craton, Bahia, Brazil: geodynamic features: Precambrian Research, v. 133, p. 1–27, doi:10.1016/j.precamres.2004.03.001.

Barrote, V.R., 2016, A sequência portadora de formações ferríferas de Guanhães, Minas Gerais, Brasil [Master's Dissertation]: UFMG, 134 p.

Barrote, V.R., Rosière, C.A., Rolim, V.K., Santos, J.O.S., and McNaughton, N.J., 2017, The proterozoic Guanhães banded iron formations, southeastern border of the São Francisco Craton, Brazil: evidence of detrital contamination: Geologia USP - Serie Cientifica, v. 17, p. 303–324, doi:10.11606/issn.2316-9095.v17-352.

Bezerra-Neto, F.E., 2016, Estudo de rochas exóticas da Formação Sopa-Brumadinho e possíveis implicações para a fonte dos diamantes do Espinhaço Meridional: UnB, 105 p.

Bowring, S.A., and Schmitz, M.D., 2003, High-precision U-Pb zircon geochronology and the stratigraphic record: Reviews in Mineralogy and Geochemistry, v. 53, p. 305–326, doi:10.1515/9781501509322-014.

Braun, O.P.G., 1968, Contribuição à estratigrafia do Grupo Bambuí, *in* XXII Congresso Brasileiro de Geologia, Belo Horizonte, SBG, Anais, v. 1, p. 155–166.

Brito-Neves, B.B., Campos-Neto, M. da C., and Fuck, R.A., 1999, From Rodinia to Western Godwana: An approach to the Brasiliano-Pan African Cycle and orogenic collage: Episodes, v. 22, p. 155–166.

Brito-Neves, B.B., and Cordani, U.G., 1991, Tectonic evolution of South America during the Late Proterozoic: Precambrian Research, v. 53, p. 23–40, doi:10.1016/0301-9268(91)90004-T.

Brito-Neves, B.B., Kawashita, K., Cordani, U.G., and Delhal, J., 1979, A evolução geocronológica da cordilheira do Espinhaço; dados novos e integração: Revista Brasileira de Geociencias, v. 9, p. 71–85.

Bucher, K., and Grapes, R., 2011, Petrogenesis of metamorphic rocks: Berlin, Springer, v. 39, 428 p., doi:10.1016/0016-7037(75)90141-6.

Burbidge, D.R., and Braun, J., 2002, Numerical models of the evolution of accretionary wedges and fold-and-thrust belts using the distinct-element method: Geophysical Journal International, v. 148, p. 542–561, doi:10.1046/j.1365-246x.2002.01579.x.

Cabral, A.R., Wiedenbeck, M., Koglin, N., Lehmann, B., and Abreu, F.R., 2012, Boron-isotopic constraints on the petrogenesis of hematitic phyllite in the southern Serra do Espinhaço, Minas Gerais, Brazil: Lithos, v. 140–141, p. 224–233, doi:10.1016/j.lithos.2012.01.011.

Carvalho, A.S., 1982, Geologia e gênese das mineralizações de quartzo no Espinhaço Meridional, Minas Gerais, Brasil [Master's Dissertation]: UnB, 94 p.

Castro, M.P., Queiroga, G.N., Martins, M.S., Alkmim, F.F., Pedrosa-Soares, A.C., Dussin, I.A., and Souza, M.E.S., 2019, An Early Tonian rifting event affecting the São Francisco-Congo paleocontinent recorded by the Lower Macaúbas Group, Araçuaí Orogen, SE Brazil: Precambrian Research, v. 331, p. 105351, doi:10.1016/j.precamres.2019.105351.

Castro, M.P., Queiroga, G.N., Martins, M.S., Pedrosa-Soares, A.C., Dias, L., Lana, C.C., Babinski, M., Alkmim, A.R., and Silva, M.A.L., 2020, Provenance shift through time in superposed basins: from Early Cryogenian glaciomarine to Late Ediacaran orogenic sedimentations (Araçuaí Orogen, SE Brazil): Gondwana Research, v. 87, p. 41–66, doi:10.1016/j.gr.2020.05.019.

Cavalcante, G.C.G., Fossen, H., Almeida, R.P., Hollanda, M.H.B.M., and Egydio-Silva, M., 2019, Reviewing the puzzling intracontinental termination of the Araçuaí-West Congo orogenic belt and its implications for orogenic development: Precambrian Research, v. 322, p. 85–98, doi:10.1016/j.precamres.2018.12.025.

Caxito, F.A. et al., 2021, Goldilocks at the dawn of complex life: mountains might have damaged Ediacaran–Cambrian ecosystems and prompted an early Cambrian greenhouse world: Scientific Reports, v. 11, p. 20010, doi:10.1038/s41598-021-99526-z.

Caxito, F.A., and Alkmim, F.F., 2023, The role of V-shaped oceans and ribbon continents in the Brasiliano/PanAfrican assembly of western Gondwana: Scientific Reports, v. 13, p. 1568, doi:10.1038/s41598-023-28717-7.

Caxito, F.A., Halverson, G.P., Uhlein, A., Stevenson, R., Gonçalves-Dias, T., and Uhlein, G.J., 2012, Marinoan glaciation in east central Brazil: Precambrian Research, v. 200–203, p. 38–58, doi:10.1016/j.precamres.2012.01.005.

Chang, H.K., Miranda, F.P., Magalhães, L., and Alkmim, F.F., 1988, Considerações sobre a evolução tectônica da Bacia do São Francisco, *in* XXXV Congresso Brasileiro de Geologia, Belém, Anais, p. 2076–2090.

Chapple, W.M., 1978, Mechanics of thin-skinned fold-and-thrust belts: Geological Society of America Bulletin, v. 89, p. 1189, doi:10.1130/0016-7606(1978)89<1189:MOTFB>2.0.CO;2.

Chaves, A.O., and Knauer, L.G., 2020, Vulcânicas potássicas intemperizadas como protólitos dos filitos hematíticos da Serra do Espinhaço Meridional (Minas Gerais): Geochimica Brasiliensis, v. 34, p. 183–194, doi:10.21715/gb2358-2812.2020342183.

Chaves, M.L.S.C., Silva, M.C.R., Chaves, A.O., and Dussin, T.M., 2012, Formações ferríferas bandadas no grupo Costa Sena (Gouveia: Minas Gerais, Brasil), *in* Para conhecer a Terra: memórias e notícias de Geociências no espaço lusófono, Imprensa da Universidade de Coimbra, p. 251–260, doi:10.14195/978-989-26-0534-0_26.

Chemale Jr., F., Dussin, I.A., Alkmim, F.F., Martins, M.S., Queiroga, G.N., Armstrong, R., and Santos, M.N., 2012, Unravelling a Proterozoic basin history through detrital zircon geochronology: the case of the Espinhaço Supergroup, Minas Gerais, Brazil: Gondwana Research, v. 22, p. 200–206, doi:10.1016/j.gr.2011.08.016.

Chemale Jr., F., Dussin, I.A., Martins, M.S., and Santos, M.N., 2011, Nova abordagem tectono-estratigráfica do Supergrupo Espinhaço em sua porção meridional (MG): Geonomos, v. 19, p. 173–179.

Cheng, P., Koyanagi, G.K., and Bohme, D.K., 2008, On the chemical resolution of the 87Rb+ (s0)/87Sr+ (s1) isobaric interference: A kinetic search for an optimum reagent: Analytica Chimica Acta, v. 627, p. 148–153, doi:10.1016/j.aca.2008.03.057.

Chiavegatto, J.R.S., 1992, Análise estratigráfica das seqüências tempestíticas da Formação Três Marias (Proterozoico Superior), na porção meridional da Bacia do São Francisco [Master's Dissertation]: UFOP, 216 p.

Chierici, G.N., Moura, V.C., and Weber, W., 2021, Mapeamento geológico em escala 1:10.000 da região da Serra do Cipó, município de Santana do Riacho [Graduation Project]: UniBH, 27 p.

Clauer, N., Rais, N., Schaltegger, U., and Piqué, A., 1995, KAr systematics of clay-to-mica minerals in a multi-stage low-grade metamorphic evolution: Chemical Geology, v. 124, p. 305–316, doi:10.1016/0009-2541(95)00055-Q.

Clauer, N., Środoń, J., Francu, J., and Šucha, V., 1997, K-Ar dating of illite fundamental particles separated from illite-smectite: Clay Minerals, v. 32, p. 181–196, doi:10.1180/claymin.1997.032.2.02.

Condie, K.C., 2005, Earth as an Evolving Planetary System: San Diego, Elsevier, 447 p., doi:10.1016/C2010-0-65818-4.

Cordani, U.G., D'Agrella-Filho, M.S., Trindade, R.I.F., and Brito-Neves, B.B., 2003, Tearing up Rodinia: the Neoproterozoic palaeogeography of South American cratonic fragments: Terra Nova, v. 15, p. 350–359.

Cordani, U.G., Pimentel, M.M., Araújo, C.E.G., Basei, M.A.S., Fuck, R.A., and Girardi, V.A.V., 2013, Was there an Ediacaran Clymene Ocean in central South America? American Journal of Science, v. 313, p. 517–539, doi:10.2475/06.2013.01.

Cordani, U.G., Ramos, V.A., Fraga, M.F., Cegarra, M., Delgado, I.M., Souza, K.G., and Gomes, F.D.M., 2016, Tectonic map of South America: CCGM.

Cordani, U.G., Teixeira, W., D'Agrella-Filho, M.S., and Trindade, R.I.F., 2009, The position of the Amazonian Craton in supercontinents: Gondwana Research, v. 15, p. 396–407.

Cordeiro, J.S., 2008, A quantificação da deformação em rochas metassedimentares dos grupos Costa Sena e Guinda, Paleoproterozóico da Serra do Espinhaço Meridional [Master's Dissertation]: UFMG, 202 p.

Costa, P.C.G., 1978, Geologia das folhas de Januária, Mata do Jaíba, Japoré e Manga, Minas Gerais, *in* XXX Congresso Brasileiro de Geologia, Recife, SBG, Anais, v. 1, p. 83–97.

Costa, M.T., and Branco, J.J.R., 1961, Roteiro para a excursão Belo Horizonte - Brasília, *in* XIV Congresso Brasileiro de Geologia, Belo Horizonte, SBG, Anais, v. 15, p. 9–25.

Cottrell, A.H., 1964, Theory of crystal dislocations: Milton Park, Gordon & Breach, 91 p.

Crawford, M.L., and Hollister, L.S., 1986, Metamorphic fluids: the evidence from fluid inclusions, *in* Walther, J.V. and Wood, B.J. eds., Fluid-Rock interactions during metamorphism, New York, Springer, Advances in Physical Geochemistry, v. 5, p. 1–35, doi:10.1007/978-1-4612-4896-5_1.

Cukrov, N., Alvarenga, C.J.S., and Uhlein, A., 2005, Litofácies da glaciação neoproterozoica nas porções sul do Cráton do São Francisco: Exemplos de Jequitaí (MG) e Cristalina (GO): Revista Brasileira de Geociências, v. 35, p. 69–76, doi:10.25249/0375-7536.20053516976.

Cutts, K., Lana, C.C., Alkmim, F.F., and Peres, G.G., 2018, Metamorphic imprints on units of the southern Araçuaí belt, SE Brazil: the history of superimposed Transamazonian and Brasiliano orogenesis: Gondwana Research, v. 58, p. 211–234, doi:10.1016/j.gr.2018.02.016.

Dahlen, F.A., 1990, Critical taper model of fold-and-thrust belts and accretionary wedges: Annual Review of Earth & Planetary Sciences, v. 18, p. 55–99, doi:10.1146/annurev.ea.18.050190.000415.

Dahlen, F.A., Suppe, J., and Davis, D., 1984, Mechanics of Fold-and-Thrust Belts and Accretionary Wedges: Cohesive Coulomb Theory.: Journal of Geophysical Research, v. 89, p. 10087–10101, doi:10.1029/JB089iB12p10087.

Danderfer-Filho, A., De Waele, B., Pedreira, A.J., and Nalini, H.A., 2009, New geochronological constraints on the geological evolution of Espinhaço basin within the São Francisco Craton-Brazil: Precambrian Research, v. 170, p. 116–128, doi:10.1016/j.precamres.2009.01.002.

Dardenne, M.A., 1978, Geologia do Grupo Bambuí no vale do Rio Paraná (Goiás), *in* XXX Congresso Brasileiro de Geologia, Recife, SBG, Anais, v. 2, p. 611–621.

Davis, D.M., and Engelder, T., 1985, The role of salt in fold-and-thrust belts: Tectonophysics, v. 119, p. 67–88, doi:10.1016/0040-1951(85)90033-2.

Davis, G.H., Reynolds, S.J., and Kluth, C.F., 2012, Structural Geology of rocks and regions: New York, John Wiley & Sons, 839 p., https://www.worldcat.org/title/structural-geology-of-rocks-and-regions/oclc/149191066.

Davis, D., Suppe, J., and Dahlen, F.A., 1983, Mechanics of fold-and- thrust belts and accretionary wedges.: Journal of Geophysical Research, v. 88, p. 1153–1172, doi:10.1029/JB088iB02p01153.

De Toni, G.B., Bitencourt, M.F., Florisbal, L.M., Martini, A., and Nardi, L.V.S., 2023, Anatomy of the transpressional Dom Feliciano Belt and its pre-collisional isotopic (Sr–Nd) signatures: A contribution towards an integrated model for the Brasiliano/Pan-African orogenic cycle: Gondwana Research, v. 125, doi:10.1016/j.gr.2023.08.008.

De Wit, M., Jeffery, M., Bergh, H., and Nicolaysen, L., 1988, Geologic map of sectors of Gondwana: AAPG and University of Witwatersrand.

Degler, R., Pedrosa-Soares, A.C., Novo, T., Tedeschi, M., Silva, L.C., Dussin, I.A., and Lana, C.C., 2018, Rhyacian-Orosirian isotopic records from the basement of the Araçuaí-Ribeira orogenic system (SE Brazil): Links in the Congo-São Francisco palaeocontinent: Precambrian Research, v. 317, p. 179–195, doi:10.1016/j.precamres.2018.08.018.

Delpomdor, F.R.A., Ilambwetsi, A.M., Caxito, F.A., and Pedrosa-Soares, A.C., 2020, New interpretation of the basal Bambuí Group, Sete Lagoas High (Minas Gerais, E Brazil) by sedimentological studies and regional implications for the aftermath of the marinoan glaciation: correlations across Brazil and Central Africa: Geologica Belgica, v. 23, p. 1–17, doi:10.20341/gb.2019.010.

Dickin, A.P., 2005, Radiogenic isotope Geology: New York, Cambridge University Press, 471 p.

Dorr, J.V.N., and Barbosa, A.L.M., 1963, Geology and ore deposits of the Alegria District, Minas Gerais, Brazil.: USGS, 110 p., doi:10.3133/pp341C.

Dorr, J.V.N., Gair, J.E., Pomerene, J.B., and Rynearson, G.A., 1957, Revisão da Estratigrafia Pré-Cambriana do Quadrilátero Ferrífero: DNPM/DFPM Single Issue 81, 31 p.

Dunlap, W.J., Hirth, G., and Teyssier, C., 1997, Thermomechanical evolution of a ductile duplex: Tectonics, v. 16, p. 983–1000, doi:10.1029/97TC00614.

Dupont, H., 1995, O Grupo Conselheiro Mata no seu quadro paleogeográfico e estratigráfico, *in* VIII Simpósio de Geologia de Minas Gerais, Diamantina, SBG-MG, Anais, p. 9–10.

Dussin, T.M., 2000, A tectônica extensional paleoproterozóica na borda sudeste do Craton do São Francisco (SE, Brasil): geoquímica e petrologia das metaígneas: Geonomos, v. 8, p. 63–68.

Dussin, T.M., 1985, Geologia e geoquímica das formações ferríferas da Serra da Serpentina, Conceição do Mato Dentro, Minas Gerais [Master’s Dissertation]: UnB, 140 p.

Dussin, I.A., 1983, Geologia, gênese e controle dos depósitos de manganês associados ao Grupo Macaúbas, na borda ocidental da Serra do Cipó, MG (Área do Inhame) [Master's Dissertation]: UnB.

Dussin, I.A., and Dussin, T.M., 1995, Supergrupo Espinhaço: modelo de evolução geodinâmica: Geonomos, v. 3, p. 19–26, doi:10.18285/geonomos.v3i1.212.

Dussin, I.A., Garcia, A.J.V., Uhlein, A., Dardenne, M.A., and Dussin, T.M., 1987, Fácies eólico na Formação Galho do Miguel, Super-grupo Espinhaço (MG), *in* Simpósio sobre sistemas deposicionais no Pré-Cambriano, Ouro Preto, CPRM, Anais, v. 1, p. 85–96.

Dussin, I.A., Uhlein, A., and Dussin, T.M., 1984, Geologia da faixa móvel Espinhaço em sua porção meridional, M.G., *in* XXXIII Congresso Brasileiro de Geologia, Rio de Janeiro, SBG, Anais, p. 3118–3132.

Feng, R., Machado, N., and Ludden, J., 1993, Lead geochronology of zircon by LaserProbe-Inductively Coupled Plasma Mass Spectrometry (LP-ICPMS): Geochimica et Cosmochimica Acta, v. 57, p. 3479–3486, doi:10.1016/0016-7037(93)90553-9.

Fernandes, M.L.S., 2001, O Granito Borrachudos na região entre Guanhães e Dores de Guanhães, MG (Plutonito Morro do Urubu): gênese e evolução [Doctoral Thesis]: UFMG, 187 p.

Fernandes, M.L.S., Marciano, V.R.P.R.O., Oliveira, R.C., Correia-Neves, J.M., and Diláscio, M.V., 1994, Granitos Borrachudos: um exemplo de granitogênese anorogênica na porção central do estado de Minas Gerais: Geonomos, v. 2, p. 23–29, doi:10.18285/geonomos.v2i2.223.

Flinn, D., 1965, On the symmetry principle and the deformation ellipsoid: Geological Magazine, v. 102, p. 36–45, doi:10.1017/S0016756800053851.

Fogaça, A.C.C., Almeida-Abreu, P.Â., and Schorscher, J.H.D., 1984, Estratigrafia da sequência supracrustal arqueana na porção mediana-central da Serra do Espinhaço, MG, *in* XXXIII Congresso Brasileiro de Geologia, Rio de Janeiro, SBG, Anais, p. 2654–2667.

Fonte-Boa, T.M.R., 2017, Registros de eventos tafrogênicos intercalados tectonicamente no Complexo Pocrane, SE Minas Gerais [Master's Dissertation]: UFMG, 95 p.

Fossen, H., Cavalcante, G.C.G., Konopásek, J., Meira, V.T., Almeida, R.P., Hollanda, M.H.B.M., and Trompette, R.R., 2020, A critical discussion of the subduction-collision model for the Neoproterozoic Araçuaí-West Congo orogen: Precambrian Research, v. 343, p. 105715, doi:10.1016/j.precamres.2020.105715.

Fossen, H., and Tikoff, B., 1998, Extended models of transpression and transtension, and application to tectonic settings: Geological Society, London, Special Publications, v. 135, p. 15–33, doi:10.1144/GSL.SP.1998.135.01.02.

Fossen, H., Tikoff, B., and Teyssier, C., 1994, Strain modeling of transpressional and transtensional deformation: Norsk Geologisk Tidsskrift, v. 74, p. 135–145.

Fryer, B.J., Jackson, S.E., and Longerich, H.P., 1993, The application of laser ablation microprobe-inductively coupled plasma-mass spectrometry (LAM-ICP-MS) to in situ (U)Pb geochronology: Chemical Geology, v. 109, p. 1–8, doi:10.1016/0009-2541(93)90058-Q.

Fuhrmann, U., Lippolt, H.J., and Hess, J.C., 1987, Examination of some proposed K-Ar standards: 40Ar/39Ar analyses and conventional K-Ar data: Chemical Geology (Isotope Geoscience Section), v. 66, p. 41–51, doi:10.1016/0168-9622(87)90027-3.

Gehrels, G.E., 2011, Excel-based tools: University of Arizona LaserChron Center, Tucson, https://sites.google.com/laserchron.org/arizonalaserchroncenter/home.

Gomes, S.D., Figueiredo e Silva, R.C., Kemp, A.I.S., Santos, J.O.S., Hagemann, S.G., Lobato, L.M., Rosière, C.A., and Novo, T.A., 2020, Zircon U–Pb ages and Hf isotope compositions of Açucena Granite (Borrachudos Suite): implications for Statherian-Cambrian tectono-magmatic evolution of the southern border of the São Francisco Craton, Brazil: Journal of South American Earth Sciences, v. 100, p. 102543, doi:10.1016/j.jsames.2020.102543.

Gradim, D.T., 2012, O Orógeno Araçuaí na região de Viçosa, sudeste de Minas Gerais [Master's Dissertation]: UFMG, 130 p.

Graveleau, F., Malavieille, J., and Dominguez, S., 2012, Experimental modelling of orogenic wedges: a review: Tectonophysics, v. 538–540, p. 1–66, doi:10.1016/j.tecto.2012.01.027.

Grochowski, J., Kuchenbecker, M., Barbuena, D., and Novo, T.A., 2021, Disclosing Rhyacian/Orosirian orogenic magmatism within the Guanhães basement inlier, Araçuaí Orogen, Brazil: A new piece on the assembly of the São Francisco-Congo paleocontinent: Precambrian Research, v. 363, p. 106329, doi:10.1016/j.precamres.2021.106329.

Grossi-Sad, J.H., 1997, Mapa geológico da Folha Guanhães, Minas Gerais, *in* Grossi-Sad, J.H., Lobato, L.M., Pedrosa-Soares, A.C., and Soares-Filho, B.S. eds., Projeto Espinhaço: textos, mapas e anexos, Belo Horizonte, COMIG/CPRM, p. 2451–2531.

Hacker, B.R., Kelemen, P.B., and Behn, M.D., 2015, Continental lower crust: Annual Review of Earth and Planetary Sciences, v. 43, p. 167–205, doi:10.1146/annurev-earth-050212-124117.

Hartmann, L.A., Endo, I., Suita, M.T.F., Santos, J.O.S., Frantz, J.C., Carneiro, M.A., McNaughton, N.J., and Barley, M.E., 2006, Provenance and age delimitation of Quadrilátero Ferrífero sandstones based on zircon U–Pb isotopes: Journal of South American Earth Sciences, v. 20, p. 273–285, doi:10.1016/j.jsames.2005.07.015.

Heinrichs, H., and Herrmann, A.G., 1990, Praktikum der Analytischen Geochemie: Berlin, Springer, 667 p.

Herrgesell, G., and Pflug, R., 1986, The Thrust Belt of the Southern Serra do Espinhaço, Minas Gerais, Brazil: Zentralblatt für Geologie und Paläontologie Teil I, v. 9–10, p. 1405–1414, doi:10.1127/zbl_geol_pal_1/1985/1986/1405.

Hirth, G., and Tullis, J., 1992, Dislocation creep regimes in quartz aggregates: Journal of Structural Geology, v. 14, p. 145–159.

Hoffman, P.F., Kaufman, A.J., Halverson, G.P., and Schrag, D.P., 1998, A neoproterozoic Snowball Earth: Science, v. 281, p. 1342–1346, doi:10.1126/science.281.5381.1342.

Hoffmann, C., 1983, The Costa Sena Group - an Early Proterozoic supracrustal succession and the evolution of the southern Serra do Espinhaço, Minas Gerais, Brazil: Zentralblatt für Geologie und Paläontologie Teil I, v. 3–4, p. 446–458.

Hogmalm, K.J., Zack, T., Karlsson, A.K.O., Sjöqvist, A.S.L., and Garbe-Schönberg, D., 2017, In situ Rb-Sr and K-Ca dating by LA-ICP-MS/MS: An evaluation of N2O and SF6 as reaction gases: Journal of Analytical Atomic Spectrometry, v. 32, p. 305–313, doi:10.1039/c6ja00362a.

Iglesias, M.M., and Uhlein, A., 2009, Estratigrafia do Grupo Bambuí e coberturas fanerozóicas no vale do rio São Francisco, norte de Minas Gerais: Revista Brasileira de Geociências, v. 39, p. 256–266, doi:10.25249/0375-7536.2009392256266.

Isotta, C.A.L., Rocha-Campos, A.C., and Yoshida, R., 1969, Striated pavement of the Upper Pre-Cambrian glaciation in Brazil: Nature, v. 222, p. 466–468, doi:10.1038/222466a0.

Jelinek, V., 1981, Characterization of the magnetic fabric of rocks: Tectonophysics, v. 79, p. T63–T67, doi:10.1016/0040-1951(81)90110-4.

Kalt, H., 1991, Untersuchungeng zur Schertektonik in der Südlichen Serra do Espinhaço und im Angrenzenden Teil des São Francisco Beckens, Minas Gerais, Brasilien [Doctoral Thesis]: Albert-Ludwigs-Universität Freiburg, 118 p.

Karfunkel, J., and Hoppe, A., 1988, Late Proterozoic glaciation in central-eastern Brazil: synthesis and model: Palaeogeography, Palaeoclimatology, Palaeoecology, v. 65, p. 1–21, doi:10.1016/0031-0182(88)90108-3.

Karfunkel, B., and Karfunkel, J., 1976, Estudos petro-faciológicos do Grupo Macaúbas na porção meridiana da Serra do Espinhaço-MG, *in* XXIX Congresso Brasileiro de Geologia, Ouro Preto, SBG, Anais, v. 2, p. 179–188.

Karfunkel, J., Noce, C.M., and Kohler, H.Ch., 1991, A geologia do Grande Abrigo de Santana do Riacho e vizinhanças, Serra do Cipó, Minas Gerais: Arquivos do Museu de História Natural, v. 12, p. 33–42.

Karfunkel, J., Pedrosa-Soares, A.C., and Dussin, I.A., 1985, O Grupo Macaúbas em Minas Gerais: revisão dos conhecimentos, *in* 3º Simpósio de Geologia de Minas Gerais, Belo Horizonte, SBG-MG, Anais, v. 2, p. 45–59.

Kearey, P., Klepeis, K.A., and Vine, F.J., 2009, Global Tectonics: Oxford, Wiley-Blackwell, 482 p., doi:10.1126/science.168.3936.1250.

Kelley, S.P., 2002, K-Ar and Ar-Ar dating: Reviews in Mineralogy and Geochemistry, v. 47, p. 785–818, doi:10.2138/rmg.2002.47.17.

Kirkland, C.L., Daly, J.S., Eide, E.A., and Whitehouse, M.J., 2007, Tectonic evolution of the Arctic Norwegian Caledonides from a texturally- and structurally-constrained multi-isotopic (Ar-Ar, Rb-Sr, Sm-Nd, U-Pb) study: American Journal of Science, v. 307, p. 459–526, doi:10.2475/02.2007.06.

Knauer, L.G., 1990, Evolução geológica do pré-Cambriano da porção centro-leste da Serra do Espinhaço Meridional e metalogênese associada [Master's Dissertation]: Unicamp, 298 p.

Knauer, L.G., 2007, O Supergrupo Espinhaço em Minas Gerais: considerações sobre sua estratigrafia e seu arranjo estrutural: Geonomos, v. 15, p. 81–90, doi:10.18285/geonomos.v15i1.109.

Knauer, L.G., 1999, Serra do Espinhaço Meridional: Considerações sobre a estratigrafia e a análise da deformação das unidades proterozóicas [Doctoral Thesis]: UNESP, 244 p.

Knauer, L.G., and Schrank, A., 1993, A origem dos filitos hematíticos da Serra do Espinhaço Meridional, Minas Gerais: Geonomos, p. 33–38, doi:10.18285/geonomos.v1i1e2.235.

Konopásek, J., Cavalcante, G.C.G., Fossen, H., and Janoušek, V., 2020, Adamastor – an ocean that never existed? Earth-Science Reviews, v. 205, p. 103201, doi:10.1016/j.earscirev.2020.103201.

Kröner, A., Wan, Y., Liu, X., and Liu, D., 2014, Dating of zircon from high-grade rocks: which is the most reliable method? Geoscience Frontiers, v. 5, p. 515–523, doi:10.1016/j.gsf.2014.03.012.

Kruhl, J.H., 1996, Prism- and basal-plane parallel subgrain boundaries in quartz: a microstructural geothermobarometer: Journal of Metamorphic Geology, v. 14, p. 581–589, doi:10.1046/j.1525-1314.1996.00413.x.

Kübler, B., 1967, La cristallinité de l'illite et les zones tout à fait supérieures du métamorphisme, *in* Etages Tectoniques, Neuchâtel, p. 105–122.

Kuchenbecker, M., Pedrosa-Soares, A.C., Babinski, M., and Fanning, M., 2015, Detrital zircon age patterns and provenance assessment for pre-glacial to post-glacial successions of the Neoproterozoic Macaúbas Group, Araçuaí Orogen, Brazil: Precambrian Research, v. 266, p. 12–26, doi:10.1016/j.precamres.2015.04.016.

Kuchenbecker, M., Pedrosa-Soares, A.C., Babinski, M., Reis, H.L.S., Atman, D., and Costa, R.D., 2020, Towards an integrated tectonic model for the interaction between the Bambuí basin and the

adjoining orogenic belts: Evidences from the detrital zircon record of syn-orogenic units: Journal of South American Earth Sciences, v. 104, p. 102831, doi:10.1016/j.jsames.2020.102831.

Kuribara, Y., Tsunogae, T., Santosh, M.W., Takamura, Y., Costa, A.G., and Rosière, C.A., 2019, Eoarchean to Neoproterozoic crustal evolution of the Mantiqueira and the Juiz de Fora Complexes, SE Brazil: petrology, geochemistry, zircon U-Pb geochronology and Lu-Hf isotopes: Precambrian Research, v. 323, p. 82–101, doi:10.1016/j.precamres.2019.01.008.

Lammie, D., McQuarrie, N., and Sak, P.B., 2020, Quantifying shortening across the central Appalachian fold-thrust belt, Virginia and West Virginia, USA: reconciling grain-, outcrop-, and map-scale shortening: Geosphere, v. 16, p. 1276–1292, doi:10.1130/GES02016.1.

Lana, C.C., Alkmim, F.F., Armstrong, R., Scholz, R., Romano, R., and Nalini jr., H.A., 2013, The ancestry and magmatic evolution of Archaean TTG rocks of the Quadrilátero Ferrífero province, southeast Brazil: Precambrian Research, v. 231, p. 157–173, doi:10.1016/j.precamres.2013.03.008.

Launeau, P., and Cruden, A.R., 1998, Magmatic fabric acquisition mechanisms in a syenite: results of a combined anisotropy of magnetic susceptibility and image analysis study: Journal of Geophysical Research: Solid Earth, v. 103, p. 5067–5089, doi:10.1029/97jb02670.

Launeau, P., and Robin, P.-Y.F., 2005, Determination of fabric and strain ellipsoids from measured sectional ellipses - implementation and applications: Journal of Structural Geology, v. 27, p. 2223–2233, doi:10.1016/j.jsg.2005.08.003.

Launeau, P., and Robin, P.-Y.F., 2003, SPO 2003: Université de Nantes, http://www.sciences.univ-nantes.fr/lpgnantes/SPO.

Lee, J.K.W., 2015, Ar-Ar and K-Ar dating, *in* Encyclopedia of scientific dating methods, Dordrecht, Springer, p. 58–72.

Li, J., and Mitra, S., 2017, Geometry and evolution of fold-thrust structures at the boundaries between frictional and ductile detachments: Marine and Petroleum Geology, v. 85, p. 16–34, doi:10.1016/j.marpetgeo.2017.04.011.

Li, Y., and Vermeesch, P., 2021, Short communication: Inverse isochron regression for Re–Os, K–Ca and other chronometers: Geochronology, v. 3, p. 415–420, doi:10.5194/gchron-2021-7.

Liebmann, J., Kirkland, C.L., Kelsey, D.E., Korhonen, F.J., and Rankenburg, K., 2022, Lithological fabric as a proxy for Rb–Sr isotopic complexity: Chemical Geology, v. 608, p. 121041, doi:10.1016/j.chemgeo.2022.121041.

Lima, O.N.B., 2005, Grupo Bambuí: estratigrafia regional no alto Rio São Francisco e geologia dos depósitos fosfáticos da Serra da Saudade-MG [Master’s Dissertation]: UFMG, 142 p.

Lima, O.N.B., Uhlein, A., and Britto, W., 2007, Estratigrafia do Grupo Bambuí na Serra da Saudade e geologia do depósito fosfático de Cedro do Abaeté, Minas Gerais: Revista Brasileira de Geociências, v. 37, p. 204–215, doi:10.25249/0375-7536.200737s4204215.

Lister, G.S., and Snoke, A.W., 1984, S-C mylonites: Journal of Structural Geology, v. 6, p. 617–638.

Lopes-Silva, L., and Knauer, L.G., 2011, Posicionamento estratigráfico da Formação Bandeirinha na região de Diamantina, Minas Gerais: Grupo Costa Sena ou Supergrupo Espinhaço? Geonomos, v. 19, p. 131–151, doi:10.18285/geonomos.v19i2.49.

Ludwig, K.R., 2008, Isoplot 4.15 - a geochronological toolkit for Microsoft Excel: UC Berkeley.

Machado, N., Noce, C.M., Ladeira, E.A., and Belo-de-Oliveira, O.A., 1992, U-Pb Geochronology of Archean magmatism and Proterozoic metamorphism in the São Francisco craton, Brazil: Geological Society of America Bulletin, v. 104, p. 1221–1227, doi:10.1130/0016-7606(1992)104<1221:UPGOAM>2.3.CO;2.

Machado, N., Schrank, A., Abreu, F.R., Knauer, L.G., and Almeida-Abreu, P.Â., 1989, Resultados preliminares da geocronologia U/Pb na Serra do Espinhaço Meridional, *in* V Simpósio de Geologia de Minas Gerais, Belo Horizonte, SBG-MG, Anais, p. 171–174.

Magalhães, L., 1988, Análise Estrutural qualitativa nos sedimentos do Grupo Bambuí: UFOP, 109 p.

Magalhães, J.R., 2019, Eventos magmáticos e metamórficos no Bloco Guanhães (MG): caracterização petrogenética e significado geodinâmico dos registros Estateriano, Criogeniano e Ediacarano na evolução do Paleocontinente São Francisco: UFMG, 286 p., http://rigeo.cprm.gov.br/jspui/handle/doc/21232.

Mainprice, D., and Nicolas, A., 1989, Development of shape and lattice preferred orientations: application to the seismic anisotropy of the lower crust: Journal of Structural Geology, v. 11, p. 175–189, doi:10.1016/0191-8141(89)90042-4.

Marshak, S., and Alkmim, F.F., 1989, Proterozoic contraction/extension tectonics of the southern São Francisco Region, Minas Gerais, Brazil: Tectonics, v. 8, p. 555–571, doi:10.1029/TC008i003p00555.

Martins, M.S., Karfunkel, J., Noce, C.M., Babinski, M., Pedrosa-Soares, A.C., Sial, A.N., and Liu, D., 2008, A sequência pré-glacial do Grupo Macaúbas na área-tipo e o registro da abertura do rifte Araçuaí: Revista Brasileira de Geociências, v. 38, p. 761–772, doi:10.25249/0375-7536.2008384761772.

Martins, M., and Lemos, V.B., 2007, Análise estratigráfica das seqüências neoproterozóicas da Bacia do São Francisco: Revista Brasileira de Geociências, v. 37, p. 156–167, doi:10.25249/0375-7536.200737S4156167.

Martins-Neto, M.A., 1998, O Supergrupo Espinhaço em Minas Gerais: registro de uma bacia Rifte-Sag do Paleo/Mesoproterozóico: Revista Brasileira de Geociências, v. 28, p. 151–168.

Martins-Neto, M.A., 2009, Sequence stratigraphic framework of Proterozoic successions in eastern Brazil: Marine and Petroleum Geology, v. 26, p. 163–176, doi:10.1016/j.marpetgeo.2007.10.001.

Martins-Neto, M.A., 2000, Tectonics and sedimentation in a paleo/mesoproterozoic rift-sag basin (Espinhaco basin, southeastern Brazil): Precambrian Research, v. 103, p. 147–173, doi:10.1016/S0301-9268(00)00080-2.

Martins-Neto, M.A., and Hercos, C.M., 2002, Sedimentation and tectonic setting of Early Neoproterozoic glacial deposits in south-eastern Brazil, *in* Alterman, W. and Corcoran, P.L. eds., Precambrian sedimentary environments: A modern approach to ancient depositional systems, Oxford, Blackwell, Special Publication of the International Association of Sedimentologists, v. 33, p. 383–403.

Martins-Neto, M.A., Pedrosa-Soares, A.C., and Lima, S.A.A., 2001, Tectono-sedimentary evolution of sedimentary basins from Late Paleoproterozoic to Late Neoproterozoic in the São Francisco craton and Araçuaí fold belt, eastern Brazil: Sedimentary Geology, v. 141–142, p. 343–370, doi:10.1016/S0037-0738(01)00082-3.

McQuarrie, N., and Ehlers, T.A., 2017, Techniques for understanding fold-and-thrust belt kinematics and thermal evolution, *in* Law, R.D., Thigpen, J.R., Merschat, A.J., and Stowell, H.H. eds., Linkages and Feedbacks in Orogenic Systems: Geological Society of America Memoir, Boulder, Geological Society of America, v. 213, p. 25–54, doi:10.1130/2017.1213(02).

McSween, H.Y., Richardson, S.M., and Uhle, M.E., 2003, Geochemistry: pathways and processes: New York, Columbia University Press, 363 p.

Meira, V.T., García-Casco, A., Juliani, C., Almeida, R.P., and Schorscher, J.H.D., 2015, The role of intracontinental deformation in supercontinent assembly: Insights from the Ribeira Belt, Southeastern Brazil (Neoproterozoic West Gondwana): Terra Nova, v. 27, p. 206–217, doi:10.1111/ter.12149.

Menezes, R.C.L., Conceição, H., Rosa, M.L.S., Macambira, M.J.B., Galarza, M.A., and Rios, D.C., 2012, Geoquímica e Geocronologia de granitos anorogênicos tonianos (ca. 914-899 Ma) da Faixa Araçuaí no sul do estado da Bahia: Geonomos, v. 20, p. 1–13, doi:10.18285/geonomos.v20i1.21.

Metzger, K., and Krogstad, E.J., 1997, Interpretation of discordant U-Pb zircon ages: An evaluation: Journal of Metamorphic Geology, v. 15, p. 127–140.

Moores, E.M., and Twiss, R.J., 1995, Tectonics (W. Press, Ed.): Long Grove, Waveland, 415 p.

Moraes, L.J., and Guimarães, D., 1930, Geologia da região diamantífera do norte de Minas Gerais: Anais da Academia Brasileira de Ciências, v. 2, p. 153–186.

Morales, L.F.G., Hinrichs, R., and Fernandes, L.A.D., 2007, A técnica de Difração de Elétrons Retro-Espalhados (EBSD) em Microscópio Eletrônico de Varredura (MEV) e sua aplicação no estudo de rochas deformadas: Pesquisas em Geociências, v. 34, p. 19, doi:10.22456/1807-9806.19459.

Moreira, I.C., Oliveira, E.P., and Sousa, D.F.M., 2022, Evolution of the 3.65–2.58 Ga Mairi Gneiss Complex, Brazil: Implications for growth of the continental crust in the São Francisco Craton: Geoscience Frontiers, v. 13, p. 101366, doi:10.1016/j.gsf.2022.101366.

Moreira, D.S., Uhlein, A., Dussin, I.A., Uhlein, G.J., and Misuzaki, A.M.P., 2020, A Cambrian age for the upper Bambuí Group, Brazil, supported by the first U-Pb dating of volcaniclastic bed: Journal of South American Earth Sciences, v. 99, p. 102503, doi:10.1016/j.jsames.2020.102503.

Morley, C.K., 1988, Out-of-sequence thrusts: Tectonics, v. 7, p. 539–561, doi:10.1029/TC007i003p00539.

Mourão, M.A.A., 1995, A unidade fosfática da Formação Sopa-Brumadinho, Supergrupo Espinhaço, região de Conceição do Mato Dentro, Minas Gerais [Master's Dissertation]: UnB, 138 p.

Nemčok, M., Schamel, S., and Gayer, R.A., 2005, Thrustbelts: New York, Cambridge University Press, 541 p.

Noce, C.M., 1995, Geocronologia dos eventos magmáticos sedimentares e metamórficos na região do Quadrilátero Ferrífero, Minas Gerais [Doctoral Thesis]: USP, 128 p.

Noce, C.M., Machado, N., and Teixeira, W., 1994, O Complexo Belo Horizonte e a evolução arqueana do Quadrilátero Ferrífero, Minas Gerais, *in* Congresso Brasileiro de Geologia, Balneário Camboriú, SBG, Anais, v. 1, p. 68–69.

Noce, C.M., Machado, N., and Teixeira, W., 1998, U-Pb Geochronology of gneisses and granitoids in the Quadrilátero Ferrífero (Southern São Francisco Craton): age constraints for Archean and Paleoproterozoic magmatism and metamorphism: Revista Brasileira de Geociências, v. 28, p. 95–102.

Noce, C.M., Pedrosa-Soares, A.C., Grossi-Sad, J.H., Baars, F.J., Guimarães, M.L.V., Mourão, M.A.A., Oliveira, M.J.R., and Roque, N.C., 1997, Nova divisão estratigráfica regional do Grupo Macaúbas na Faixa Araçuaí: o registro de uma bacia neoproterozóica, *in* IX Simpósio de Geologia de Minas Gerais, Ouro Preto, SBG-MG, Anais, p. 29–31.

Okudaira, T., Takeshita, T., and Toriumi, M., 1998, Discussion - Prism- and basal-plane parallel subgrain boundaries in quartz: a microstructural geothermobarometer: Journal of Metamorphic Geology, v. 16, p. 141–146.

Olierook, H.K.H. et al., 2020, Resolving multiple geological events using in situ Rb–Sr geochronology: implications for metallogenesis at Tropicana, Western Australia: Geochronology, v. 2, p. 283–303, doi:10.5194/gchron-2-283-2020.

Oliveira, M.A.M., 1967, Contribuição à geologia da parte sul da Bacia do São Francisco e áreas adjacentes: Petrobras Série Técnica, 35 p.

Oliveira, F.V.C., 1994, Estilo estrutural e curvatura da zona limite do Cráton do São Francisco nas regiões de Presidente Juscelino e Cardeal Mota - MG [Master's Dissertation]: UFOP, 214 p.

Oliveira, A.A.K., 2002, Estruturação e alteração metassomática do ortognaisse Açucena (Suíte Borrachudos) na região de Ipatinga, Minas Gerais [Master's Dissertation]: UFMG, 90 p., http://rigeo.cprm.gov.br/jspui/handle/doc/243%0A.

Oliveira, M.J.R., Fogaça, A.C.C., and Mourão, M.A.A., 1997, Mapa geológico da Folha Baldim, Minas Gerais, Brasil: COMIG/CPRM Projeto Espinhaço.

Oliveira, R.G., Martins, M.S., Queiroga, G.N., Souza, M.E.S., Lana, C.C., Alkmim, A.R., Silva, M.A.L., Bueno, C., and Linhares, D., 2021, Sedimentary provenance and role of tectonic inheritance on the control of the Macaúbas group, eastern margin of São Francisco Craton (SE Brazil): Journal of South American Earth Sciences, v. 109, p. 103210, doi:10.1016/j.jsames.2021.103210.

Oliveira, E.P., McNaughton, N.J., Zincone, S.A., and Talavera, C., 2020, Birthplace of the São Francisco Craton, Brazil: evidence from 3.60 to 3.64 Ga gneisses of the Mairi Gneiss Complex: Terra Nova, v. 32, p. 281–289, doi:10.1111/ter.12460.

Oliveira, L.B.E.R., Rosière, C.A., Rolim, V.K., and Santos, J.O.S., 2019, Novos dados geocronológicos U-Pb de zircões detríticos na Serra do Espinhaço Meridional, regiões de Altamira e Ipoema: Geociências, v. 38, p. 611–637, doi:10.5016/geociencias.v38i3.13775.

Oliveira, I.P.O., and Torres, J.L.L., 2014, Mapeamento geológico em escala 1:25.000 da região de Santana do Riacho, Minas Gerais [Graduation Project]: UFMG, 117 p.

Padilha, A.F., and Sandim, H.R.Z., 2021, EBSD (Electron Backscatter Diffraction) para Iniciantes:

Pagung, R., Rosière, C.A., and Figueiredo e Silva, R.C., 2023, The Serra da Serpentina Group: a back-arc basin related to the Paleoproterozoic Minas-Bahia orogeny? Journal of South American Earth Sciences, v. 128, p. 104427, doi:10.1016/j.jsames.2023.104427.

Paiva-Filho, A., and Ponçano, W.L., 1972, Mapa geológico preliminar da região de Jequitaí, Estado de Minas Gerais, *in* XXVI Congresso Brasileiro de Geologia, Belém, SBG, Anais, v. 1, p. 95–102.

Passchier, C.W., and Trouw, R.A.J., 2005, Microtectonics: Berlin, Springer, v. 275, 366 p.

Paton, C., Hellstrom, J., Paul, B., Woodhead, J., and Hergt, J., 2011, Iolite: Freeware for the visualisation and processing of mass spectrometric data: Journal of Analytical Atomic Spectrometry, v. 26, p. 2508, doi:10.1039/c1ja10172b.

Paul, A., Kaviani, A., Hatzfeld, D., Vergne, J., and Mokhtari, M., 2006, Seismological evidence for crustal-scale thrusting in the Zagros mountain belt (Iran): Geophysical Journal International, v. 166, p. 227–237, doi:10.1111/j.1365-246X.2006.02920.x.

Paula-Santos, G.M., Babinski, M., Kuchenbecker, M., Caetano-Filho, S., Trindade, R.I.F., and Pedrosa-Soares, A.C., 2015, New evidence of an Ediacaran age for the Bambuí Group in southern São Francisco craton (eastern Brazil) from zircon U-Pb data and isotope chemostratigraphy: Gondwana Research, v. 28, p. 702–720, doi:10.1016/j.gr.2014.07.012.

Paula-Santos, G.M., Caetano-Filho, S., Babinski, M., Trindade, R.I.F., and Guacaneme, C., 2017, Tracking connection and restriction of West Gondwana São Francisco Basin through isotope chemostratigraphy: Gondwana Research, v. 42, p. 280–305, doi:10.1016/j.gr.2016.10.012.

Pedrosa-Soares, A.C., and Alkmim, F.F., 2011, How many rifting events preceded the development of the Araçuaí-West Congo Orogen? Geonomos, v. 19, p. 244–251.

Pedrosa-Soares, A.C., Babinski, M., Noce, C.M., Martins, M.S., Queiroga, G.N., and Vilela, F., 2011, The Neoproterozoic Macaúbas Group, Araçuaí Orogen, SE Brazil, *in* Arnaud, E., Halverson, G.P., and Shields-Zhou, G. eds., The geological record of Neoproterozoic glaciations, London, The Geological Society of London, v. 36, p. 523–534, doi:10.1144/M36.49.

Pedrosa-Soares, A.C., Dardenne, M.A., Hasui, Y., Castro, F.D.C., Carvalho, M.V.A., and Reis, A.C., 1994, Mapa geológico do estado de Minas Gerais e nota explicativa: Belo Horizonte, SEME/COMIG.

Pedrosa-Soares, A.C., Noce, C.M., Vidal, P., Monteiro, R.L.B.P., and Leonardos, O.H., 1992, Toward a new tectonic model for the late Proterozoic Araçuaí (SE Brazil) - West Congolian (SW Africa) Belt: Journal of South American Earth Sciences, v. 6, p. 33–47, doi:10.1016/0895-9811(92)90015-Q.

Pedrosa-Soares, A.C., Noce, C.M., Wiedemann, C.M., and Pinto, C.P., 2001, The Araçuaí-West-Congo Orogen in Brazil: an overview of a confined orogen formed during Gondwanaland assembly: Precambrian Research, v. 110, p. 307–323.

Pedrosa-Soares, A.C., Vidal, P., Leonardos, O.H., and Brito-Neves, B.B., 1998, Neoproterozoic oceanic remnants in eastern Brazil: further evidence and refutation of an exclusively ensialic evolution for the Araçuaí-West Congo Orogen: Geology, v. 26, p. 519–522, doi:10.1130/0091-7613(1998)026<0519:NORIEB>2.3.CO;2.

Peixoto, E.I.N., 2013, Caracterização estratigráfica, tectônica, metamórfica e geocronológica do Orógeno Araçuaí na região de São José da Safira-Virgolândia, Minas Gerais [Master's Dissertation]: UFMG, 169 p.

Peixoto, E.I.N., Pedrosa-Soares, A.C., Alkmim, F.F., and Dussin, I.A., 2015, A suture-related accretionary wedge formed in the Neoproterozoic Araçuaí orogen (SE Brazil) during Western Gondwanaland assembly: Gondwana Research, v. 27, p. 878–896, doi:10.1016/j.gr.2013.11.010.

Perrella, P., Uhlein, A., Uhlein, G.J., Sial, A.N., Pedrosa-Soares, A.C., and Lima, O.N.B., 2017, Facies analysis, sequence stratigraphy and chemostratigraphy of the Sete Lagoas Formation (Bambui Group), northern Minas Gerais State, Brazil: evidence of a cap carbonate deposited on the Januária basement high: Brazilian Journal of Geology, v. 47, p. 59–77, doi:10.1590/2317-4889201720160112.

Pfiffner, O.A., 2006, Thick-skinned and thin-skinned styles of continental contraction, *in* Stefano Mazzoli and Butler, R.W.H. eds., Styles of continental contraction, Boulder, Geological Society of America, v. 2414, p. 153–177, doi:10.1130/2006.2414(09).

Pfiffner, O.A., 2017, Thick-skinned and thin-skinned Tectonics: a global perspective: Geosciences, v. 7, p. 71, doi:10.3390/geosciences7030071.

Pflug, R., 1965, A geologia da parte meridional da Serra do Espinhaço e zonas adjacentes, Minas Gerais: Rio de Janeiro, DNPM/DGM, v. 226, 55 p.

Pflug, R., 1968, Observações sobre a estratigrafia da Série Minas na região de Diamantina, Minas Gerais: Rio de Janeiro, DNPM/DGM, 20 p.

Pickhardt, C., Dietze, H.-J., and Becker, J.S., 2005, Laser ablation inductively coupled plasma mass spectrometry for direct isotope ratio measurements on solid samples: International Journal of Mass Spectrometry, v. 242, p. 273–280, doi:10.1016/j.ijms.2004.12.014.

Pimentel, M.M., 2016, The tectonic evolution of the Neoproterozoic Brasília Belt, central Brazil: A geochronological and isotopic approach: Brazilian Journal of Geology, v. 46, p. 67–82, doi:10.1590/2317-4889201620150004.

Pimentel, M.M., Dardenne, M.A., Fuck, R.A., Viana, M.G., Junges, S.L., Fischel, D.P., Seer, H.J., and Dantas, E.L., 2001, Nd isotopes and the provenance of detrital sediments of the Neoproterozoic Brasília Belt, central Brazil: Journal of South American Earth Sciences, v. 14, p. 571–585.

Pimentel, M.M., Rodrigues, J.B., DellaGiustina, M.E.S., Junges, S., Matteini, M., and Armstrong, R., 2011, The tectonic evolution of the Neoproterozoic Brasília Belt, central Brazil, based on SHRIMP and LA-ICPMS U–Pb sedimentary provenance data: a review: Journal of South American Earth Sciences, v. 31, p. 345–357, doi:10.1016/j.jsames.2011.02.011.

Pisarevsky, S.A., Murphy, J.B., Cawood, P.A., and Collins, A.S., 2008, Late Neoproterozoic and Early Cambrian palaeogeography: models and problems: Geological Society Special Publication, v. 294, p. 9–31, doi:10.1144/SP294.2.

Porada, H., 1989, Pan-African rifting and orogenesis in southern to equatorial Africa and Eastern Brazil: Precambrian Research, v. 44, p. 103–136.

Prior, D.J. et al., 1999, The application of electron backscatter diffraction and orientation contrast imaging in the SEM to textural problems in rocks: American Mineralogist, v. 84, p. 1741–1759, doi:10.2138/am-1999-11-1204.

Queiroga, G.N., 2010, Caracterização de restos de litosfera oceânica do Orógeno Araçuaí entre os paralelos 17º e 21ºS [Doctoral Thesis]: UFMG, 180 p.

Queiroga, G.N., Pedrosa-Soares, A.C., Noce, C.M., Alkmim, F.F., Pimentel, M.M., Dantas, E.L., Martins, M.S., Castañeda, C., Suita, M.T.F., and Prichard, H., 2007, Age of the Ribeirão Da Folha Ophiolite, Araçuaí Orogen: the U-Pb Zircon (LA-ICPMS) dating of a Plagiogranite: Geonomos, v. 15, p. 61–65, doi:10.18285/geonomos.v15i1.107.

Queiroga, G.N., Schulz, B., Martins, M.S., Castro, M.P., Pedrosa-Soares, A.C., Jordt-Evangelista, H., and Silva, A.L., 2016, Thermobarometry and electron-microprobe Th-U-Pb monazite dating in garnet metapelites from the Capelinha Formation, Araçuaí Orogen, Brazil: Revista Escola de Minas, v. 69, p. 33–44, doi:10.1590/0370-44672015690066.

Queiroz, Y.S. et al., 2019, Pseudosection modeling and U-Pb geochronology on Piranga schists: role of Brasiliano Orogeny in the Southeastern Quadrilátero Ferrífero, Minas Gerais, Brazil: Brazilian Journal of Geology, v. 49, p. e20180136, doi:10.1590/2317-4889201920180136.

Ragan, D.M., 2009, Structural Geology: an introduction to geometrical techniques: New York, Cambridge University Press, v. 148, 602 p.

Ramsay, J.G., and Huber, M.I., 1983, The techniques of modern Structural Geology. Volume 1, Strain analysis.: London, Academic Press, 307 p.

Ramsay, J.G., and Wood, D.S., 1973, The geometric effects of volume change during deformation processes: Tectonophysics, v. 16, p. 263–277, doi:10.1016/0040-1951(73)90015-2.

Redaa, A., Farkaš, J., Gilbert, S., Collins, A.S., Wade, B., Löhr, S., Zack, T., and Garbe-Schönberg, D., 2021, Assessment of elemental fractionation and matrix effects during in situ Rb–Sr dating of phlogopite by LA-ICP-MS/MS: implications for the accuracy and precision of mineral ages: Journal of Analytical Atomic Spectrometry, v. 36, p. 322–344, doi:10.1039/D0JA00299B.

Reis, H.L.S., 2016, Neoproterozoic evolution of the São Francisco Basin, SE Brazil: effects of tectonic inheritance on foreland sedimentation and deformation [Doctoral Thesis]: UFOP, 191 p.

Reis, H.L.S., Suss, J.F., Fonseca, R.C.S., and Alkmim, F.F., 2017, Ediacaran forebulge grabens of the southern São Francisco basin, SE Brazil: Craton interior dynamics during West Gondwana assembly: Precambrian Research, v. 302, p. 150–170, doi:10.1016/j.precamres.2017.09.023.

Ribeiro, J.H., 2010, Carta geológica - Folha SE-23-Z-C-III Baldim: CPRM Projeto Sete Lagoas-Abaeté.

Ribeiro, B.V., Kirkland, C.L., Kelsey, D.E., Reddy, S.M., Hartnady, M.I.H., Faleiros, F.M., Rankenburg, K., Liebmann, J., Korhonen, F.J., and Clark, C., 2023, Time-strain evolution of shear zones from petrographically constrained Rb–Sr muscovite analysis: Earth and Planetary Science Letters, v. 602, p. 117969, doi:10.1016/j.epsl.2022.117969.

Rocha-Campos, A.C., Brito-Neves, B.B., Babinski, M., Santos, P.R., Oliveira, S.M.B., and Romano, A.W., 2011, Moema laminites: a newly recognized Neoproterozoic (?) glaciogenic unit, São Francisco Basin, Brazil, *in* Arnaud, E., Halverson, G.P., and Shields-Zhou, G. eds., Geological Society Memoir, Londres, The Geological Society of London, v. 36, p. 535–540, doi:10.1144/M36.50.

Rocha-Campos, A.C., and Hasui, Y., 1981, Tillites of the Macaúbas Group (Proterozoic) in central Minas Gerais and Southern Bahia, Brazil, *in* Hambrey, M.J. and Harland, W.B. eds., Earth's Pre-Pleistocene glacial record, Cambridge, Cambridge University Press, p. 924–927.

Rocha-Campos, A.C., Young, G.M., and Santos, P.R., 1996, Re-examination of a striated pavement near Jequitaí, MG: Implications for Proterozoic stratigraphy and glacial geology: Anais da Academia Brasileira de Ciências, v. 68, p. 593.

Rodrigues, J.B., 2008, Proveniência de sedimentos dos grupos Canastra , Ibiá , Vazante e Bambuí – Um estudo de zircões detríticos e Idades Modelo Sm-Nd:

Rolim, V.K., 2016, As formações ferríferas da região de Conceição Do Mato Dentro - MG: posicionamento estratigráfico, evolução tectônica, geocronologia, características geoquímicas e gênese dos minérios [Doctoral Thesis]: UFMG, 215 p.

Rolim, V.K., Rosière, C.A., Santos, J.O.S., and McNaughton, N.J., 2016, The Orosirian-Statherian banded iron formation-bearing sequences of the southern border of the Espinhaço Range, Southeast Brazil: Journal of South American Earth Sciences, v. 65, p. 43–66, doi:10.1016/j.jsames.2015.11.003.

Romano, A.W., 2007, Geologia da Folha Pará de Minas SE.23-Z-C-IV: CPRM Programa Geologia do Brasil.

Romano, A.W., Araújo, J.C.S., Knauer, L.G., and Paiva, C.T., 2014, Geologia e recursos minerais da folha Contagem - SE.23-Z-C-V: CPRM Programa Geologia do Brasil.

Romano, A.W., and Knauer, L.G., 2003, Evidências da glaciação neoproterozoica na base do Grupo Bambuí - região de Onça do Pitangui - Minas Gerais, *in* 12º Simpósio de Geologia de Minas Gerais, Ouro Preto, SBG-MG, Anais, v. 1.

Romeiro-Silva, P.C., and Zalán, P.V., 2005, Contribuição da sísmica de reflexão na determinação do limite oeste do Cráton do São Francisco, *in* III Simpósio sobre o Cráton do São Francisco, Salvador, SBG, Anais, v. 1, p. 44–47.

Rösel, D., and Zack, T., 2022, LA-ICP-MS/MS single-spot Rb-Sr dating: Geostandards and Geoanalytical Research, v. 46, p. 143–168, doi:10.1111/ggr.12414.

Sanderson, D.J., and Marchini, W.R.D., 1984, Transpression: Journal of Structural Geology, v. 6, p. 449–458, doi:10.1016/0191-8141(84)90058-0.

Santos, M.N., 2015, Geocronologia U/Pb em zircões detríticos e a evolução tectônica e estratigráfica da Bacia Espinhaço no setor meridional [Doctoral Thesis]: UnB, 143 p.

Santos, M.N., Chemale Jr., F., Dussin, I.A., Martins, M.S., Assis, T.A.R., Jelinek, A.R., Guadagnin, F., and Armstrong, R., 2013, Sedimentological and paleoenvironmental constraints of the Statherian and Stenian Espinhaço rift system, Brazil: Sedimentary Geology, v. 290, p. 47–59, doi:10.1016/j.sedgeo.2013.03.002.

Santos, M.N., Chemale Jr., F., Dussin, I.A., Martins, M.S., Queiroga, G.N., Pinto, R.T.R., Santos, A.N., and Armstrong, R., 2015, Provenance and paleogeographic reconstruction of a mesoproterozoic intracratonic sag basin (Upper Espinhaço Basin, Brazil): Sedimentary Geology, v. 318, p. 40–57.

Santos, C., Danderfer-Filho, A., Queiroga, G.N., Zincone, S.A., Castro, M.P., and Lana, C., 2020, Ferroan alkalic volcanism associated with Calymmian rifting in the Paramirim aulacogen, São Francisco craton, Brazil: New insights from lithofacies analysis and evidence of mantle-derived alkaline H2O-rich metasomatic fluids affecting ancient crustal materials: Precambrian Research, v. 340, p. 105632, doi:10.1016/j.precamres.2020.105632.

Schaltegger, U., Schmitt, A.K., and Horstwood, M.S.A., 2015, U-Th-Pb zircon geochronology by ID-TIMS, SIMS, and laser ablation ICP-MS: recipes, interpretations, and opportunities: Chemical Geology, v. 402, p. 89–110, doi:10.1016/j.chemgeo.2015.02.028.

Schmid, S.M., 1994, Textures of geologic material: computer model predictions versus empirical interpretations based on rock deformation experiments and field studies, *in* Bunge, H.J., Siegesmund, S., Skrotzki, W., and Weber, K. eds., Textures of geological materials, Oberursel, DGM Informationsgesellschaft, p. 279–301.

Schmid, S.M., and Casey, M., 1986, Complete fabric analysis of some commonly observed quartz C-axis patterns, *in* Hobbs, B.E. and Heard, H.C. eds., Mineral and rock deformation: laboratory studies - the Patterson volume, Washington, D.C., American Geophysical Union, p. 263–286, doi:10.1029/GM036p0263.

Schobbenhaus, C., 1996, As tafrogêneses superpostas Espinhaço e Santo Onofre, estado da Bahia: revisão e novas propostas: Revista Brasileira de Geociências, v. 26, p. 265–276, doi:10.25249/0375-7536.19964265276.

Schoene, B., 2014, U-Th-Pb Geochronology, *in* Holland, H.D. and Turekian, K.K. eds., Treatise on geochemistry, Amsterdam, Elsevier, v. 4, p. 341–378, doi:10.1016/B978-0-08-095975-7.00310-7.

Schöll, W.U., 1972, Der südwestliche Randbereich der Espinhaço-Zone, Minas Gerais, Brasilien: Geologische Rundschau, v. 61, p. 201–216.

Schöll, W.U., 1973, Sedimentologie und Geochemie der Bambuí Gruppe am SE-Rand des São Francisco Beckens, Minas Gerais, Brasilien [Doctoral Thesis]: Universität Heidelberg, 90 p.

Schöll, W.U., and Fogaça, A.C.C., 1979, Estratigrafia da Serra do Espinhaço na região de Diamantina, *in* I Simpósio de Geologia de Minas Gerais, Diamantina, SBG-MG, Anais, p. 55–73.

Schumacher, E., 1975, Herstellung von 99,9997% 38Ar für die 40K/40Ar Geochronologie: Geochronologia Chimia, v. 24, p. 441–442.

Sgarbi, G.N.C., Tuller, M.P., Ribeiro, J.H., and Martins-Neto, M.A., 2003, The Carrancas Facies and the Sete Lagoas Formation: the record of the Neoproterozoic Snowball Earth glaciation in the Bambuí Group, São Francisco Basin, *in* 12º Simpósio de Geologia de Minas Gerais, Ouro Preto, SBG-MG, Anais, v. 1.

Silva, G.L., Freitas, M.A., and Silveira, V.D., 2007, Geologia da região centro-oeste do Parque Nacional da Serra do Cipó, MG - municípios de Jaboticatubas e Santana do Riacho [Graduation Project]: UFMG, 149 p.

Silva, L.C., Pedrosa-Soares, A.C., Armstrong, R., and Noce, C.M., 2011, Determinando a duração do período colisional do Orógeno Araçuaí com base em geocronologia U-Pb de alta resolução em zircão: uma contribuição para a história da amalgamação do Gondwana Ocidental: Geonomos, v. 19, p. 180–197.

Silva, L.C., Pedrosa-Soares, A.C., Teixeira, L.R., and Armstrong, R., 2008, Tonian rift-related, A-type continental plutonism in the Araçuaí Orogen, eastern Brazil: New evidence for the breakup stage of the São Francisco-Congo Paleocontinent: Gondwana Research, v. 13, p. 527–537, doi:10.1016/j.gr.2007.06.002.

Silveira, V.D., 2017, Geologia e Geocronologia de zircões detríticos da região de Serro, Serra do Espinhaço Meridional, Minas Gerais, Brasil [Master's Dissertation]: UFMG, 38 p.

Smit, J.H.W., Brun, J.P., and Sokoutis, D., 2003, Deformation of brittle-ductile thrust wedges in experiments and nature: Journal of Geophysical Research: Solid Earth, v. 108, doi:10.1029/2002jb002190.

Souza, M.E.S., Martins, M.S., Queiroga, G.N., Leite, M., Oliveira, R.G., Dussin, I.A., and Pedrosa-Soares, A.C., 2019, Paleoenvironment, sediment provenance and tectonic setting of Tonian basal deposits of the Macaúbas basin system, Araçuaí Orogen, southeast Brazil: Journal of South American Earth Sciences, v. 96, p. 102393, doi:10.1016/j.jsames.2019.102393.

Steiger, R.H., and Jäger, E., 1977, Subcomission on geochronology: convention on the use of decay constants in geo- and cosmochronology: Earth and Planetary Science Letters, v. 36, p. 359–362, doi:10.1016/0012-821X(77)90060-7.

Stern, R.A., and Berman, R.G., 2001, Monazite U-Pb and Th-Pb geochronology by ion microprobe, with application to in situ dating of an Archean metasedimentary rock: Chemical Geology, v. 172, p. 113–130, doi:10.1016/S0009-2541(00)00239-4.

Stipp, M., Stünitz, H., Heilbronner, R., and Schmid, S.M., 2002, Dynamic recrystallization of quartz: Correlation between natural and experimental conditions: Geological Society Special Publication, v. 200, p. 171–190, doi:10.1144/GSL.SP.2001.200.01.11.

Suppe, J., 2007, Absolute fault and crustal strength from wedge tapers: Geology, v. 35, p. 1127–1130, doi:10.1130/G24053A.1.

Suppe, J., 1983, Geometry and kinematics of fault-bend folding: American Journal of Science, v. 283, p. 684–721, doi:10.2475/ajs.283.7.684.

Süssenberger, A., Brito-Neves, B.B., and Wemmer, K., 2014, Dating low-grade metamorphism and deformation of the espinhaço supergroup in the Chapada Diamantina (Bahia, NE Brazil): a K/Ar fine-fraction study: Brazilian Journal of Geology, v. 44, p. 207–220, doi:10.5327/Z2317-4889201400020003.

Taufner, R., Lagoeiro, L.E., Cavalcante, G.C.G., Barbosa, P., and Silveira, C.S., 2021, Deformation mechanisms accommodating progressive simple shear thrusting of quartzite and metacarbonate in the southwestern Espinhaço Range, Brazil: Journal of South American Earth Sciences, v. 107, p. 102944, doi:10.1016/j.jsames.2020.102944.

Tavares, T.D., Martins, M.S., Alkmim, F.F., and Lana, C.C., 2020, Detrital zircons from the Upper Três Marias Formation, São Francisco Basin, SE Brazil: record of foreland deposition during the Cambrian? Journal of South American Earth Sciences, v. 97, p. 102395, doi:10.1016/j.jsames.2019.102395.

Teixeira, W., Ávila, C.A., Dussin, I.A., and Bongiolo, E., 2022, U-Pb provenance fingerprints of metavolcanic-sedimentary successions of the Mineiro belt: Proxies for the continuity of plate tectonics through the Paleoproterozoic: Geoscience Frontiers, v. 13, p. 101293, doi:10.1016/j.gsf.2021.101293.

Teixeira, W., Cordani, U.G., Kawashita, K., Taylor, P.N., and Van Schmus, W.R., 1987, Archean and Early Proterozoic crustal evolution in the southern part of the São Francisco craton, *in* International Symposium on Granites and Associated Mineralization, Salvador, SBG-SME/SGM-ORSTOM, Annals, p. 37–40.

Teixeira, W., Sabaté, P., Barbosa, J.S.F., Noce, C.M., and Carneiro, M.A., 2000, Archean and Paleoproterozoic tectonic evolution of the São Francisco Craton, Brazil, *in* Cordani, U.G., Milani, E.J., Thomaz Filho, A., and Campos, D.A. eds., Tectonic evolution of South America, Rio de Janeiro, 31º Congresso Internacional de Geologia, p. 101–137.

Tesei, T., Cruciani, F., and Barchi, M.R., 2021, Gravity-driven deepwater fold-and-thrust belts as Critical Coulomb Wedges: Model limitations and the role of friction vs. fluid pressure: Journal of Structural Geology, v. 153, p. 104451, doi:10.1016/j.jsg.2021.104451.

Tohver, E., Cawood, P.A., Rossello, E.A., and Jourdan, F., 2012, Closure of the Clymene Ocean and formation of West Gondwana in the Cambrian: evidence from the Sierras Australes of the southernmost Rio de la Plata craton, Argentina: Gondwana Research, v. 21, p. 394–405, doi:10.1016/j.gr.2011.04.001.

Tohver, E., and Trindade, R.I.F., 2014, Comment on “Was there an ediacaran Clymene Ocean in Central South America?” by U. G. Cordani and others: American Journal of Science, v. 314, p. 805–813, doi:10.2475/03.2014.03.

Tohver, E., Trindade, R.I.F., Solum, J.G., Hall, C.M., Riccomini, C., and Nogueira, A.C.R., 2010, Closing the Clymene ocean and bending a Brasiliano belt: Evidence for the Cambrian formation of Gondwana, southeast Amazon craton: Geology, v. 38, p. 267–270, doi:10.1130/G30510.1.

Trimby, P.W., Prior, D.J., and Wheeler, J., 1998, Grain boundary hierarchy development in a quartz mylonite: Journal of Structural Geology, v. 20, p. 917–935, doi:10.1016/S0191-8141(98)00026-1.

Trindade, R.I.F., D’Agrella-Filho, M.S., Epof, I., and Brito-Neves, B.B., 2006, Paleomagnetism of Early Cambrian Itabaiana mafic dikes (NE Brazil) and the final assembly of Gondwana: Earth and Planetary Science Letters, v. 244, p. 361–377, doi:10.1016/j.epsl.2005.12.039.

Trindade, R.I.F., Font, E.C., D’Agrella-Filho, M.S., Nogueira, A.C.R., and Riccomini, C., 2003, Low-latitude and multiple geomagnetic reversals in the Neoproterozoic Puga cap carbonate, Amazon craton: Terra Nova, v. 15, p. 441–446, doi:10.1046/j.1365-3121.2003.00510.x.

Trompette, R.R., 2000, Gondwana evolution; its assembly at around 600 Ma: Comptes Rendus de l’Academie de Sciences - Serie IIa: Sciences de la Terre et des Planetes, v. 330, p. 305–315, doi:10.1016/S1251-8050(00)00125-7.

Tuller, M.P., Ribeiro, J.H., Signorelli, N., Féboli, W.L., and Pinho, J.M.M., 2010, Projeto Sete Lagoas - Abaeté: Belo Horizonte, CPRM, 160 p.

Tuller, M.P., Ribeiro, J.H., Signorelli, N., Féboli, W.L., and Pinho, J.M.M., 2008, Proposta de uma nova seção-tipo da Formação Carrancas, Grupo Bambuí, na região de Inhaúma, Minas Gerais, *in* 44º Congresso Brasileiro de Geologia, Curitiba, SBG, Anais, p. 929.

Tullis, J., 1970, Quartz: Preferred orientation in rocks produced by Dauphiné twinning: Science, v. 168, p. 1342–1344.

Twiss, R.J., and Moores, E.M., 2007, Structural Geology: New York, W. H. Freeman and Company, 736 p.

Uhlein, A., 1991, Transição cráton-faixa dobrada: exemplo do Cráton do São Francisco e da Faixa Araçuaí (Ciclo Brasiliano) no estado de Minas Gerais - aspectos estratigráficos e estruturais [Doctoral Thesis]: USP, 245 p.

Uhlein, A., Alvarenga, C.J.S., Dardenne, M.A., and Trompette, R.R., 2011, The glaciogenic Jequitaí Formation, southeastern Brazil, *in* Arnaud, E., Halverson, G.P., and Shields-Zhou, G. eds., The geological record of Neoproterozoic glaciations, London, The Geological Society of London, Geological Society, London, Memoirs, v. 36, p. 541–546, doi:10.1144/M36.51.

Uhlein, G.J., Carvalho, J.F.M.G., Uhlein, A., Caxito, F.A., Halverson, G.P., and Sial, A.N., 2012, Estratigrafia e sedimentologia da Formação Carrancas, Grupo Bambuí, nas regiões de Belo Horizonte e Pitangui, MG: Geonomos, v. 20, p. 79–97, doi:10.18285/geonomos.v2i20.250.

Uhlein, A., Lima, O.N.B., Fantinel, L.M., and Baptista, M.C., 2004, Estratigrafia e evolução geológica do Grupo Bambuí, Minas Gerais, *in* XLII Congresso Brasileiro de Geologia, Araxá, SBG, Anais, p. 30–61.

Uhlein, A., Trompette, R.R., and Alvarenga, C.J.S., 1999, Neoproterozoic glacial and gravitational sedimentation on a continental rifted margin: The Jequitaí-Macaubas sequence (Minas Gerais, Brazil): Journal of South American Earth Sciences, v. 12.

Uhlein, A., Trompette, R.R., and Egydio-Silva, M., 1998, Proterozoic rifting and closure, SE border of the São Francisco Craton, Brazil: Journal of South American Earth Sciences, v. 11, p. 191–203, doi:10.1016/S0895-9811(98)00010-8.

Uhlein, G.J., Uhlein, A., Halverson, G.P., Stevenson, R., Caxito, F.A., Cox, G.M., and Carvalho, J.F.M.G., 2016, The Carrancas Formation, Bambuí Group: a record of pre-Marinoan sedimentation on the southern São Francisco Craton, Brazil: Journal of South American Earth Sciences, v. 71, p. 1–16, doi:10.1016/j.jsames.2016.06.009.

Uhlein, G.J., Uhlein, A., Stevenson, R., Halverson, G.P., Caxito, F.A., and Cox, G.M., 2017, Early to late Ediacaran conglomeratic wedges from a complete foreland basin cycle in the southwest São Francisco Craton, Bambuí Group, Brazil: Precambrian Research, v. 299, p. 101–116, doi:10.1016/j.precamres.2017.07.020.

van Daalen, M., Heilbronner, R., and Kunze, K., 1999, Orientation analysis of localized shear deformation in quartz fibres at the brittle–ductile transition: Tectonophysics, v. 303, p. 83–107, doi:10.1016/S0040-1951(98)00264-9.

van den Kerkhof, A.M., and Hein, U.F., 2001, Fluid inclusion petrography: Lithos, v. 55, p. 27–47, doi:10.1016/S0024-4937(00)00037-2.

van der Pluijm, B.A., and Marshak, S., 2004, Earth Structure: New York, W. W. Norton & Company, 656 p.

Vauchez, A., Hollanda, M.H.B.M., Monié, P., Mondou, M., and Egydio-Silva, M., 2019, Slow cooling and crystallization of the roots of the Neoproterozoic Araçuaí hot orogen (SE Brazil): Implications for rheology, strain distribution, and deformation analysis: Tectonophysics, v. 766, p. 500–518, doi:10.1016/j.tecto.2019.05.013.

Vermeesch, P., 2018, IsoplotR: A free and open toolbox for geochronology: Geoscience Frontiers, v. 9, p. 1479–1493, doi:10.1016/j.gsf.2018.04.001.

Victoria, A.M., and Moy, S.L., 2014, Mapeamento geológico, em escala 1:25.000, da região de Lapinha da Serra, município de Santana do Riacho, MG [Graduation Project]: UFMG, 233 p.

Vieira, L.C., Trindade, R.I.F., Nogueira, A.C.R., and Ader, M., 2007, Identification of a Sturtian cap carbonate in the Neoproterozoic Sete Lagoas carbonate platform, Bambuí Group, Brazil: Comptes Rendus - Geoscience, v. 339, p. 240–258, doi:10.1016/j.crte.2007.02.003.

Villa, I.M., De Bièvre, P., Holden, N.E., and Renne, P.R., 2015, IUPAC-IUGS recommendation on the half life of 87Rb: Geochimica et Cosmochimica Acta, v. 164, p. 382–385, doi:10.1016/j.gca.2015.05.025.

Warr, L.N., 2018, A new collection of clay mineral ‘Crystallinity’ Index Standards and revised guidelines for the calibration of Kübler and Árkai indices: Clay Minerals, v. 53, p. 339–350, doi:10.1180/clm.2018.42.

Warren, L.V., Quaglio, F., Riccomini, C., Simões, M.G., Poiré, D.G., Strikis, N.M., Anelli, L.E., and Strikis, P.C., 2014, The puzzle assembled: Ediacaran guide fossil Cloudina reveals an old proto-Gondwana seaway: Geology, v. 42, p. 391–394, doi:10.1130/G35304.1.

Wemmer, K., 1991, K/Ar-Altersbestimmungsmöglichkeiten für retrograde Deformationsprozesse im spröden und duktilen Bereich - Beispiele aus der KTB-Vorbohrung (Oberpfalz) und dem Bereich der Insubrischen Linie (N-Italien): Göttinger Arbeiten zur Geologie und Paläontologie, v. 51, p. 1–61.

Woodhead, J.D., and Hergt, J.M., 2001, Strontium, Neodymium and Lead isotope analyses of NIST glass certified reference materials: SRM 610, 612, 614: Geostandards Newsletter, v. 25, p. 261–266, doi:10.1111/j.1751-908X.2001.tb00601.x.

Yang, J., Peng, J., Hu, R., Bi, X., Zhao, J., Fu, Y., and Shen, N.-P., 2013, Garnet geochemistry of tungsten-mineralized Xihuashan granites in South China: Lithos, v. 177, p. 79–90, doi:10.1016/j.lithos.2013.06.008.

Zack, T., and Hogmalm, K.J., 2016, Laser ablation Rb/Sr dating by online chemical separation of Rb and Sr in an oxygen-filled reaction cell: Chemical Geology, v. 437, p. 120–133, doi:10.1016/j.chemgeo.2016.05.027.

Zalán, P.V., and Romeiro-Silva, P.C., 2007, Bacia do São Francisco: Boletim de Geociências da Petrobras, v. 15, p. 561–571.

APPENDIX A – GEOLOGICAL MAP OF THE REGION OF SERRA DO CIPÓ-MG

Geological Map of the Region of Serra do Cipó-MG

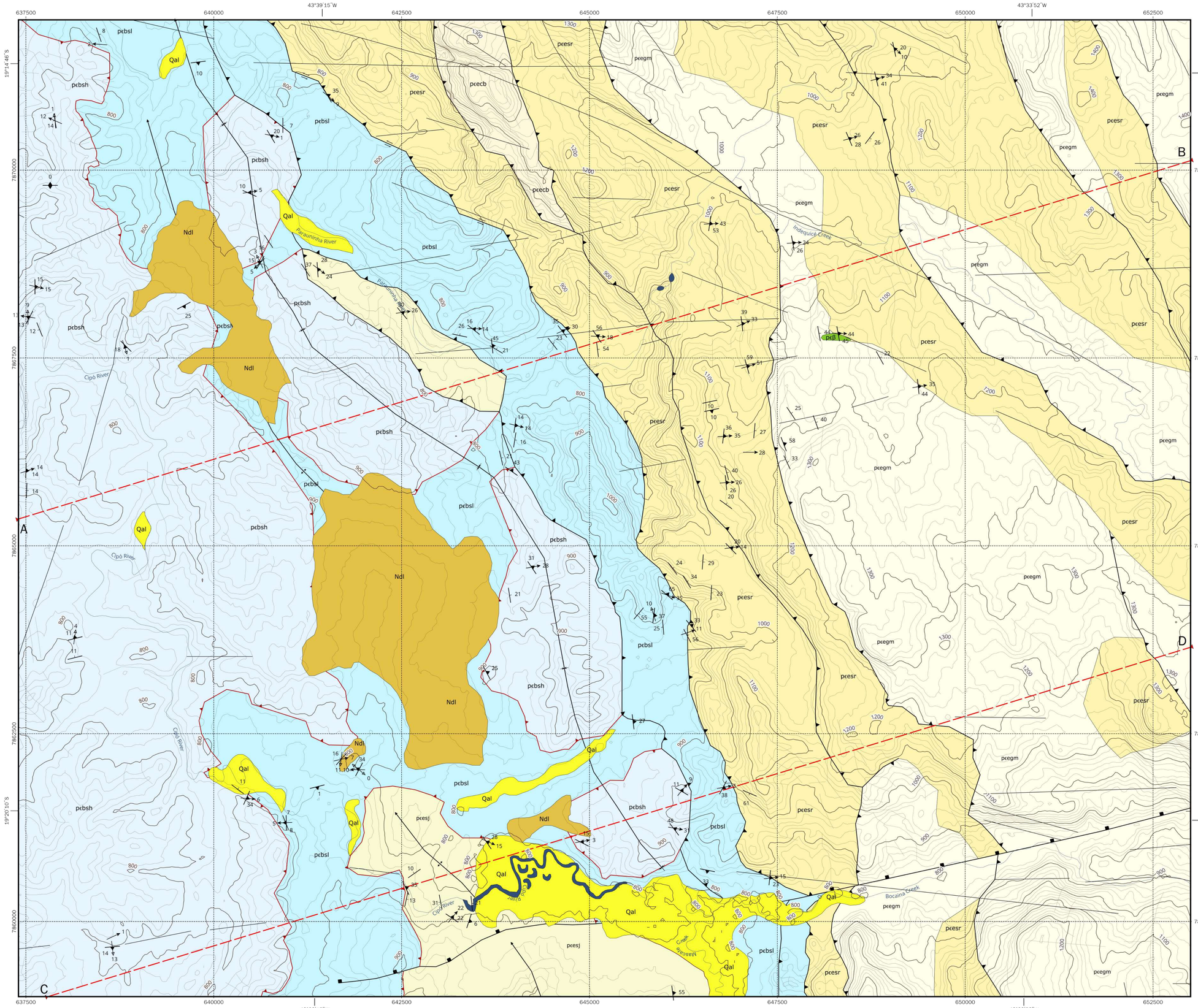

STRATIGRAPHY

CENOZOIC / QUATERNARY

- **Qal** Alluvial deposits
  Inconsolidated, poorly selected sandy deposits, with presence of clay, silt and gravel
- **Ndl** Detrital covers
  Inconsolidated autochtonous sediments (clay, silt, sand and gravel) and soil

NEOPROTEROZOIC / EDIACARAN

- **pcbsh** Serra de Santa Helena Formation
  Low-energy marine pelitic succesions
  Siltstone, metasiltstone, rhythmite, metarhythmite
- **pcbsl** Sete Lagoas Formation
  Carbonatic platform successions
  Limestone, marl, marble

NEOPROTEROZOIC / TONIAN

- **pcβ** Pedro Lessa Suite
  Metamafic dikes - metadiabase

MESOPROTEROZOIC / CALYMMIAN-STENIAN

- **pcecb** Córrego dos Borges Formation
  Beach-surf successions
  Well-selected, fine-medium quartzite
- **pcesr** Santa Rita Formation
  Shallow marine successions
  Poorly selected micaceous coarse quartzite, fine micaceous quartzite, phyllite, schist, mylonite
- **pcegm** Galho do Miguel Formation
  Aeolian succession
  Well-selected, pure, fine-medium quartzite

PALEOPROTEROZOIC / STATHERIAN

- **pcesj** São João da Chapada Formation
  Alluvial fan succession
  Poorly selected medium-coarse quartzite, meta-paraconglomerate, metadiamictite

STRUCTURES

- Thrust fault
- Detachment surface
- Normal fault
- Plunging antiform
- Plunging synform
- Indiscriminated faults, fractures and structural lineaments

STRUCTURE ATTITUDES

- Tectonic foliation
- Contact and bedding
- Stretch lineation
- b-Lineation

CROSS-SECTIONS

- Traces

PHYSIOGRAPHY

- Rivers and creeks
- Elevation (20 m contours)

N
W
E
S

1 0 1 2 km

1:25.000

Sirgas2000 / Universal Transverse Mercator - Zone 23K
Topography - © JAXA/METI ALOS PALSAR (2007)
Magnetic declination: 23°14' W (0°05' W/year)

Universidade de São Paulo
Instituto de Geociências

Tectonic evolution of the Southern Espinhaço Front in Serra do Cipó-MG

Tese de Doutorado
Appendix A

Henrique Chaves Joncew

2024

APPENDIX B – CROSS-SECTIONS AB AND CD OF THE REGION OF SERRA DO CIPÓ-MG

Cross-sections of the Region of Serra do Cipó-MG

Cross-section AB

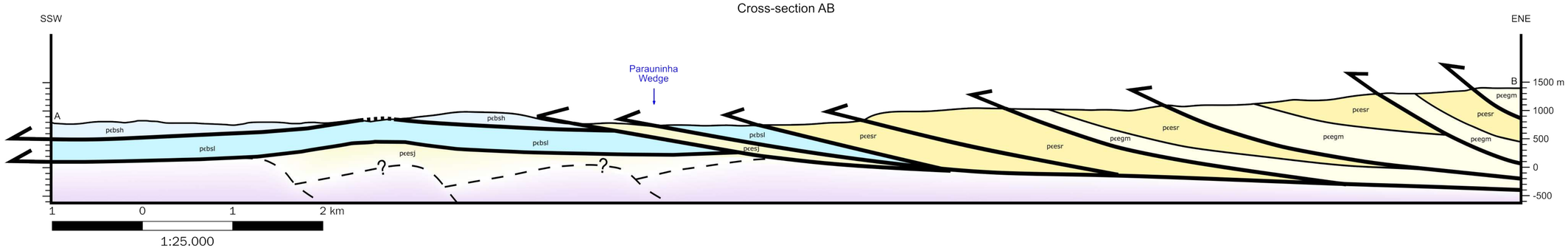

Cross-section CD

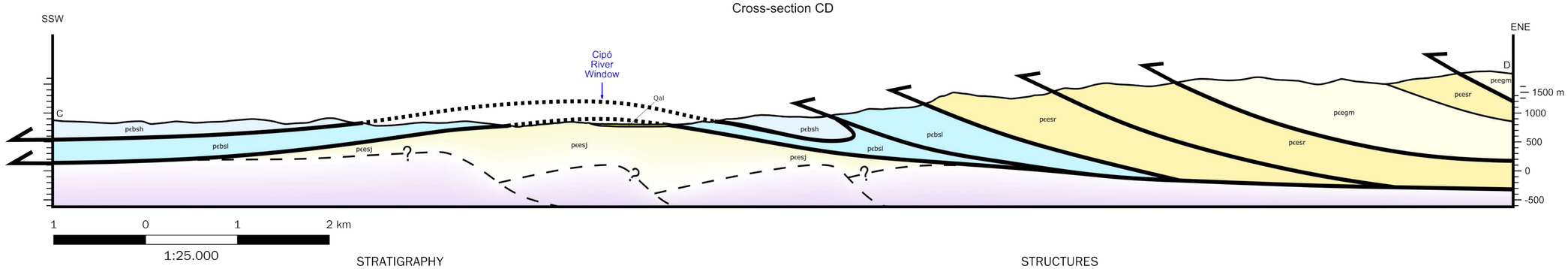

STRATIGRAPHY

- Qal — Alluvial deposits
  Inconsolidated, poorly selected sandy deposits, with presence of clay, silt and gravel
- pcbsh — Serra de Santa Helena Formation
  Low-energy marine pelitic succesions
  Siltstone, metasiltstone, rhythmite, metarhythmite
- pcbsl — Sete Lagoas Formation
  Carbonatic platform successions
  Limestone, marl, marble
- pcesr — Santa Rita Formation
  Shallow marine successions
  Poorly selected micaceous coarse quartzite, fine micaceous quartzite, phyllite, schist, mylonite
- pcegm — Galho do Miguel Formation
  Aeolian succession
  Well-selected, pure, fine-medium quartzite
- pcesj — São João da Chapada Formation
  Alluvial fan succession
  Poorly selected medium-coarse quartzite, meta-paraconglomerate, metadiamictite
- Crystalline basement

STRUCTURES

- Thrust fault/detachment surface
- Fold trace (interpreted)
- Inferred/estimated contact

Universidade de São Paulo
Instituto de Geociências

Tectonic evolution of the Southern Espinhaço Front in Serra do Cipó-MG

Tese de Doutorado
Appendix B

Henrique Chaves Joncew

2024

APPENDIX C – FIELD POINTS REGISTERED IN THE REGION OF SERRA DO CIPÓ

Field points described in the region of Serra do Cipó-MG

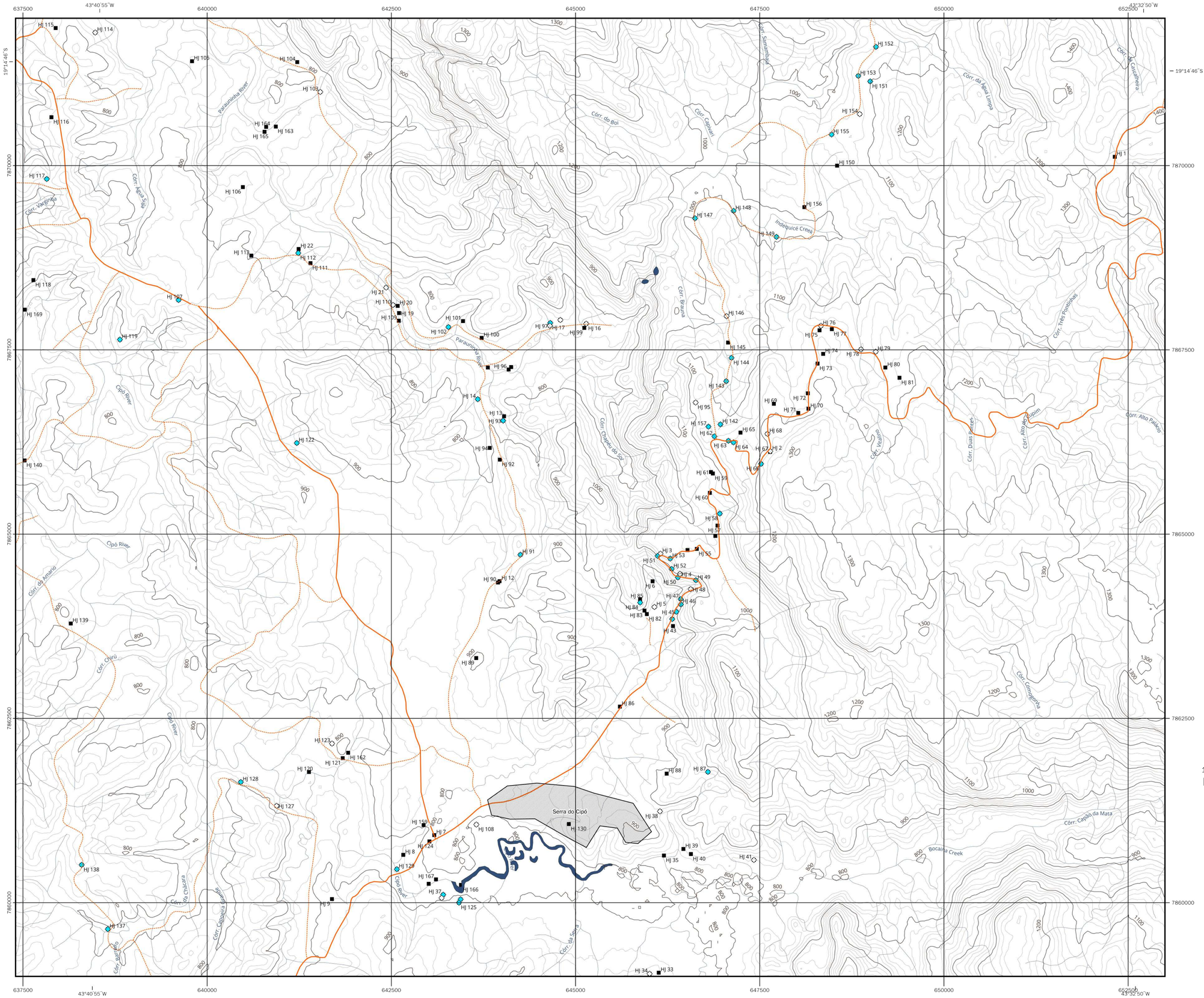

Field work

- Field point (no sample)
- Field point (rock sample)
- Field point (rock sample and thin section)
- Field point (quartz vein sample)

Physiography

- Elevation (20 m contours)
- Rivers and Creeks

Infrastructure

- Urban area
- Road (paved)
- Road (unpaved)

N
W E
S

1 0 1 2 km

1:25.000

Sirgas2000 / Universal Transverse Mercator - Zone 23K
Topography - © JAXA/METI ALOS PALSAR (2007)
Magnetic declination: 23°14' W (0°05' W/year)

Universidade de São Paulo
Instituto de Geociências

Tectonic evolution of the Southern Espinhaço Front in Serra do Cipó-MG

Tese de Doutorado
Appendix C

Henrique Chaves Joncew
2024

APPENDIX D – U-PB DATING RESULTS TABLES

Detrital zircon U-Pb analyses – Results for Sample HJ 4

Spot	RATIOS											AGES (Ma)							
	$^{207}Pb/^{235}U$	σ	$^{206}Pb/^{238}U$	σ	Corr. coef.	$^{238}U/^{206}Pb$	σ	$^{207}Pb/^{206}Pb$	σ	$^{208}Pb/^{206}Pb$	σ	$T_{206Pb/238U}$	σ	$T_{207Pb/235U}$	σ	$T_{207Pb/206Pb}$	σ	Conc. (%)	Histogram ($^{207}Pb/^{206}Pb$ Ages)
1.1	14.6801	0.1748	0.5476	0.0044	0.9100	1.8263	0.0147	0.1944	0.0021	0.2245	0.0887	2815	18	2795	12	2780	18	100	Concordant data
2.1	15.2051	0.1547	0.5487	0.0039	0.9600	1.8226	0.0129	0.2010	0.0019	0.0986	0.0127	2820	17	2828	10	2834	15	99	
3.1	13.6372	0.1576	0.5192	0.0040	0.9800	1.9260	0.0149	0.1905	0.0019	0.1701	0.0381	2696	17	2725	11	2746	17	98	
5.1	7.6384	0.1108	0.4149	0.0025	0.9500	2.4100	0.0144	0.1335	0.0020	0.1652	0.0485	2238	11	2189	13	2145	26	102	
6.1	11.4875	0.1452	0.4324	0.0026	0.9900	2.3129	0.0139	0.1927	0.0023	0.2243	0.0310	2316	12	2564	11	2765	20	90	
10.1	14.8691	0.2047	0.5540	0.0033	0.9000	1.8051	0.0106	0.1947	0.0026	0.2570	0.0044	2842	14	2807	13	2782	22	101	
15.1	10.9087	0.1690	0.4218	0.0022	0.9900	2.3710	0.0122	0.1876	0.0028	0.1797	0.0202	2268	10	2515	14	2721	25	90	
16.1	14.5511	0.2204	0.5354	0.0029	0.6500	1.8677	0.0100	0.1971	0.0031	0.3242	0.0267	2764	12	2786	15	2802	26	99	
17.1	7.5310	0.1280	0.4025	0.0024	0.5400	2.4846	0.0149	0.1357	0.0024	0.0947	0.0073	2180	11	2177	15	2173	30	100	
20.1	7.2990	0.1204	0.4091	0.0040	0.3700	2.4444	0.0237	0.1294	0.0024	0.1374	0.0090	2211	18	2149	14	2090	32	102	
22.1	16.8930	0.2633	0.5857	0.0050	0.9000	1.7074	0.0145	0.2092	0.0034	0.3397	0.0258	2972	20	2929	15	2899	26	101	
23.1	16.6094	0.2857	0.5813	0.0048	0.5400	1.7203	0.0141	0.2072	0.0032	0.1803	0.0039	2954	19	2913	16	2884	25	101	
26.1	7.4656	0.1749	0.4119	0.0044	0.5600	2.4277	0.0259	0.1314	0.0030	0.0844	0.0138	2224	20	2169	21	2117	40	102	
27.1	7.2534	0.1494	0.4012	0.0046	0.6200	2.4923	0.0289	0.1311	0.0029	0.2050	0.0169	2175	22	2143	19	2113	39	101	
28.1	7.1242	0.1865	0.3949	0.0058	0.5100	2.5325	0.0371	0.1309	0.0033	0.1813	0.0177	2145	27	2127	23	2110	44	100	
29.1	7.2077	0.1525	0.4096	0.0033	0.9600	2.4416	0.0200	0.1276	0.0022	0.2583	0.0121	2213	15	2138	19	2066	31	103	
30.1	7.4613	0.1620	0.4054	0.0038	0.8500	2.4669	0.0234	0.1335	0.0025	0.0922	0.0072	2194	18	2168	20	2144	33	101	
31.1	3.9937	0.0873	0.2965	0.0029	0.9700	3.3732	0.0328	0.0977	0.0018	0.3369	0.0632	1674	14	1633	18	1581	35	102	
32.1	6.9836	0.1762	0.3853	0.0039	0.8800	2.5952	0.0263	0.1314	0.0025	0.1009	0.0233	2101	18	2109	22	2117	34	99	
35.1	7.6387	0.1240	0.4074	0.0042	0.7200	2.4543	0.0254	0.1360	0.0019	0.1318	0.0065	2203	19	2189	15	2177	24	100	
37.1	12.9347	0.1934	0.5114	0.0049	0.9200	1.9556	0.0187	0.1835	0.0020	0.2515	0.0182	2662	21	2675	14	2684	19	99	
38.1	7.3866	0.1048	0.4076	0.0036	0.8900	2.4536	0.0214	0.1314	0.0015	0.1606	0.0044	2204	16	2159	13	2117	20	102	
42.1	4.5814	0.0764	0.3072	0.0024	0.9600	3.2552	0.0250	0.1082	0.0015	0.3326	0.0379	1727	12	1746	14	1769	26	98	
43.1	3.9619	0.0649	0.2821	0.0020	0.9900	3.5442	0.0257	0.1018	0.0014	0.2035	0.0555	1602	10	1626	13	1658	25	98	
44.1	14.6186	0.2408	0.5510	0.0041	0.9800	1.8148	0.0136	0.1924	0.0029	0.2714	0.0306	2829	17	2791	16	2763	25	101	

Detrital zircon U-Pb analyses – Results for Sample HJ 4 (cont.)

Spot	RATIOS											AGES (Ma)							
	$^{207}Pb/^{235}U$	σ	$^{206}Pb/^{238}U$	σ	Corr. coef.	$^{238}U/^{206}Pb$	σ	$^{207}Pb/^{206}Pb$	σ	$^{208}Pb/^{206}Pb$	σ	$T_{206Pb/238U}$	σ	$T_{207Pb/235U}$	σ	$T_{207Pb/206Pb}$	σ	Conc. (%)	Histogram ($^{207}Pb/^{206}Pb$ Ages)
44.1	14.6186	0.2408	0.5510	0.0041	0.9800	1.8148	0.0136	0.1924	0.0029	0.2714	0.0306	2829	17	2791	16	2763	25	101	Concordant data
45.1	7.3603	0.1278	0.4018	0.0029	0.9200	2.4888	0.0181	0.1329	0.0022	0.1787	0.0180	2177	13	2156	16	2136	29	100	
50.1	7.0885	0.1008	0.3942	0.0028	0.8400	2.5365	0.0183	0.1304	0.0017	0.1810	0.0090	2143	13	2123	13	2103	23	100	
51.1	6.5944	0.0961	0.3789	0.0023	0.6900	2.6393	0.0163	0.1262	0.0016	0.1790	0.0050	2071	11	2059	13	2046	22	100	
55.1	13.3382	0.2481	0.5045	0.0034	0.9900	1.9822	0.0132	0.1917	0.0033	0.2515	0.1551	2633	14	2704	18	2757	28	97	
57.1	16.2229	0.2244	0.5973	0.0050	0.9900	1.6743	0.0141	0.1970	0.0023	0.1327	0.0313	3019	20	2890	14	2801	19	104	
60.1	19.9443	0.2611	0.6413	0.0050	0.8800	1.5594	0.0121	0.2256	0.0026	0.1303	0.0068	3194	20	3089	13	3021	18	103	
61.1	6.9950	0.0945	0.3861	0.0031	0.9900	2.5900	0.0205	0.1314	0.0016	0.1832	0.0758	2105	14	2111	12	2117	21	99	
66.1	3.8807	0.0488	0.2882	0.0017	0.9900	3.4702	0.0203	0.0977	0.0011	0.1788	0.0285	1632	9	1610	10	1580	21	101	
67.1	7.0972	0.0982	0.3888	0.0031	0.7400	2.5720	0.0207	0.1324	0.0017	0.2098	0.0093	2117	15	2124	12	2130	23	99	
69.1	7.2735	0.0926	0.3959	0.0026	0.8000	2.5260	0.0166	0.1332	0.0014	0.1047	0.0055	2150	12	2146	11	2141	18	100	
71.1	14.0707	0.1865	0.5480	0.0034	0.9900	1.8249	0.0114	0.1862	0.0021	0.2238	0.0289	2817	15	2755	13	2709	18	102	
72.1	13.2546	0.1699	0.5180	0.0032	0.9900	1.9304	0.0118	0.1856	0.0022	0.5120	0.1054	2691	14	2698	13	2703	20	99	
74.1	3.8318	0.0704	0.2769	0.0028	0.6200	3.6118	0.0366	0.1004	0.0020	0.1879	0.0235	1576	14	1600	15	1631	37	98	
75.1	13.5997	0.1958	0.5368	0.0050	0.9400	1.8629	0.0175	0.1837	0.0027	0.2699	0.0104	2770	21	2722	14	2687	24	101	
81.1	20.1581	0.2731	0.6226	0.0050	0.9900	1.6063	0.0130	0.2348	0.0027	0.1646	0.0389	3120	21	3099	15	3085	19	100	
82.1	7.2867	0.1252	0.4022	0.0043	0.8500	2.4864	0.0267	0.1314	0.0018	0.1766	0.0074	2179	20	2147	15	2117	23	101	
83.1	11.8798	0.1917	0.4856	0.0046	0.8800	2.0595	0.0194	0.1774	0.0022	0.4244	0.0891	2551	20	2595	15	2629	21	98	
84.1	4.3334	0.0822	0.3027	0.0021	0.6900	3.3039	0.0234	0.1038	0.0020	0.1243	0.0047	1705	11	1700	16	1694	35	100	
85.1	15.2066	0.2467	0.5646	0.0035	0.9400	1.7711	0.0110	0.1953	0.0032	0.1749	0.0181	2886	14	2828	15	2788	27	102	
86.1	10.0934	0.1541	0.4699	0.0028	0.9900	2.1280	0.0128	0.1558	0.0026	0.1015	0.0130	2483	13	2443	15	2410	29	101	
87.1	14.1540	0.2487	0.5517	0.0057	0.9700	1.8125	0.0187	0.1861	0.0026	0.2897	0.0297	2832	24	2760	17	2708	23	102	
90.1	7.2098	0.1346	0.4006	0.0043	0.9000	2.4964	0.0271	0.1305	0.0021	0.1779	0.0360	2172	20	2138	17	2105	29	101	
94.1	3.9184	0.1059	0.2892	0.0027	0.2800	3.4579	0.0319	0.0983	0.0026	0.2857	0.0315	1638	13	1618	22	1592	48	101	
92.1	14.2248	0.1937	0.5359	0.0038	0.8200	1.8659	0.0132	0.1925	0.0026	0.2611	0.0101	2766	16	2765	13	2764	22	100	

Detrital zircon U-Pb analyses – Results for Sample HJ 4 (cont.)

Spot	RATIOS											AGES (Ma)							
	$^{207}Pb/^{235}U$	σ	$^{206}Pb/^{238}U$	σ	Corr. coef.	$^{238}U/^{206}Pb$	σ	$^{207}Pb/^{206}Pb$	σ	$^{208}Pb/^{206}Pb$	σ	$T_{206Pb/238U}$	σ	$T_{207Pb/235U}$	σ	$T_{207Pb/206Pb}$	σ	Conc. (%)	Histogram ($^{207}Pb/^{206}Pb$ Ages)
95.1	12.0175	0.2426	0.4989	0.0039	0.8200	2.0044	0.0155	0.1747	0.0026	0.1416	0.0279	2609	17	2606	19	2603	25	100	
98.1	14.9858	0.2759	0.5644	0.0044	0.0800	1.7718	0.0139	0.1926	0.0027	0.1715	0.0136	2885	18	2814	18	2764	23	102	**Concordant data**
99.1	14.0773	0.2198	0.5459	0.0044	0.6200	1.8319	0.0148	0.1870	0.0023	0.1525	0.0062	2808	18	2755	15	2716	20	101	
100.1	14.7217	0.2384	0.5684	0.0053	0.9300	1.7594	0.0163	0.1879	0.0025	0.1696	0.0063	2901	22	2797	15	2724	22	103	
4.1	0.2780	0.0046	0.0945	0.0007	0.7900	10.5850	0.0827	0.0213	0.0003	1.3234	0.0449	582	4	249	4	0	0	233	
7.1	14.1866	0.1679	0.4845	0.0028	0.7700	2.0639	0.0117	0.2124	0.0025	0.4319	0.2036	2547	12	2762	11	2924	20	92	
8.1	5.0570	0.0706	0.2995	0.0017	0.9900	3.3394	0.0184	0.1225	0.0017	0.3188	0.0286	1689	8	1829	12	1993	25	92	
9.1	14.2554	0.1802	0.5414	0.0027	0.9900	1.8470	0.0093	0.1910	0.0024	0.2354	0.1855	2789	12	2767	12	2750	22	100	
11.1	4.5350	0.0568	0.2126	0.0011	0.7300	4.7038	0.0253	0.1547	0.0018	0.4737	0.0777	1243	6	1737	11	2399	21	71	
12.1	6.9605	0.1131	0.2929	0.0020	0.9900	3.4138	0.0228	0.1723	0.0022	0.2643	0.0649	1656	9	2106	12	2581	20	78	
13.1	4.1912	0.0581	0.2444	0.0013	0.2300	4.0914	0.0225	0.1244	0.0017	0.6911	0.0980	1410	7	1672	11	2020	22	84	
14.1	7.6199	0.1296	0.3215	0.0018	0.7700	3.1104	0.0174	0.1719	0.0027	0.3979	0.1663	1797	9	2187	14	2576	26	82	
18.1	1.3252	0.0245	0.1185	0.0009	0.8900	8.4401	0.0636	0.0811	0.0016	1.0604	0.1042	722	5	857	10	1224	37	84	
19.1	0.0543	0.0029	0.0741	0.0006	0.5200	13.4993	0.1134	0.0053	0.0003	1.4086	0.0611	461	4	54	3	0	0	858	
21.1	7.6227	0.1087	0.3281	0.0023	0.9800	3.0482	0.0215	0.1685	0.0026	0.4272	0.0574	1829	11	2188	13	2543	25	83	**Discordant data**
24.1	0.7730	0.0257	0.0993	0.0008	0.9800	10.0675	0.0859	0.0564	0.0014	0.9446	0.2449	611	5	582	11	470	30	104	
25.1	7.6020	0.0900	0.3069	0.0017	0.9900	3.2579	0.0181	0.1796	0.0025	0.2705	0.0928	1726	9	2185	13	2649	24	78	
33.1	15.9303	0.2249	0.5892	0.0051	0.9900	1.6973	0.0147	0.1961	0.0029	0.3928	0.2094	2986	21	2873	14	2794	24	103	
34.1	3.3774	0.0642	0.1833	0.0018	0.9900	5.4545	0.0533	0.1336	0.0020	0.6577	0.2382	1085	9	1499	12	2146	24	72	
36.1	6.6319	0.0882	0.3165	0.0027	0.5600	3.1591	0.0266	0.1520	0.0018	0.9762	0.1533	1773	13	2064	13	2368	20	85	
39.1	9.6749	0.1397	0.3542	0.0023	0.9700	2.8233	0.0186	0.1981	0.0024	0.6202	0.1327	1955	11	2404	14	2811	20	81	
40.1	10.1790	0.1656	0.3668	0.0027	0.9900	2.7266	0.0201	0.2013	0.0026	0.5268	0.1318	2014	13	2451	15	2837	21	82	
41.1	2.2462	4.4363	-0.0304	0.0887	0.5400	-32.9349	96.2265	-0.5365	0.0200	2.4568	1.6825	0	430	1196	781	0	980	0	
46.1	3.6251	0.0516	0.1864	0.0011	0.9800	5.3662	0.0322	0.1411	0.0019	0.7156	0.0782	1102	6	1555	11	2241	22	70	
47.1	6.7358	0.1009	0.3739	0.0022	0.9900	2.6742	0.0157	0.1306	0.0019	0.3181	0.1282	2048	10	2077	14	2107	26	98	
48.1	3.4515	0.0551	0.2492	0.0015	0.9600	4.0124	0.0242	0.1004	0.0015	0.8756	0.1487	1435	8	1516	12	1632	26	94	

Detrital zircon U-Pb analyses – Results for Sample HJ 4 (cont.)

Spot	RATIOS											AGES (Ma)							
	$^{207}Pb/^{235}U$	σ	$^{206}Pb/^{238}U$	σ	Corr. coef.	$^{238}U/^{206}Pb$	σ	$^{207}Pb/^{206}Pb$	σ	$^{208}Pb/^{206}Pb$	σ	$T_{206Pb/238U}$	σ	$T_{207Pb/235U}$	σ	$T_{207Pb/206Pb}$	σ	Conc. (%)	Histogram ($^{207}Pb/^{206}Pb$ Ages)
49.1	6.0228	0.0888	0.3368	0.0022	0.8600	2.9690	0.0194	0.1297	0.0017	0.3985	0.2061	1871	11	1979	13	2094	24	94	Discordant data
52.1	5.6689	0.0691	0.3247	0.0018	0.9500	3.0799	0.0172	0.1266	0.0014	0.3564	0.0862	1813	9	1927	11	2052	20	94	
53.1	9.0170	0.1112	0.3701	0.0021	0.9900	2.7022	0.0152	0.1767	0.0020	0.4388	0.1683	2030	10	2340	11	2622	19	86	
54.1	6.6385	0.1304	0.3647	0.0023	0.9900	2.7418	0.0176	0.1320	0.0026	0.3013	0.1464	2005	11	2065	18	2125	35	97	
56.1	5.0928	0.0925	0.3052	0.0018	0.9700	3.2764	0.0198	0.1210	0.0020	0.4137	0.1784	1717	9	1835	16	1971	30	93	
58.1	5.8502	0.1051	0.2673	0.0026	0.9800	3.7406	0.0364	0.1587	0.0019	0.4500	0.1764	1527	13	1954	12	2442	19	78	
59.1	7.0400	0.0927	0.3202	0.0025	0.9700	3.1228	0.0243	0.1594	0.0018	0.3166	0.1053	1791	12	2117	11	2450	19	84	
62.1	7.3787	0.1009	0.4021	0.0025	0.9800	2.4869	0.0154	0.1331	0.0021	0.3932	0.2969	2179	12	2158	14	2139	28	100	
63.1	8.3589	0.0870	0.3279	0.0016	0.9800	3.0492	0.0145	0.1849	0.0023	0.7478	0.2769	1828	8	2271	11	2697	21	80	
64.1	5.6879	0.0580	0.2410	0.0012	0.9900	4.1490	0.0201	0.1712	0.0021	0.8730	0.1433	1392	6	1930	12	2569	24	72	
65.1	3.7360	0.0569	0.1737	0.0011	0.6600	5.7573	0.0358	0.1560	0.0023	1.0756	0.1546	1032	6	1579	12	2413	25	65	
68.1	5.3225	0.0603	0.2182	0.0013	0.8800	4.5819	0.0267	0.1769	0.0016	0.7141	0.1118	1273	7	1873	10	2624	15	67	
70.1	3.8111	0.0503	0.2256	0.0014	0.9300	4.4321	0.0284	0.1225	0.0014	0.6890	0.1186	1312	8	1595	11	1993	21	82	
73.1	4.0857	0.0559	0.2876	0.0019	0.9800	3.4772	0.0226	0.1030	0.0013	0.3441	0.1422	1630	10	1652	12	1680	23	98	
76.1	12.3770	0.1338	0.4739	0.0036	0.9900	2.1102	0.0158	0.1894	0.0026	0.2405	0.1229	2501	17	2633	14	2737	25	94	
77.1	2.5929	0.0447	0.1747	0.0017	0.9900	5.7227	0.0557	0.1076	0.0017	0.7946	0.2684	1038	9	1299	11	1760	27	79	
78.1	7.3378	0.0970	0.2815	0.0024	0.9800	3.5529	0.0302	0.1891	0.0027	0.6704	0.1821	1599	12	2153	12	2734	24	74	
79.1	5.7787	0.0888	0.3281	0.0030	0.9500	3.0477	0.0278	0.1277	0.0016	0.3069	0.0527	1829	15	1943	13	2067	22	94	
80.1	2.4591	0.0472	0.1938	0.0021	0.9700	5.1604	0.0548	0.0920	0.0013	0.4218	0.1118	1142	11	1260	13	1468	26	90	
88.1	5.8937	0.0773	0.3442	0.0026	0.9700	2.9050	0.0220	0.1242	0.0017	0.4602	0.2836	1907	13	1960	14	2017	26	97	
89.1	4.4128	0.0710	0.2562	0.0025	0.9900	3.9033	0.0377	0.1249	0.0017	0.3396	0.0476	1470	13	1715	13	2028	24	85	
91.1	2.4895	0.0354	0.1992	0.0015	0.9900	5.0206	0.0366	0.0906	0.0013	0.3759	0.0519	1171	8	1269	10	1439	26	92	
93.1	10.6791	0.1304	0.4324	0.0029	0.9700	2.3126	0.0157	0.1791	0.0022	0.2670	0.0245	2317	13	2496	11	2645	20	92	
96.1	3.1605	0.0587	0.2372	0.0018	0.9900	4.2165	0.0315	0.0967	0.0014	0.3704	0.0949	1372	9	1448	15	1561	29	94	
97.1	1.7692	0.0327	0.1524	0.0011	0.9900	6.5629	0.0468	0.0842	0.0013	0.8448	0.1414	914	6	1034	12	1298	29	88	

Same grain

Detrital zircon U-Pb analyses – Results for Sample HJ 4 (Standards)	
Standard GJ data on 22/03/2022 Concordia Age = 605.0 +/- 1.1 Ma GJ reference age: 608.5 +/- 0.4 Ma (TIMS) - Jackson et al, 2004.	Pleosovic secondary standard on 22/03/2022 Concordia Age = 339.6 +/- 1.0 Ma Pleosovic reference age: 337.13 +/- 0.37 - Sláma et al, 2008.

Detrital zircon U-Pb analyses – Results for Sample HJ 110B

Spot	RATIOS											AGES (Ma)							
	$^{207}Pb/^{235}U$	σ	$^{206}Pb/^{238}U$	σ	Corr. coef.	$^{238}U/^{206}Pb$	σ	$^{207}Pb/^{206}Pb$	σ	$^{208}Pb/^{206}Pb$	σ	$T_{206Pb/238U}$	σ	$T_{207Pb/235U}$	σ	$T_{207Pb/206Pb}$	σ	Conc. (%)	Histogram ($^{207}Pb/^{206}Pb$ Ages)
1.1	25.9693	0.4019	0.7118	0.0069	0.8400	1.4050	0.0137	0.2646	0.0036	0.1182	0.0218	3465	26	3345	15	3274	22	103	Concordant data
2.1	10.3789	0.1658	0.4460	0.0043	0.9900	2.2420	0.0218	0.1688	0.0023	0.1559	0.0504	2378	19	2469	15	2546	23	96	
4.1	7.2586	0.1318	0.4258	0.0047	0.0100	2.3483	0.0260	0.1236	0.0027	0.1846	0.1165	2287	22	2144	18	2009	34	106	
6.1	14.4261	0.2151	0.5437	0.0048	0.6200	1.8392	0.0161	0.1924	0.0026	0.2391	0.0060	2799	20	2778	14	2763	22	100	
7.1	9.6632	0.1298	0.4531	0.0038	0.9900	2.2069	0.0186	0.1547	0.0021	0.2310	0.0234	2409	17	2403	12	2398	23	100	
8.1	6.7647	0.0841	0.3813	0.0029	0.9900	2.6229	0.0197	0.1287	0.0018	0.1072	0.0195	2082	14	2081	12	2080	25	100	
10.1	7.2341	0.1146	0.3918	0.0027	0.8600	2.5521	0.0173	0.1339	0.0019	0.2395	0.0262	2131	2	2141	14	2150	25	99	
11.1	12.9358	0.1792	0.5167	0.0030	0.9900	1.9355	0.0114	0.1816	0.0023	0.1620	0.0047	2685	13	2675	13	2667	21	100	
12.1	4.8018	0.0905	0.3199	0.0025	0.5400	3.1259	0.0245	0.1089	0.0021	0.3462	0.0265	1789	12	1785	16	1780	35	100	
13.1	6.2378	0.0920	0.3674	0.0022	0.9900	2.7219	0.0165	0.1231	0.0017	0.7678	0.0515	2017	11	2010	13	2002	25	100	
14.1	8.2960	0.1269	0.4185	0.0029	0.3800	2.3893	0.0164	0.1438	0.0020	0.1268	0.0050	2254	13	2264	14	2273	25	99	
15.1	6.8976	0.1137	0.3891	0.0030	0.8500	2.5700	0.0201	0.1286	0.0020	0.1171	0.0084	2119	14	2098	14	2079	28	100	
16.1	7.0453	0.0973	0.3843	0.0026	0.9900	2.6019	0.0173	0.1329	0.0019	0.3263	0.0105	2097	12	2117	13	2137	27	99	
17.1	3.8471	0.0978	0.2806	0.0026	0.6800	3.5633	0.0329	0.0994	0.0025	0.2112	0.0096	1595	13	1603	21	1613	47	99	
18.1	7.8482	0.1335	0.4190	0.0033	0.9300	2.3869	0.0186	0.1359	0.0022	0.1181	0.0042	2256	15	2214	15	2175	28	101	
19.1	7.6015	0.1251	0.4088	0.0032	0.9800	2.4463	0.0192	0.1349	0.0021	0.1024	0.0036	2209	15	2185	15	2162	28	101	
20.1	7.0171	0.1073	0.3933	0.0025	0.9400	2.5425	0.0161	0.1294	0.0018	0.2119	0.0142	2138	12	2114	14	2090	25	101	
21.1	6.3200	0.0887	0.3595	0.0021	0.9000	2.7816	0.0164	0.1275	0.0016	0.1059	0.0152	1980	10	2021	12	2064	22	97	
22.1	7.2014	0.1087	0.3933	0.0025	0.5200	2.5423	0.0163	0.1328	0.0019	0.1267	0.0070	2138	12	2137	14	2135	25	100	
23.1	7.3457	0.1033	0.4037	0.0022	0.9900	2.4770	0.0134	0.1320	0.0019	0.1904	0.0441	2186	10	2154	14	2124	25	101	

Detrital zircon U-Pb analyses – Results for Sample HJ 110B (cont.)

Spot	RATIOS											AGES (Ma)							
	$^{207}Pb/^{235}U$	σ	$^{206}Pb/^{238}U$	σ	Corr. coef.	$^{238}U/^{206}Pb$	σ	$^{207}Pb/^{206}Pb$	σ	$^{208}Pb/^{206}Pb$	σ	$T_{206Pb/238U}$	σ	$T_{207Pb/235U}$	σ	$T_{207Pb/206Pb}$	σ	Conc. (%)	Histogram ($^{207}Pb/^{206}Pb$ Ages)
25.1	6.3109	0.0644	0.3683	0.0025	0.9900	2.7155	0.0183	0.1243	0.0015	0.2610	0.0661	2021	12	2020	10	2019	22	100	
26.1	18.2109	0.2219	0.5975	0.0051	0.8500	1.6737	0.0142	0.2211	0.0030	0.1952	0.0110	3020	20	3001	12	2988	22	100	
27.1	6.2176	0.0666	0.3610	0.0025	0.9900	2.7700	0.0194	0.1249	0.0016	0.0692	0.0354	1987	12	2007	10	2028	23	99	
29.1	14.3141	0.1965	0.5398	0.0040	0.8200	1.8525	0.0138	0.1923	0.0027	0.3068	0.0103	2783	17	2771	13	2762	23	100	
32.1	4.8923	0.0919	0.3205	0.0031	0.7200	3.1201	0.0299	0.1107	0.0020	0.2524	0.0080	1792	15	1801	16	1811	33	99	
33.1	15.0751	0.2205	0.5553	0.0043	0.9100	1.8007	0.0138	0.1969	0.0025	0.2417	0.0052	2847	18	2820	14	2801	21	100	
34.1	11.9330	0.1874	0.4959	0.0040	0.8100	2.0164	0.0161	0.1745	0.0023	0.1632	0.0049	2596	17	2599	15	2601	22	99	
35.1	10.5994	0.1395	0.4726	0.0026	0.9200	2.1161	0.0117	0.1627	0.0020	0.1979	0.0109	2495	11	2489	12	2484	21	100	
37.1	6.6035	0.0978	0.3800	0.0022	0.9800	2.6315	0.0151	0.1260	0.0017	0.2711	0.0102	2076	10	2060	13	2043	24	100	
38.1	7.6336	0.1163	0.4069	0.0024	0.9400	2.4573	0.0147	0.1360	0.0019	0.4868	0.0207	2201	11	2189	14	2178	25	100	
39.1	7.1254	0.0928	0.3888	0.0021	0.9800	2.5723	0.0141	0.1329	0.0016	0.1565	0.0277	2117	10	2127	12	2137	21	99	
40.1	7.2710	0.1426	0.3913	0.0036	0.5800	2.5553	0.0234	0.1348	0.0024	0.0849	0.0106	2129	17	2145	18	2161	31	99	
41.1	9.7806	0.1196	0.4122	0.0022	0.9900	2.4259	0.0130	0.1721	0.0021	0.2765	0.0488	2225	10	2414	12	2578	21	92	Concordant data
42.1	6.8141	0.1052	0.3849	0.0025	0.8900	2.5983	0.0169	0.1284	0.0017	0.0788	0.0047	2099	12	2088	13	2076	24	100	
43.1	6.8413	0.0924	0.3925	0.0037	0.8400	2.5477	0.0237	0.1264	0.0017	0.0872	0.0044	2135	17	2091	12	2049	25	102	
44.1	15.3762	0.2097	0.5576	0.0033	0.8700	1.7934	0.0108	0.2000	0.0025	0.2177	0.0068	2857	14	2839	13	2826	21	100	
46.1	6.7978	0.0715	0.3867	0.0024	0.9900	2.5863	0.0161	0.1275	0.0015	0.2177	0.0149	2107	11	2085	10	2064	21	101	
47.1	6.3326	0.0773	0.3564	0.0024	0.9800	2.8058	0.0187	0.1289	0.0018	0.2257	0.0219	1965	11	2023	11	2083	24	97	
48.1	7.2725	0.0994	0.3950	0.0027	0.8200	2.5318	0.0174	0.1335	0.0019	0.1082	0.0043	2146	13	2145	12	2145	24	100	
51.1	4.6368	0.0410	0.2888	0.0017	0.9900	3.4627	0.0205	0.1164	0.0012	0.2239	0.0178	1636	9	1756	8	1902	19	93	
52.1	19.8107	0.1975	0.5914	0.0042	0.8600	1.6909	0.0120	0.2430	0.0026	0.1437	0.0110	2995	17	3082	10	3139	17	97	
53.1	7.2702	0.0993	0.3857	0.0033	0.9800	2.5927	0.0224	0.1367	0.0020	0.2332	0.0331	2103	15	2145	12	2186	25	98	
54.1	6.8913	0.0792	0.3801	0.0026	0.9900	2.6309	0.0181	0.1315	0.0018	0.0644	0.0060	2077	12	2098	11	2118	24	99	
55.1	6.9432	0.0762	0.3799	0.0031	0.9200	2.6324	0.0212	0.1326	0.0017	0.0903	0.0125	2076	15	2104	10	2132	22	98	
56.1	7.6038	0.0909	0.4064	0.0023	0.8700	2.4606	0.0140	0.1357	0.0015	0.1302	0.0038	2199	11	2185	11	2173	20	100	

Detrital zircon U-Pb analyses – Results for Sample HJ 110B (cont.)

Spot	RATIOS											AGES (Ma)							Histogram ($^{207}Pb/^{206}Pb$ Ages)
	$^{207}Pb/^{235}U$	σ	$^{206}Pb/^{238}U$	σ	Corr. coef.	$^{238}U/^{206}Pb$	σ	$^{207}Pb/^{206}Pb$	σ	$^{208}Pb/^{206}Pb$	σ	$T_{206Pb/238U}$	σ	$T_{207Pb/235U}$	σ	$T_{207Pb/206Pb}$	σ	Conc. (%)	
57.1	7.7250	0.0873	0.4167	0.0021	0.9900	2.3998	0.0120	0.1345	0.0014	0.1878	0.1398	2246	10	2200	11	2157	19	102	Concordant data
58.1	10.2664	0.1190	0.4644	0.0025	0.7600	2.1533	0.0117	0.1603	0.0017	0.3015	0.0076	2459	11	2459	11	2459	18	99	
59.1	12.9433	0.1547	0.5195	0.0040	0.9200	1.9250	0.0147	0.1807	0.0022	0.2180	0.0118	2697	17	2676	12	2659	21	100	
60.1	6.7212	0.0727	0.3803	0.0026	0.8000	2.6295	0.0177	0.1282	0.0014	0.1398	0.0028	2078	12	2075	10	2073	20	100	
61.1	7.0358	0.1052	0.3844	0.0033	0.8700	2.6016	0.0222	0.1328	0.0021	0.1708	0.0084	2097	15	2116	13	2135	28	99	
62.1	5.9165	0.0591	0.3264	0.0021	0.9700	3.0638	0.0198	0.1315	0.0015	0.1419	0.0080	1821	10	1964	9	2118	20	92	
64.1	7.5758	0.1047	0.4138	0.0025	0.9400	2.4164	0.0146	0.1328	0.0018	0.1111	0.0055	2232	11	2182	12	2135	24	102	
65.1	7.7747	0.1176	0.4177	0.0033	0.8800	2.3938	0.0186	0.1350	0.0021	0.1482	0.0575	2250	15	2205	14	2164	27	102	
66.1	12.7721	0.1974	0.5170	0.0038	0.8700	1.9341	0.0144	0.1792	0.0027	0.3644	0.0593	2687	16	2663	15	2645	25	100	
67.1	12.8028	0.1941	0.5245	0.0040	0.9900	1.9067	0.0146	0.1770	0.0026	0.3338	0.0762	2718	17	2665	14	2625	24	101	
68.1	7.1614	0.1123	0.3914	0.0029	0.8600	2.5552	0.0186	0.1327	0.0020	0.1791	0.0092	2129	13	2132	14	2134	27	99	
69.1	6.7856	0.1190	0.3817	0.0033	0.7100	2.6196	0.0227	0.1289	0.0024	0.2414	0.0164	2084	15	2084	15	2083	32	100	
70.1	7.3535	0.1104	0.3932	0.0029	0.9700	2.5433	0.0190	0.1356	0.0020	0.1384	0.0125	2138	14	2155	13	2172	26	99	
71.1	13.9761	0.1575	0.5332	0.0035	0.9900	1.8753	0.0123	0.1901	0.0023	0.0910	0.0075	2755	15	2748	11	2743	20	100	
72.1	7.2061	0.0840	0.4040	0.0025	0.9900	2.4750	0.0154	0.1294	0.0017	0.1631	0.0243	2188	12	2137	11	2089	23	102	
73.1	6.3515	0.0944	0.3587	0.0022	0.9500	2.7881	0.0170	0.1284	0.0018	0.1752	0.0206	1976	10	2026	14	2077	25	97	
74.1	7.8533	0.1428	0.4200	0.0035	0.8900	2.3809	0.0199	0.1356	0.0023	0.1305	0.0176	2261	16	2214	16	2172	30	102	
75.1	6.9515	0.1150	0.3577	0.0026	0.9900	2.7953	0.0200	0.1409	0.0020	0.2007	0.0055	1972	12	2105	14	2239	24	93	
76.1	6.9033	0.1127	0.3908	0.0028	0.9800	2.5589	0.0180	0.1281	0.0019	0.1616	0.0058	2127	13	2099	15	2072	26	101	
77.1	7.7856	0.1222	0.4160	0.0029	0.6900	2.4038	0.0166	0.1357	0.0019	0.3033	0.0074	2242	13	2207	14	2174	24	101	
78.1	6.9369	0.1096	0.3938	0.0022	0.9700	2.5395	0.0143	0.1278	0.0021	0.1318	0.0104	2140	10	2103	14	2068	28	101	
79.1	6.5414	0.0998	0.3768	0.0021	0.7700	2.6539	0.0146	0.1259	0.0018	0.1048	0.0055	2061	10	2052	14	2042	26	100	
80.1	7.9025	0.1463	0.4121	0.0030	0.8100	2.4265	0.0174	0.1391	0.0025	0.0886	0.0115	2225	14	2220	17	2216	31	100	
82.1	25.7833	0.3642	0.6866	0.0040	0.9700	1.4564	0.0086	0.2723	0.0038	0.1714	0.0453	3370	15	3338	14	3320	22	100	
84.1	6.4646	0.0854	0.3766	0.0029	0.9000	2.6554	0.0207	0.1245	0.0017	0.2138	0.0142	2060	14	2041	12	2022	24	100	
85.1	6.8019	0.0862	0.3783	0.0030	0.8600	2.6435	0.0213	0.1304	0.0017	0.1484	0.0235	2068	14	2086	11	2104	23	99	
86.1	15.1798	0.1877	0.5563	0.0042	0.7700	1.7974	0.0136	0.1979	0.0025	0.1004	0.0045	2852	18	2827	12	2809	20	100	

Detrital zircon U-Pb analyses – Results for Sample HJ 110B (cont.)

Spot	RATIOS											AGES (Ma)							
	$^{207}Pb/^{235}U$	σ	$^{206}Pb/^{238}U$	σ	Corr. coef.	$^{238}U/^{206}Pb$	σ	$^{207}Pb/^{206}Pb$	σ	$^{208}Pb/^{206}Pb$	σ	$T_{206Pb/238U}$	σ	$T_{207Pb/235U}$	σ	$T_{207Pb/206Pb}$	σ	Conc. (%)	Histogram ($^{207}Pb/^{206}Pb$ Ages)
87.1	6.8238	0.0846	0.3868	0.0029	0.9900	2.5853	0.0192	0.1279	0.0016	0.1396	0.0097	2108	13	2089	11	2070	23	100	Concordant data
89.1	13.6749	0.2232	0.5364	0.0032	0.9900	1.8643	0.0110	0.1849	0.0029	0.3610	0.0450	2768	14	2728	17	2697	27	101	
91.1	6.9804	0.1408	0.3919	0.0029	0.5000	2.5515	0.0187	0.1292	0.0024	0.1140	0.0053	2132	13	2109	18	2087	33	101	
92.1	4.7010	0.0973	0.3207	0.0022	0.8500	3.1181	0.0217	0.1063	0.0021	0.2436	0.0420	1793	11	1767	18	1737	36	101	
94.1	7.1072	0.1250	0.3982	0.0031	0.4200	2.5112	0.0194	0.1294	0.0022	0.1673	0.0135	2161	14	2125	16	2090	30	101	
95.1	7.5688	0.1307	0.4096	0.0031	0.8900	2.4417	0.0182	0.1340	0.0022	0.3576	0.0062	2213	14	2181	16	2152	29	101	
96.1	6.5497	0.0780	0.3773	0.0025	0.9900	2.6505	0.0174	0.1259	0.0016	0.2345	0.0222	2064	12	2053	11	2042	22	100	
97.1	6.7941	0.0911	0.3854	0.0029	0.9600	2.5944	0.0196	0.1278	0.0018	0.0893	0.0077	2102	14	2085	12	2069	24	100	
98.1	7.6639	0.0987	0.4119	0.0028	0.6600	2.4276	0.0167	0.1349	0.0017	0.1074	0.0090	2224	13	2192	12	2163	22	101	
99.1	17.2762	0.2215	0.5841	0.0042	0.9900	1.7119	0.0122	0.2145	0.0026	0.2048	0.0120	2966	17	2950	13	2940	20	100	
100.1	7.2078	0.0891	0.4009	0.0026	0.9900	2.4943	0.0163	0.1304	0.0018	0.2153	0.0174	2173	12	2138	12	2103	24	101	
3.1	3.4597	0.0628	0.2263	0.0023	0.9900	4.4191	0.0453	0.1109	0.0017	0.1547	0.0192	1315	12	1518	13	1814	26	86	Discordant data
5.1	7.2858	0.1313	0.3961	0.0044	0.9600	2.5248	0.0281	0.1334	0.0023	0.2956	0.3052	2151	20	2147	16	2143	29	100	
9.1	3.3436	0.0426	0.1845	0.0014	0.9700	5.4213	0.0404	0.1315	0.0016	0.1789	0.0375	1091	8	1491	9	2118	21	73	
24.1	1.9184	0.0221	0.1411	0.0007	0.9500	7.0884	0.0360	0.0986	0.0011	0.2311	0.0345	851	4	1088	9	1598	23	78	
28.1	3.8766	0.0296	0.2492	0.0013	0.9900	4.0121	0.0209	0.1128	0.0014	0.3366	0.1878	1435	7	1609	8	1845	24	89	
30.1	4.2709	0.0580	0.2502	0.0020	0.9900	3.9963	0.0326	0.1238	0.0016	0.2327	0.0312	1440	10	1688	10	2012	23	85	
31.1	2.8976	0.0484	0.1924	0.0016	0.9900	5.1978	0.0425	0.1092	0.0014	0.2053	0.0319	1134	8	1381	11	1787	23	82	
36.1	1.8714	0.0265	0.1304	0.0008	0.9500	7.6669	0.0445	0.1041	0.0013	0.3656	0.0478	790	4	1071	9	1698	24	73	
45.1	4.1699	0.0929	0.2065	0.0012	0.9900	4.8418	0.0287	0.1464	0.0022	0.1376	0.0387	1210	6	1668	12	2305	19	72	
49.1	1.8254	0.0331	0.0775	0.0008	0.9900	12.8993	0.1320	0.1708	0.0022	0.5009	0.2415	481	5	1055	9	2565	21	45	
50.1	7.0580	0.0931	0.3246	0.0022	0.9800	3.0806	0.0212	0.1577	0.0018	0.1679	0.0059	1812	11	2119	10	2431	19	85	
63.1	3.0369	0.0445	0.1817	0.0011	0.9900	5.5038	0.0326	0.1212	0.0017	0.2521	0.0480	1076	6	1417	11	1974	26	75	
81.1	2.9602	0.0437	0.2047	0.0011	0.9700	4.8842	0.0258	0.1049	0.0015	0.2693	0.0134	1201	6	1398	11	1712	25	85	
83.1	8.1421	0.1165	0.3206	0.0029	0.9900	3.1191	0.0281	0.1842	0.0024	0.1589	0.0238	1793	13	2247	12	2691	22	79	
88.1	-0.0151	-0.0001	0.0080	0.0001	0.6800	124.5344	0.7894	-0.0137	0.0000	1.6061	0.0450	52	0	0	0	0	0	5155741	
90.1	3.0657	0.0668	0.1640	0.0010	0.9800	6.0981	0.0390	0.1356	0.0023	0.2212	0.0390	979	6	1424	14	2172	27	68	
93.1	5.2064	0.0880	0.2919	0.0017	0.9900	3.4256	0.0200	0.1293	0.0022	0.2604	0.0842	1651	9	1854	16	2089	30	89	

Same grain

Same grain

Same grain

Detrital zircon U-Pb analyses – Results for Sample HJ 110B (cont.)

Same grain

Same grain

Detrital zircon U-Pb analyses – Results for Sample HJ 110B (Standards)

Standard GJ data on 25/03/2022 Concordia Age = 602.5 +/- 1.2 Ma GJ reference age: 608.5 +/- 0.4 Ma (TIMS) - Jackson et al, 2004.	Pleosovic secondary standard on 25/03/2022 Concordia Age = 336.7 +/- 0.85 Ma Pleosovic reference age: 337.13 +/- 0.37 - Sláma et al, 2008.

Detrital zircon U-Pb analyses – Results for Sample HJ 129

Spot	RATIOS											AGES (Ma)							
	$^{207}Pb/^{235}U$	σ	$^{206}Pb/^{238}U$	σ	Corr. coef.	$^{238}U/^{206}Pb$	σ	$^{207}Pb/^{206}Pb$	σ	$^{208}Pb/^{206}Pb$	σ	$T_{206Pb/238U}$	σ	$T_{207Pb/235U}$	σ	$T_{207Pb/206Pb}$	σ	Conc. (%)	Histogram ($^{207}Pb/^{206}Pb$ Ages)
2.1	6.1922	0.0895	0.3569	0.0025	0.9800	2.8019	0.0196	0.1258	0.0015	0.1038	0.0105	1967	12	2003	13	2041	22	98	Concordant data
3.1	5.9218	0.0957	0.3273	0.0026	0.9800	3.0552	0.0241	0.1312	0.0019	0.2211	0.0244	1825	13	1964	14	2114	25	92	
4.1	6.7622	0.1129	0.3819	0.0033	0.6600	2.6187	0.0227	0.1284	0.0021	0.1314	0.0063	2085	15	2081	15	2077	28	100	
5.1	10.4555	0.1529	0.4652	0.0033	0.8600	2.1497	0.0151	0.1630	0.0022	0.4580	0.0048	2462	14	2476	14	2487	22	99	
6.1	10.1603	0.1475	0.4655	0.0038	0.6500	2.1485	0.0177	0.1583	0.0023	0.3046	0.0066	2464	17	2450	14	2438	24	100	
8.1	6.1203	0.0738	0.3456	0.0026	0.9800	2.8931	0.0221	0.1284	0.0013	0.1753	0.0173	1914	13	1993	11	2077	17	96	
9.1	7.9583	0.1815	0.4162	0.0062	0.4900	2.4028	0.0360	0.1387	0.0033	0.1102	0.0204	2243	28	2226	21	2211	40	100	
10.1	7.2551	0.0915	0.3921	0.0031	0.9600	2.5502	0.0204	0.1342	0.0013	0.1700	0.0166	2133	15	2143	11	2154	17	99	
11.1	7.0514	0.0856	0.3962	0.0030	0.9700	2.5237	0.0191	0.1291	0.0013	0.1301	0.0032	2152	14	2118	11	2085	17	101	
14.1	9.2556	0.1335	0.4475	0.0035	0.9300	2.2348	0.0173	0.1500	0.0020	0.1645	0.0039	2384	15	2364	13	2346	23	100	
15.1	6.2215	0.0798	0.3367	0.0021	0.9900	2.9701	0.0186	0.1340	0.0016	0.3148	0.0662	1871	10	2008	12	2151	21	93	
16.1	4.0677	0.0618	0.2900	0.0023	0.7600	3.4483	0.0268	0.1017	0.0014	0.1906	0.0151	1642	11	1648	13	1656	26	99	
17.1	6.9067	0.0855	0.3903	0.0026	0.9800	2.5619	0.0173	0.1283	0.0016	0.2064	0.0517	2124	13	2100	12	2075	22	101	
18.1	10.7106	0.1476	0.4504	0.0027	0.9700	2.2204	0.0133	0.1725	0.0021	0.1750	0.0373	2397	12	2498	12	2582	20	95	
19.1	7.0115	0.1044	0.3886	0.0025	0.9900	2.5733	0.0163	0.1309	0.0019	0.1923	0.0100	2116	12	2113	14	2110	26	100	

Detrital zircon U-Pb analyses – Results for Sample HJ 129

Spot	RATIOS											AGES (Ma)							
	$^{207}Pb/^{235}U$	σ	$^{206}Pb/^{238}U$	σ	Corr. coef.	$^{238}U/^{206}Pb$	σ	$^{207}Pb/^{206}Pb$	σ	$^{208}Pb/^{206}Pb$	σ	$T_{206Pb/238U}$	σ	$T_{207Pb/235U}$	σ	$T_{207Pb/206Pb}$	σ	Conc. (%)	Histogram ($^{207}Pb/^{206}Pb$ Ages)
20.1	9.5862	0.1311	0.4399	0.0023	0.9800	2.2732	0.0121	0.1580	0.0021	0.2067	0.0431	2350	11	2396	13	2435	23	98	Concordant data
23.1	6.9809	0.1297	0.3504	0.0032	0.9700	2.8541	0.0264	0.1445	0.0019	0.2086	0.0075	1936	15	2109	16	2282	23	91	
24.1	7.6042	0.1606	0.4036	0.0045	0.8800	2.4780	0.0276	0.1367	0.0022	0.1661	0.0149	2185	21	2185	19	2185	28	100	
25.1	6.9332	0.1328	0.3922	0.0035	0.9900	2.5498	0.0228	0.1282	0.0018	0.1398	0.0153	2133	17	2103	17	2074	25	101	
28.1	7.4551	0.1178	0.4026	0.0026	0.9200	2.4838	0.0163	0.1343	0.0018	0.1489	0.0082	2181	12	2168	14	2155	24	100	
29.1	7.1817	0.1247	0.3882	0.0027	0.7900	2.5760	0.0180	0.1342	0.0020	0.1083	0.0068	2115	12	2134	15	2153	26	99	
30.1	7.0320	0.1098	0.3865	0.0026	0.7100	2.5876	0.0172	0.1320	0.0019	0.2997	0.0215	2106	12	2116	14	2124	26	99	
31.1	7.6909	0.1155	0.4043	0.0031	0.7800	2.4733	0.0190	0.1380	0.0020	0.2002	0.0048	2189	14	2196	14	2202	26	99	
32.1	6.8140	0.1116	0.3755	0.0026	0.8000	2.6632	0.0187	0.1316	0.0020	0.2687	0.0174	2055	12	2088	14	2120	27	98	
35.1	6.8739	0.1024	0.3873	0.0029	0.8400	2.5821	0.0191	0.1287	0.0020	0.1317	0.0122	2110	13	2095	13	2081	27	100	
36.1	13.0140	0.1768	0.5172	0.0035	0.9600	1.9337	0.0130	0.1825	0.0026	0.1679	0.0290	2687	15	2681	13	2676	23	100	
37.1	6.3675	0.0822	0.3623	0.0021	0.9800	2.7604	0.0163	0.1275	0.0017	0.1496	0.0149	1993	10	2028	11	2064	23	98	
39.1	6.9862	0.0764	0.3906	0.0028	0.9700	2.5601	0.0181	0.1297	0.0015	0.1090	0.0056	2126	13	2110	10	2094	20	100	
40.1	5.4101	0.0611	0.3093	0.0020	0.9900	3.2330	0.0210	0.1269	0.0014	0.3708	0.0266	1737	10	1887	10	2055	20	92	
43.1	6.4688	0.1055	0.3747	0.0032	0.8700	2.6689	0.0224	0.1252	0.0019	0.1325	0.0071	2051	15	2042	14	2032	27	100	
44.1	7.0393	0.1153	0.3894	0.0038	0.8100	2.5681	0.0252	0.1311	0.0020	0.2226	0.2110	2120	18	2116	15	2113	28	100	
45.1	6.9071	0.1234	0.3829	0.0035	0.5500	2.6116	0.0239	0.1308	0.0022	0.1403	0.0088	2090	16	2100	16	2109	29	99	
47.1	6.7368	0.0962	0.3816	0.0027	0.8500	2.6204	0.0184	0.1280	0.0016	0.2702	0.0078	2084	13	2078	13	2071	22	100	
48.1	10.1586	0.1270	0.4735	0.0032	0.9900	2.1121	0.0142	0.1556	0.0017	0.2607	0.0239	2499	14	2449	12	2409	19	102	
49.1	10.1511	0.1543	0.4471	0.0039	0.9900	2.2364	0.0197	0.1646	0.0022	0.1097	0.0055	2383	17	2449	13	2504	22	97	
50.1	12.3615	0.1511	0.4953	0.0033	0.9900	2.0190	0.0136	0.1810	0.0020	0.1279	0.0060	2594	15	2632	12	2662	19	98	
51.1	6.4843	0.0949	0.3581	0.0026	0.9700	2.7927	0.0204	0.1313	0.0016	0.1494	0.0079	1973	12	2044	13	2116	21	96	
52.1	5.9836	0.0957	0.3425	0.0028	0.9800	2.9197	0.0235	0.1267	0.0021	0.2065	0.0181	1899	13	1974	14	2053	29	96	
54.1	6.8140	0.1041	0.3816	0.0030	0.9200	2.6203	0.0205	0.1295	0.0020	0.1542	0.0058	2084	14	2088	13	2091	28	99	
55.1	13.4803	0.2292	0.5255	0.0041	0.9900	1.9028	0.0149	0.1860	0.0033	0.2254	0.0363	2723	18	2714	17	2707	29	100	
58.1	10.0240	0.1162	0.4554	0.0025	0.9900	2.1958	0.0123	0.1596	0.0018	0.2287	0.0683	2419	12	2437	11	2452	20	99	

Detrital zircon U-Pb analyses – Results for Sample HJ 129 (cont.)

Spot	RATIOS											AGES (Ma)							
	$^{207}Pb/^{235}U$	σ	$^{206}Pb/^{238}U$	σ	Corr. coef.	$^{238}U/^{206}Pb$	σ	$^{207}Pb/^{206}Pb$	σ	$^{208}Pb/^{206}Pb$	σ	$T_{206Pb/238U}$	σ	$T_{207Pb/235U}$	σ	$T_{207Pb/206Pb}$	σ	Conc. (%)	Histogram ($^{207}Pb/^{206}Pb$ Ages)
59.1	5.5969	0.0690	0.3168	0.0017	0.9600	3.1569	0.0166	0.1281	0.0014	0.2103	0.0132	1774	8	1916	11	2073	19	92	Concordant data
60.1	5.1853	0.0616	0.3227	0.0016	0.9900	3.0984	0.0157	0.1165	0.0012	0.1474	0.0083	1803	8	1850	10	1904	19	97	
62.1	9.5011	0.1439	0.4517	0.0035	0.7300	2.2138	0.0172	0.1525	0.0021	0.1226	0.0055	2403	16	2388	14	2375	23	100	
64.1	12.7889	0.1837	0.5067	0.0040	0.9200	1.9735	0.0155	0.1831	0.0025	0.2687	0.0127	2643	17	2664	14	2681	23	99	
65.1	6.3289	0.0756	0.3523	0.0028	0.9900	2.8383	0.0223	0.1303	0.0015	0.2118	0.0432	1946	13	2023	11	2102	21	96	
67.1	5.1768	0.0655	0.2993	0.0025	0.9900	3.3412	0.0277	0.1254	0.0014	0.1711	0.0841	1688	12	1849	11	2035	19	91	
68.1	11.4041	0.2363	0.4468	0.0071	0.9000	2.2381	0.0354	0.1851	0.0037	1.6123	1.0204	2381	31	2557	18	2699	32	93	
70.1	5.1824	0.0832	0.2948	0.0021	0.9900	3.3918	0.0238	0.1275	0.0021	0.2319	0.0128	1666	10	1850	13	2064	29	90	
72.1	9.8226	0.1636	0.4570	0.0035	0.9900	2.1883	0.0167	0.1559	0.0027	0.5447	0.0408	2426	16	2418	17	2412	30	100	
74.1	23.6675	0.2897	0.6734	0.0051	0.4500	1.4850	0.0113	0.2549	0.0031	0.0066	0.0014	3319	20	3255	12	3215	19	101	
75.1	7.5479	0.1139	0.4045	0.0036	0.9000	2.4723	0.0221	0.1353	0.0022	0.1103	0.0089	2190	17	2179	14	2168	28	100	
76.1	7.6154	0.1176	0.4024	0.0038	0.8200	2.4850	0.0232	0.1373	0.0022	0.1594	0.0087	2180	17	2187	14	2193	29	99	
77.1	7.7494	0.1068	0.4068	0.0036	0.9900	2.4580	0.0215	0.1381	0.0020	0.1236	0.0205	2200	16	2202	12	2204	25	99	
78.1	7.2162	0.0993	0.3971	0.0036	0.8900	2.5183	0.0231	0.1318	0.0017	0.1549	0.0128	2156	17	2139	12	2122	22	100	
79.1	10.2186	0.1428	0.4626	0.0043	0.8500	2.1618	0.0199	0.1602	0.0020	0.2254	0.0041	2451	19	2455	13	2458	21	99	
80.1	15.4458	0.2072	0.5642	0.0052	0.7800	1.7725	0.0163	0.1986	0.0025	0.2213	0.0062	2884	21	2843	13	2814	20	101	
81.1	6.6074	0.0854	0.3830	0.0031	0.9900	2.6109	0.0213	0.1251	0.0014	0.1524	0.0171	2090	15	2060	12	2031	21	101	
82.1	6.9860	0.0913	0.3958	0.0026	0.6900	2.5265	0.0163	0.1280	0.0017	0.1055	0.0138	2150	12	2110	12	2071	23	101	
83.1	7.8122	0.1036	0.4152	0.0031	0.8100	2.4082	0.0182	0.1365	0.0018	0.2192	0.0190	2239	14	2210	12	2183	23	101	
84.1	7.7171	0.1227	0.4070	0.0032	0.3900	2.4572	0.0191	0.1375	0.0023	0.1590	0.0036	2201	15	2199	14	2196	29	100	
85.1	6.7788	0.1153	0.3839	0.0032	0.6400	2.6051	0.0218	0.1281	0.0022	0.1491	0.0079	2094	15	2083	15	2072	30	100	
86.1	13.1294	0.2075	0.5173	0.0042	0.8900	1.9330	0.0155	0.1841	0.0029	0.1415	0.0037	2688	18	2689	15	2690	26	99	
87.1	7.1026	0.1149	0.3861	0.0031	0.9800	2.5897	0.0208	0.1334	0.0022	0.1345	0.0102	2105	14	2124	14	2143	28	99	
88.1	7.8958	0.1331	0.4260	0.0032	0.9900	2.3472	0.0177	0.1344	0.0023	0.1324	0.0115	2288	15	2219	16	2156	30	103	
89.1	7.6711	0.1809	0.4037	0.0043	0.4300	2.4771	0.0264	0.1378	0.0033	0.2200	0.0137	2186	20	2193	21	2200	42	99	
92.1	7.1264	0.1078	0.4041	0.0039	0.8100	2.4746	0.0238	0.1279	0.0023	0.1541	0.0162	2188	18	2127	14	2069	32	102	

Detrital zircon U-Pb analyses – Results for Sample HJ 129 (cont.)

Spot	RATIOS											AGES (Ma)							
	$^{207}Pb/^{235}U$	σ	$^{206}Pb/^{238}U$	σ	Corr. coef.	$^{238}U/^{206}Pb$	σ	$^{207}Pb/^{206}Pb$	σ	$^{208}Pb/^{206}Pb$	σ	$T_{206Pb/238U}$	σ	$T_{207Pb/235U}$	σ	$T_{207Pb/206Pb}$	σ	Conc. (%)	Histogram ($^{207}Pb/^{206}Pb$ Ages)
93.1	5.7406	0.1029	0.3249	0.0031	0.9900	3.0777	0.0298	0.1281	0.0020	0.1943	0.0647	1814	15	1938	15	2073	28	93	Concordant data
94.1	5.5140	0.0813	0.3108	0.0024	0.9900	3.2177	0.0253	0.1287	0.0018	0.2471	0.0571	1745	12	1903	14	2080	25	91	
95.1	18.3870	0.2800	0.5776	0.0051	0.9000	1.7314	0.0153	0.2309	0.0031	0.1620	0.0469	2939	21	3010	15	3058	22	97	
96.1	9.5112	0.1638	0.4592	0.0041	0.9900	2.1775	0.0194	0.1502	0.0024	0.2604	0.1222	2436	18	2389	17	2348	28	101	
98.1	6.4750	0.1328	0.3735	0.0031	0.9700	2.6777	0.0223	0.1257	0.0025	0.1636	0.0098	2046	15	2043	18	2039	34	100	
100.1	21.9384	0.4164	0.6458	0.0057	0.9900	1.5484	0.0136	0.2464	0.0045	0.1323	0.0362	3212	22	3181	19	3162	29	100	
1.1	14.4764	0.1794	0.3916	0.0024	0.9800	2.5538	0.0154	0.2681	0.0030	0.4328	0.1889	2130	11	2782	13	3295	18	76	Discordant data
7.1	5.8422	0.0716	0.3267	0.0022	0.9900	3.0609	0.0205	0.1297	0.0016	0.3795	0.1429	1822	11	1953	12	2094	24	93	
12.1	12.1323	0.1409	0.4035	0.0032	0.9900	2.4781	0.0195	0.2181	0.0019	0.1982	0.0702	2185	15	2615	11	2966	14	83	
13.1	3.5597	0.0548	0.2316	0.0017	0.9900	4.3181	0.0325	0.1115	0.0013	0.2060	0.0151	1343	9	1541	11	1824	20	87	
21.1	4.8876	0.0833	0.2746	0.0019	0.9900	3.6414	0.0254	0.1291	0.0019	0.5035	0.3219	1564	9	1800	13	2086	28	86	
22.1	2.7523	0.0394	0.1795	0.0010	0.9800	5.5722	0.0308	0.1112	0.0014	0.5644	0.1246	1064	5	1343	10	1820	23	79	
26.1	5.5202	0.0689	0.3128	0.0021	0.9900	3.1969	0.0216	0.1280	0.0017	0.3934	0.2351	1755	11	1904	15	2071	25	92	
27.1	6.5973	0.1481	0.2866	0.0031	0.9900	3.4894	0.0378	0.1670	0.0026	0.7211	0.0544	1624	15	2059	18	2527	25	78	
33.1	14.4749	0.1810	0.3941	0.0023	0.7200	2.5377	0.0150	0.2664	0.0033	0.4007	0.0613	2142	11	2781	12	3285	20	76	
34.1	2.4364	0.0444	0.1563	0.0014	0.9900	6.3973	0.0576	0.1130	0.0016	0.4941	0.2595	936	7	1253	10	1849	24	74	
38.1	5.0619	0.0561	0.2933	0.0022	0.9900	3.4096	0.0260	0.1252	0.0017	0.6269	0.2769	1658	11	1830	10	2031	25	90	
41.1	0.8444	0.0267	0.0685	0.0008	0.9900	14.5895	0.1736	0.0894	0.0018	0.6220	0.2858	427	5	622	9	1412	24	68	
42.1	5.3922	0.0608	0.3214	0.0021	0.9800	3.1111	0.0202	0.1217	0.0014	0.2824	0.0569	1797	11	1884	10	1981	21	95	
46.1	3.1329	0.0505	0.1809	0.0016	0.9800	5.5287	0.0480	0.1256	0.0018	0.3829	0.0404	1072	9	1441	12	2038	26	74	
53.1	6.0487	0.0913	0.3470	0.0026	0.9800	2.8822	0.0216	0.1264	0.0021	0.2086	0.0733	1920	13	1983	14	2049	29	96	
56.1	3.8020	0.0581	0.2305	0.0016	0.9900	4.3377	0.0297	0.1196	0.0013	0.2100	0.0673	1337	8	1593	10	1950	18	83	
57.1	4.7824	0.0539	0.2849	0.0015	0.9900	3.5097	0.0180	0.1217	0.0012	0.2177	0.0122	1616	7	1782	10	1982	18	90	
61.1	9.4144	0.1238	0.3883	0.0027	0.9900	2.5754	0.0181	0.1759	0.0021	0.2198	0.0228	2115	13	2379	12	2614	20	88	
63.1	4.4349	0.0615	0.2290	0.0017	0.9900	4.3672	0.0333	0.1405	0.0017	0.3829	0.0175	1329	9	1719	11	2233	21	77	

Detrital zircon U-Pb analyses – Results for Sample HJ 129 (cont.)

Spot	RATIOS											AGES (Ma)							
	$^{207}Pb/^{235}U$	σ	$^{206}Pb/^{238}U$	σ	Corr. coef.	$^{238}U/^{206}Pb$	σ	$^{207}Pb/^{206}Pb$	σ	$^{208}Pb/^{206}Pb$	σ	$T_{206Pb/238U}$	σ	$T_{207Pb/235U}$	σ	$T_{207Pb/206Pb}$	σ	Conc. (%)	Histogram ($^{207}Pb/^{206}Pb$ Ages)
66.1	2.1410	0.0270	0.1332	0.0011	0.9900	7.5079	0.0613	0.1166	0.0013	0.3942	0.1146	806	6	1162	9	1905	20	69	Discordant data
69.1	4.3941	0.0637	0.2565	0.0023	0.9900	3.8989	0.0354	0.1243	0.0015	0.2052	0.0225	1472	12	1711	11	2018	21	86	
71.1	9.8217	0.0920	0.4588	0.0018	0.9900	2.1796	0.0085	0.1553	0.0023	0.3925	0.1087	2434	9	2418	13	2405	25	100	
73.1	2.5216	0.0550	0.1713	0.0018	0.9900	5.8390	0.0611	0.1068	0.0016	0.3886	0.1738	1019	9	1278	11	1745	23	79	
90.1	3.2222	0.0348	0.2226	0.0014	0.9900	4.4914	0.0279	0.1050	0.0016	0.7479	0.2437	1296	8	1463	10	1714	31	88	
91.1	3.4550	0.0737	0.1994	0.0023	0.9900	5.0146	0.0585	0.1257	0.0021	0.2192	0.0464	1172	12	1517	12	2038	29	77	
97.1	3.4786	0.0637	0.2151	0.0017	0.9900	4.6485	0.0371	0.1173	0.0022	0.2792	0.0892	1256	9	1522	15	1915	33	82	
99.1	0.3878	0.0087	0.0481	0.0004	0.9900	20.7841	0.1747	0.0585	0.0014	1.0007	0.3641	303	3	333	7	547	42	91	

Detrital zircon U-Pb analyses – Results for Sample HJ 129 (Standards)

Standard GJ data on 31/03/2022 Concordia Age = 604.1 +/- 1.3 Ma GJ reference age: 608.5 +/- 0.4 Ma (TIMS) - Jackson et al, 2004.	Pleosovic secondary standard on 31/03/2022 Concordia Age = 335.1 +/- 1.1 Ma Pleosovic reference age: 337.13 +/- 0.37 - Sláma et al, 2008.

Detrital zircon U-Pb analyses – Results for Sample HJ 152

Spot	RATIOS											AGES (Ma)							
	$^{207}Pb/^{235}U$	σ	$^{206}Pb/^{238}U$	σ	Corr. coef.	$^{238}U/^{206}Pb$	σ	$^{207}Pb/^{206}Pb$	σ	$^{208}Pb/^{206}Pb$	σ	$T_{206Pb/238U}$	σ	$T_{207Pb/235U}$	σ	$T_{207Pb/206Pb}$	σ	Conc. (%)	Histogram ($^{207}Pb/^{206}Pb$ Ages)
5.1	17.1987	0.2613	0.5860	0.0060	0.9000	1.7064	0.0175	0.2129	0.0031	0.1471	0.0041	2973	24	2946	15	2927	24	100	Concordant data
7.1	7.2394	0.1521	0.4011	0.0029	0.8000	2.4931	0.0179	0.1309	0.0025	0.1651	0.0129	2174	13	2141	19	2110	34	101	
8.1	15.9500	0.2823	0.5731	0.0043	0.6100	1.7448	0.0132	0.2018	0.0034	0.2688	0.0109	2921	18	2874	17	2841	27	101	
11.1	14.1924	0.2072	0.5281	0.0034	0.6900	1.8938	0.0123	0.1949	0.0030	0.1418	0.0097	2733	14	2763	14	2784	25	98	
13.1	13.5966	0.2037	0.4704	0.0032	0.9900	2.1259	0.0146	0.2096	0.0032	0.1491	0.0330	2485	14	2722	13	2903	24	91	
16.1	16.6652	0.2344	0.5820	0.0050	0.8400	1.7181	0.0147	0.2077	0.0031	0.1573	0.0103	2957	20	2916	14	2887	25	101	
17.1	17.2712	0.2204	0.5911	0.0040	0.9600	1.6919	0.0116	0.2119	0.0028	0.2927	0.0631	2994	16	2950	12	2920	22	101	
18.1	13.9706	0.1928	0.5228	0.0038	0.9600	1.9128	0.0139	0.1938	0.0028	0.1354	0.0116	2711	16	2748	13	2775	24	98	
20.1	9.6130	0.1884	0.4472	0.0033	0.9700	2.2364	0.0163	0.1559	0.0026	0.1678	0.0113	2383	15	2398	19	2412	29	99	

Detrital zircon U-Pb analyses – Results for Sample HJ 152

Spot	RATIOS											AGES (Ma)							
	$^{207}Pb/^{235}U$	σ	$^{206}Pb/^{238}U$	σ	Corr. coef.	$^{238}U/^{206}Pb$	σ	$^{207}Pb/^{206}Pb$	σ	$^{208}Pb/^{206}Pb$	σ	$T_{206Pb/238U}$	σ	$T_{207Pb/235U}$	σ	$T_{207Pb/206Pb}$	σ	Conc. (%)	Histogram ($^{207}Pb/^{206}Pb$ Ages)
21.1	14.1156	0.2083	0.5408	0.0030	0.9900	1.8492	0.0104	0.1893	0.0028	0.4330	0.2331	2787	14	2758	18	2736	25	101	Concordant data
22.1	10.0703	0.2123	0.4661	0.0043	0.6500	2.1454	0.0199	0.1567	0.0030	0.3517	0.0090	2467	19	2441	20	2420	33	101	
23.1	13.1682	0.2606	0.5210	0.0036	0.6200	1.9196	0.0134	0.1833	0.0028	0.0897	0.0077	2703	15	2692	19	2683	25	100	
24.1	7.4498	0.1824	0.4045	0.0042	0.8600	2.4723	0.0258	0.1336	0.0032	0.1800	0.0126	2190	19	2167	22	2146	42	101	
26.1	6.3257	0.1075	0.3610	0.0024	0.9900	2.7699	0.0182	0.1271	0.0022	0.1226	0.0085	1987	11	2022	15	2058	32	98	
27.1	7.0113	0.1319	0.3865	0.0026	0.2700	2.5875	0.0172	0.1316	0.0024	0.1053	0.0037	2106	12	2113	17	2119	32	99	
28.1	11.9493	0.2111	0.4492	0.0034	0.9700	2.2264	0.0171	0.1930	0.0036	0.2024	0.0149	2392	15	2600	17	2768	31	91	
29.1	6.5788	0.1096	0.3721	0.0027	0.9600	2.6874	0.0198	0.1282	0.0020	0.2475	0.0154	2039	13	2057	15	2074	27	99	
30.1	6.3447	0.1055	0.3564	0.0024	0.9800	2.8059	0.0187	0.1291	0.0018	0.1146	0.0102	1965	11	2025	15	2086	25	97	
31.1	13.0870	0.2122	0.5189	0.0038	0.9500	1.9270	0.0141	0.1829	0.0026	0.1805	0.0078	2695	16	2686	16	2679	23	100	
32.1	15.0694	0.2571	0.5634	0.0041	0.8700	1.7751	0.0128	0.1940	0.0028	0.0910	0.0130	2881	17	2820	16	2776	23	102	
33.1	7.7126	0.1435	0.4066	0.0030	0.9800	2.4597	0.0184	0.1376	0.0021	0.1370	0.0084	2199	14	2198	16	2197	27	100	
34.1	10.2161	0.1522	0.4108	0.0031	0.9900	2.4345	0.0183	0.1804	0.0020	0.2930	0.0617	2218	14	2455	14	2656	18	90	
37.1	13.6047	0.2174	0.5366	0.0041	0.7900	1.8637	0.0142	0.1839	0.0022	0.2483	0.0174	2769	17	2723	15	2688	20	101	
40.1	29.7487	0.4558	0.7130	0.0067	0.9800	1.4025	0.0131	0.3026	0.0042	0.1143	0.0044	3470	25	3479	15	3484	22	99	
47.1	14.4491	0.2066	0.5454	0.0035	0.9900	1.8337	0.0117	0.1922	0.0028	0.0908	0.0840	2806	15	2780	14	2761	24	100	
48.1	3.8912	0.0609	0.2850	0.0016	0.9600	3.5087	0.0196	0.0990	0.0015	0.3110	0.0133	1617	8	1612	13	1606	29	100	
49.1	3.9590	0.2019	0.2685	0.0047	0.5700	3.7244	0.0649	0.1069	0.0058	0.2505	0.1436	1533	24	1626	42	1748	102	94	
50.1	3.8084	0.0843	0.2769	0.0028	0.4000	3.6112	0.0370	0.0997	0.0025	0.2520	0.0163	1576	14	1595	18	1619	47	98	
53.1	7.0424	0.1121	0.3946	0.0035	0.7400	2.5343	0.0225	0.1294	0.0019	0.0971	0.0062	2144	16	2117	14	2090	26	101	
54.1	5.9776	0.0811	0.3578	0.0025	0.9900	2.7951	0.0196	0.1212	0.0015	0.1928	0.0389	1972	12	1973	12	1974	22	99	
57.1	6.3177	0.1083	0.3577	0.0023	0.9700	2.7955	0.0182	0.1281	0.0022	0.2009	0.0343	1971	11	2021	15	2072	30	97	
60.1	6.5757	0.1168	0.3611	0.0029	0.9900	2.7691	0.0224	0.1321	0.0019	0.1918	0.0255	1988	14	2056	16	2126	26	96	
63.1	4.8252	0.0917	0.3077	0.0026	0.9900	3.2499	0.0277	0.1137	0.0016	0.2812	0.0124	1729	13	1789	16	1860	26	96	
64.1	7.8389	0.1040	0.4104	0.0026	0.9600	2.4369	0.0157	0.1385	0.0019	0.1777	0.0187	2217	12	2213	12	2209	24	100	
66.1	15.9733	0.2545	0.5518	0.0045	0.8300	1.8122	0.0147	0.2099	0.0034	0.1260	0.0193	2833	19	2875	15	2905	26	98	

Detrital zircon U-Pb analyses – Results for Sample HJ 152 (cont.)

Spot	RATIOS											AGES (Ma)							
	$^{207}Pb/^{235}U$	σ	$^{206}Pb/^{238}U$	σ	Corr. coef.	$^{238}U/^{206}Pb$	σ	$^{207}Pb/^{206}Pb$	σ	$^{208}Pb/^{206}Pb$	σ	$T_{206Pb/238U}$	σ	$T_{207Pb/235U}$	σ	$T_{207Pb/206Pb}$	σ	Conc. (%)	Histogram ($^{207}Pb/^{206}Pb$ Ages)
67.1	7.3268	0.1233	0.3881	0.0034	0.4100	2.5767	0.0226	0.1369	0.0024	0.0729	0.0055	2114	16	2152	15	2189	30	98	
68.1	12.8198	0.1810	0.4936	0.0036	0.9900	2.0260	0.0147	0.1884	0.0026	0.2569	0.0665	2586	16	2667	13	2728	23	96	
69.1	14.8041	0.2512	0.5520	0.0050	0.9900	1.8114	0.0165	0.1945	0.0029	0.2447	0.0606	2834	21	2803	16	2781	24	101	
70.1	14.0818	0.2394	0.5420	0.0049	0.9000	1.8450	0.0168	0.1884	0.0028	0.2268	0.0059	2792	21	2755	16	2729	24	101	
79.1	4.7082	0.0745	0.3182	0.0026	0.9800	3.1425	0.0257	0.1073	0.0018	0.2569	0.0340	1781	13	1769	14	1754	32	100	
85.1	7.3076	0.1240	0.3963	0.0039	0.9200	2.5235	0.0247	0.1337	0.0020	0.1254	0.0100	2152	18	2150	15	2148	26	100	
86.1	9.0669	0.1494	0.4424	0.0036	0.9900	2.2606	0.0182	0.1487	0.0020	0.1748	0.0262	2361	16	2345	17	2331	23	100	**Concordant data**
87.1	12.3968	0.2053	0.4960	0.0040	0.9900	2.0163	0.0163	0.1813	0.0024	0.5499	0.0778	2596	17	2635	17	2665	22	98	
90.1	9.1858	0.1370	0.4409	0.0038	0.9400	2.2681	0.0196	0.1511	0.0019	0.0938	0.0229	2355	17	2357	14	2359	21	99	
92.1	3.7699	0.1209	0.2763	0.0042	0.5600	3.6196	0.0554	0.0990	0.0030	0.2651	0.0264	1573	21	1586	26	1605	58	99	
95.1	3.7957	0.0878	0.2820	0.0024	0.9700	3.5465	0.0297	0.0976	0.0022	0.4332	0.1155	1601	12	1592	19	1579	40	100	
98.1	6.6078	0.1059	0.3759	0.0026	0.9900	2.6599	0.0187	0.1275	0.0019	0.1562	0.0581	2057	12	2060	15	2064	27	99	
100.1	6.9372	0.1273	0.3750	0.0034	0.9400	2.6669	0.0240	0.1342	0.0025	0.1504	0.0214	2053	16	2103	17	2153	32	97	
1.1	13.2949	0.1544	0.5146	0.0038	0.9900	1.9434	0.0142	0.1874	0.0028	0.5606	0.4402	2676	18	2701	14	2719	26	99	
2.1	10.6512	0.1424	0.3818	0.0040	0.9900	2.6188	0.0277	0.2023	0.0033	0.2277	0.0811	2085	20	2493	14	2845	29	83	
3.1	6.0344	0.0933	0.2522	0.0023	0.9800	3.9657	0.0365	0.1736	0.0026	0.3876	0.0472	1450	12	1981	13	2592	24	73	
4.1	3.9129	0.0594	0.2408	0.0022	0.9900	4.1537	0.0386	0.1179	0.0017	0.3481	0.0653	1391	12	1616	12	1924	26	86	
6.1	5.2624	0.0946	0.2451	0.0016	0.9900	4.0796	0.0264	0.1557	0.0024	0.4750	0.0828	1413	8	1863	14	2410	26	75	
9.1	2.9600	0.0588	0.1658	0.0011	0.9800	6.0317	0.0390	0.1295	0.0023	0.5701	0.0854	989	6	1397	13	2091	27	70	**Discordant data**
10.1	5.5435	0.0964	0.2543	0.0016	0.9300	3.9331	0.0254	0.1581	0.0025	0.5080	0.0715	1460	8	1907	14	2436	27	76	
12.1	8.0050	0.1160	0.3310	0.0021	0.9800	3.0211	0.0194	0.1754	0.0025	0.2283	0.0248	1843	10	2232	12	2610	24	82	
14.1	1.7427	0.0264	0.1483	0.0008	0.9800	6.7425	0.0364	0.0852	0.0015	0.6099	0.1195	892	5	1025	11	1321	34	87	
15.1	2.7377	0.0373	0.2122	0.0010	0.9900	4.7136	0.0232	0.0936	0.0014	0.4755	0.2180	1240	6	1339	11	1500	28	92	
19.1	2.3239	0.0711	0.1169	0.0011	0.9900	8.5579	0.0833	0.1442	0.0025	0.7672	0.2645	712	6	1220	15	2279	27	58	
25.1	11.9222	0.2209	0.4124	0.0029	0.9900	2.4251	0.0173	0.2097	0.0036	0.2566	0.0832	2226	13	2598	17	2903	28	85	

Detrital zircon U-Pb analyses – Results for Sample HJ 152 (cont.)

Spot	RATIOS											AGES (Ma)							
	$^{207}Pb/^{235}U$	σ	$^{206}Pb/^{238}U$	σ	Corr. coef.	$^{238}U/^{206}Pb$	σ	$^{207}Pb/^{206}Pb$	σ	$^{208}Pb/^{206}Pb$	σ	$T_{206Pb/238U}$	σ	$T_{207Pb/235U}$	σ	$T_{207Pb/206Pb}$	σ	Conc. (%)	Histogram ($^{207}Pb/^{206}Pb$ Ages)
35.1	0.8418	0.0079	0.0788	0.0006	0.9700	12.6916	0.0959	0.0775	0.0007	1.1532	0.1066	489	4	620	6	1134	12	78	
36.1	9.9011	0.1439	0.3952	0.0026	0.9900	2.5306	0.0164	0.1817	0.0022	0.4833	0.0933	2147	12	2426	15	2669	20	88	
38.1	1.4111	0.0251	0.1248	0.0010	0.9500	8.0129	0.0668	0.0820	0.0011	0.9507	0.1245	758	6	894	11	1246	25	84	
39.1	1.5602	0.0274	0.1225	0.0010	0.0100	8.1619	0.0673	0.0924	0.0012	1.2719	0.0517	745	6	955	11	1475	24	78	
41.1	2.5555	0.0368	0.1681	0.0014	0.9900	5.9497	0.0504	0.1103	0.0016	0.6732	0.2424	1002	8	1288	11	1804	26	77	
42.1	2.3749	0.0399	0.1892	0.0018	0.9800	5.2857	0.0494	0.0910	0.0014	0.4618	0.0562	1117	10	1235	12	1448	28	90	
43.1	6.6147	0.1010	0.2652	0.0024	0.9900	3.7714	0.0339	0.1809	0.0025	0.3377	0.0404	1516	12	2061	14	2661	23	73	
44.1	3.3065	0.0596	0.2024	0.0020	0.9700	4.9410	0.0485	0.1185	0.0019	0.3638	0.1144	1188	11	1483	13	1934	28	80	
45.1	15.9514	0.2174	0.5386	0.0043	0.9900	1.8568	0.0147	0.2148	0.0030	0.1999	0.0744	2777	18	2874	14	2942	23	96	
46.1	3.9050	0.0519	0.2075	0.0011	0.8100	4.8197	0.0261	0.1365	0.0019	0.6035	0.0478	1215	6	1615	11	2183	24	75	
51.1	2.7243	0.0398	0.1553	0.0012	0.8800	6.4372	0.0495	0.1272	0.0016	0.7309	0.0938	931	7	1335	11	2060	22	69	
52.1	13.5371	0.2195	0.5302	0.0048	0.9600	1.8859	0.0170	0.1852	0.0024	0.5398	0.3553	2743	20	2718	14	2700	21	100	
55.1	0.5104	0.0111	0.0779	0.0005	0.3700	12.8374	0.0831	0.0475	0.0010	1.0850	0.0402	484	3	419	7	76	33	115	**Discordant data**
56.1	4.1186	0.0682	0.2187	0.0013	0.9900	4.5735	0.0275	0.1366	0.0021	0.4720	0.0576	1275	7	1658	14	2185	27	76	
58.1	8.1197	0.1206	0.2897	0.0018	0.9900	3.4523	0.0216	0.2033	0.0033	0.5840	0.1369	1640	9	2244	14	2853	26	73	
59.1	0.8727	0.0137	0.0930	0.0007	0.9800	10.7538	0.0822	0.0681	0.0008	1.0297	0.0894	573	4	637	8	870	25	89	
61.1	5.0159	0.0827	0.2891	0.0021	0.9900	3.4590	0.0250	0.1258	0.0016	0.2472	0.1072	1637	11	1822	15	2041	23	89	
62.1	6.1910	0.1216	0.2471	0.0020	0.9900	4.0478	0.0332	0.1818	0.0024	0.3751	0.0883	1423	10	2003	15	2669	22	71	
65.1	7.1524	0.0964	0.3003	0.0020	0.8700	3.3305	0.0220	0.1728	0.0023	0.6498	0.2191	1693	10	2131	12	2585	23	79	
71.1	2.6818	0.0588	0.2005	0.0021	0.9300	4.9878	0.0534	0.0970	0.0025	0.4263	0.0489	1178	12	1324	17	1568	49	89	
72.1	8.9957	0.1095	0.3501	0.0024	0.9900	2.8566	0.0194	0.1864	0.0023	0.2031	0.0612	1935	11	2338	11	2710	20	82	
73.1	12.4329	0.1646	0.4051	0.0032	0.9900	2.4688	0.0197	0.2226	0.0028	0.2307	0.0374	2192	15	2638	12	3000	21	83	
74.1	7.8696	0.1006	0.3490	0.0029	0.9900	2.8657	0.0234	0.1636	0.0022	0.4360	0.1593	1930	14	2216	12	2493	23	87	
75.1	2.1409	0.0264	0.1354	0.0009	0.9500	7.3830	0.0496	0.1146	0.0014	0.7418	0.1352	819	5	1162	9	1874	22	70	
76.1	3.5993	0.0401	0.2256	0.0014	0.9900	4.4317	0.0276	0.1157	0.0015	0.3500	0.0047	1312	8	1549	10	1891	24	84	
77.1	5.2372	0.0740	0.2545	0.0018	0.9900	3.9293	0.0284	0.1493	0.0022	0.2086	0.0620	1462	9	1859	11	2337	24	78	

Detrital zircon U-Pb analyses – Results for Sample HJ 152 (cont.)

Spot	RATIOS											AGES (Ma)							
	$^{207}Pb/^{235}U$	σ	$^{206}Pb/^{238}U$	σ	Corr. coef.	$^{238}U/^{206}Pb$	σ	$^{207}Pb/^{206}Pb$	σ	$^{208}Pb/^{206}Pb$	σ	$T_{206Pb/238U}$	σ	$T_{207Pb/235U}$	σ	$T_{207Pb/206Pb}$	σ	Conc. (%)	Histogram ($^{207}Pb/^{206}Pb$ Ages)
78.1	4.2674	0.0709	0.2900	0.0028	0.9800	3.4479	0.0332	0.1067	0.0020	0.2519	0.0556	1642	14	1687	14	1744	35	97	Discordant data
80.1	4.0101	0.0507	0.2466	0.0017	0.9900	4.0550	0.0274	0.1179	0.0017	0.4829	0.5159	1421	9	1636	11	1925	27	86	
81.1	3.6862	0.0712	0.2736	0.0025	0.8600	3.6549	0.0331	0.0977	0.0018	0.1919	0.0216	1559	13	1568	15	1581	34	99	
82.1	8.4805	0.1608	0.2986	0.0028	0.9800	3.3493	0.0315	0.2060	0.0028	0.1593	0.0301	1684	14	2284	14	2874	21	73	
83.1	9.5660	0.1767	0.3636	0.0044	0.0100	2.7503	0.0336	0.1908	0.0027	0.7184	0.5136	1999	19	2394	15	2749	24	83	
84.1	3.3707	0.0569	0.1748	0.0014	0.6900	5.7213	0.0459	0.1399	0.0018	0.6936	0.0870	1038	8	1498	12	2226	22	69	
88.1	11.3652	0.1576	0.4565	0.0030	0.9900	2.1907	0.0144	0.1806	0.0023	0.2701	0.1452	2424	14	2554	15	2658	22	94	
89.1	3.9009	0.0704	0.2290	0.0020	0.9100	4.3661	0.0385	0.1235	0.0016	0.1460	0.0333	1330	11	1614	14	2008	24	82	
91.1	5.9156	0.0795	0.3239	0.0024	0.9900	3.0872	0.0230	0.1325	0.0018	0.4183	0.1591	1809	12	1964	14	2131	24	92	
93.1	12.4074	0.1854	0.4709	0.0041	0.9900	2.1234	0.0187	0.1911	0.0024	0.2619	0.0558	2488	18	2636	14	2751	21	94	
94.1	9.6140	0.1616	0.3953	0.0041	0.9900	2.5299	0.0260	0.1764	0.0022	0.0803	0.0200	2147	18	2399	14	2619	21	89	
96.1	1.8055	0.0276	0.1211	0.0009	0.7000	8.2610	0.0620	0.1082	0.0015	1.0516	0.2348	737	5	1048	10	1769	26	70	
97.1	3.2564	0.0506	0.2071	0.0014	0.9800	4.8278	0.0333	0.1140	0.0015	0.3511	0.1134	1214	8	1471	12	1865	25	82	
99.1	6.4163	0.1062	0.3501	0.0028	0.9400	2.8565	0.0226	0.1329	0.0019	0.2404	0.0270	1935	13	2035	14	2137	25	95	

Detrital zircon U-Pb analyses – Results for Sample HJ 152 (Standards)

Standard GJ data on 04/04/2022 Concordia Age = 603.9 +/- 1.2 Ma GJ reference age: 608.5 +/- 0.4 Ma (TIMS) - Jackson et al, 2004.	Pleosovic secondary standard on 04/04/2022 Concordia Age = 336.7 +/- 1.0 Ma Pleosovic reference age: 337.13 +/- 0.37 - Sláma et al, 2008.

Detrital zircon U-Pb analyses – Results for Sample HJ 160B

Spot	RATIOS											AGES (Ma)							
	$^{207}Pb/^{235}U$	σ	$^{206}Pb/^{238}U$	σ	Corr. coef.	$^{238}U/^{206}Pb$	σ	$^{207}Pb/^{206}Pb$	σ	$^{208}Pb/^{206}Pb$	σ	$T_{206Pb/238U}$	σ	$T_{207Pb/235U}$	σ	$T_{207Pb/206Pb}$	σ	Conc. (%)	Histogram ($^{207}Pb/^{206}Pb$ Ages)
2.1	7.0041	0.1294	0.3906	0.0032	0.7500	2.5599	0.0212	0.1300	0.0024	0.2740	0.0151	2126	15	2112	17	2099	33	100	Concordant data
3.1	14.3464	0.2427	0.5277	0.0041	0.9300	1.8951	0.0147	0.1972	0.0030	0.4463	0.0051	2732	17	2773	15	2803	24	98	
4.1	14.0816	0.2220	0.5483	0.0041	0.4100	1.8237	0.0136	0.1863	0.0028	0.4238	0.0111	2818	17	2755	15	2709	25	102	

Detrital zircon U-Pb analyses – Results for Sample HJ 160B

Spot	RATIOS											AGES (Ma)							
	$^{207}Pb/^{235}U$	σ	$^{206}Pb/^{238}U$	σ	Corr. coef.	$^{238}U/^{206}Pb$	σ	$^{207}Pb/^{206}Pb$	σ	$^{208}Pb/^{206}Pb$	σ	$T_{206Pb/238U}$	σ	$T_{207Pb/235U}$	σ	$T_{207Pb/206Pb}$	σ	Conc. (%)	Histogram ($^{207}Pb/^{206}Pb$ Ages)
5.1	6.4088	0.0967	0.3591	0.0024	0.7800	2.7848	0.0186	0.1294	0.0018	0.1112	0.0024	1978	11	2034	13	2090	24	97	Concordant data
6.1	6.7416	0.1153	0.3814	0.0031	0.9500	2.6217	0.0216	0.1282	0.0021	0.0875	0.0045	2083	15	2078	15	2073	29	100	
7.1	9.9356	0.1312	0.4590	0.0028	0.9900	2.1787	0.0134	0.1570	0.0024	0.2593	0.0150	2435	13	2429	14	2424	27	100	
8.1	5.9018	0.0960	0.3493	0.0025	0.9800	2.8630	0.0206	0.1225	0.0019	0.2622	0.0270	1931	12	1962	14	1994	28	98	
9.1	11.3889	0.1775	0.4863	0.0035	0.9900	2.0563	0.0147	0.1698	0.0026	0.1529	0.0203	2555	15	2556	15	2556	26	99	
10.1	7.2659	0.1101	0.4036	0.0029	0.9400	2.4779	0.0181	0.1306	0.0020	0.0535	0.0065	2185	14	2145	14	2106	27	101	
13.1	10.0967	0.1463	0.4694	0.0034	0.9400	2.1305	0.0155	0.1560	0.0022	0.2070	0.0037	2481	15	2444	14	2413	24	101	
16.1	6.6919	0.0937	0.3720	0.0028	0.9200	2.6880	0.0203	0.1305	0.0017	0.0965	0.0030	2039	13	2072	12	2104	23	98	
17.1	6.0346	0.2602	0.3420	0.0140	0.9900	2.9244	0.1201	0.1280	0.0018	0.1892	0.0052	1896	66	1981	35	2071	24	95	
18.1	7.6349	0.3112	0.4112	0.0159	0.9800	2.4322	0.0939	0.1347	0.0019	0.2087	0.0082	2220	72	2189	36	2160	24	101	
19.1	7.0977	0.2980	0.4078	0.0151	0.9900	2.4524	0.0908	0.1262	0.0021	0.0904	0.0054	2205	70	2124	38	2046	29	103	
20.1	5.9232	0.2315	0.3451	0.0131	0.9900	2.8974	0.1102	0.1245	0.0017	0.1566	0.0076	1911	63	1965	34	2021	24	97	
21.1	6.8398	0.2706	0.3873	0.0147	0.9600	2.5821	0.0981	0.1281	0.0018	0.1512	0.0310	2110	68	2091	35	2072	24	100	
22.1	13.6294	0.5733	0.5388	0.0221	0.8600	1.8561	0.0762	0.1835	0.0030	0.2839	0.0085	2778	93	2724	40	2685	28	101	
24.1	6.7888	0.2919	0.3741	0.0155	0.9500	2.6734	0.1109	0.1316	0.0022	0.1663	0.0076	2049	72	2084	37	2120	30	98	
25.1	6.9325	0.1054	0.3838	0.0028	0.8200	2.6053	0.0190	0.1310	0.0018	0.2348	0.0134	2094	13	2103	13	2111	25	99	
28.1	7.0607	0.0964	0.3932	0.0033	0.8500	2.5430	0.0214	0.1302	0.0017	0.1276	0.0075	2138	15	2119	12	2101	23	100	
29.1	7.5293	0.1027	0.4051	0.0032	0.8800	2.4684	0.0196	0.1348	0.0018	0.1596	0.0072	2193	15	2177	12	2161	23	100	
30.1	7.1168	0.0893	0.3933	0.0027	0.1700	2.5424	0.0174	0.1312	0.0016	0.1471	0.0039	2138	12	2126	11	2115	21	100	
31.1	7.3749	0.1316	0.3947	0.0033	0.7300	2.5339	0.0213	0.1355	0.0023	0.2016	0.0315	2144	15	2158	16	2171	31	99	
33.1	7.4947	0.0920	0.4023	0.0028	0.6800	2.4855	0.0176	0.1351	0.0016	0.1293	0.0057	2180	13	2172	11	2165	21	100	
36.1	7.8541	0.1199	0.4149	0.0034	0.9400	2.4104	0.0199	0.1373	0.0021	0.0888	0.0092	2237	16	2214	14	2194	26	101	
37.1	7.0414	0.1006	0.3862	0.0042	0.9900	2.5896	0.0280	0.1323	0.0018	0.1011	0.0104	2105	20	2117	14	2128	24	99	
40.1	7.5785	0.0974	0.4108	0.0042	0.6600	2.4343	0.0250	0.1338	0.0014	0.1544	0.0026	2219	19	2182	12	2148	18	101	
41.1	7.4367	0.0939	0.4071	0.0040	0.9800	2.4564	0.0242	0.1325	0.0014	0.1424	0.0104	2202	19	2165	12	2131	18	101	
42.1	9.7335	0.1332	0.4499	0.0024	0.9900	2.2228	0.0121	0.1569	0.0020	0.2313	0.0629	2395	11	2410	13	2423	22	99	

Detrital zircon U-Pb analyses – Results for Sample HJ 160B (cont.)

Spot	RATIOS											AGES (Ma)							
	$^{207}Pb/^{235}U$	σ	$^{206}Pb/^{238}U$	σ	Corr. coef.	$^{238}U/^{206}Pb$	σ	$^{207}Pb/^{206}Pb$	σ	$^{208}Pb/^{206}Pb$	σ	$T_{206Pb/238U}$	σ	$T_{207Pb/235U}$	σ	$T_{207Pb/206Pb}$	σ	Conc. (%)	Histogram ($^{207}Pb/^{206}Pb$ Ages)
43.1	6.5617	0.0973	0.3751	0.0022	0.9800	2.6663	0.0156	0.1269	0.0017	0.1108	0.0030	2053	10	2054	13	2055	24	99	Concordant data
44.1	6.6173	0.0990	0.3810	0.0022	0.8900	2.6244	0.0151	0.1260	0.0017	0.1059	0.0018	2081	10	2062	13	2042	23	100	
45.1	6.9392	0.1034	0.3835	0.0026	0.9400	2.6072	0.0177	0.1312	0.0018	0.1469	0.0122	2093	12	2104	13	2114	25	99	
46.1	7.7001	0.1033	0.4115	0.0026	0.9800	2.4301	0.0154	0.1357	0.0016	0.1141	0.0052	2222	12	2197	12	2173	21	101	
52.1	6.3752	0.0819	0.3607	0.0023	0.9700	2.7720	0.0178	0.1282	0.0017	0.1132	0.0037	1986	11	2029	12	2073	23	97	
54.1	10.0164	0.1792	0.4574	0.0030	0.9500	2.1862	0.0145	0.1588	0.0027	0.3802	0.0094	2428	13	2436	16	2443	28	99	
56.1	6.7837	0.1066	0.3647	0.0021	0.9700	2.7421	0.0161	0.1349	0.0022	0.1860	0.0073	2004	10	2084	14	2163	29	96	
57.1	7.0884	0.1242	0.3883	0.0021	0.5900	2.5753	0.0136	0.1324	0.0022	0.1308	0.0088	2115	10	2123	16	2130	29	99	
58.1	6.9394	0.1186	0.3877	0.0025	0.8700	2.5795	0.0167	0.1298	0.0021	0.2175	0.0059	2112	12	2104	15	2096	29	100	
59.1	4.7472	0.0632	0.2903	0.0017	0.9900	3.4446	0.0205	0.1186	0.0014	0.1689	0.0062	1643	9	1776	11	1935	22	92	
60.1	6.6809	0.0997	0.3755	0.0026	0.9100	2.6631	0.0183	0.1290	0.0018	0.0920	0.0032	2055	12	2070	13	2085	25	99	
61.1	7.0140	0.1062	0.3922	0.0029	0.8600	2.5497	0.0188	0.1297	0.0019	0.1469	0.0029	2133	13	2113	13	2094	26	100	
62.1	6.5406	0.0901	0.3566	0.0023	0.9900	2.8041	0.0183	0.1330	0.0019	0.0564	0.0173	1966	11	2051	13	2138	25	95	
63.1	5.7807	0.0881	0.3297	0.0023	0.9800	3.0332	0.0210	0.1272	0.0019	0.2065	0.0040	1837	11	1944	13	2059	26	94	
64.1	6.9676	0.1058	0.3909	0.0028	0.9500	2.5581	0.0181	0.1293	0.0019	0.0943	0.0062	2127	13	2107	14	2088	26	100	
65.1	6.9709	0.1041	0.3849	0.0028	0.6800	2.5982	0.0191	0.1314	0.0019	0.1222	0.0034	2099	13	2108	13	2116	26	99	
66.1	7.3242	0.1320	0.3928	0.0031	0.9600	2.5456	0.0203	0.1352	0.0025	0.0920	0.0214	2136	15	2152	16	2167	32	99	
67.1	7.0139	0.1295	0.3834	0.0028	0.9300	2.6081	0.0193	0.1327	0.0022	0.1265	0.0061	2092	13	2113	16	2134	29	99	
68.1	7.2154	0.1290	0.3990	0.0028	0.9600	2.5061	0.0178	0.1311	0.0022	0.1197	0.0276	2165	13	2138	16	2113	29	101	
69.1	7.5414	0.1324	0.4072	0.0030	0.0100	2.4560	0.0179	0.1343	0.0022	0.1725	0.0061	2202	14	2178	16	2155	28	101	
70.1	16.6744	0.2919	0.5834	0.0045	0.8500	1.7140	0.0131	0.2073	0.0032	0.1708	0.0064	2963	18	2916	17	2885	25	101	
71.1	16.0070	0.2990	0.5550	0.0046	0.9900	1.8018	0.0148	0.2092	0.0036	0.1078	0.0117	2846	19	2877	18	2899	28	98	
75.1	6.0747	0.1151	0.3620	0.0026	0.9200	2.7621	0.0199	0.1217	0.0023	0.1421	0.0030	1992	12	1987	16	1981	34	100	
77.1	5.6520	0.0996	0.3255	0.0023	0.9900	3.0727	0.0220	0.1260	0.0022	0.0905	0.0033	1816	11	1924	15	2042	30	94	
78.1	7.2936	0.1112	0.4096	0.0042	0.9800	2.4412	0.0250	0.1291	0.0019	0.2137	0.0154	2213	19	2148	14	2086	26	103	
79.1	6.8254	0.1005	0.3800	0.0031	0.9600	2.6319	0.0212	0.1303	0.0016	0.1486	0.0322	2076	14	2089	13	2102	22	99	

Detrital zircon U-Pb analyses – Results for Sample HJ 160B (cont.)

Spot	RATIOS											AGES (Ma)							
	$^{207}Pb/^{235}U$	σ	$^{206}Pb/^{238}U$	σ	Corr. coef.	$^{238}U/^{206}Pb$	σ	$^{207}Pb/^{206}Pb$	σ	$^{208}Pb/^{206}Pb$	σ	$T_{206Pb/238U}$	σ	$T_{207Pb/235U}$	σ	$T_{207Pb/206Pb}$	σ	Conc. (%)	Histogram ($^{207}Pb/^{206}Pb$ Ages)
80.1	5.7130	0.0782	0.3360	0.0025	0.9900	2.9764	0.0226	0.1233	0.0015	0.2634	0.0065	1867	12	1933	12	2005	21	96	Concordant data
83.1	9.3397	0.1310	0.4558	0.0037	0.9900	2.1938	0.0177	0.1486	0.0018	0.1044	0.0088	2421	16	2372	13	2330	21	102	
84.1	4.9588	0.0739	0.3213	0.0019	0.7000	3.1127	0.0188	0.1119	0.0016	0.1435	0.0041	1796	9	1812	13	1831	26	99	
85.1	6.8142	0.0846	0.3882	0.0023	0.9000	2.5758	0.0153	0.1273	0.0016	0.1242	0.0021	2115	11	2088	11	2061	22	101	
87.1	7.4372	0.0981	0.4029	0.0023	0.8600	2.4823	0.0144	0.1339	0.0017	0.2645	0.0058	2182	11	2166	12	2150	23	100	
88.1	22.4660	0.2994	0.6457	0.0041	0.9200	1.5487	0.0099	0.2523	0.0032	0.1165	0.0024	3211	16	3204	12	3200	19	100	
89.1	6.6028	0.1142	0.3710	0.0032	0.9200	2.6956	0.0231	0.1291	0.0024	0.2564	0.0095	2034	15	2060	15	2086	32	98	
92.1	6.1035	0.1004	0.3614	0.0035	0.8500	2.7668	0.0267	0.1225	0.0020	0.0800	0.0075	1989	17	1991	14	1993	29	99	
93.1	6.8190	0.0986	0.3765	0.0032	0.9900	2.6560	0.0228	0.1314	0.0020	0.1208	0.0078	2060	16	2088	14	2116	27	98	
94.1	7.0955	0.1229	0.3847	0.0042	0.5000	2.5991	0.0287	0.1338	0.0023	0.1082	0.0099	2098	20	2124	15	2148	30	98	
95.1	13.3181	0.2425	0.5174	0.0060	0.6700	1.9327	0.0226	0.1867	0.0034	0.0949	0.0110	2688	26	2703	17	2713	30	99	
96.1	33.9113	0.5053	0.7300	0.0067	0.9800	1.3698	0.0127	0.3369	0.0050	0.1422	0.0262	3534	25	3608	15	3649	24	97	
97.1	10.5118	0.1545	0.4736	0.0036	0.9400	2.1114	0.0161	0.1610	0.0023	0.3134	0.0082	2499	16	2481	14	2466	24	100	
98.1	17.3085	0.2868	0.5712	0.0049	0.8300	1.7506	0.0151	0.2198	0.0035	0.1799	0.0057	2913	20	2952	16	2979	25	98	
100.1	5.8159	0.0995	0.3190	0.0028	0.9900	3.1351	0.0273	0.1322	0.0021	0.1037	0.0201	1785	13	1949	14	2128	28	91	
1.1	1.9587	0.0235	0.1615	0.0009	0.9900	6.1913	0.0329	0.0880	0.0012	0.3392	0.0885	965	5	1101	9	1382	26	87	Discordant data
11.1	13.8601	0.1303	0.4392	0.0021	0.9900	2.2769	0.0108	0.2289	0.0027	0.2306	0.0514	2347	10	2740	12	3044	19	85	
12.1	7.5815	0.1008	0.2767	0.0019	0.9900	3.6139	0.0248	0.1987	0.0025	0.1800	0.0100	1575	10	2183	12	2816	21	72	
14.1	0.5778	0.0123	0.0431	0.0004	0.9900	23.1919	0.2315	0.0972	0.0014	0.3030	0.0818	272	3	463	7	1571	24	58	
23.1	1.2033	0.0538	0.0994	0.0041	0.9700	10.0623	0.4201	0.0878	0.0019	0.7628	0.4335	611	24	802	25	1378	38	76	
26.1	0.4088	0.0098	0.0310	0.0003	0.9900	32.2929	0.3603	0.0957	0.0014	0.4783	0.1825	197	2	348	6	1543	25	56	
27.1	1.3184	0.0253	0.0862	0.0008	0.9900	11.5996	0.1096	0.1109	0.0014	0.2049	0.0468	533	5	854	9	1815	22	62	
32.1	5.3657	0.0963	0.2237	0.0024	0.9900	4.4697	0.0476	0.1739	0.0021	0.0680	0.0146	1302	12	1879	11	2596	20	69	
34.1	4.5744	0.0460	0.1718	0.0011	0.9900	5.8222	0.0358	0.1932	0.0022	0.2026	0.0642	1022	6	1745	10	2769	19	58	
35.1	15.0452	0.2133	0.4647	0.0043	0.9900	2.1520	0.0198	0.2348	0.0033	0.0214	0.0176	2460	19	2818	14	3085	23	87	

Detrital zircon U-Pb analyses – Results for Sample HJ 160B (cont.)

Spot	RATIOS											AGES (Ma)							
	$^{207}Pb/^{235}U$	σ	$^{206}Pb/^{238}U$	σ	Corr. coef.	$^{238}U/^{206}Pb$	σ	$^{207}Pb/^{206}Pb$	σ	$^{208}Pb/^{206}Pb$	σ	$T_{206Pb/238U}$	σ	$T_{207Pb/235U}$	σ	$T_{207Pb/206Pb}$	σ	Conc. (%)	Histogram ($^{207}Pb/^{206}Pb$ Ages)
38.1	1.9879	0.0267	0.1235	0.0012	0.9700	8.0987	0.0809	0.1168	0.0012	0.2452	0.0464	751	7	1111	9	1907	18	67	Discordant data
39.1	3.1035	0.0387	0.1870	0.0018	0.9900	5.3489	0.0508	0.1204	0.0013	0.2110	0.0178	1105	10	1434	10	1962	19	77	
47.1	1.3334	0.0197	0.1081	0.0007	0.9900	9.2477	0.0631	0.0894	0.0010	0.3141	0.0491	662	4	860	8	1413	21	76	
48.1	4.3007	0.0491	0.2535	0.0015	0.9900	3.9451	0.0240	0.1231	0.0015	0.1099	0.0116	1456	8	1694	10	2001	22	85	
49.1	2.6508	0.0306	0.1668	0.0009	0.9900	5.9938	0.0321	0.1152	0.0014	0.2346	0.0211	995	5	1315	9	1884	22	75	
50.1	4.0554	0.0518	0.2312	0.0015	0.9900	4.3253	0.0273	0.1272	0.0015	0.1687	0.0060	1341	8	1645	10	2060	21	81	
51.1	0.4256	0.0080	0.0362	0.0003	0.9900	27.6494	0.2206	0.0854	0.0012	0.3161	0.1128	229	2	360	5	1324	22	63	
53.1	6.6064	0.1047	0.3106	0.0017	0.9800	3.2192	0.0172	0.1542	0.0023	0.1382	0.0029	1744	8	2060	14	2394	26	84	
55.1	4.2678	0.0747	0.2484	0.0014	0.9900	4.0262	0.0220	0.1246	0.0019	0.1321	0.0192	1430	7	1687	14	2024	27	84	
72.1	2.6449	0.0719	0.1814	0.0018	0.9900	5.5141	0.0548	0.1058	0.0019	0.1440	0.0394	1074	9	1313	13	1728	28	81	
73.1	3.9230	0.0736	0.1991	0.0015	0.9900	5.0218	0.0372	0.1429	0.0025	0.2180	0.0074	1171	8	1618	14	2262	30	72	
74.1	13.3740	0.2522	0.3731	0.0030	0.9900	2.6802	0.0217	0.2600	0.0046	0.0545	0.0296	2044	14	2706	17	3247	28	75	
76.1	6.7464	0.1249	0.3552	0.0026	0.7400	2.8150	0.0209	0.1377	0.0024	0.2591	0.0603	1960	12	2079	16	2199	31	94	
81.1	0.4205	0.0074	0.0366	0.0003	0.9900	27.3506	0.2514	0.0834	0.0011	0.4422	0.0811	232	2	356	5	1279	27	64	
82.1	4.0060	0.0598	0.2402	0.0020	0.9900	4.1626	0.0339	0.1209	0.0017	0.2141	0.0042	1388	10	1635	13	1970	25	84	
86.1	4.6894	0.0834	0.3159	0.0033	0.9400	3.1654	0.0327	0.1077	0.0021	0.4679	0.2438	1770	16	1765	13	1760	35	100	
90.1	4.6637	0.0542	0.1832	0.0013	0.9900	5.4594	0.0384	0.1847	0.0026	0.1866	0.0727	1084	7	1761	11	2695	23	61	
91.1	5.5904	0.0754	0.3346	0.0026	0.9700	2.9888	0.0235	0.1212	0.0017	0.2547	0.1019	1861	13	1915	12	1974	25	97	
99.1	3.3311	0.0497	0.1490	0.0010	0.9900	6.7119	0.0449	0.1622	0.0023	0.3293	0.0132	895	6	1488	12	2478	24	60	

Same grain

Detrital zircon U-Pb analyses – Results for Sample HJ 160B (Standards)

Standard GJ data on 13/04/2022 Concordia Age = 605.2 +/- 1.5 Ma GJ reference age: 608.5 +/- 0.4 Ma (TIMS) - Jackson et al, 2004.	Pleosovic secondary standard on 13/04/2022 Concordia Age = 335.6 +/- 1.0 Ma Pleosovic reference age: 337.13 +/- 0.37 - Sláma et al, 2008

APPENDIX E – COMPLETE K-S TEST TABLES FOR DETRITAL ZIRCON U-PB AGE DATA

Set I. Samples *versus* age data from various authors for each lithological unit considered

KS-Test results for our samples and a compilation of age data from the units of the Costa Sena Affinity Group and the Bandeirinha Formation (Espinhaço Supergroup).

Sample/Costa Sena Affinity/Bandeirinha Fm.	HJ 4	HJ 110B	HJ 129	HJ 152	HJ 160B	Barão do Guaicuí Fm. (Santos, 2015)	Meloso Fm. (Rolim et al., 2016)	Bandeirinha Fm. (Chemale Jr et al., 2012; Santos et al., 2013)
HJ 4	-	0.008	0.001	**1.000**	0.000	0.001	0.000	0.027
HJ 110B	0.008	-	**0.981**	0.035	**0.937**	0.000	0.000	0.011
HJ 129	0.001	**0.981**	-	0.011	**0.528**	0.000	0.000	0.034
HJ 152	**1.000**	0.035	0.011	-	0.006	0.001	0.000	**0.179**
HJ 160B	0.000	**0.937**	**0.528**	0.006	-	0.000	0.000	0.001
Barão do Guaicuí Fm. (Santos, 2015)	0.001	0.000	0.000	0.001	0.000	-	**0.097**	0.000
Meloso Fm. (Rolim et al., 2016)	0.000	0.000	0.000	0.000	0.000	**0.097**	-	0.000
Bandeirinha Fm. (Chemale Jr et al., 2012; Santos et al., 2013)	0.027	0.011	0.034	**0.179**	0.001	0.000	0.000	-

KS-Test results for our samples and a compilation of age data from the units of the Espinhaço Supergroup.

Sample/Espinhaço Supergroup	HJ 4	HJ 110B	HJ 129	HJ 152	HJ 160B	São João da Chapada Fm. (Chemale Jr et al., 2012; Santos et al., 2013; Santos, 2015; Silveira, 2017; Oliveira et al., 2019)	Itapanhoacanga Fm. (Rolim et al., 2016)
HJ 4	-	0.008	0.001	**1.000**	0.000	0.011	**0.393**
HJ 110B	0.008	-	**0.981**	0.035	**0.937**	**0.090**	**0.104**
HJ 129	0.001	**0.981**	-	0.011	**0.527**	**0.183**	0.019
HJ 152	**1.000**	0.035	0.011	-	0.006	**0.057**	**0.501**
HJ 160B	0.000	**0.937**	**0.527**	0.006	-	0.042	0.009
São João da Chapada Fm. (Chemale Jr et al., 2012; Santos et al., 2013; Santos, 2015; Silveira, 2017; Oliveira et al., 2019)	0.011	**0.090**	**0.183**	**0.057**	0.042	-	**0.232**
Itapanhoacanga Fm. (Rolim et al., 2016)	**0.393**	**0.104**	0.019	**0.501**	0.009	**0.232**	-
Sopa-Brumadinho Fm. Ext (Chemale Jr et al., 2012)	0.004	**0.628**	**0.314**	0.008	**0.379**	**0.146**	**0.052**
Sopa-Brumadinho Fm. (Santos et al., 2013; Santos, 2015; Silveira, 2017)	0.009	**0.300**	**0.292**	**0.057**	0.013	**0.313**	**0.155**
Galho do Miguel Fm. (Chemale Jr et al., 2012; Santos, 2015)	0.000	**0.961**	**0.622**	0.001	**0.494**	0.004	0.001
Santa Rita Fm. (Chemale Jr et al., 2012; Santos et al., 2015)	0.002	**0.159**	0.030	0.025	**0.126**	0.000	**0.055**
Córrego dos Borges Fm. (Chemale Jr et al., 2012; Santos et al., 2015)	0.000	0.000	0.000	0.000	0.000	0.000	0.000
Córrego Pereira Fm. (Chemale Jr et al., 2012; Santos et al., 2015)	0.000	0.000	0.000	0.000	0.000	0.000	0.000
Rio Pardo Grande Fm. (Chemale Jr et al., 2012; Santos et al., 2015)	0.000	0.000	0.000	0.000	0.000	0.000	0.000

KS-Test results for our samples and a compilation of age data from the units of the Espinhaço Supergroup (cont.).

Sample/Espinhaço Supergroup	Sopa-Brumadinho Fm. Ext (Chemale Jr et al., 2012)	Sopa-Brumadinho Fm. (Santos et al., 2013; Santos, 2015; Silveira, 2017)	Galho do Miguel Fm. (Chemale Jr et al., 2012; Santos, 2015)	Santa Rita Fm. (Chemale Jr et al., 2012; Santos et al., 2015)	Córrego dos Borges Fm. (Chemale Jr et al., 2012; Santos et al., 2015)	Córrego Pereira Fm. (Chemale Jr et al., 2012; Santos et al., 2015)	Rio Pardo Grande Fm. (Chemale Jr et al., 2012; Santos et al., 2015)
HJ 4	0.004	0.009	0.000	0.002	0.000	0.000	0.000
HJ 110B	**0.628**	**0.300**	**0.961**	**0.159**	0.000	0.000	0.000
HJ 129	**0.314**	**0.292**	**0.622**	0.030	0.000	0.000	0.000
HJ 152	0.008	**0.057**	0.001	0.025	0.000	0.000	0.000
HJ 160B	**0.379**	0.013	**0.494**	**0.126**	0.000	0.000	0.000
São João da Chapada Fm. (Chemale Jr et al., 2012; Santos et al., 2013; Santos, 2015; Silveira, 2017; Oliveira et al., 2019)	**0.146**	**0.313**	0.004	0.000	0.000	0.000	0.000
Itapanhoacanga Fm. (Rolim et al., 2016)	**0.052**	**0.155**	0.001	**0.055**	0.000	0.000	0.000
Sopa-Brumadinho Fm. Ext (Chemale Jr et al., 2012)	-	0.039	**0.130**	**0.086**	0.000	0.000	0.000
Sopa-Brumadinho Fm. (Santos et al., 2013; Santos, 2015; Silveira, 2017)	0.039	-	0.006	0.006	0.000	0.000	0.000
Galho do Miguel Fm. (Chemale Jr et al., 2012; Santos, 2015)	**0.130**	0.006	-	**0.071**	0.000	0.000	0.000
Santa Rita Fm. (Chemale Jr et al., 2012; Santos et al., 2015)	**0.086**	0.006	**0.071**	-	0.000	0.000	0.000
Córrego dos Borges Fm. (Chemale Jr et al., 2012; Santos et al., 2015)	0.000	0.000	0.000	0.000	-	0.000	0.000
Córrego Pereira Fm. (Chemale Jr et al., 2012; Santos et al., 2015)	0.000	0.000	0.000	0.000	0.000	-	0.041
Rio Pardo Grande Fm. (Chemale Jr et al., 2012; Santos et al., 2015)	0.000	0.000	0.000	0.000	0.000	0.041	-

KS-Test results for our samples and a compilation of age data from the units of the Macaúbas Group.

Sample/Macaúbas Group	HJ 4	HJ 110B	HJ 129	HJ 152	HJ 160B	Rio Peixe Bravo Fm. (Babinski et al., 2012)	Matão-Duas Barras Fm. (Martins et al., 2008; Chemale Jr et al., 2012; Souza, 2019; Oliveira, 2021)	Capelinha Fm. (Castro et al., 2019; Amaral, 2020)	Serra do Catuni Fm. (Kuchenbecker et al., 2015; Oliveira et al., 2021)	Nova Aurora Fm. (Kuchenbecker et al., 2015)	Chapada Acauã Fm. (Kuchenbecker et al., 2015; Castro et al., 2020)	Ribeirão da Folha Fm. (Peixoto, 2013; Amaral, 2020)
HJ 4	-	0.008	0.001	**1.000**	0.000	0.019	0.000	0.000	0.000	0.000	0.000	0.000
HJ 110B	0.008	-	**0.981**	0.035	**0.937**	**0.607**	0.000	0.000	0.000	0.000	0.000	0.000
HJ 129	0.001	**0.981**	-	0.011	**0.527**	**0.608**	0.000	0.000	0.000	0.000	0.000	0.000
HJ 152	**1.000**	0.035	0.011	-	0.006	0.044	0.000	0.000	0.000	0.004	0.000	0.000
HJ 160B	0.000	**0.937**	**0.527**	0.006	-	**0.883**	0.000	0.000	0.000	0.000	0.000	0.000
Rio Peixe Bravo Fm. (Babinski et al., 2012)	0.019	**0.607**	**0.608**	0.044	**0.883**	-	**0.303**	0.002	**0.164**	**0.415**	**0.159**	0.005
Matão-Duas Barras Fm. (Martins et al., 2008; Chemale Jr et al., 2012; Souza, 2019; Oliveira, 2021)	0.000	0.000	0.000	0.000	0.000	**0.303**	-	0.000	**0.391**	0.027	0.000	0.000
Capelinha Fm. (Castro et al., 2019; Amaral, 2020)	0.000	0.000	0.000	0.000	0.000	0.002	0.000	-	0.000	0.000	0.000	**0.218**
Serra do Catuni Fm. (Kuchenbecker et al., 2015; Oliveira et al., 2021)	0.000	0.000	0.000	0.000	0.000	**0.164**	**0.391**	0.000	-	**0.050**	0.001	0.000
Nova Aurora Fm. (Kuchenbecker et al., 2015)	0.000	0.000	0.000	0.004	0.000	**0.415**	0.027	0.000	**0.050**	-	**0.996**	0.005
Chapada Acauã Fm. (Kuchenbecker et al., 2015; Castro et al., 2020)	0.000	0.000	0.000	0.000	0.000	**0.159**	0.000	0.000	0.001	**0.996**	-	0.000
Ribeirão da Folha Fm. (Peixoto, 2013; Amaral, 2020)	0.000	0.000	0.000	0.000	0.000	0.005	0.000	**0.218**	0.000	0.005	0.000	-

KS-Test results for our samples and a compilation of age data from the units of the Jequitaí Formation.

Sample/Jequitaí Fm.	HJ 4	HJ 110B	HJ 129	HJ 152	HJ 160B	Jequitaí Fm. (Rodrigues, 2008)
HJ 4	-	0.008	0.001	**1.000**	0.000	0.000
HJ 110B	0.008	-	**0.982**	0.035	**0.937**	0.005
HJ 129	0.001	**0.982**	-	0.011	**0.532**	0.002
HJ 152	**1.000**	0.035	0.011	-	0.006	0.000
HJ 160B	0.000	**0.937**	**0.532**	0.006	-	0.003
Jequitaí Fm. (Rodrigues, 2008)	0.000	0.005	0.002	0.000	0.003	-

Set II. Samples *versus* age data from each author for each lithological unit considered

KS-Test results for our samples and a age data obtained by various authors for the units of the Costa Sena Affinity Group and the Bandeirinha Formation (Espinhaço Supergroup).

Sample/Costa Sena Affinity/Bandeirinha Fm.	HJ 4	HJ 110B	HJ 129	HJ 152	HJ 160B	Barão do Guaicuí Fm. (Santos, 2015)	Meloso Fm. (Rolim, 2016)	Bandeirinha Fm. (Chemale Jr et al., 2012)	Bandeirinha Fm. (Santos et al., 2013)
HJ 4	-	0.008	0.001	**1.000**	0.000	0.001	0.000	0.005	0.035
HJ 110B	0.008	-	**0.981**	0.035	**0.937**	0.000	0.000	0.003	0.001
HJ 129	0.001	**0.981**	-	0.011	**0.528**	0.000	0.000	0.006	0.000
HJ 152	**1.000**	0.035	0.011	-	0.006	0.001	0.000	0.041	**0.069**
HJ 160B	0.000	**0.937**	**0.528**	0.006	-	0.000	0.000	0.000	0.000
Barão do Guaicuí Fm. (Santos, 2015)	0.001	0.000	0.000	0.001	0.000	-	**0.096**	0.000	0.000
Meloso Fm. (Rolim, 2016)	0.000	0.000	0.000	0.000	0.000	**0.096**	-	0.000	0.000
Bandeirinha Fm. (Chemale Jr et al., 2012)	0.005	0.003	0.006	0.041	0.000	0.000	0.000	-	0.001
Bandeirinha Fm. (Santos et al., 2013)	0.035	0.001	0.000	**0.069**	0.000	0.000	0.000	0.001	-

KS-Test results for our samples and a age data obtained by various authors for the units of the Lower Espinhaço Supergroup.

Sample/Lower Espinhaço	HJ 4	HJ 110B	HJ 129	HJ 152	HJ 160B	São João da Chapada Fm. (Chemale Jr et al., 2012)	São João da Chapada (Santos et al., 2013)	São João da Chapada Fm. (Santos, 2015)	São João da Chapada Fm. (Silveira-Braga et al., 2015)	São João da Chapada Fm. (Silveira, 2017)	São João da Chapada Fm. (Oliveira et al., 2019)
HJ 4	-	0.008	0.001	**1.000**	0.000	**0.052**	0.007	**0.580**	0.037	0.006	**0.088**
HJ 110B	0.008	-	**0.981**	0.035	**0.937**	**0.081**	**0.741**	0.031	0.001	0.044	0.050
HJ 129	0.001	**0.981**	-	0.011	**0.527**	**0.167**	**0.282**	0.006	0.000	**0.092**	**0.097**
HJ 152	**1.000**	0.035	0.011	-	0.006	0.037	0.041	**0.766**	**0.087**	0.012	**0.104**
HJ 160B	0.000	**0.937**	**0.527**	0.006	-	**0.087**	**0.242**	0.003	0.000	**0.050**	0.033
São João da Chapada Fm. (Chemale Jr et al., 2012)	**0.052**	**0.081**	**0.167**	0.037	**0.087**	-	**0.177**	**0.095**	0.001	**0.926**	**0.729**
São João da Chapada (Santos et al., 2013)	0.007	**0.741**	**0.282**	0.041	**0.242**	**0.177**	-	0.038	0.000	**0.077**	**0.099**
São João da Chapada Fm. (Santos, 2015)	**0.580**	0.031	0.006	**0.766**	0.003	**0.095**	0.038	-	0.007	0.022	**0.208**
São João da Chapada Fm. (Silveira-Braga et al., 2015)	0.037	0.001	0.000	**0.087**	0.000	0.001	0.000	0.007	-	0.001	0.002
São João da Chapada Fm. (Silveira, 2017)	0.006	0.044	**0.092**	0.012	**0.050**	**0.926**	**0.077**	0.022	0.001	-	**0.716**
São João da Chapada Fm. (Oliveira et al., 2019)	**0.088**	0.050	**0.097**	**0.104**	0.033	**0.729**	**0.099**	**0.208**	0.002	**0.716**	-
Itapanhoacanga Fm. (Rolim, 2016)	**0.378**	**0.085**	0.015	**0.549**	0.007	**0.050**	**0.066**	**0.824**	0.013	**0.093**	**0.242**
Sopa-Brumadinho Fm. Ext (Chemale Jr et al., 2012)	0.004	**0.628**	**0.314**	0.008	**0.379**	**0.332**	**0.481**	0.021	0.000	**0.162**	**0.208**
Sopa-Brumadinho Fm. (Santos et al., 2013)	0.005	**0.466**	**0.365**	0.026	**0.052**	**0.269**	**0.968**	0.026	0.000	**0.237**	**0.284**
Sopa-Brumadinho Fm. (Santos, 2015)	**0.053**	**0.287**	**0.082**	**0.254**	0.016	**0.107**	**0.578**	**0.299**	0.000	**0.197**	**0.269**
Galho do Miguel Fm. (Chemale Jr et al., 2012)	0.002	**0.170**	**0.241**	0.014	**0.086**	**0.505**	**0.484**	0.006	0.000	**0.980**	**0.342**
Galho do Miguel Fm. (Santos, 2015)	0.000	**0.968**	**0.538**	0.001	**0.616**	0.017	**0.278**	0.001	0.000	0.010	0.007
Galho do Miguel Fm. (Souza et al., 2019)	0.000	**0.267**	**0.121**	0.000	**0.779**	**0.054**	0.031	0.000	0.000	0.047	0.021
Galho do Miguel Fm. (Oliveira et al., 2021)	0.000	0.000	0.000	0.000	0.000	0.000	0.000	0.000	0.000	0.000	0.000

KS-Test results for our samples and a age data obtained by various authors for the units of the Lower Espinhaço Supergroup (cont.).

Sample/Lower Espinhaço	Itapanhoacanga Fm. (Rolim, 2016)	Sopa-Brumadinho Fm. Ext (Chemale Jr et al., 2012)	Sopa-Brumadinho Fm. (Santos et al., 2013)	Sopa-Brumadinho Fm. (Santos, 2015)	Galho do Miguel Fm. (Chemale Jr et al., 2012)	Galho do Miguel Fm. (Santos, 2015)	Galho do Miguel Fm. (Souza et al., 2019)	Galho do Miguel Fm. (Oliveira et al., 2021)
HJ 4	**0.378**	0.004	0.005	**0.053**	0.002	0.000	0.000	0.000
HJ 110B	**0.085**	**0.628**	**0.466**	**0.287**	**0.170**	**0.968**	**0.267**	0.000
HJ 129	0.015	**0.314**	**0.365**	**0.082**	**0.241**	**0.538**	**0.121**	0.000
HJ 152	**0.549**	0.008	0.026	**0.254**	0.014	0.001	0.000	0.000
HJ 160B	0.007	**0.379**	**0.052**	0.016	**0.086**	**0.616**	**0.779**	0.000
São João da Chapada Fm. (Chemale Jr et al., 2012)	**0.050**	**0.332**	**0.269**	**0.107**	**0.505**	0.017	**0.054**	0.000
São João da Chapada (Santos et al., 2013)	**0.066**	**0.481**	**0.968**	**0.578**	**0.484**	**0.278**	0.031	0.000
São João da Chapada Fm. (Santos, 2015)	**0.824**	0.021	0.026	**0.299**	0.006	0.001	0.000	0.000
São João da Chapada Fm. (Silveira-Braga et al., 2015)	0.013	0.000	0.000	0.000	0.000	0.000	0.000	0.000
São João da Chapada Fm. (Silveira, 2017)	**0.093**	**0.162**	**0.237**	**0.197**	**0.980**	0.010	0.047	0.000
São João da Chapada Fm. (Oliveira et al., 2019)	**0.242**	**0.208**	**0.284**	**0.269**	**0.342**	0.007	0.021	0.000
Itapanhoacanga Fm. (Rolim, 2016)	-	0.042	**0.063**	**0.566**	0.026	0.001	0.000	0.000
Sopa-Brumadinho Fm. Ext (Chemale Jr et al., 2012)	0.042	-	**0.235**	**0.064**	**0.577**	**0.144**	0.031	0.000
Sopa-Brumadinho Fm. (Santos et al., 2013)	**0.063**	**0.235**	-	**0.327**	**0.510**	**0.095**	0.020	0.000
Sopa-Brumadinho Fm. (Santos, 2015)	**0.566**	**0.064**	**0.327**	-	**0.059**	0.002	0.000	0.000
Galho do Miguel Fm. (Chemale Jr et al., 2012)	0.026	**0.577**	**0.510**	**0.059**	-	**0.090**	**0.207**	0.000
Galho do Miguel Fm. (Santos, 2015)	0.001	**0.144**	**0.095**	0.002	**0.090**	-	**0.347**	0.000
Galho do Miguel Fm. (Souza et al., 2019)	0.000	0.031	0.020	0.000	**0.207**	**0.347**	-	0.000
Galho do Miguel Fm. (Oliveira et al., 2021)	0.000	0.000	0.000	0.000	0.000	0.000	0.000	-

KS-Test results for our samples and a age data obtained by various authors for the units of the Upper Espinhaço Supergroup.

Sample/Upper Espinhaço	HJ 4	HJ 110B	HJ 129	HJ 152	HJ 160B	Santa Rita Fm. (Chemale Jr et al., 2012)	Santa Rita Fm. (Santos et al., 2015)	Córrego dos Borges Fm. (Chemale Jr et al., 2012)	Córrego dos Borges Fm. (Santos et al., 2015)	Córrego Pereira Fm. (Chemale Jr et al., 2012)	Córrego Pereira Fm. (Santos et al., 2015)	Rio Pardo Grande Fm. (Chemale Jr et al., 2012)	Rio Pardo Grande Fm. (Santos et al., 2015)
HJ 4	-	0.008	0.001	**1.000**	0.000	**0.102**	0.003	0.000	0.000	0.000	0.000	0.000	0.000
HJ 110B	0.008	-	**0.981**	0.035	**0.937**	**0.694**	**0.094**	0.000	0.000	0.000	0.000	0.000	0.000
HJ 129	0.001	**0.981**	-	0.011	**0.528**	**0.786**	0.024	0.000	0.000	0.000	0.000	0.000	0.000
HJ 152	**1.000**	0.035	0.011	-	0.006	**0.295**	0.030	0.000	0.000	0.000	0.000	0.000	0.000
HJ 160B	0.000	**0.937**	**0.528**	0.006	-	**0.230**	**0.079**	0.000	0.000	0.000	0.000	0.000	0.000
Santa Rita Fm. (Chemale Jr et al., 2012)	**0.102**	**0.694**	**0.786**	**0.295**	**0.230**	-	**0.695**	0.010	**0.120**	0.000	0.000	0.000	0.000
Santa Rita Fm. (Santos et al., 2015)	0.003	**0.094**	0.024	0.030	**0.079**	**0.695**	-	0.001	0.039	0.000	0.000	0.000	0.000
Córrego dos Borges Fm. (Chemale Jr et al., 2012)	0.000	0.000	0.000	0.000	0.000	0.010	0.001	-	**0.064**	0.000	0.011	0.000	**0.081**
Córrego dos Borges Fm. (Santos et al., 2015)	0.000	0.000	0.000	0.000	0.000	**0.120**	0.039	**0.064**	-	0.000	0.015	0.001	0.003
Córrego Pereira Fm. (Chemale Jr et al., 2012)	0.000	0.000	0.000	0.000	0.000	0.000	0.000	0.000	0.000	-	0.004	0.000	**0.085**
Córrego Pereira Fm. (Santos et al., 2015)	0.000	0.000	0.000	0.000	0.000	0.000	0.000	0.011	0.015	0.004	-	**0.474**	**0.584**
Rio Pardo Grande Fm. (Chemale Jr et al., 2012)	0.000	0.000	0.000	0.000	0.000	0.000	0.000	0.000	0.001	0.000	**0.474**	-	0.016
Rio Pardo Grande Fm. (Santos et al., 2015)	0.000	0.000	0.000	0.000	0.000	0.000	0.000	**0.081**	0.003	**0.085**	**0.584**	0.016	-

KS-Test results for our samples and a age data obtained by various authors for the units of the Macaúbas Group.

Sample/ Macaúbas Group	HJ 4	HJ 110B	HJ 129	HJ 152	HJ 160B	Rio Peixe Bravo Fm. (Babinski et al., 2012)	Capelinha Fm. (Castro et al., 2019)	Capelinha Fm. (Amaral et al., 2020)	Matão Fm. (Martins et al., 2008)	Matão Fm. (Souza et al., 2019)	Duas Barras Fm. (Chemale Jr et al., 2012)	Duas Barras Fm. (Souza et al., 2019)	Matão-Duas Barras Fm. (Oliveira et al., 2021)
HJ 4	-	0.008	0.001	**1.000**	0.000	0.019	0.000	0.000	0.014	0.000	0.000	0.000	0.000
HJ 110B	0.008	-	**0.981**	0.035	**0.937**	**0.607**	0.000	0.000	0.005	0.036	0.000	0.000	0.000
HJ 129	0.001	**0.981**	-	0.011	**0.535**	**0.605**	0.000	0.000	0.002	0.004	0.000	0.000	0.000
HJ 152	**1.000**	0.035	0.011	-	0.006	0.044	0.000	0.000	0.028	0.000	0.000	0.000	0.000
HJ 160B	0.000	**0.937**	**0.535**	0.006	-	**0.882**	0.000	0.000	0.004	0.026	0.000	0.000	0.000
Rio Peixe Bravo Fm. (Babinski et al., 2012)	0.019	**0.607**	**0.605**	0.044	**0.882**	-	0.002	0.001	**0.214**	**0.999**	0.011	0.005	**0.715**
Capelinha Fm. (Castro et al., 2019)	0.000	0.000	0.000	0.000	0.000	0.002	-	0.043	**0.403**	0.000	0.000	0.000	0.000
Capelinha Fm. (Amaral et al., 2020)	0.000	0.000	0.000	0.000	0.000	0.001	0.043	-	**0.456**	0.000	0.000	0.005	0.000
Matão Fm. (Martins et al., 2008)	0.014	0.005	0.002	0.028	0.004	**0.214**	**0.403**	**0.456**	-	**0.106**	**0.731**	**0.873**	**0.455**
Matão Fm. (Souza et al., 2019)	0.000	0.036	0.004	0.000	0.026	**0.999**	0.000	0.000	**0.106**	-	0.000	0.000	**0.320**
Duas Barras Fm. (Chemale Jr et al., 2012)	0.000	0.000	0.000	0.000	0.000	0.011	0.000	0.000	**0.731**	0.000	-	**0.342**	0.000
Duas Barras Fm. (Souza et al., 2019)	0.000	0.000	0.000	0.000	0.000	0.005	0.000	0.005	**0.873**	0.000	**0.342**	-	0.000
Matão-Duas Barras Fm. (Oliveira et al., 2021)	0.000	0.000	0.000	0.000	0.000	**0.715**	0.000	0.000	**0.455**	**0.320**	0.000	0.000	-
Serra do Catuni Fm. (Babinski et al., 2012)	0.000	0.000	0.000	0.000	0.000	**0.134**	0.009	0.005	**1.000**	0.001	**0.205**	**0.105**	0.041
Serra do Catuni Fm. (Kuchenbecker et al., 2015)	0.000	0.000	0.000	0.000	0.000	**0.130**	0.000	0.000	**0.661**	0.006	**0.169**	0.018	0.005
Serra do Catuni Fm. (Oliveira et al., 2021)	0.000	0.000	0.000	0.001	0.000	**0.250**	0.001	0.001	**0.958**	0.011	**0.118**	0.042	**0.221**

KS-Test results for our samples and a age data obtained by various authors for the units of the Macaúbas Group (cont.).

Sample/ Macaúbas Group	HJ 4	HJ 110B	HJ 129	HJ 152	HJ 160B	Rio Peixe Bravo Fm. (Babinski et al., 2012)	Capelinha Fm. (Castro et al., 2019)	Capelinha Fm. (Amaral et al., 2020)	Matão Fm. (Martins et al., 2008)	Matão Fm. (Souza et al., 2019)	Duas Barras Fm. (Chemale Jr et al., 2012)	Duas Barras Fm. (Souza et al., 2019)	Matão-Duas Barras Fm. (Oliveira et al., 2021)
Nova Aurora Fm. (Kuchenbecker et al., 2015)	0.000	0.000	0.000	0.004	0.000	**0.415**	0.000	0.000	**0.863**	0.004	0.006	0.001	0.023
Chapada Acauã Fm. (Pedrosa-Soares et al., 2000)	0.000	0.000	0.000	0.000	0.000	0.005	0.013	0.000	0.004	0.000	0.000	0.000	0.000
Chapada Acauã Fm. (Babinski et al., 2012)	0.013	0.013	0.003	0.014	0.009	**0.347**	0.027	0.047	**0.992**	**0.083**	**0.221**	**0.185**	**0.492**
Chapada Acauã Fm. (Kuchenbecker et al., 2015)	0.000	0.000	0.000	0.000	0.000	**0.212**	0.000	0.000	**0.482**	0.000	0.000	0.000	0.000
Chapada Acauã Fm. (Castro et al., 2020)	0.000	0.000	0.000	0.000	0.000	**0.127**	0.000	0.000	**0.975**	0.000	0.006	0.001	0.000
Chapada Acauã Fm. (Pacheco et al., 2023) – base	0.000	0.000	0.000	0.000	0.000	0.002	**0.995**	0.038	**0.264**	0.000	0.000	0.000	0.000
Ribeirão da Folha Fm. (Peixoto, 2013)	0.000	0.000	0.000	0.000	0.000	**0.095**	0.000	0.001	**0.311**	0.000	0.004	0.000	0.000
Ribeirão da Folha Fm. (Amaral et al., 2020)	0.000	0.000	0.000	0.000	0.000	0.000	0.006	**0.227**	**0.099**	0.000	0.000	0.000	0.000

KS-Test results for our samples and a age data obtained by various authors for the units of the Macaúbas Group (cont.).

Sample/ Macaúbas Group	Serra do Catuni Fm. (Babinski et al., 2012)	Serra do Catuni Fm. (Kuchenbecker et al., 2015)	Serra do Catuni Fm. (Oliveira et al., 2021)	Nova Aurora Fm. (Kuchenbecker et al., 2015)	Chapada Acauã Fm. (Pedrosa-Soares et al., 2000)	Chapada Acauã Fm. (Babinski et al., 2012)	Chapada Acauã Fm. (Kuchenbecker et al., 2015)	Chapada Acauã Fm. (Castro et al., 2020)	Chapada Acauã Fm. (Pacheco et al., 2023) – base	Ribeirão da Folha Fm. (Peixoto, 2013)	Ribeirão da Folha Fm. (Amaral et al., 2020)
HJ 4	0.000	0.000	0.000	0.000	0.000	0.013	0.000	0.000	0.000	0.000	0.000
HJ 110B	0.000	0.000	0.000	0.000	0.000	0.013	0.000	0.000	0.000	0.000	0.000
HJ 129	0.000	0.000	0.000	0.000	0.000	0.003	0.000	0.000	0.000	0.000	0.000
HJ 152	0.000	0.000	0.001	0.004	0.000	0.014	0.000	0.000	0.000	0.000	0.000
HJ 160B	0.000	0.000	0.000	0.000	0.000	0.009	0.000	0.000	0.000	0.000	0.000
Rio Peixe Bravo Fm. (Babinski et al., 2012)	**0.134**	**0.130**	**0.250**	**0.415**	0.005	**0.347**	**0.212**	**0.127**	0.002	**0.095**	0.000
Capelinha Fm. (Castro et al., 2019)	0.009	0.000	0.001	0.000	0.013	0.027	0.000	0.000	**0.995**	0.000	0.006
Capelinha Fm. (Amaral et al., 2020)	0.005	0.000	0.001	0.000	0.000	0.047	0.000	0.000	0.038	0.001	**0.227**
Matão Fm. (Martins et al., 2008)	**1.000**	**0.661**	**0.958**	**0.863**	0.004	**0.992**	**0.482**	**0.975**	**0.264**	**0.311**	**0.099**
Matão Fm. (Souza et al., 2019)	0.001	0.006	0.011	0.004	0.000	**0.083**	0.000	0.000	0.000	0.000	0.000
Duas Barras Fm. (Chemale Jr et al., 2012)	**0.205**	**0.169**	**0.118**	0.006	0.000	**0.221**	0.000	0.006	0.000	0.004	0.000
Duas Barras Fm. (Souza et al., 2019)	**0.105**	0.018	0.042	0.001	0.000	**0.185**	0.000	0.001	0.000	0.000	0.000
Matão-Duas Barras Fm. (Oliveira et al., 2021)	0.041	0.005	**0.221**	0.023	0.000	**0.492**	0.000	0.000	0.000	0.000	0.000
Serra do Catuni Fm. (Babinski et al., 2012)	-	**0.150**	**0.970**	**0.499**	0.000	**0.990**	0.034	**0.503**	0.007	0.011	0.000
Serra do Catuni Fm. (Kuchenbecker et al., 2015)	**0.150**	-	**0.555**	0.016	0.000	**0.916**	0.000	0.005	0.000	0.000	0.000
Serra do Catuni Fm. (Oliveira et al., 2021)	**0.970**	**0.555**	-	**0.346**	0.000	**1.000**	0.016	**0.783**	0.004	0.005	0.000

KS-Test results for our samples and a age data obtained by various authors for the units of the Macaúbas Group (cont.).

Sample/ Macaúbas Group	Serra do Catuni Fm. (Babinski et al., 2012)	Serra do Catuni Fm. (Kuchenbecker et al., 2015)	Serra do Catuni Fm. (Oliveira et al., 2021)	Nova Aurora Fm. (Kuchenbecker et al., 2015)	Chapada Acauã Fm. (Pedrosa-Soares et al., 2000)	Chapada Acauã Fm. (Babinski et al., 2012)	Chapada Acauã Fm. (Kuchenbecker et al., 2015)	Chapada Acauã Fm. (Castro et al., 2020)	Chapada Acauã Fm. (Pacheco et al., 2023) – base	Ribeirão da Folha Fm. (Peixoto, 2013)	Ribeirão da Folha Fm. (Amaral et al., 2020)
Nova Aurora Fm. (Kuchenbecker et al., 2015)	**0.499**	0.016	**0.346**	-	0.006	**0.450**	**0.925**	**0.628**	0.001	**0.081**	0.000
Chapada Acauã Fm. (Pedrosa-Soares et al., 2000)	0.000	0.000	0.000	0.006	-	0.000	0.007	0.000	0.042	0.021	0.003
Chapada Acauã Fm. (Babinski et al., 2012)	**0.990**	**0.916**	**1.000**	**0.450**	0.000	-	**0.162**	**0.778**	0.032	**0.087**	0.005
Chapada Acauã Fm. (Kuchenbecker et al., 2015)	0.034	0.000	0.016	**0.925**	0.007	**0.162**	-	0.004	0.000	0.011	0.000
Chapada Acauã Fm. (Castro et al., 2020)	**0.503**	0.005	**0.783**	**0.628**	0.000	**0.778**	0.004	-	0.000	0.001	0.000
Chapada Acauã Fm. (Pacheco et al., 2023) – base	0.007	0.000	0.004	0.001	0.042	0.032	0.000	0.000	-	0.001	0.021
Ribeirão da Folha Fm. (Peixoto, 2013)	0.011	0.000	0.005	**0.081**	0.021	**0.087**	0.011	0.001	0.001	-	0.000
Ribeirão da Folha Fm. (Amaral et al., 2020)	0.000	0.000	0.000	0.000	0.003	0.005	0.000	0.000	0.021	0.000	-

KS-Test results for our samples and a compilation of age data from the units of the Jequitaí Formation.

Sample/Jequitaí Fm.	HJ 4	HJ 110B	HJ 129	HJ 152	HJ 160B	Jequitaí Fm. (Rodrigues, 2008)
HJ 4	-	0.008	0.001	**1.000**	0.000	0.000
HJ 110B	0.008	-	**0.982**	0.035	**0.937**	0.005
HJ 129	0.001	**0.982**	-	0.011	**0.532**	0.002
HJ 152	**1.000**	0.035	0.011	-	0.006	0.000
HJ 160B	0.000	**0.937**	**0.532**	0.006	-	0.003
Jequitaí Fm. (Rodrigues, 2008)	0.000	0.005	0.002	0.000	0.003	-

Set III. Samples *versus* age data from each sample used by each author for each lithological unit considered

KS-Test results for our samples and individual samples from studies about units from the Costa Sena Affinity Group and the Bandeirinha Formation (Espinhaço Supergroup).

Sample/Costa Sena Affinity/Bandeirinha Fm.	HJ 4	HJ 110B	HJ 129	HJ 152	HJ 160B	Barão do Guaicuí Fm. (Santos, 2015) – PE-GO-01	Meloso Fm. (Rolim, 2016) – 6669	Meloso Fm. (Rolim, 2016) – Bebeto 2	Bandeirinha Fm. (Chemale Jr et al., 2012) – PE-GU-28	Bandeirinha Fm. (Santos et al., 2013) – PE-GU-30
HJ 4	-	0.008	0.001	**1.000**	0.000	0.001	0.000	0.000	0.005	0.035
HJ 110B	0.008	-	**0.981**	0.035	**0.937**	0.000	0.000	0.000	0.003	0.001
HJ 129	0.001	**0.981**	-	0.011	**0.528**	0.000	0.000	0.000	0.006	0.000
HJ 152	**1.000**	0.035	0.011	-	0.006	0.001	0.000	0.000	0.041	**0.069**
HJ 160B	0.000	**0.937**	**0.528**	0.006	-	0.000	0.000	0.000	0.000	0.000
Barão do Guaicuí Fm. (Santos, 2015) – PE-GO-01	0.001	0.000	0.000	0.001	0.000	-	**0.636**	0.023	0.000	0.000
Meloso Fm. (Rolim, 2016) – 6669	0.000	0.000	0.000	0.000	0.000	**0.636**	-	**0.239**	0.000	0.000
Meloso Fm. (Rolim, 2016) – Bebeto 2	0.000	0.000	0.000	0.000	0.000	0.023	**0.239**	-	0.000	0.000
Bandeirinha Fm. (Chemale Jr et al., 2012) – PE-GU-28	0.005	0.003	0.006	0.041	0.000	0.000	0.000	0.000	-	0.001
Bandeirinha Fm. (Santos et al., 2013) – PE-GU-30	0.035	0.001	0.000	**0.069**	0.000	0.000	0.000	0.000	0.001	-

KS-Test results for our samples and individual samples from studies about units from the Espinhaço Supergroup.

Sample/Espinhaço (1)	HJ 4	HJ 110B	HJ 129	HJ 152	HJ 160B	São João da Chapada Fm. (Chemale Jr et al., 2012) – PE-SM-05	Santos et al., 2013 – PE-SM-07 – São João da Chapada Fm.	Santos et al., 2013 – PE-SM-09 – São João da Chapada Fm.	São João da Chapada Fm. (Santos, 2015) – PE-SM-06
HJ 4	-	0.008	0.001	**1.000**	0.000	**0.051**	0.008	**0.053**	**0.159**
HJ 110B	0.008	-	**0.981**	0.035	**0.937**	**0.080**	**0.185**	**0.356**	**0.944**
HJ 129	0.001	**0.981**	-	0.011	**0.528**	**0.171**	**0.096**	**0.514**	**0.786**
HJ 152	**1.000**	0.035	0.011	-	0.006	0.036	0.027	**0.196**	**0.233**
HJ 160B	0.000	**0.937**	**0.528**	0.006	-	**0.084**	**0.082**	**0.063**	**0.784**
São João da Chapada Fm. (Chemale Jr et al., 2012) – PE-SM-05	**0.051**	**0.080**	**0.171**	0.036	**0.084**	-	**0.392**	**0.195**	**0.758**
Santos et al., 2013 – PE-SM-07 – São João da Chapada Fm.	0.008	**0.185**	**0.096**	0.027	**0.082**	**0.392**	-	**0.207**	**0.953**
Santos et al., 2013 – PE-SM-09 – São João da Chapada Fm.	**0.053**	**0.356**	**0.514**	**0.196**	**0.063**	**0.195**	**0.207**		**0.737**

KS-Test results for our samples and individual samples from studies about units from the Espinhaço Supergroup (cont.).

Sample/Espinhaço	HJ 4	HJ 110B	HJ 129	HJ 152	HJ 160B	São João da Chapada Fm. (Chemale Jr et al., 2012) – PE-SM-05	Santos et al., 2013 – PE-SM-07 – São João da Chapada Fm.	Santos et al., 2013 – PE-SM-09 – São João da Chapada Fm.	São João da Chapada Fm. (Santos, 2015) – PE-SM-06
São João da Chapada Fm. (Santos, 2015) – PE-SM-06	**0.159**	**0.944**	**0.786**	**0.233**	**0.784**	**0.758**	**0.953**	**0.737**	-
São João da Chapada Fm. (Santos, 2015) – PE-GO-31	**0.960**	0.002	0.000	**0.737**	0.000	0.010	0.002	0.023	**0.057**
São João da Chapada Fm. (Silveira-Braga et al., 2015) – PTG 106	**0.197**	**0.062**	0.019	**0.376**	0.021	0.031	**0.059**	**0.086**	**0.134**
São João da Chapada Fm. (Silveira-Braga et al., 2015) – PTG 93	**0.793**	**0.662**	**0.328**	**0.889**	**0.237**	**0.561**	**0.469**	**0.926**	**0.680**
São João da Chapada Fm. (Silveira-Braga et al., 2015) – PTG 226	0.002	0.000	0.000	0.004	0.000	0.000	0.000	0.000	0.001
São João da Chapada Fm. (Silveira, 2017) – PT049	0.006	0.043	**0.093**	0.012	0.048	**0.927**	**0.100**	**0.100**	**0.572**
São João da Chapada Fm. (Oliveira et al., 2019) – Jana 1	**0.573**	**0.742**	**0.520**	**0.423**	**0.608**	**0.796**	**0.399**	**0.687**	**0.624**
São João da Chapada Fm. (Oliveira et al., 2019) – Jana 2	**0.127**	**0.476**	**0.585**	**0.296**	**0.318**	**0.878**	**0.653**	**0.704**	**0.846**
São João da Chapada Fm. (Oliveira et al., 2019) – Jana 3	**0.321**	**0.419**	**0.521**	**0.317**	**0.316**	**0.985**	**0.405**	**0.646**	**0.822**
São João da Chapada Fm. (Oliveira et al., 2019) – Jana 5	**0.289**	**0.195**	**0.285**	**0.453**	**0.187**	**0.676**	**0.431**	**0.281**	**0.597**
Itapanhoacanga Fm. (Rolim, 2016) – 6666	**0.261**	**0.496**	**0.685**	**0.270**	**0.103**	**0.355**	**0.683**	**0.904**	**0.705**
Itapanhoacanga Fm. (Rolim, 2016) – 6667	**0.306**	0.004	0.001	**0.493**	0.001	0.005	0.004	0.021	0.034
Itapanhoacanga Fm. (Rolim, 2016) – 6668	**0.241**	**0.145**	**0.135**	**0.583**	0.028	**0.087**	**0.136**	**0.525**	**0.374**
Itapanhoacanga Fm. (Rolim, 2016) – Bebeto 1	**0.110**	**0.195**	**0.115**	**0.088**	**0.099**	0.038	**0.616**	**0.264**	**0.864**

	KS-Test results for our samples and individual samples from studies about units from the Espinhaço Supergroup (cont.).							
Sample/Espinhaço	**São João da Chapada Fm. (Santos, 2015) – PE-GO-31**	**São João da Chapada Fm. (Silveira-Braga et al., 2015) – PTG 93**	**São João da Chapada Fm. (Silveira-Braga et al., 2015) – PTG 226**	**São João da Chapada Fm. (Silveira, 2017) – PT049**	**São João da Chapada Fm. (Oliveira et al., 2019) – Jana 1**	**São João da Chapada Fm. (Oliveira et al., 2019) – Jana 2**	**São João da Chapada Fm. (Oliveira et al., 2019) – Jana 3**	**São João da Chapada Fm. (Oliveira et al., 2019) – Jana 5**
HJ 4	**0.960**	**0.197**	**0.793**	0.002	0.006	**0.573**	**0.127**	**0.321**
HJ 110B	0.002	**0.062**	**0.662**	0.000	0.043	**0.742**	**0.476**	**0.419**
HJ 129	0.000	0.019	**0.328**	0.000	**0.093**	**0.520**	**0.585**	**0.521**
HJ 152	**0.737**	**0.376**	**0.889**	0.004	0.012	**0.423**	**0.296**	**0.317**
HJ 160B	0.000	0.021	**0.237**	0.000	0.048	**0.608**	**0.318**	**0.316**
São João da Chapada Fm. (Chemale Jr et al., 2012) – PE-SM-05	0.010	0.031	**0.561**	0.000	**0.927**	**0.796**	**0.878**	**0.985**
Santos et al., 2013 – PE-SM-07 – São João da Chapada Fm.	0.002	**0.059**	**0.469**	0.000	**0.100**	**0.399**	**0.653**	**0.405**
Santos et al., 2013 – PE-SM-09 – São João da Chapada Fm.	0.023	**0.086**	**0.926**	0.000	**0.100**	**0.687**	**0.704**	**0.646**
São João da Chapada Fm. (Santos, 2015) – PE-SM-06	**0.057**	**0.134**	**0.680**	0.001	**0.572**	**0.624**	**0.846**	**0.822**
São João da Chapada Fm. (Santos, 2015) – PE-GO-31	-	**0.120**	**0.288**	0.004	0.001	**0.166**	**0.064**	**0.088**
São João da Chapada Fm. (Silveira-Braga et al., 2015) – PTG 106	**0.120**	-	**0.633**	**0.070**	0.012	**0.102**	**0.159**	**0.117**
São João da Chapada Fm. (Silveira-Braga et al., 2015) – PTG 93	**0.288**	**0.633**	-	0.034	**0.343**	**0.756**	**0.817**	**0.839**
São João da Chapada Fm. (Silveira-Braga et al., 2015) – PTG 226	0.004	**0.070**	0.034	-	0.000	0.043	0.001	0.015
São João da Chapada Fm. (Silveira, 2017) – PT049	0.001	0.012	**0.343**	0.000	-	**0.621**	**0.998**	**0.976**

KS-Test results for our samples and individual samples from studies about units from the Espinhaço Supergroup (cont.).

Sample/Espinhaço	São João da Chapada Fm. (Santos, 2015) – PE-GO-31	São João da Chapada Fm. (Silveira-Braga et al., 2015) – PTG 93	São João da Chapada Fm. (Silveira-Braga et al., 2015) – PTG 226	São João da Chapada Fm. (Silveira, 2017) – PT049	São João da Chapada Fm. (Oliveira et al., 2019) – Jana 1	São João da Chapada Fm. (Oliveira et al., 2019) – Jana 2	São João da Chapada Fm. (Oliveira et al., 2019) – Jana 3	São João da Chapada Fm. (Oliveira et al., 2019) – Jana 5
São João da Chapada Fm. (Oliveira et al., 2019) – Jana 1	**0.166**	**0.102**	**0.756**	0.043	**0.621**	-	**0.767**	**1.000**
São João da Chapada Fm. (Oliveira et al., 2019) – Jana 2	**0.064**	**0.159**	**0.817**	0.001	**0.998**	**0.767**	-	**0.973**
São João da Chapada Fm. (Oliveira et al., 2019) – Jana 3	**0.088**	**0.117**	**0.839**	0.015	**0.976**	**1.000**	**0.973**	-
São João da Chapada Fm. (Oliveira et al., 2019) – Jana 5	**0.272**	**0.055**	**0.456**	0.001	**0.905**	**0.564**	**1.000**	**0.979**
Itapanhoacanga Fm. (Rolim, 2016) – 6666	**0.059**	**0.257**	**0.871**	0.001	**0.782**	**0.960**	**1.000**	**0.950**
Itapanhoacanga Fm. (Rolim, 2016) – 6667	**0.210**	**0.127**	**0.342**	**0.254**	0.003	**0.232**	0.020	**0.216**
Itapanhoacanga Fm. (Rolim, 2016) – 6668	**0.624**	0.036	**0.586**	0.002	**0.103**	**0.443**	**0.599**	**0.560**
Itapanhoacanga Fm. (Rolim, 2016) – Bebeto 1	0.021	**0.279**	**0.540**	0.001	0.019	**0.268**	**0.232**	**0.219**

KS-Test results for our samples and individual samples from studies about units from the Espinhaço Supergroup (cont.).

Sample/Espinhaço	Itapanhoacanga Fm. (Rolim, 2016) – 6666	Itapanhoacanga Fm. (Rolim, 2016) – 6667	Itapanhoacanga Fm. (Rolim, 2016) – 6668	Itapanhoacanga Fm. (Rolim, 2016) – Bebeto 1
HJ 4	**0.261**	**0.306**	**0.241**	**0.110**
HJ 110B	**0.496**	0.004	**0.145**	**0.195**
HJ 129	**0.685**	0.001	**0.135**	**0.115**
HJ 152	**0.270**	**0.493**	**0.583**	**0.088**
HJ 160B	**0.103**	0.001	0.028	**0.099**

KS-Test results for our samples and individual samples from studies about units from the Espinhaço Supergroup (cont.).

Sample/Espinhaço	Itapanhoacanga Fm. (Rolim, 2016) – 6666	Itapanhoacanga Fm. (Rolim, 2016) – 6667	Itapanhoacanga Fm. (Rolim, 2016) – 6668	Itapanhoacanga Fm. (Rolim, 2016) – Bebeto 1
São João da Chapada Fm. (Chemale Jr et al., 2012) – PE-SM-05	**0.355**	0.005	**0.087**	0.038
Santos et al., 2013 – PE-SM-07 – São João da Chapada Fm.	**0.683**	0.004	**0.136**	**0.616**
Santos et al., 2013 – PE-SM-09 – São João da Chapada Fm.	**0.904**	0.021	**0.525**	**0.264**
São João da Chapada Fm. (Santos, 2015) – PE-SM-06	**0.705**	0.034	**0.374**	**0.864**
São João da Chapada Fm. (Santos, 2015) – PE-GO-31	**0.059**	**0.210**	**0.624**	0.021
São João da Chapada Fm. (Silveira-Braga et al., 2015) – PTG 106	**0.257**	**0.127**	0.036	**0.279**
São João da Chapada Fm. (Silveira-Braga et al., 2015) – PTG 93	**0.871**	**0.342**	**0.586**	**0.540**
São João da Chapada Fm. (Silveira-Braga et al., 2015) – PTG 226	0.001	**0.254**	0.002	0.001
São João da Chapada Fm. (Silveira, 2017) – PT049	**0.782**	0.003	**0.103**	0.019
São João da Chapada Fm. (Oliveira et al., 2019) – Jana 1	**0.960**	**0.232**	**0.443**	**0.268**
São João da Chapada Fm. (Oliveira et al., 2019) – Jana 2	**1.000**	0.020	**0.599**	**0.232**
São João da Chapada Fm. (Oliveira et al., 2019) – Jana 3	**0.950**	**0.216**	**0.560**	**0.219**
São João da Chapada Fm. (Oliveira et al., 2019) – Jana 5	**0.859**	0.037	**0.957**	**0.073**
Itapanhoacanga Fm. (Rolim, 2016) – 6666	-	**0.053**	**0.702**	**0.450**
Itapanhoacanga Fm. (Rolim, 2016) – 6667	**0.053**	-	**0.060**	**0.072**
Itapanhoacanga Fm. (Rolim, 2016) – 6668	**0.702**	**0.060**	-	**0.185**
Itapanhoacanga Fm. (Rolim, 2016) – Bebeto 1	**0.450**	**0.072**	**0.185**	-

KS-Test results for our samples and individual samples from studies about units from the Espinhaço Supergroup (cont.).

Sample/Espinhaço	HJ 4	HJ 110B	HJ 129	HJ 152	HJ 160B	Sopa-Brumadinho Fm. Ext (Chemale Jr et al., 2012) – PE-EX-34-B	Sopa-Brumadinho Fm. Ext (Chemale Jr et al., 2012) – PE-EX-34C	Sopa-Brumadinho Fm. Ext (Chemale Jr et al., 2012) – PE-EX-34D
HJ 4	-	0.008	0.001	**1.000**	0.000	**0.329**	0.001	0.000
HJ 110B	0.008	-	**0.981**	0.035	**0.937**	0.037	**0.153**	0.000
HJ 129	0.001	**0.981**	-	0.011	**0.527**	0.049	**0.273**	0.000
HJ 152	**1.000**	0.035	0.011	-	0.006	**0.538**	0.001	0.000
HJ 160B	0.000	**0.937**	**0.527**	0.006	-	0.020	**0.117**	0.000
Sopa-Brumadinho Fm. Ext (Chemale Jr et al., 2012) – PE-EX-34-B	**0.329**	0.037	0.049	**0.538**	0.020	-	0.024	0.000
Sopa-Brumadinho Fm. Ext (Chemale Jr et al., 2012) – PE-EX-34C	0.001	**0.153**	**0.273**	0.001	**0.117**	0.024	-	0.000
Sopa-Brumadinho Fm. Ext (Chemale Jr et al., 2012) – PE-EX-34D	0.000	0.000	0.000	0.000	0.000	0.000	0.000	-
Santos et al., 2013 – PE-GU-33A – Sopa-Brumadinho Fm.	**0.120**	**0.264**	**0.363**	**0.303**	**0.085**	**0.954**	**0.336**	0.000
Santos et al., 2013 – PE-GU-33B – Sopa-Brumadinho Fm.	**0.065**	**0.454**	**0.159**	**0.209**	**0.099**	**0.072**	**0.109**	0.000
Santos et al., 2013 – PE-GU-66 – Sopa-Brumadinho Fm.	**0.054**	**0.347**	**0.539**	0.041	**0.374**	**0.377**	**0.714**	0.000
Santos et al., 2013 – PE-GU-102 – Sopa-Brumadinho Fm.	0.007	**0.132**	**0.188**	0.018	0.025	**0.163**	**0.453**	0.000
Santos et al., 2013 – PE-GU-103 – Sopa-Brumadinho Fm.	0.034	**0.083**	0.025	**0.126**	0.044	0.010	0.026	0.001
Sopa-Brumadinho Fm. (Santos, 2015) - Sample PE-CM-11	**0.172**	**0.058**	**0.109**	**0.170**	0.023	**0.959**	**0.200**	0.000
Sopa-Brumadinho Fm. (Santos, 2015) - Sample PE-GO-39	0.002	0.001	0.000	0.012	0.000	0.000	0.000	0.001
Sopa-Brumadinho Fm. (Santos, 2015) - Sample PE-GO-59	**0.985**	0.001	0.000	**0.821**	0.000	**0.079**	0.000	0.000
Sopa-Brumadinho Fm. (Santos, 2015) - Sample PE-GO-61	0.013	0.046	**0.087**	0.047	0.032	**0.224**	**0.684**	0.000
Sopa-Brumadinho Fm. (Silveira, 2017) – PT053	**0.053**	**0.312**	**0.408**	**0.132**	**0.065**	**0.560**	**0.207**	0.000

KS-Test results for our samples and individual samples from studies about units from the Espinhaço Supergroup (cont.).

Sample/Espinhaço	Sopa-Brumadinho Fm. (Santos et al., 2013) – PE-GU-33A	Sopa-Brumadinho Fm. (Santos et al., 2013) – PE-GU-33B	Sopa-Brumadinho Fm. (Santos et al., 2013) – PE-GU-66	Sopa-Brumadinho Fm. (Santos et al., 2013) – PE-GU-102	Sopa-Brumadinho Fm. (Santos et al., 2013) – PE-GU-103	Sopa-Brumadinho Fm. (Santos, 2015) - Sample PE-CM-11	Sopa-Brumadinho Fm. (Santos, 2015) - Sample PE-GO-39	Sopa-Brumadinho Fm. (Santos, 2015) - Sample PE-GO-59	Sopa-Brumadinho Fm. (Santos, 2015) - Sample PE-GO-61	Sopa-Brumadinho Fm. (Silveira, 2017) – PT053
HJ 4	**0.120**	**0.065**	**0.054**	0.007	0.034	**0.172**	0.002	**0.985**	0.013	**0.053**
HJ 110B	**0.264**	**0.454**	**0.347**	**0.132**	**0.083**	**0.058**	0.001	0.001	0.046	**0.312**
HJ 129	**0.363**	**0.159**	**0.539**	**0.188**	0.025	**0.109**	0.000	0.000	**0.087**	**0.408**
HJ 152	**0.303**	**0.209**	0.041	0.018	**0.126**	**0.170**	0.012	**0.821**	0.047	**0.132**
HJ 160B	**0.085**	**0.099**	**0.374**	0.025	0.044	0.023	0.000	0.000	0.032	**0.065**
Sopa-Brumadinho Fm. Ext (Chemale Jr et al., 2012) – PE-EX-34-B	**0.954**	**0.072**	**0.377**	**0.163**	0.010	**0.959**	0.000	**0.079**	**0.224**	**0.560**
Sopa-Brumadinho Fm. Ext (Chemale Jr et al., 2012) – PE-EX-34C	**0.336**	**0.109**	**0.714**	**0.453**	0.026	**0.200**	0.000	0.000	**0.684**	**0.207**
Sopa-Brumadinho Fm. Ext (Chemale Jr et al., 2012) – PE-EX-34D	0.000	0.000	0.000	0.000	0.001	0.000	0.001	0.000	0.000	0.000
Santos et al., 2013 – PE-GU-33A – Sopa-Brumadinho Fm.	-	**0.388**	**0.378**	**0.733**	**0.169**	**0.995**	0.004	**0.067**	**0.989**	**0.887**
Santos et al., 2013 – PE-GU-33B – Sopa-Brumadinho Fm.	**0.388**	-	**0.301**	**0.248**	**0.986**	**0.082**	**0.131**	0.020	**0.084**	**0.589**
Santos et al., 2013 – PE-GU-66 – Sopa-Brumadinho Fm.	**0.378**	**0.301**	-	**0.179**	**0.110**	**0.184**	0.002	0.004	**0.269**	**0.227**
Santos et al., 2013 – PE-GU-102 – Sopa-Brumadinho Fm.	**0.733**	**0.248**	**0.179**	-	**0.087**	**0.576**	0.001	0.001	**0.990**	**0.982**
Santos et al., 2013 – PE-GU-103 – Sopa-Brumadinho Fm.	**0.169**	**0.986**	**0.110**	**0.087**	-	0.017	**0.588**	0.008	0.023	**0.260**
Sopa-Brumadinho Fm. (Santos, 2015) - Sample PE-CM-11	**0.995**	**0.082**	**0.184**	**0.576**	0.017	-	0.000	0.019	**0.475**	**0.745**
Sopa-Brumadinho Fm. (Santos, 2015) - Sample PE-GO-39	0.004	**0.131**	0.002	0.001	**0.588**	0.000	-	0.000	0.000	0.016
Sopa-Brumadinho Fm. (Santos, 2015) - Sample PE-GO-59	**0.067**	0.020	0.004	0.001	0.008	0.019	0.000	-	0.012	0.029

KS-Test results for our samples and individual samples from studies about units from the Espinhaço Supergroup (cont.).

Sample/Espinhaço	Sopa-Brumadinho Fm. (Santos et al., 2013) – PE-GU-33A	Sopa-Brumadinho Fm. (Santos et al., 2013) – PE-GU-33B	Sopa-Brumadinho Fm. (Santos et al., 2013) – PE-GU-66	Sopa-Brumadinho Fm. (Santos et al., 2013) – PE-GU-102	Sopa-Brumadinho Fm. (Santos et al., 2013) – PE-GU-103	Sopa-Brumadinho Fm. (Santos, 2015) - Sample PE-CM-11	Sopa-Brumadinho Fm. (Santos, 2015) - Sample PE-GO-39	Sopa-Brumadinho Fm. (Santos, 2015) - Sample PE-GO-59	Sopa-Brumadinho Fm. (Santos, 2015) - Sample PE-GO-61	Sopa-Brumadinho Fm. (Silveira, 2017) – PT053
Sopa-Brumadinho Fm. (Santos, 2015) - Sample PE-GO-61	**0.989**	**0.084**	**0.269**	**0.990**	0.023	**0.475**	0.000	0.012	-	**0.824**
Sopa-Brumadinho Fm. (Silveira, 2017) – PT053	**0.887**	**0.589**	**0.227**	**0.982**	**0.260**	**0.745**	0.016	0.029	**0.824**	-

KS-Test results for our samples and individual samples from studies about units from the Espinhaço Supergroup (cont.).

Sample/Espinhaço	HJ 4	HJ 110B	HJ 129	HJ 152	HJ 160B	Galho do Miguel Fm. (Chemale Jr et al., 2012) – PE-GU-40	Galho do Miguel Fm. (Santos, 2015) – PE-CM-14	Galho do Miguel Fm. (Santos, 2015) – PE-CM-15A	Galho do Miguel Fm. (Santos, 2015) – PE-CM-15B
HJ 4	-	0.008	0.001	**1.000**	0.000	0.002	0.000	**0.274**	0.000
HJ 110B	0.008	-	**0.981**	0.035	**0.937**	**0.171**	**0.617**	**0.992**	**0.361**
HJ 129	0.001	**0.981**	-	0.011	**0.532**	**0.241**	**0.365**	**0.996**	**0.154**
HJ 152	**1.000**	0.035	0.011	-	0.006	0.014	0.003	**0.322**	0.000
HJ 160B	0.000	**0.937**	**0.532**	0.006	-	**0.086**	**0.840**	**0.797**	**0.586**
Galho do Miguel Fm. (Chemale Jr et al., 2012) – PE-GU-40	0.002	**0.171**	**0.241**	0.014	**0.086**	-	0.034	**0.926**	**0.679**
Galho do Miguel Fm. (Santos, 2015) – PE-CM-14	0.000	**0.617**	**0.365**	0.003	**0.840**	0.034	-	**0.589**	**0.294**
Galho do Miguel Fm. (Santos, 2015) – PE-CM-15A	**0.274**	**0.992**	**0.996**	**0.322**	**0.797**	**0.926**	**0.589**	-	**0.694**
Galho do Miguel Fm. (Santos, 2015) – PE-CM-15B	0.000	**0.361**	**0.154**	0.000	**0.586**	**0.679**	**0.294**	**0.694**	-
Galho do Miguel Fm. (Santos, 2015) – PE-SC-43	0.000	**0.096**	0.042	0.000	**0.077**	**0.105**	**0.327**	**0.363**	0.033
Galho do Miguel Fm. (Santos, 2015) – PE-SC-45	**0.565**	0.037	0.005	**0.830**	0.002	0.006	0.001	**0.502**	0.000

KS-Test results for our samples and individual samples from studies about units from the Espinhaço Supergroup (cont.).

Sample/Espinhaço	HJ 4	HJ 110B	HJ 129	HJ 152	HJ 160B	Galho do Miguel Fm. (Chemale Jr et al., 2012) – PE-GU-40	Galho do Miguel Fm. (Santos, 2015) – PE-CM-14	Galho do Miguel Fm. (Santos, 2015) – PE-CM-15A	Galho do Miguel Fm. (Santos, 2015) – PE-CM-15B
Galho do Miguel Fm. (Santos, 2015) – PE-SC-48	0.000	**0.684**	**0.410**	0.002	**0.813**	**0.064**	**0.829**	**0.699**	**0.213**
Galho do Miguel Fm. (Santos, 2015) – PE-FM-71	0.001	**0.303**	**0.120**	0.001	**0.656**	**0.124**	**0.982**	**0.595**	**0.471**
Galho do Miguel Fm. (Souza et al., 2019) – CL-03	0.000	**0.363**	**0.225**	0.000	**0.846**	0.034	**0.801**	**0.734**	**0.185**
Galho do Miguel Fm. (Souza et al., 2019) – IT-95	0.000	**0.514**	**0.242**	0.000	**0.280**	**0.872**	**0.128**	**0.860**	**1.000**
Galho do Miguel Fm. (Oliveira et al., 2021) – DB 04	0.000	0.000	0.000	0.000	0.000	0.000	0.000	0.001	0.000
Santa Rita Fm. (Chemale Jr et al., 2012)	**0.102**	**0.695**	**0.789**	**0.296**	**0.232**	**0.524**	**0.175**	**0.955**	**0.089**
Santa Rita Fm. (Santos et al., 2015) - Sample PE-CM-17	0.001	0.001	0.000	0.005	0.001	0.005	0.014	0.049	0.000
Santa Rita Fm. (Santos et al., 2015) - Sample PE-CM-16-SR	**0.178**	**0.324**	**0.081**	**0.601**	0.047	**0.057**	0.025	**0.942**	0.008
Córrego dos Borges Fm. (Chemale Jr et al., 2012) – PE-CM-19	0.000	0.000	0.000	0.000	0.000	0.000	0.000	0.001	0.000
Córrego dos Borges Fm. (Santos et al., 2015) - Sample PE-CM-20	0.001	**0.208**	0.044	0.009	**0.168**	0.041	**0.157**	**0.246**	0.028
Córrego dos Borges Fm. (Santos et al., 2015) - Sample PE-SC-42	0.001	0.000	0.000	0.004	0.000	0.000	0.001	0.007	0.000
Córrego dos Borges Fm. (Santos et al., 2015) - Sample PE-JQ-52	0.000	0.000	0.000	0.000	0.000	0.000	0.000	0.001	0.000
Córrego Pereira Fm. (Chemale Jr et al., 2012) – PE-SM-26	0.000	0.000	0.000	0.000	0.000	0.000	0.000	0.000	0.000
Córrego Pereira Fm. (Santos et al., 2015) - Sample PE-CM-18	0.000	0.000	0.000	0.000	0.000	0.000	0.000	0.000	0.000
Rio Pardo Grande Fm. (Chemale Jr et al., 2012) – PE-CM-35	0.000	0.000	0.000	0.000	0.000	0.000	0.000	0.000	0.000
Rio Pardo Grande Fm. (Santos et al., 2015) - Sample PE-CM-54	0.000	0.000	0.000	0.000	0.000	0.000	0.000	0.000	0.000

KS-Test results for our samples and individual samples from studies about units from the Espinhaço Supergroup (cont.).

Sample/Espinhaço	Galho do Miguel Fm. (Santos, 2015) – PE-SC-43	Galho do Miguel Fm. (Santos, 2015) – PE-SC-45	Galho do Miguel Fm. (Santos, 2015) – PE-SC-48	Galho do Miguel Fm. (Santos, 2015) – PE-FM-71	Galho do Miguel Fm. (Souza et al., 2019) – CL-03	Galho do Miguel Fm. (Souza et al., 2019) – IT-95	Galho do Miguel Fm. (Oliveira et al., 2021) – DB 04
HJ 4	0.000	**0.565**	0.000	0.001	0.000	0.000	0.000
HJ 110B	**0.096**	0.037	**0.684**	**0.303**	**0.363**	**0.514**	0.000
HJ 129	0.042	0.005	**0.410**	**0.120**	**0.225**	**0.242**	0.000
HJ 152	0.000	**0.830**	0.002	0.001	0.000	0.000	0.000
HJ 160B	**0.077**	0.002	**0.813**	**0.656**	**0.846**	**0.280**	0.000
Galho do Miguel Fm. (Chemale Jr et al., 2012) – PE-GU-40	**0.105**	0.006	**0.064**	**0.124**	0.034	**0.872**	0.000
Galho do Miguel Fm. (Santos, 2015) – PE-CM-14	**0.327**	0.001	**0.829**	**0.982**	**0.801**	**0.128**	0.000
Galho do Miguel Fm. (Santos, 2015) – PE-CM-15A	**0.363**	**0.502**	**0.699**	**0.595**	**0.734**	**0.860**	0.001
Galho do Miguel Fm. (Santos, 2015) – PE-CM-15B	0.033	0.000	**0.213**	**0.471**	**0.185**	**1.000**	0.000
Galho do Miguel Fm. (Santos, 2015) – PE-SC-43	-	0.000	**0.147**	**0.976**	**0.056**	**0.070**	0.008
Galho do Miguel Fm. (Santos, 2015) – PE-SC-45	0.000	-	0.002	0.001	0.000	0.000	0.000
Galho do Miguel Fm. (Santos, 2015) – PE-SC-48	**0.147**	0.002	-	**0.591**	**1.000**	**0.210**	0.003
Galho do Miguel Fm. (Santos, 2015) – PE-FM-71	**0.976**	0.001	**0.591**	-	**0.620**	**0.345**	0.012
Galho do Miguel Fm. (Souza et al., 2019) – CL-03	**0.056**	0.000	**1.000**	**0.620**	-	**0.131**	0.001
Galho do Miguel Fm. (Souza et al., 2019) – IT-95	**0.070**	0.000	**0.210**	**0.345**	**0.131**	-	0.000
Galho do Miguel Fm. (Oliveira et al., 2021) – DB 04	0.008	0.000	0.003	0.012	0.001	0.000	-

KS-Test results for our samples and individual samples from studies about units from the Espinhaço Supergroup (cont.).

Sample/Espinhaço	Galho do Miguel Fm. (Santos, 2015) – PE-SC-43	Galho do Miguel Fm. (Santos, 2015) – PE-SC-45	Galho do Miguel Fm. (Santos, 2015) – PE-SC-48	Galho do Miguel Fm. (Santos, 2015) – PE-FM-71	Galho do Miguel Fm. (Souza et al., 2019) – CL-03	Galho do Miguel Fm. (Souza et al., 2019) – IT-95	Galho do Miguel Fm. (Oliveira et al., 2021) – DB 04
Santa Rita Fm. (Chemale Jr et al., 2012)	**0.084**	**0.384**	**0.215**	**0.064**	**0.115**	**0.134**	0.013
Santa Rita Fm. (Santos et al., 2015) - Sample PE-CM-17	0.025	0.001	0.002	**0.167**	0.000	0.000	**0.148**
Santa Rita Fm. (Santos et al., 2015) - Sample PE-CM-16-SR	0.017	**0.830**	0.037	0.021	0.004	0.015	0.000
Córrego dos Borges Fm. (Chemale Jr et al., 2012) – PE-CM-19	0.005	0.000	0.000	0.005	0.000	0.000	**0.964**
Córrego dos Borges Fm. (Santos et al., 2015) - Sample PE-CM-20	0.035	0.007	**0.202**	0.045	**0.081**	**0.051**	0.022
Córrego dos Borges Fm. (Santos et al., 2015) - Sample PE-SC-42	**0.075**	0.000	0.000	0.043	0.000	0.000	**0.204**
Córrego dos Borges Fm. (Santos et al., 2015) - Sample PE-JQ-52	0.022	0.000	0.003	0.022	0.000	0.000	**0.994**
Córrego Pereira Fm. (Chemale Jr et al., 2012) – PE-SM-26	0.000	0.000	0.000	0.000	0.000	0.000	0.001
Córrego Pereira Fm. (Santos et al., 2015) - Sample PE-CM-18	0.000	0.000	0.000	0.000	0.000	0.000	**0.126**
Rio Pardo Grande Fm. (Chemale Jr et al., 2012) – PE-CM-35	0.000	0.000	0.000	0.000	0.000	0.000	**0.053**
Rio Pardo Grande Fm. (Santos et al., 2015) - Sample PE-CM-54	0.000	0.000	0.000	0.000	0.000	0.000	**0.478**

KS-Test results for our samples and individual samples from studies about units from the Espinhaço Supergroup (cont.).

Sample/Espinhaço	Santa Rita Fm. (Chemale Jr et al., 2012)	Santa Rita Fm. (Santos et al., 2015) - Sample PE-CM-17	Santa Rita Fm. (Santos et al., 2015) - Sample PE-CM-16-SR	Córrego dos Borges Fm. (Chemale Jr et al., 2012) – PE-CM-19	Córrego dos Borges Fm. (Santos et al., 2015) - Sample PE-CM-20	Córrego dos Borges Fm. (Santos et al., 2015) - Sample PE-SC-42	Córrego dos Borges Fm. (Santos et al., 2015) - Sample PE-JQ-52
HJ 4	**0.102**	0.001	**0.178**	0.000	0.001	0.001	0.000
HJ 110B	**0.695**	0.001	**0.324**	0.000	**0.208**	0.000	0.000
HJ 129	**0.789**	0.000	**0.081**	0.000	0.044	0.000	0.000
HJ 152	**0.296**	0.005	**0.601**	0.000	0.009	0.004	0.000
HJ 160B	**0.232**	0.001	0.047	0.000	**0.168**	0.000	0.000
Galho do Miguel Fm. (Chemale Jr et al., 2012) – PE-GU-40	**0.524**	0.005	**0.057**	0.000	0.041	0.000	0.000
Galho do Miguel Fm. (Santos, 2015) – PE-CM-14	**0.175**	0.014	0.025	0.000	**0.157**	0.001	0.000
Galho do Miguel Fm. (Santos, 2015) – PE-CM-15A	**0.955**	0.049	**0.942**	0.001	**0.246**	0.007	0.001
Galho do Miguel Fm. (Santos, 2015) – PE-CM-15B	**0.089**	0.000	0.008	0.000	0.028	0.000	0.000
Galho do Miguel Fm. (Santos, 2015) – PE-SC-43	**0.084**	0.025	0.017	0.005	0.035	**0.075**	0.022
Galho do Miguel Fm. (Santos, 2015) – PE-SC-45	**0.384**	0.001	**0.830**	0.000	0.007	0.000	0.000
Galho do Miguel Fm. (Santos, 2015) – PE-SC-48	**0.215**	0.002	0.037	0.000	**0.202**	0.000	0.003
Galho do Miguel Fm. (Santos, 2015) – PE-FM-71	**0.064**	**0.167**	0.021	0.005	0.045	0.043	0.022
Galho do Miguel Fm. (Souza et al., 2019) – CL-03	**0.115**	0.000	0.004	0.000	**0.081**	0.000	0.000
Galho do Miguel Fm. (Souza et al., 2019) – IT-95	**0.134**	0.000	0.015	0.000	**0.051**	0.000	0.000
Galho do Miguel Fm. (Oliveira et al., 2021) – DB 04	0.013	**0.148**	0.000	**0.964**	0.022	**0.204**	**0.994**

KS-Test results for our samples and individual samples from studies about units from the Espinhaço Supergroup (cont.).

Sample/Espinhaço	Santa Rita Fm. (Chemale Jr et al., 2012)	Santa Rita Fm. (Santos et al., 2015) - Sample PE-CM-17	Santa Rita Fm. (Santos et al., 2015) - Sample PE-CM-16-SR	Córrego dos Borges Fm. (Chemale Jr et al., 2012) – PE-CM-19	Córrego dos Borges Fm. (Santos et al., 2015) - Sample PE-CM-20	Córrego dos Borges Fm. (Santos et al., 2015) - Sample PE-SC-42	Córrego dos Borges Fm. (Santos et al., 2015) - Sample PE-JQ-52
Santa Rita Fm. (Chemale Jr et al., 2012)	-	**0.085**	**0.895**	0.010	**0.927**	0.019	0.018
Santa Rita Fm. (Santos et al., 2015) - Sample PE-CM-17	**0.085**	-	0.002	**0.405**	0.023	0.012	**0.316**
Santa Rita Fm. (Santos et al., 2015) - Sample PE-CM-16-SR	**0.895**	0.002	-	0.000	**0.231**	0.000	0.000
Córrego dos Borges Fm. (Chemale Jr et al., 2012) – PE-CM-19	0.010	**0.405**	0.000	-	0.003	**0.119**	**0.901**
Córrego dos Borges Fm. (Santos et al., 2015) - Sample PE-CM-20	**0.927**	0.023	**0.231**	0.003	-	0.004	0.046
Córrego dos Borges Fm. (Santos et al., 2015) - Sample PE-SC-42	0.019	0.012	0.000	**0.119**	0.004	-	**0.328**
Córrego dos Borges Fm. (Santos et al., 2015) - Sample PE-JQ-52	0.018	**0.316**	0.000	**0.901**	0.046	**0.328**	-
Córrego Pereira Fm. (Chemale Jr et al., 2012) – PE-SM-26	0.000	0.000	0.000	0.000	0.000	0.000	0.001
Córrego Pereira Fm. (Santos et al., 2015) - Sample PE-CM-18	0.000	0.007	0.000	0.011	0.001	0.032	**0.221**
Rio Pardo Grande Fm. (Chemale Jr et al., 2012) – PE-CM-35	0.000	0.000	0.000	0.000	0.000	0.000	0.039
Rio Pardo Grande Fm. (Santos et al., 2015) - Sample PE-CM-54	0.000	0.001	0.000	**0.080**	0.000	0.026	**0.455**

KS-Test results for our samples and individual samples from studies about units from the Espinhaço Supergroup (cont.).

Sample/Espinhaço	Córrego Pereira Fm. (Chemale Jr et al., 2012) – PE-SM-26	Córrego Pereira Fm. (Santos et al., 2015) - Sample PE-CM-18	Rio Pardo Grande Fm. (Chemale Jr et al., 2012) – PE-CM-35	Rio Pardo Grande Fm. (Santos et al., 2015) - Sample PE-CM-54
HJ 4	0.000	0.000	0.000	0.000
HJ 110B	0.000	0.000	0.000	0.000
HJ 129	0.000	0.000	0.000	0.000
HJ 152	0.000	0.000	0.000	0.000
HJ 160B	0.000	0.000	0.000	0.000
Galho do Miguel Fm. (Chemale Jr et al., 2012) – PE-GU-40	0.000	0.000	0.000	0.000
Galho do Miguel Fm. (Santos, 2015) – PE-CM-14	0.000	0.000	0.000	0.000
Galho do Miguel Fm. (Santos, 2015) – PE-CM-15A	0.000	0.000	0.000	0.000
Galho do Miguel Fm. (Santos, 2015) – PE-CM-15B	0.000	0.000	0.000	0.000
Galho do Miguel Fm. (Santos, 2015) – PE-SC-43	0.000	0.000	0.000	0.000
Galho do Miguel Fm. (Santos, 2015) – PE-SC-45	0.000	0.000	0.000	0.000
Galho do Miguel Fm. (Santos, 2015) – PE-SC-48	0.000	0.000	0.000	0.000
Galho do Miguel Fm. (Santos, 2015) – PE-FM-71	0.000	0.000	0.000	0.000
Galho do Miguel Fm. (Souza et al., 2019) – CL-03	0.000	0.000	0.000	0.000
Galho do Miguel Fm. (Souza et al., 2019) – IT-95	0.000	0.000	0.000	0.000
Galho do Miguel Fm. (Oliveira et al., 2021) – DB 04	0.001	**0.126**	**0.053**	**0.478**

KS-Test results for our samples and individual samples from studies about units from the Espinhaço Supergroup (cont.).

Sample/Espinhaço	Córrego Pereira Fm. (Chemale Jr et al., 2012) – PE-SM-26	Córrego Pereira Fm. (Santos et al., 2015) - Sample PE-CM-18	Rio Pardo Grande Fm. (Chemale Jr et al., 2012) – PE-CM-35	Rio Pardo Grande Fm. (Santos et al., 2015) - Sample PE-CM-54
Santa Rita Fm. (Chemale Jr et al., 2012)	0.000	0.000	0.000	0.000
Santa Rita Fm. (Santos et al., 2015) - Sample PE-CM-17	0.000	0.007	0.000	0.001
Santa Rita Fm. (Santos et al., 2015) - Sample PE-CM-16-SR	0.000	0.000	0.000	0.000
Córrego dos Borges Fm. (Chemale Jr et al., 2012) – PE-CM-19	0.000	0.011	0.000	**0.080**
Córrego dos Borges Fm. (Santos et al., 2015) - Sample PE-CM-20	0.000	0.001	0.000	0.000
Córrego dos Borges Fm. (Santos et al., 2015) - Sample PE-SC-42	0.000	0.032	0.000	0.026
Córrego dos Borges Fm. (Santos et al., 2015) - Sample PE-JQ-52	0.001	**0.221**	0.039	**0.455**
Córrego Pereira Fm. (Chemale Jr et al., 2012) – PE-SM-26	-	0.004	0.000	**0.088**
Córrego Pereira Fm. (Santos et al., 2015) - Sample PE-CM-18	0.004	-	**0.473**	**0.583**
Rio Pardo Grande Fm. (Chemale Jr et al., 2012) – PE-CM-35	0.000	**0.473**	-	0.017
Rio Pardo Grande Fm. (Santos et al., 2015) - Sample PE-CM-54	**0.088**	**0.583**	0.017	-

APPENDIX F – *IN SITU* RB-SR DATING RESULTS TABLE

***In situ* Rb-Sr analyses – Results for Sample HJ 98B.**

Spot	Uncorrected matrix						Matrix corrected ratios				ρ
	$^{87}Rb/^{87}Sr$	$^{87}Rb/^{87}Sr$ (2SE, int)	$^{87}Rb/^{86}Sr$	$^{87}Rb/^{86}Sr$ (2SE, int)	$^{87}Sr/^{86}Sr$	$^{87}Sr/^{86}Sr$ (2SE, int)	$^{87}Rb/^{86}Sr$	$^{87}Rb/^{86}Sr$ (2SE, prop)	$^{87}Sr/^{86}Sr$	$^{87}Sr/^{86}Sr$ (2SE, prop)	
1.d	79.374	1.265	145.199	3.035	1.802	0.048	131.521	3.956	1.802	0.048	0.800
2.d	81.519	1.288	159.890	3.915	1.923	0.051	144.827	4.732	1.923	0.051	0.813
3.d	77.729	1.099	142.031	2.891	1.796	0.043	128.651	3.821	1.796	0.043	0.807
4.d	71.741	1.160	118.486	2.498	1.627	0.043	107.324	3.242	1.627	0.043	0.791
5.d	75.147	1.147	136.648	2.707	1.786	0.045	123.775	3.631	1.786	0.045	0.791
6.d	64.060	0.940	96.495	1.884	1.473	0.033	87.405	2.547	1.473	0.033	0.766
7.d	73.728	0.969	131.803	2.843	1.754	0.042	119.386	3.647	1.754	0.042	0.840
8.d	72.626	1.202	122.699	2.431	1.662	0.042	111.141	3.260	1.662	0.042	0.760
9.d	75.665	1.145	130.916	2.787	1.706	0.044	118.583	3.599	1.706	0.044	0.813
10.d	76.219	1.250	137.456	3.387	1.779	0.051	124.507	4.082	1.779	0.051	0.820
11.d	75.996	1.249	136.035	2.746	1.776	0.048	123.220	3.646	1.776	0.048	0.799
12.d	77.500	2.287	135.804	5.221	1.744	0.088	123.011	5.427	1.744	0.088	0.810
13.d	76.003	1.338	137.116	2.983	1.792	0.049	124.199	3.810	1.792	0.049	0.770
14.d	77.700	1.125	144.986	3.362	1.822	0.048	131.328	4.165	1.822	0.048	0.838
15.d	78.090	1.223	150.484	3.220	1.882	0.045	136.308	4.148	1.882	0.045	0.767
16.d	77.175	1.026	142.368	3.033	1.800	0.039	128.956	3.916	1.800	0.039	0.808
17.d	75.541	1.471	130.571	3.264	1.694	0.043	118.271	3.910	1.694	0.043	0.700
18.d	66.336	0.866	104.742	1.795	1.552	0.033	94.875	2.618	1.552	0.033	0.791
19.d	68.182	0.922	109.703	1.831	1.573	0.032	99.369	2.715	1.573	0.032	0.744
20.d	73.490	1.139	128.949	2.665	1.723	0.046	116.802	3.495	1.723	0.046	0.819
21.d	71.642	1.011	124.594	2.499	1.698	0.039	112.857	3.329	1.698	0.039	0.795
22.d	75.085	1.210	137.026	2.640	1.774	0.046	124.118	3.596	1.774	0.046	0.784
23.d	77.181	1.351	139.117	2.888	1.756	0.045	126.012	3.778	1.756	0.045	0.732
24.d	78.474	1.047	147.259	2.734	1.826	0.038	133.387	3.803	1.826	0.038	0.772
25.d	76.251	1.272	141.153	2.708	1.811	0.043	127.856	3.697	1.811	0.043	0.712
26.d	75.372	1.212	135.125	2.813	1.742	0.042	122.396	3.675	1.742	0.042	0.755

***In situ* Rb-Sr analyses – Results for Sample HJ 98B (cont.).**

Spot	Uncorrected matrix						Matrix corrected ratios				ρ
	$^{87}Rb/^{87}Sr$	$^{87}Rb/^{87}Sr$ (2SE, int)	$^{87}Rb/^{86}Sr$	$^{87}Rb/^{86}Sr$ (2SE, int)	$^{87}Sr/^{86}Sr$	$^{87}Sr/^{86}Sr$ (2SE, int)	$^{87}Rb/^{86}Sr$	$^{87}Rb/^{86}Sr$ (2SE, prop)	$^{87}Sr/^{86}Sr$	$^{87}Sr/^{86}Sr$ (2SE, prop)	
27.d	77.748	1.266	142.697	3.222	1.789	0.044	129.254	4.042	1.789	0.044	0.768
28.d	73.950	1.198	133.397	2.507	1.764	0.043	120.831	3.462	1.764	0.043	0.751
29.d	73.493	1.339	123.144	2.384	1.642	0.041	111.543	3.238	1.642	0.041	0.687
30.d	78.557	1.221	145.903	2.953	1.809	0.042	132.158	3.915	1.809	0.042	0.756
31.d	73.558	1.210	127.742	2.454	1.695	0.038	115.708	3.348	1.695	0.038	0.695
32.d	82.927	1.297	169.385	4.021	1.993	0.056	153.428	4.927	1.993	0.056	0.831
33.d	74.778	1.128	138.987	3.314	1.818	0.052	125.894	4.053	1.818	0.052	0.852
34.d	76.297	1.126	141.992	3.343	1.810	0.046	128.616	4.112	1.810	0.046	0.821
35.d	80.523	1.343	147.489	2.971	1.811	0.046	133.595	3.949	1.811	0.046	0.759
36.d	76.675	1.142	144.345	2.769	1.847	0.043	130.747	3.781	1.847	0.043	0.767
37.d	64.635	1.005	100.098	1.928	1.527	0.037	90.668	2.626	1.527	0.037	0.767
38.d	79.066	1.209	150.081	3.113	1.874	0.049	135.943	4.074	1.874	0.049	0.813
39.d	76.312	1.263	135.471	2.930	1.754	0.047	122.709	3.754	1.754	0.047	0.786
40.d	68.802	1.008	113.033	2.220	1.605	0.039	102.385	2.991	1.605	0.039	0.796
41.d	80.063	1.267	157.091	3.762	1.913	0.046	142.293	4.592	1.913	0.046	0.784
42.d	79.391	1.286	155.193	3.062	1.911	0.044	140.573	4.116	1.911	0.044	0.722
43.d	77.610	1.356	142.386	2.888	1.786	0.037	128.973	3.825	1.786	0.037	0.634
44.d	83.591	1.318	172.146	3.629	2.017	0.051	155.929	4.710	2.017	0.051	0.780
45.d	79.757	1.196	148.987	3.231	1.835	0.049	134.952	4.134	1.835	0.049	0.825
46.d	69.355	1.086	114.972	2.356	1.622	0.040	104.142	3.103	1.622	0.040	0.770
47.d	75.595	1.175	137.465	3.081	1.785	0.048	124.515	3.879	1.785	0.048	0.817
48.d	70.062	1.017	114.963	2.476	1.601	0.037	104.133	3.179	1.601	0.037	0.791
49.d	76.167	1.057	142.205	2.514	1.839	0.043	128.809	3.599	1.839	0.043	0.800
50.d	78.720	1.281	147.665	3.630	1.830	0.053	133.754	4.380	1.830	0.053	0.826
51.d	71.089	1.081	117.568	2.297	1.615	0.040	106.493	3.104	1.615	0.040	0.792

***In situ* Rb-Sr analyses – Results for Sample HJ 98 (cont.).**

Spot	Uncorrected matrix						Matrix corrected ratios				ρ
	$^{87}Rb/^{87}Sr$	$^{87}Rb/^{87}Sr$ (2SE, int)	$^{87}Rb/^{86}Sr$	$^{87}Rb/^{86}Sr$ (2SE, int)	$^{87}Sr/^{86}Sr$	$^{87}Sr/^{86}Sr$ (2SE, int)	$^{87}Rb/^{86}Sr$	$^{87}Rb/^{86}Sr$ (2SE, prop)	$^{87}Sr/^{86}Sr$	$^{87}Sr/^{86}Sr$ (2SE, prop)	
52.d	74.749	1.146	129.431	2.774	1.699	0.047	117.238	3.570	1.699	0.047	0.837
53.d	75.220	1.362	131.150	2.626	1.713	0.039	118.795	3.502	1.713	0.039	0.653
54.d	74.342	1.277	127.272	3.168	1.681	0.044	115.283	3.802	1.681	0.044	0.778
55.d	71.156	1.099	119.891	2.216	1.640	0.038	108.597	3.090	1.640	0.038	0.745
58.d	74.756	1.205	131.195	2.628	1.716	0.039	118.836	3.504	1.716	0.039	0.721
59.d	83.229	1.383	170.035	3.818	1.995	0.053	154.017	4.802	1.995	0.053	0.780
60.d	70.229	1.057	121.703	2.621	1.695	0.045	110.238	3.365	1.695	0.045	0.820

***In situ* Rb-Sr analyses – Reference material.**

Spot	Uncorrected matrix				Matrix corrected ratios			
	$^{87}Rb/^{87}Sr$ (2SE, int)	$^{87}Rb/^{86}Sr$ (2SE, int)	$^{87}Sr/^{86}Sr$	$^{87}Sr/^{86}Sr$ (2SE, int)	$^{87}Rb/^{86}Sr$	$^{87}Rb/^{86}Sr$ (2SE, prop)	$^{87}Sr/^{86}Sr$	$^{87}Sr/^{86}Sr$ (2SE, prop)
610 - 2.d	2.389	0.009	0.710	0.003				
610 - 3.d	2.394	0.011	0.709	0.003				
610 - 4.d	2.385	0.011	0.710	0.003				
610 - 5.d	2.393	0.011	0.708	0.003				
610 - 6.d	2.389	0.011	0.711	0.002				
610 - 7.d	2.390	0.011	0.709	0.002				
610 - 8.d	2.391	0.012	0.710	0.003				
610 - 9.d	2.390	0.012	0.710	0.003				
610 - 18.d	2.391	0.011	0.711	0.003				
610 - 19.d	2.388	0.013	0.709	0.003				
610 - 20.d	2.391	0.010	0.709	0.003				
610 - 21.d	2.390	0.012	0.710	0.003				
610 - 22.d	2.391	0.013	0.709	0.003				
610 - 23.d	2.389	0.013	0.708	0.003				

***In situ* Rb-Sr analyses – Reference material (cont.).**

Spot	Uncorrected matrix				Matrix corrected ratios			
	$^{87}Rb/^{87}Sr$ (2SE, int)	$^{87}Rb/^{86}Sr$ (2SE, int)	$^{87}Sr/^{86}Sr$	$^{87}Sr/^{86}Sr$ (2SE, int)	$^{87}Rb/^{86}Sr$	$^{87}Rb/^{86}Sr$ (2SE, prop)	$^{87}Sr/^{86}Sr$	$^{87}Sr/^{86}Sr$ (2SE, prop)
610 - 24.d	2.391	0.010	0.712	0.002				
610 - 25.d	2.389	0.010	0.710	0.003				
610 - 26.d	2.392	0.011	0.709	0.003				
610 - 27.d	2.388	0.011	0.708	0.003				
610 - 28.d	2.391	0.011	0.710	0.003				
612 - 1.d	1.171	0.013	0.711	0.006				
612 - 2.d	1.171	0.014	0.715	0.007				
612 - 3.d	1.147	0.014	0.707	0.008				
612 - 4.d	1.182	0.014	0.712	0.006				
612 - 5.d	1.179	0.015	0.715	0.007				
612 - 6.d	1.177	0.014	0.720	0.007				
612 - 7.d	1.165	0.014	0.707	0.007				
612 - 8.d	1.174	0.013	0.706	0.007				
612 - 9.d	1.178	0.014	0.716	0.008				
612 - 10.d	1.171	0.012	0.709	0.008				
612 - 11.d	1.167	0.014	0.708	0.007				
612 - 12.d	1.176	0.013	0.708	0.006				
612 - 13.d	1.149	0.014	0.711	0.006				
612 - 14.d	1.152	0.015	0.708	0.007				
612 - 15.d	1.161	0.013	0.709	0.007				
612 - 16.d	1.156	0.013	0.711	0.007				
612 - 17.d	1.142	0.011	0.702	0.008				
612 - 18.d	1.164	0.015	0.710	0.006				
612 - 19.d	1.172	0.012	0.711	0.007				
612 - 20.d	1.165	0.013	0.710	0.007				
612 - 21.d	1.169	0.014	0.710	0.006				
612 - 22.d	1.171	0.016	0.709	0.007				
612 - 23.d	1.181	0.012	0.714	0.007				

***In situ* Rb-Sr analyses – Reference material (cont.).**

Spot	Uncorrected matrix				Matrix corrected ratios			
	$^{87}Rb/^{87}Sr$ (2SE, int)	$^{87}Rb/^{86}Sr$ (2SE, int)	$^{87}Sr/^{86}Sr$	$^{87}Sr/^{86}Sr$ (2SE, int)	$^{87}Rb/^{86}Sr$	$^{87}Rb/^{86}Sr$ (2SE, prop)	$^{87}Sr/^{86}Sr$	$^{87}Sr/^{86}Sr$ (2SE, prop)
612 - 24.d	1.161	0.012	0.706	0.007				
612 - 25.d	1.152	0.012	0.714	0.007				
612 - 26.d	1.165	0.014	0.713	0.007				
612 - 27.d	1.169	0.014	0.713	0.008				
612 - 28.d	1.162	0.014	0.711	0.007				
MicaMg - 1.d	169.998	2.795	1.876	0.027	153.984	4.184	1.876	0.027
MicaMg - 2.d	176.029	2.796	1.856	0.028	159.447	4.279	1.856	0.028
MicaMg - 3.d	176.809	3.567	1.906	0.034	160.153	4.738	1.906	0.034
MicaMg - 4.d	176.427	2.844	1.874	0.030	159.807	4.311	1.874	0.030
MicaMg - 5.d	169.956	2.516	1.854	0.028	153.946	4.036	1.854	0.028
MicaMg - 6.d	173.520	3.290	1.839	0.035	157.174	4.521	1.839	0.035
MicaMg - 7.d	176.565	2.597	1.899	0.027	159.932	4.184	1.899	0.027
MicaMg - 8.d	174.926	2.937	1.872	0.033	158.447	4.339	1.872	0.033
MicaMg - 9.d	171.383	3.156	1.864	0.036	155.238	4.410	1.864	0.036
MicaMg - 10.d	174.440	2.953	1.875	0.029	158.007	4.341	1.875	0.029
MicaMg - 11.d	168.152	3.015	1.889	0.036	152.312	4.280	1.889	0.036
MicaMg - 12.d	173.499	2.759	1.874	0.033	157.155	4.219	1.874	0.033
MicaMg - 13.d	173.133	2.281	1.866	0.033	156.824	3.972	1.866	0.033
MicaMg - 14.d	172.850	2.816	1.883	0.034	156.567	4.240	1.883	0.034
MicaMg - 15.d	169.714	4.428	1.846	0.030	153.726	5.210	1.846	0.030
MicaMg - 16.d	169.926	2.405	1.841	0.029	153.919	3.979	1.841	0.029
MicaMg - 17.d	159.117	5.963	1.777	0.046	144.127	6.237	1.777	0.046
MicaMg - 18.d	170.379	2.691	1.868	0.031	154.328	4.134	1.868	0.031
MicaMg - 19.d	175.964	2.963	1.874	0.034	159.387	4.370	1.874	0.034
MicaMg - 20.d	171.846	2.785	1.846	0.032	155.658	4.208	1.846	0.032
MicaMg - 21.d	175.355	2.614	1.846	0.028	158.836	4.173	1.846	0.028

***In situ* Rb-Sr analyses – Reference material (cont.).**

Spot	Uncorrected matrix				Matrix corrected ratios			
	$^{87}Rb/^{87}Sr$ (2SE, int)	$^{87}Rb/^{86}Sr$ (2SE, int)	$^{87}Sr/^{86}Sr$	$^{87}Sr/^{86}Sr$ (2SE, int)	$^{87}Rb/^{86}Sr$	$^{87}Rb/^{86}Sr$ (2SE, prop)	$^{87}Sr/^{86}Sr$	$^{87}Sr/^{86}Sr$ (2SE, prop)
MicaMg - 22.d	176.798	3.121	1.876	0.029	160.143	4.471	1.876	0.029
MicaMg - 23.d	174.996	3.124	1.884	0.028	158.510	4.446	1.884	0.028
MicaMg - 24.d	177.813	2.372	1.901	0.031	161.063	4.093	1.901	0.031
MicaMg - 25.d	171.937	2.506	1.835	0.030	155.740	4.062	1.835	0.030
MicaMg - 26.d	176.094	2.497	1.878	0.031	159.505	4.126	1.878	0.031
MicaMg - 27.d	173.534	3.272	1.897	0.036	157.186	4.511	1.897	0.036
MicaMg - 28.d	176.170	2.992	1.927	0.036	159.574	4.389	1.927	0.036
CK001 - 1.d	1585.955	126.178	9.163	0.707	1436.553	118.441	9.163	0.707
CK001 - 2.d	630.286	40.570	4.044	0.245	570.911	38.768	4.044	0.245
CK001 - 3.d	1220.945	64.743	7.346	0.392	1105.929	63.336	7.346	0.392
CK001 - 4.d	758.652	40.438	4.798	0.252	687.184	39.531	4.798	0.252
CK001 - 5.d	71.360	5.702	1.112	0.042	64.638	5.350	1.112	0.042
CK001 - 6.d	705.775	40.005	4.304	0.230	639.289	38.786	4.304	0.230
CK001 - 7.d	611.656	36.110	3.904	0.201	554.036	34.835	3.904	0.201
CK001 - 8.d	1234.231	81.960	7.437	0.495	1117.963	78.079	7.437	0.495
CK001 - 9.d	1051.249	59.786	6.394	0.373	952.219	57.940	6.394	0.373
CK001 - 10.d	1568.797	117.818	9.302	0.729	1421.012	111.059	9.302	0.729
CK001 - 11.d	1512.876	106.617	8.740	0.621	1370.359	101.021	8.740	0.621
CK001 - 12.d	1194.697	58.142	7.091	0.386	1082.153	57.633	7.091	0.386
CK001 - 13.d	1063.663	49.186	6.418	0.320	963.463	49.187	6.418	0.320
CK001 - 14.d	897.140	40.471	5.516	0.278	812.627	40.655	5.516	0.278
CK001 - 15.d	1065.046	58.934	6.468	0.382	964.716	57.317	6.468	0.382
CK001 - 16.d	871.845	41.527	5.157	0.239	789.714	41.313	5.157	0.239
CK001 - 17.d	538.255	27.814	3.636	0.171	487.550	27.313	3.636	0.171
CK001 - 18.d	861.791	43.610	5.417	0.253	780.608	42.960	5.417	0.253
CK001 - 19.d	1280.181	73.785	7.529	0.440	1159.584	71.387	7.529	0.440
CK001 - 20.d	920.852	68.748	5.582	0.394	834.105	64.833	5.582	0.394
CK001 - 21.d	1505.068	108.471	8.559	0.593	1363.286	102.583	8.559	0.593

***In situ* Rb-Sr analyses – Reference material (cont.).**

Spot	Uncorrected matrix				Matrix corrected ratios			
	$^{87}Rb/^{87}Sr$ (2SE, int)	$^{87}Rb/^{86}Sr$ (2SE, int)	$^{87}Sr/^{86}Sr$	$^{87}Sr/^{86}Sr$ (2SE, int)	$^{87}Rb/^{86}Sr$	$^{87}Rb/^{86}Sr$ (2SE, prop)	$^{87}Sr/^{86}Sr$	$^{87}Sr/^{86}Sr$ (2SE, prop)
CK001 - 22.d	292.961	13.582	2.244	0.088	265.364	13.576	2.244	0.088
CK001 - 23.d	1433.199	119.958	8.368	0.707	1298.188	112.228	8.368	0.707
CK001 - 24.d	1174.383	77.045	6.889	0.445	1063.753	73.483	6.889	0.445
CK001 - 25.d	1048.146	53.433	6.418	0.347	949.407	52.577	6.418	0.347